Studies of the dosimetric verification of intensity modulated radiotherapy

Andrew G Glendinning

Thesis submitted to the
University of Leicester
for the award of
Doctor of Philosophy

Department of Medical Physics
Faculty of Medicine
University of Leicester
LEICESTER UK

2001

ProQuest LLC
789 East Eisenhower Parkway
P.O. Box 1346
Ann Arbor, MI 48106-1346

Studies of the dosimetric verification of intensity modulated radiotherapy

Andrew G Glendinning

The ability to verify absorbed dose distributions produced by intensity modulated radiotherapy (IMRT) using dynamic multileaf collimation is of great concern in the clinical application of this technique. This thesis investigates two approaches using an Elekta SL*i* linear accelerator operating in dynamic mode (Elekta Oncology Systems, Crawley, UK).

A novel strip ionisation chamber array, located at the beam aperture, was designed and used in conjunction with a specialised electrometer. This also recorded cumulative accelerator monitor units (MU) via an isolated interface to the accelerator. The chamber signal, recorded as a function of MU, proved suitable for collimator position verification for the case of a dynamic wedge, but was found not to be suitable for more general cases in which the leaves moved independently.

A tube camera-based electronic portal imaging device (EPID) (Theraview™, Cablon Medical, Leusden, The Netherlands) was investigated in a further approach to verification. This EPID has not been previously studied for dosimetry and several unreported effects associated with the video system were identified. The phosphor Gd_2O_2S:Tb, which is used as the x-ray detector, was also studied by direct measurements of luminescence using a photomultiplier tube. It was confirmed that the optical signal was independent of accelerator pulse repetition frequency, and that there was no long-lived luminescence (afterglow) following prolonged irradiation, which is of concern in dosimetry of dynamic deliveries. The EPID was applied to the verification of collimator position using a specially constructed camera interface that triggered recording of the cumulative MU. The EPID was also assessed as a method of measuring the integrated dose distribution delivered during a dynamic sequence, and a method proposed to overcome unreliable triggering of image acquisition in such cases. Dark current and persistence of the camera target were found to complicate measurements. Images were also found to exhibit optical scattering, which is an inherent characteristic of camera-based EPIDs. Results of a physical means of reducing the effect using an optical rejection screen were compared to an ionisation chamber for static and dynamic cases, and it was shown that the optical rejection screen is limited in its effectiveness in removing optical scatter. Dose profiles obtained from the EPID agree with ionisation chamber measurements in-air within 6 % for plain fields, and within 15-25 % for static and dynamically produced wedged fields.

It was concluded that both approaches studied can be applied to the verification of IMRT but with limitations, and that an ideal system has yet to be found.

Statement of Originality

The material contained within this thesis which is presented without reference to the work of others is original. I have personally undertaken this work between the period January 1998 and January 2001 at the Department of Medical Physics, University of Leicester. The material has not been presented previously for a Higher Degree. Some of the material presented in this thesis is contained within:

Glendinning,AG; Bonnett,DE (2000a): Dosimetric properties of the Theraview™ fluoroscopic electronic portal imaging device. Brit. J. Radiol. 73, 517-530. *(Chapter 5)*

Glendinning,AG; Bonnett,DE (2000b): Dosimetric properties of the Theraview electronic portal imaging device. Proc. 6th International Workshop on Electronic Portal Imaging (EPI 2K), June 5-7th 2000, Brussels, Belgium, 79. Academic Hospital - Free University, Brussels, Belgium. *(Chapter 5)*

Glendinning,AG; Hunt,SG; Bonnett,DE (2001a): A method for controlling image acquisition in electronic portal imaging devices. Phys. Med. Biol. 46, N39-N44. *(Chapter 7)*

Glendinning,AG; Hunt,SG; Bonnett,DE (2001b): Measurement of the response of Gd_2O_2S:Tb phosphor to 6MV x-rays. Phys. Med. Biol. 46, 517-530. *(Chapter 4)*

Glendinning,AG; Hunt,SG; Bonnett,DE (2001c): Recording accelerator monitor units during electronic portal imaging: application to collimator position verification in IMRT. Phys. Med. Biol. 46, N159-N167. *(Chapter 6)*

Acknowledgements

I am grateful to Professor David Evans, Head of Medical Physics, for supporting this project together with providing excellent facilities within the Department of Medical Physics. I am very grateful for the award of a Research Fellowship from Leicester Royal Infirmary NHS Trust which supported the first two years of this study. It is my hope that this work will improve in some way the outcome of radiotherapy treatment in cancer patients.

There are many people I must acknowledge both at Leicester and elsewhere. The work reported uses in part a purpose-built dosimetry system, which was designed in conjunction with Steve Hunt who constructed the system. I am very grateful to Steve for the tremendous effort involved in constructing the system, for his flair in electronics development and for his expert knowledge of linear accelerator technology from which I have learned much. I am also grateful to others from the Instrumentation section, particularly Troy Johnson for his knowledge of Suns and networks, and Mick Squires from the mechanical workshop for modifying the Theraview elbow and many other jobs!

I must acknowledge Jürgen Meyer at Coventry University for machining the strip ionisation chamber. Thanks also to Cablon Medical (Leusden, The Netherlands) and Mike Sweeney of Qados (Sandhurst, UK) for loan of a Theraview elbow. I must acknowledge Elekta Oncology Systems (Crawley, UK) for release of the software and the upgrade of an SL15*i* at Leicester to allow dynamic multileaf collimation. I must also thank Geoff Budgell and Judith Mott (Christie Hospital, Manchester) for advice on the Elekta IMRT system and providing several dynamic prescriptions.

Thanks also to Dr Mike Kirby (Royal Preston Hospital) for useful discussions regarding the SRI-100/*i*View EPIDs. I must also thank Professor Sue Bayliss (De Montfort University, Leicester), Dr Martin Yaffe (University of Toronto, Ontario,

Canada) and Dr Peter Munro (London Regional Cancer, Ontario, Canada) for assistance and discussions regarding Gd_2O_2S:Tb luminescence measurements. Also thanks to Dr Herb Zeman (University of Memphis, Tennessee, USA) for information on his CsI:Tl camera-based EPID.

From a practical point of view in terms of getting experimental time on the three linear accelerators, I must thank the Radiographers at Leicester who tried their very best to accommodate myself and my equipment! I also have to thank Joan Mowbray, Research Radiographer, for her encouragement and for sharing her experience using the EPID clinically.

I am very grateful to Dr David Bonnett who supported my application for a Research Fellowship in order to commence this work, and who has provided day-to-day supervision throughout the inevitable up and downs. David has also read and advised on several drafts of this present text without complaint!

Finally, I have to thank my parents for their steadfast confidence in my abilities throughout all my studies, and my wife, Sarah, for her love, patience and support. Sarah's interest in the work has never wavered during the three years of study which must have seemed *much* longer as I have almost constantly relayed plans for and progress of the work (or lack of it!). Without her help the work would have seemed overwhelming.

Studies of the dosimetric verification of intensity modulated radiotherapy

List of Figures

List of Tables

Chapter 1. Introduction

1.1 Intensity modulated radiotherapy

1.1.1 Clinical basis for conformal and intensity modulated radiotherapy

The accurate and controlled delivery of a prescribed dose of radiation is the aim of radiotherapy. However, inherent to the delivery of therapeutic radiation is a compromise between irradiation of the intended target to a dose sufficient to effect cure, and minimising damage to surrounding normal tissues. The situation is described by classic sigmoid dose response curves for the tissues involved which relate the probability of tumour control and normal tissue complication to the dose delivered (Figure 1-1).

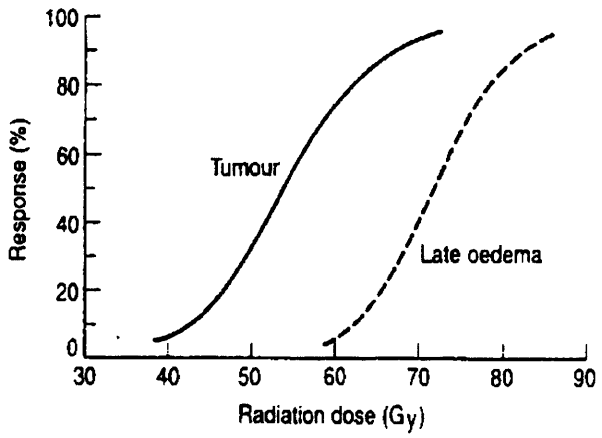

Figure 1-1: Dose response curves for local control of laryngeal carcinoma and late laryngeal oedema. Data is for conventional treatment over a six week time interval [taken from Steel (1997) p83].

Excessive irradiation of normal tissues is to be avoided since it may generate such extreme acute reactions as to necessitate a reduction or compromise in the original prescription. This would inevitably lead to a loss in local control of the tumour (Royal College of Radiologists 1996). Furthermore, excessive exposure of normal tissues may also result in irrecoverable normal tissue complications, although such effects can be reduced by limiting the volume of normal tissue irradiated (Emami *et al.* 1991).

There is potential benefit, therefore, in terms of tumour control and normal tissue complication, of shaping or *conforming* uniform regions of high dose closely to the targeted structures whilst reducing the volume of normal tissues irradiated to therapeutic levels. The technique is known as conformal radiotherapy (Tait 1990) and may allow additional clinical benefit through escalation of tumour dose levels (Leibel *et al.* 1991). Conformal dose delivery of each treatment portal can be achieved using patient-specific field shaping blocks or the use of a multileaf collimator (MLC, e.g. Jordan & Williams 1994). A further treatment technique achievable with computer controlled linear accelerators is that of using treatment fields in which the distribution of incident radiation is varied in the plane perpendicular to the beam direction. Combining such beams may allow a complex three-dimensional dose distribution to be achieved. Such beams can be designed through inverse planning techniques which allow calculation of the two-dimensional dose distribution (or intensity modulated beam, IMB) required for each portal based on the three-dimensional dose distribution desired (Mohan *et al.* 1994). Using this approach it is possible to achieve dose distributions conforming in three dimensions to irregularly shaped target volumes. Both Purdy (1996) and Webb (1998) have described the technique, which is known as intensity modulated radiotherapy (IMRT).

The technique has many potential benefits. IMRT allows conformal treatment of concave or invaginated volumes which Webb (1998) estimated account for 30% of treatment volumes which undergo radiotherapy. IMRT has been used to reduce the irradiated volume by compensation for beam penumbra (Dirkx *et al.* 1997, Dirkx *et al.* 2000) and improve dose homogeneity by customised compensation for contour irregularities or tissue inhomogeneities (Mott *et al.* 1999). It may also ultimately be possible to adapt the delivered intensity modulated beam (IMB) from fraction to

fraction by accounting for intra-fraction and inter-fraction variations in beam profile, patient set-up and internal organ motion (Löf *et al.* 1998).

Clinical trials are required to confirm the potential benefits of conformal and IMRT treatments as they develop. In the United Kingdom a prostate cancer study at the Royal Marsden Hospital compared conventional and conformal treatments to 64 Gy and showed at two-year minimum follow-up there was significant reduction in late rectal effects although no difference was observed in acute effects (Dearnaley 1998, Dearnaley *et al.* 1999). A prospective nation-wide trial to investigate dose escalation to 74 Gy in conformal therapy is underway (Medical Research Council Trial RT01). Recently Nutting *et al.* (2000) reviewed clinical results from reported IMRT studies. Although patient numbers are generally small, the head and neck cancer cases reviewed showed good sparing of normal tissue function, and in prostate cancer treatment Nutting *et al.* (2000) reported that IMRT has allowed dose escalation to 81 Gy without increase in rectal complications. As yet there is no data on long term survival.

1.1.2 Producing intensity modulated beams (IMBs)

There are various ways of producing IMBs for x-ray therapy. The simplest method, which is common practice in radiotherapy, is the use of fixed (missing tissue) compensators for regions of irregular contour (Ellis *et al.* 1959). Indeed, the most common use of the treatment machine wedge beam modifier fulfils a similar purpose. The principle of IMB production using fixed compensators has been extended beyond missing tissue compensation and has been applied to IMRT by designing compensators via an inverse planning process to produce IMBs which achieve a required dose distribution (*e.g.* Haas 1997, Meyer *et al.* 2000). However, for the concurrent treatment of several patients with IMRT, there is obvious difficulty with the storage, manufacture and cost of several field-specific compensators for use with each patient. Such devices

could however be considered a safe means of implementing IMRT since they benefit from fixed, repeatable geometry.

A more flexible approach that is of great current interest is to make controlled use of the collimation system. IMB production in this way was first developed by utilising independent movement of a single conventional collimator to achieve wedge-shaped distributions (Kijewski *et al.* 1978). A natural extension is to use the independently controlled leaves of the MLC assembly. There are two methods of producing IMBs based on MLC technology. IMBs can be constructed from a sequence of static exposures made with different MLC field shapes (*e.g.* Galvin *et al.* 1993, Kestin *et al.* 2000). The radiation beam is switched off whilst the leaf motions occur, and this is consequently described as a 'step and shoot' or 'multiple-static-field' approach. The second means of achieving intensity modulation with an MLC is by independently moving leaf pairs across the treatment portal to create a series of one-dimensional IMBs produced by irradiation through the inter-leaf aperture as it is moved. This technique for IMRT production is known as dynamic multileaf collimation (DMLC) (Källman *et al.* 1988). The MLC sequences required to achieve a desired IMB are based on minimising delivery time (*e.g.* Svenson *et al.* 1994, Ma *et al.* 1998), limitations on leaf acceleration or velocity (*e.g.* Svenson *et al.* 1994) and limitations on leaf proximity (*e.g.* Convery & Webb 1998, Budgell *et al.* 1998). Radiation transmission through the leaves and collimator scatter must also be considered (*e.g.* Dirkx *et al.* 1998) together with the problem of 'tongue and groove' under-dosage (*e.g.* van Santvoort & Heijmen 1996) associated with the stepped nature of the leaf sides designed to reduce interleaf leakage. The delivery of IMBs using the DMLC technique is the focus of this present work. IMRT implementation by DMLC benefits from not being patient-specific, unlike compensators. Furthermore, compared

to multiple-static-field MLC techniques it reduces treatment time and any effect of beam instability at beam-start.

A further means of IMRT production is the technique which is known as tomotherapy ('slice therapy'). This is possible with the commercially available MIMiC™ device (NOMOS Corporation, Sewickley, PA, USA) which consists of a linear arrangement of multiple absorbing vanes (Carol 1995). Mackie and co-workers at the University of Wisconsin, USA (Mackie *et al.* 1993) are developing a tomotherapy system based on the same irradiation principle. In this case the accelerator is mounted on a ring gantry to allow continuous rotation whilst translating the patient. IMRT can also be produced using scanning beams (Brahme 1987) from accelerators such as the Microtron produced by Scanditronix Medical AB (Uppsala, Sweden) and installed at the University of Stockholm. By scanning the elementary beam in a time-dependent non-uniform pattern IMBs can be created. The use of proton beams for IMRT is also being considered. Lomax (1999) described how proton fields allow truly three-dimensional localisation of the dose distribution produced by a single field since it is possible to modulate proton beam intensities both across the plane *and* in depth. For fixed energy photon beams, intensity modulation with depth is not possible, thus limiting intensity modulation of a single photon field to two dimensions and necessitating the combination of such fields to optimise the three-dimensional distribution.

1.2 Dosimetric verification of IMRT

1.2.1 Requirement for dosimetric verification

For clinical implementation of such techniques the user must be confident that the desired IMBs have been delivered, and in fact Webb (1997) has described the problem of confirming the accuracy of IMRT as a 'major impediment' to the implementation of the technology. In external beam radiotherapy the issue of confirming the geometric and dosimetric accuracy of a delivered treatment against that planned is termed verification.

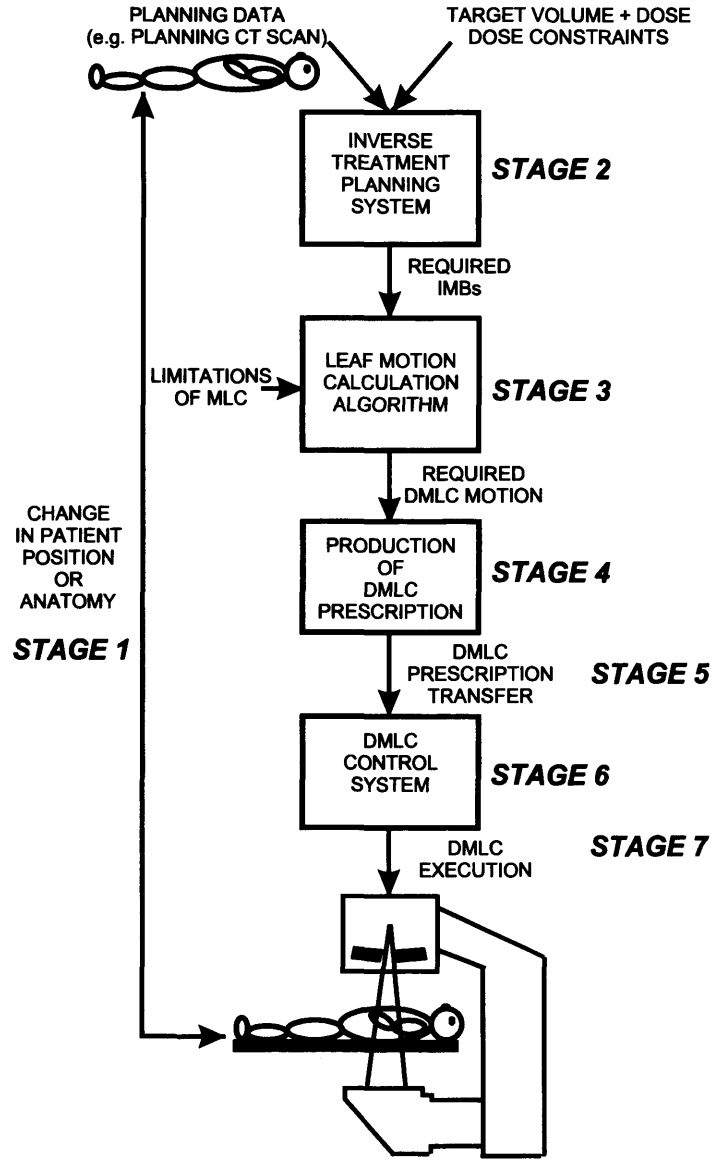

Figure 1-2: Stages involved in planning and delivering IMRT by DMLC

The dose distribution delivered is dependent on both the planning and delivery stages. Figure 1-2 shows the process of planning an IMRT treatment using an inverse treatment planning system and delivering the treatment using an accelerator with DMLC. The dose distribution delivered to a patient is dependent on the factors listed below (which correspond to the stages numbers indicated on Figure 1-2):

(1) The geometry of the patient (*i.e.* patient position and internal anatomy) at the time of treatment compared with acquisition of the planning data.

(2) Accurate dose modelling by the planning system.

(3) Accurate calculation of the DMLC motion required to deliver the desired IMB.

(4) Correct production of DMLC prescription (*i.e.* correct production of accelerator control data) for the required leaf sequences.

(5) Correct DMLC prescription transferred to the DMLC control system

(6) The ability of the MLC control system to store and recall the DMLC prescription without any loss or corruption.

(7) The accuracy and absence of errors in the DMLC delivery system during patient treatment and selection of the correct DMLC prescription for the particular patient.

Aspects of this list apply to conventional treatment techniques using static beams as well as IMRT delivery. For conventional dose delivery with static beams, methods of quality assurance for the treatment planning system and accelerator are well understood (*e.g.* IPEM 1996, IPEM 1999). Furthermore, quality assurance of the actual patient treatment can be performed by *in vivo* dose measurement using semiconductor diode detectors or thermoluminescent dosimeters (TLD) (Essers and Mijnheer 1999). Furthermore, electronic portal imaging devices (EPIDs) are being increasingly applied in the clinic for the assessment of geometric accuracy of such treatments. However, in

the case of DMLC there are clearly additional stages involved in the planning and delivery process, together with more complex dose modelling, more complex prescription information and a more complex mode of dose delivery. Additionally, the influence of patient geometry changes (both inter- and intra-fraction) may be greater (Yu *et al.* 1998, Chui 1999, Hector *et al.* 2000). As a result, specialised verification techniques must be developed for IMRT to allow its introduction into clinical practice.

Guidance on the accuracy required for dose delivery in conventional radiotherapy has been published. In 1976, ICRU Report 24 stated that, based on the limited dose-effect data available at that time, ±5 % accuracy was required in the delivery of absorbed dose to the target volume in order to achieve primary tumour eradication. Although this limit is often quoted, considerable ambiguity surrounds the exact meaning of this statement, and it has been considered as an overall limit, or interpreted as 1 or 1.5 standard deviations about the mean dose prescribed. Subsequently, Brahme (1984) considered the consequences of dose variability on loss of tumour control. He showed that high tumour control rates can only be achieved with high accuracy in dose delivery, and concluded that the relative standard deviation of the mean dose in the target must be less than 3 % to achieve reasonable control. Mijnheer *et al.* (1987) rigorously considered the degree of accuracy required and reviewed dose-effect curves for damage to normal tissues after photon irradiation, from which they suggested a similar required accuracy of 3.5 % at the one standard deviation level.

1.2.2 Methods of dosimetric verification

Having outlined the process of delivering IMRT by DMLC and the factors affecting the dose delivered, it is useful to consider the approaches available for verification of IMRT and the reported implementation of these techniques in the literature.

1.2.2.1 Pre-treatment verification

Pre-treatment verification involves the measurement of delivered dose to a phantom and comparison with that planned. There are various reports of this approach in the literature using verification film in phantoms (Bortfeld *et al.* 1994, Wang *et al.* 1996, Boyer *et al.* 1997, Oldham & Webb 1997, Verellen *et al.* 1997, Milliken *et al.* 1998, Wilkinson *et al.* 1998), or ion chamber measurements at selected points (Ling *et al.* 1996). Scanning ion chamber measurements have also been used in the case of multiple-static-field IMRT (Wittkämper *et al.* 1998). Absolute dose measurement with TLDs (De Neve & De Wagter 1997, Tsai *et al.* 1998) or TLD and ion chambers (Low *et al.* 1998a) have also been reported for phantom measurements in conjunction with film for assessment of relative dose distributions. Polymer gel (Maryanski *et al.* 1994) has also been used in anthropomorphic phantoms (De Deene *et al.* 1998a and 1998b, Oldham *et al.* 1998).

1.2.2.2 Post-treatment verification

Post-treatment verification can be performed by measuring the dose delivered *in vivo* during DMLC delivery, and comparing this to that planned *following completion* of the treatment. Absolute point dose measurement using TLDs placed on the skin at the centre of the treatment volume has been reported (*e.g.* Verellen *et al.* 1997). Kippenes *et al.* (1998) reported inserting catheters loaded with TLD rods into the nasal meatus, oral cavity or oesophagus of canine subjects, which could be located on pre-treatment planning CT scans. Two-dimensional measurements of the delivered IMB have also been reported by De Neve & De Wagter (1997) who placed verification film across the beam aperture of their accelerator to record the delivered energy fluence distribution during both phantom studies and patient treatment to confirm consistency of dose delivery. A further type of post-treatment verification has been described by

Burman *et al.* (1997) who compared log files generated by their accelerator, which recorded leaf location as a function of dose delivered against that expected following completion of the IMRT irradiation sequence. Beavis *et al.* (1998) have described the use of post-treatment verification using such a log file as 'virtual dosimetry'.

EPIDs are also being applied to post-treatment verification since they may allow the assessment of the delivered IMB in two dimensions. The application of such a device to verification of DMLC is the subject of much interest and forms a central component to this work, particularly as verification could be achieved in real-time.

1.2.3 Limitations of current techniques of dosimetric verification

Having considered the possible approaches to dosimetric verification of IMRT by DMLC, it is clear that *pre-treatment verification* is valuable and such assessments would form part of the commissioning process of an IMRT planning or delivery system. However, the technique is impractical to use for every patient case since this would be very time-consuming. Furthermore, pre-treatment studies are limited in that they do not confirm correct treatment delivery to the patient which may be in error due to incorrect dose modelling within the patient, or a change in patient geometry between planning and treatment. Furthermore, dosimetric errors may result from incorrect selection of the required DMLC prescription, corruption of this prescription or incorrect accelerator operation.

Such discrepancies may be identifiable using the *post-treatment verification* techniques described, since they provide information about the *actual* patient dose delivery. However, by its very nature this information is only available *after* the completion of the delivery of a single fraction at best.

Clearly the verification approach required depends on the complexity of treatments, and the observed performance characteristics and stability of the delivery

system. However, the value of *real-time verification* techniques for this mode of dose delivery, particularly in gaining confidence in the techniques used during the initial phase of implementation, is very readily apparent. Such a system may allow monitoring of the dose distribution forming within the patient in real time, providing information about accelerator performance and patient position, internal anatomy or motion. This use of real-time verification ensures that the accelerator and DMLC system are being monitored independently during actual patient treatment and gives the potential for interruption should a major discrepancy occur.

1.2.4 Application of EPIDs to verification of IMRT

There is considerable interest in extending the role of electronic portal imaging devices (EPIDs) in external beam radiotherapy beyond the assessment of treatment geometry. Current interest centres on both commercial devices and in-house built systems. Of the commercial devices there has been particular interest in the matrix ion chamber EPID commercially known as PortalVision™ (Varian Associates Palo Alto, CA, USA) (Meertens *et al.* 1985, van Herk & Meertens 1988), and the camera-based EPID SRI-100™ (Elekta Oncology Systems, Crawley, UK; formerly Philips Medical Systems) (Visser *et al.* 1990).

Several groups have considered the potential use of EPIDs for design and quality assurance of compensators (Yin *et al.* 1994, Roback & Gerbi 1995, Curtin-Savard *et al.* 1997, Symonds-Tayler *et al.* 1997, Pasma *et al.* 1999a). EPIDs are being investigated for megavoltage computed tomography (MVCT) of the patient in the treatment position (Nakagawa *et al.* 1994, Guan *et al.* 1998, Midgley *et al.* 1998, Mosleh-Shirazi *et al.* 1998a). Quality assurance of the treatment machine has been reported (Kirby & Williams 1993, Kirby & Williams 1995, Luchka *et al.* 1996, Curtin-Savard *et al.* 1997). EPIDs have also been used for the measurement of exit dose

during patient treatment (Kirby & Williams 1993, Kirby & Williams 1995, Heijmen *et al.* 1995, Conte *et al.* 1997, Pasma *et al.* 1998).

EPIDs are being investigated for the purpose of IMRT verification for both post-treatment and real-time applications. IMRT verification is an obvious extension of the role played by EPIDs because of their two-dimensional nature, which makes it possible to measure the spatial distribution of IMRT dose delivery during patient treatment. This could be exploited for real-time IMRT verification applications. A review of reported implementation of EPIDs for IMRT verification at the time of commencement of this work is presented below. More recently reported work, including developments in imager technology, is presented in later chapters.

1.2.4.1 Camera-based EPIDs

The possibility of using a camera-based imaging system for 'real-time supervision' of dynamic treatments was first proposed by Dörner & Neumann (1995) using the camera-based beam imaging system (BIS, Wellhöfer Dosimetrie, Schwarzenbruck, Germany) which is of similar design to camera-based EPIDs and intended as a quality assurance tool in external beam radiotherapy. Ma *et al.* (1997) subsequently presented a quality assurance procedure developed for DMLC using this device at Stanford (CA, USA) based on comparison of a composite image of the treatment against reference images derived from the DMLC prescription. Their approach was sensitive to randomly introduced leaf motion errors of less than 0.5 mm and showed that the DMLC leaf sequencing files could be transferred to the control computer correctly, and that delivery was made without error.

Kirby & Williams (1995) at the Christie Hospital (Manchester, UK) discussed the suitability of the SRI-100 EPID for verification of IMRT following dosimetric study of the device. They showed a profile from a composite image for a multiple-static field

treatment, which ignored non-uniformity effects but showed good visual agreement with expected modulation.

1.2.4.2 Matrix ion chamber EPIDs

Van Herk *et al.* (1996) assessed the feasibility of PortalVision for DMLC and outlined two problems associated with the device for measuring 'moving' beams. They used the Mark II system with a read-out time of around 1.6 s (which is faster than the imaging speed of the original Mark I PortalVision device). To simulate MLC leaf movement they rotated the collimator with an elongated field to give a speed of around 20 mm s^{-1} at isocentre. The images acquired suffered 'motion distortion' due to the scanned read-out process that meant a rectangular field appeared curved. However, a de-warping process could be applied on a line-by-line basis using temporal knowledge of the scan. Additionally, a blurring effect was evident, with profiles exhibiting broadened penumbra on the tail 'following' the motion, with a quoted penumbra increase from 2 to 6 mm. The effect was associated with non-linear recombination processes within the detector medium, and as a result of reduced recombination, worsened at reduced dose rates. However, the penumbra changes occurred below 50 % of the maximum dose rate level, and the effect was believed to be less than 1 mm at the 50 % level. As a result, the authors concluded that the *geometric* verification with the system was not compromised by the blurring phenomenon.

1.4 Objective of this study and overview of thesis

The aim of this present work is to investigate methods of dosimetric verification of IMRT produced by the DMLC technique on a linear accelerator. The work has been conducted prior to the clinical introduction of IMRT at the Leicester Royal Infirmary NHS Trust.

In considering methods of dosimetric verification, it is useful to identify possible measurement locations which could be used in both conventional radiotherapy and IMRT verification (Figure 1-3). Table 1-1 details the information which verification measurements at each location might be able to provide about any effect on dose delivered of the accelerator performance, the patient geometry or both.

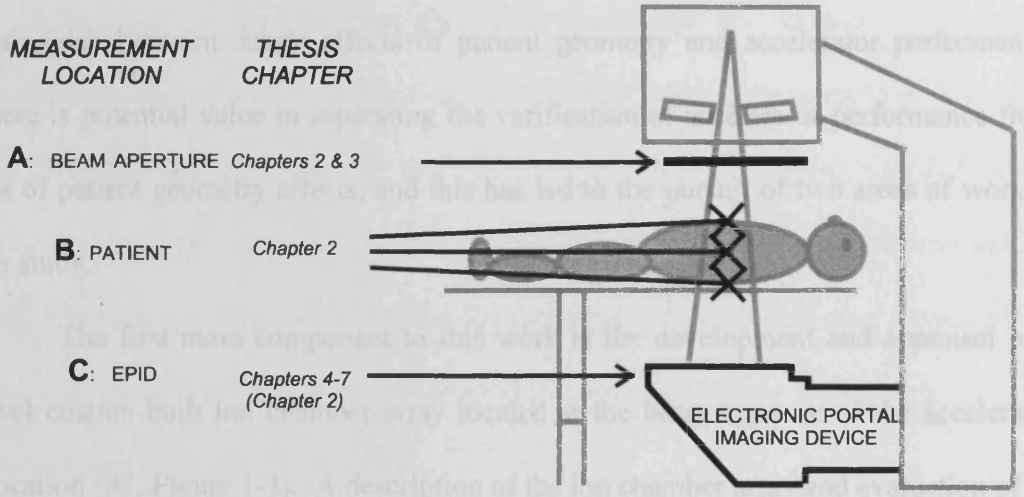

Location 'A': Measurement proximal to the patient at the x-ray beam aperture, involving characterising the beam exiting the accelerator using a detection system mounted directly at the accelerator treatment head.

Location 'B': Measurement at locations where the radiation beam enters and exits the surface of the patient, or measurement within the patient following the location of an appropriate detector.

Location 'C': Measurement using an EPID.

Figure 1-3: Measurement locations for in-vivo dosimetry

Location	Information Available			
	Accelerator performance	Patient geometry		
		Positioning	Inter- or intra-fraction movement	Internal organ movement
A: Beam exiting accelerator	✔	✘	✘	✘
B: Patient surface or internal location	✔	✔	✔	✘
C: EPID	✔	✔	✔	✔

Table 1-1: Information available at measurement locations in Figure 1-3

It is clear from Table 1-1 that most information is available from measurement at location 'C', which has contributed to current interest in the application of EPIDs. However, verification measurements using an EPID may suffer from an inability to distinguish between subtle effects of patient geometry and accelerator performance. There is potential value in separating the verification of accelerator performance from that of patient geometry effects, and this has led to the pursuit of two areas of work in this study.

The first main component to this work is the development and appraisal of a novel custom-built ion chamber array located at the beam aperture of the accelerator (Location 'A', Figure 1-3). A description of the ion chamber array and evaluation of its application to the verification and quality assurance of DMLC is given in Chapter 3. In this present work the ion chamber array is used in conjunction with a multi-channel electrometer system designed and constructed for application to the continuous real-time measurement of dynamically-produced dose distributions. The system is described and characterised in Chapter 2 and its potential applications considered, including direct patient measurement (Location 'B', Figure 1-3). There are no reports in the literature of such a system under development.

The flexibility of this electrometer system has been also been exploited in measurements which form part of an investigation of the suitability of a camera-based EPID (Theraview™, Cablon Medical BV, Leusden, The Netherlands) for IMRT verification (Location 'C', Figure 1-3). The investigation of this EPID forms the second main component of this work (Chapters 4-7). Chapter 4 considers the characteristics of the phosphor used as the x-ray detector for dosimetry of dynamically-produced dose distributions, which have not previously been reported. Chapter 5 reports properties of the Theraview EPID pertinent to dosimetric applications, which are essentially related to the characteristics of the tube camera. This was the first reported study of this EPID. Chapter 6 applies the EPID to collimator position verification during DMLC by making use of a novel interface from the EPID camera to the electrometer system, and has also been reported in the literature. Chapter 7 considers the characteristics and limitations of the EPID for measurement of integrated dose distribution delivered during DMLC. A novel method of overcoming difficulties in triggering image acquisition for this application is proposed which has been reported in the literature. Finally, results of the first reported comparison of dose measurement using a physical correction for non-ideal optical transport within the imaging chain of camera-based EPIDs are also given.

Chapter 2. Development and performance of a multi-channel electrometer

2.1 Introduction

A dosimetry system has been constructed to investigate continuous, real-time verification of IMRT produced by DMLC techniques on a linear accelerator. The system, which was synchronised to the accelerator dose pulse train, was named the Synchronised Multi-channel Electrometer (SME). The SME has been designed to be suitable for continuous recording of the temporal variation of dose signal from up to 20 ion chambers or semiconductor diode radiation detectors. In addition, the SME simultaneously records the cumulative number of monitor units (MU) delivered by the accelerator. This is achieved via a custom-built interface to the Elekta SL15*i* linear accelerator (Elekta Oncology Systems, Crawley, UK) used for DMLC.

The SME was used with a specially designed and constructed strip ion chamber array for application to the verification of DMLC. A description and experimental evaluation of the ion chamber array for this purpose is presented in Chapter 3. The flexibility of the SME has been also been exploited in various other measurements reported in this present work (Chapters 4, 7) and is also central to the application of the locally available camera-based EPID to collimator position verification during DMLC (Chapter 6).

2.2 System requirements and limitations of commercial devices

It is useful to consider the specific requirements for this system, and in so doing to highlight the shortcomings and limitations of using a commercial multi-channel electrometer system. A limited number of such devices are available for patient

dosimetry using semiconductor diode detectors (*e.g.* during total body irradiation), or for quality assurance of the treatment machine (*e.g.* in the measurement of dose rate flatness profiles). However, at present there is no electrometer system commercially available that has comparable temporal resolution, sensitivity, flexibility, or the ability to record cumulative accelerator MU. There are no reports in the literature of such a device under development.

1. The most obvious requirement was flexibility of the measurement configuration. Specifically:-

- a range of input sources including various radiation detectors;
- control of sample rate (depending on detector, dose rate and required temporal resolution);
- operation at all pulse repetition frequencies (PRFs) available on the Elekta accelerator.

2. High temporal resolution necessitated short integration periods and hence the measurement of small charge levels which may not be possible with a commercial electrometer.
3. Interfacing locally developed software and detector hardware to a commercial electrometer is impracticable because of the lack of knowledge of the commercial system and specification of the interface.
4. The electrometers often used in a commercial multi-channel system (*e.g.* Thebes 7000-2, Victoreen Inc., Cleveland, Ohio, USA, or the Profiler, Sun Nuclear Corporation, Melbourne, FL, USA) are physically integral to the detector array. In these devices the detectors are directly connected to electrometers which are all

contained within the detector assembly. There is no possibility of other detectors being connected to dedicated electrometers in such a configuration.

5. As far as can be established from technical specifications provided by manufacturers, commercial electrometers with a rate mode often obtain rate values from calculations based on the difference between two consecutive measurements of integrated signal. For improved resolution in the measurement of a time-varying dose signal an alternative method is required. The approach used in the SME enables the signal associated with a number of radiation pulses to be integrated and measured, following which the system is reset before beginning the next integration period.
6. Many commercial dosimetry systems obtain a 'radiation on' signal, and thus commence acquisition, either from a reference detector or from a detector within the array itself. This is a significant disadvantage for DMLC applications since it may not be possible to ensure that these detectors are always directly irradiated at beam-start. A similar difficulty exists for some camera-based EPIDs which is considered in Chapter 7.

2.3 System overview

An overview of the SME system and interfaces to the accelerator is shown schematically in Figure 2-1. The SME data acquisition module is located in the treatment room adjacent to the accelerator and was based on a microprocessor system running a custom command language. A host application running on a PC at the accelerator control area invokes the commands via a serial link routed down the accelerator maze to provide control of the SME data acquisition module functions.

This provides a Windows™-based front-end in which SME commands are grouped together into functions such as 'Auto-zero', 'Calibrate', 'Collect Dose', 'Save' *etc.*

In the present configuration data is saved from the SME data acquisition module to the PC off-line in ASCII format for import to a standard spreadsheet for further analysis. The SME performs extensive diagnostics and data logging at switch-on, and there are diagnostic and low level calibration facilities.

The overview shows twenty dose input channels to the electrometer hardware of the SME data acquisition module, together with the provision of a high tension supply for ion chamber applications. Also within the treatment room an optically isolated interface to the dosimetry system of the accelerator (located on accelerator gantry) provided pulses representing $1/64^{th}$ monitor unit (MU) from the accelerator to the SME data acquisition system. An optically isolated input from an accelerator test point in the control area provided the accelerator thyratron drive voltage to the SME which was necessary for dose pulse synchronisation. An optically isolated external trigger interface to the camera control unit of the Theraview EPID (which is located in the control area) also exists and has allowed collimator position verification with the EPID (Chapter 6).

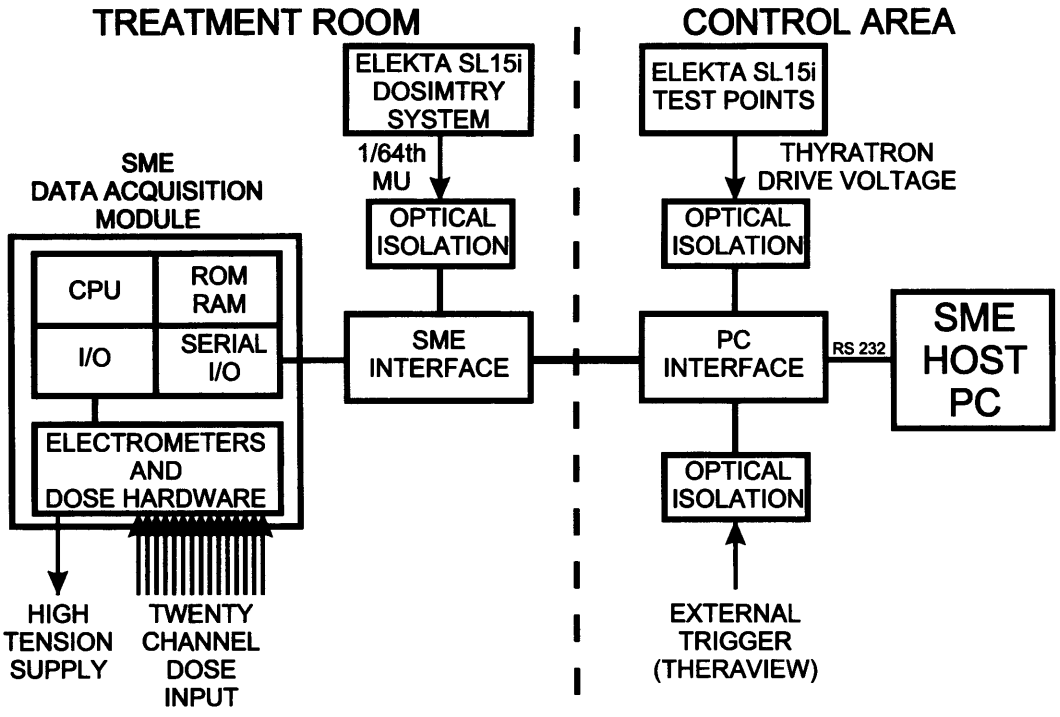

Figure 2-1: Overview of SME

2.4 Electrometer and data acquisition

2.4.1 Electrometer design

Each of the twenty channels of the SME were based on an integrating capacitor electrometer with common reset shown schematically in Figure 2-2. Each channel used a precision electrometer (Analog Devices AD549) which exhibits ultra-low input current and is designed specifically for such applications.

The SME was designed for uni-polar signal input, compatible with commercially available semiconductor diode detectors (EDP-10 *in vivo* detectors and field plotting detectors, Scanditronix Medical AB, Uppsala, Sweden). The polarity of signals for ionisation chamber detectors was matched to this by using a negative polarity high tension supply (Chapter 2.6).

Auto-zero of input bias current, including any introduced by the detector (for example leakage or dark current) was achieved by applying a DC voltage via a 10 GΩ

precision resistor (Welwyn 3811, Welwyn Components Ltd) which is shown schematically in Figure 2-2. Separate auto-zero compensation was applied continuously to each electrometer channel via buffered outputs refreshed at a rate of 10 Hz from a twenty channel digital-to-analogue converter (DAC) system. Auto-zero compensation was under software control and was achieved using a zero routine in which the signal levels from each electrometer channel were measured for two compensation settings (DAC values), and the required value to null signal offset calculated assuming linearity. Auto-zero was performed following connection of the detectors to their corresponding electrometers. After the period of warm-up specified for the electrometers (15 minutes) the auto-zero procedure did not normally need repeating during a measurement session.

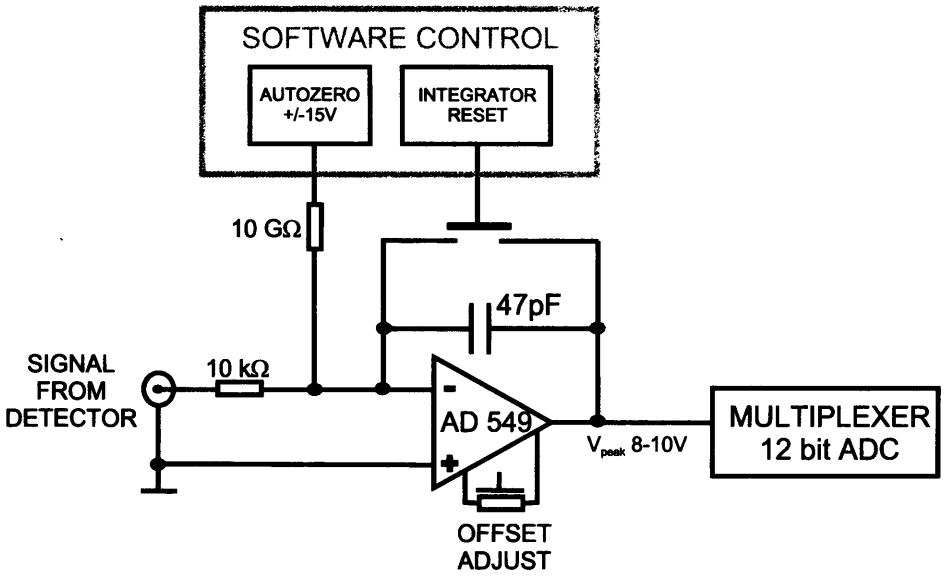

Figure 2-2: Schematic of a single electrometer channel.

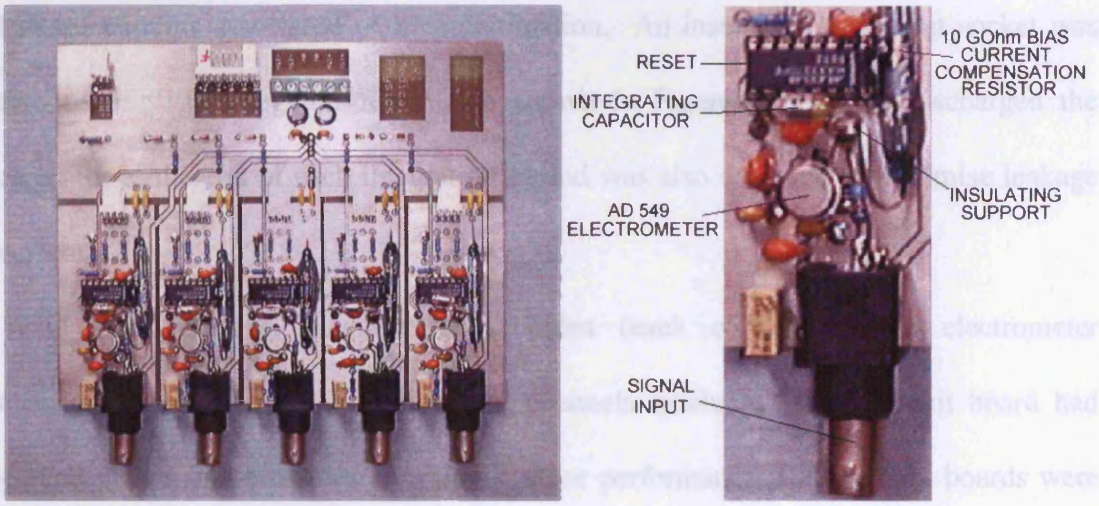

Figure 2-3: Photograph of five channel electrometer board (left) and detail of single channel (right). Overall dimensions 175 mm x 140 mm.

Integrating capacitors of 47 pF were used on all channels and proved adequate for initial applications. This extremely small capacitance allows the electrometer to measure very small charge levels (compared to a standard electrometer) and hence allows assessment of very short integration periods. The use of such small capacitance values required a guarding scheme around signal input circuitry to avoid current paths between power rails and signal lines at the electrometer input, including current paths through the circuit board substrate itself (known as parasitic leakage). The encapsulation (*i.e.* casing) of each operational amplifier was also connected to signal input ground to include the electrometer integrating circuit in the guarding scheme. The integrating capacitors used were polystyrene because this type of capacitor has excellent low leakage characteristics. In order to reduce leakage further, the electrometer input, integrating capacitor and connection to the 10 GΩ resistance (providing input bias current compensation) were air spaced above the circuit board and supported by a polytetrafluoroethylene (PTFE) insulating pillar. After construction of the circuit the pillar was thoroughly cleaned with suitable solvent to eliminate surface

leakage currents associated with contamination. An insulated BNC input socket was also used. The integrator reset (also shown in Figure 2-2) which discharged the capacitor at the end of each integration period was also designed to minimise leakage currents.

Four identical electrometer modules (each containing five electrometer channels) provided the total number of channels available. Each circuit board had ground planes on both sides to optimise noise performance, and the four boards were housed in a separate screened compartment of the SME enclosure. A photograph of one of the electrometer boards (containing five electrometer channels) is shown in Figure 2-3.

2.4.2 Electrometer operation and dose acquisition

In order to allow integration of the entire dose delivery, the electrometer was required to integrate signals simultaneously on all channels with no 'loss' of data during the data acquisition period. This was possible because of the pulsed nature of linear accelerator dose delivery, which allowed data acquisition in the inter-pulse period. This required the signal integration period to be locked to the accelerator pulse train, which was achieved via a trigger interface to the accelerator thyratron drive voltage (shown schematically in Figure 2-1). Following each period of signal integration (corresponding to an adjustable number of radiation pulses), the voltage output from each electrometer was rapidly sampled by a single 12-bit analogue-to-digital converter (ADC) via a multiplexer. To sample all 20 channels required a period of 650 μs. Immediately following data acquisition, all electrometers were simultaneously reset by discharging the integrating capacitors via a reset pulse applied to all reset switches simultaneously. The reset pulse was 40 μs in duration and thus

many times the RC time constant of the integrating capacitor (47 pF) and the 'on' resistance of the reset switch (7 kΩ) giving an RC value of 0.33 ns. This ensured complete discharge of the electrometer after sampling the signal for each integration period.

The trigger interface to the accelerator thyratron drive voltage also allowed the SME to initiate signal integration and data acquisition prior to beam-start since this waveform is available from the accelerator before dose delivery commences. The thyratron drive voltage waveform was chosen for synchronisation in preference to the magnetron current waveform (which was also available at a test socket and exists before commencement of dose delivery) in order to allow a 'missed pulse' to be identified. If this occurs, no radiation is produced due to magnetron mis-firing and there will be no magnetron current pulse, but the thyratron drive voltage waveform will be present and hence detected by the system. The existence of a timing error associated with mis-firing of the magnetron or operation of the accelerator at a PRF different from that expected, is immediately indicated by the SME and recorded in the data file produced.

Figure 2-4 is a timing diagram showing each radiation pulse, the resulting integrated dose signal on each electrometer channel, and the timing of data acquisition followed by reset of the charge on the integrating capacitor. The time between the last radiation pulse and data acquisition, called the *settle time T,* was adjustable in software between the approximate range 70-1000 μs. The time was chosen to allow the signal from the detector to settle on the integrator and give a stable output voltage on all electrometers after the last radiation pulse of the integration period before data

acquisition. Data sampling *after* the last radiation pulse also had the advantage of avoiding spurious radio-frequency (RF) interference during the dose pulse.

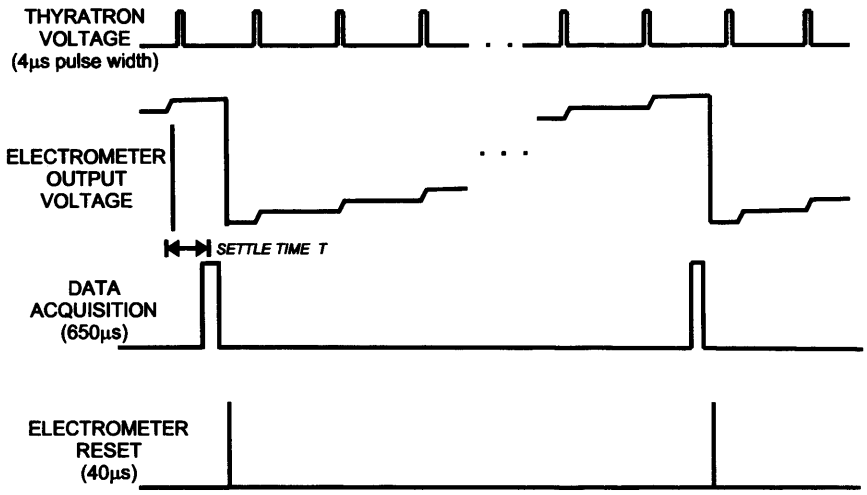

Figure 2-4: Timing diagram for SME data acquisition (not shown to scale). Radiation occurs during the thyratron drive voltage pulse (4 μs in duration). The increase in the electrometer output voltage following each radiation pulse is indicated (again not to scale). Data acquisition occupies 650 μs, and integrator reset is 40 μs in duration.

The signal on the output from an electrometer of the SME measured using an oscilloscope is shown in Figure 2-5. In this case the detector used was plate 5 of the strip ion chamber array (Chapter 3) and the accelerator was operated at 400 Hz PRF. Note that the waveforms are shown with different gain and time-base values and indicate:

- the voltage ramp from the output of the integrator during the period of dose integration and dose reset (left)
- dose reset and the contribution of the first few radiation pulses (at 2.5 ms intervals) to the output voltage of the electrometer (centre)
- the increment in output voltage of the electrometer following a single radiation pulse in relation to the magnetron current pulse (oscilloscope trace B, right)

showing how long charge from the detector takes to 'settle' on the integrating capacitor.

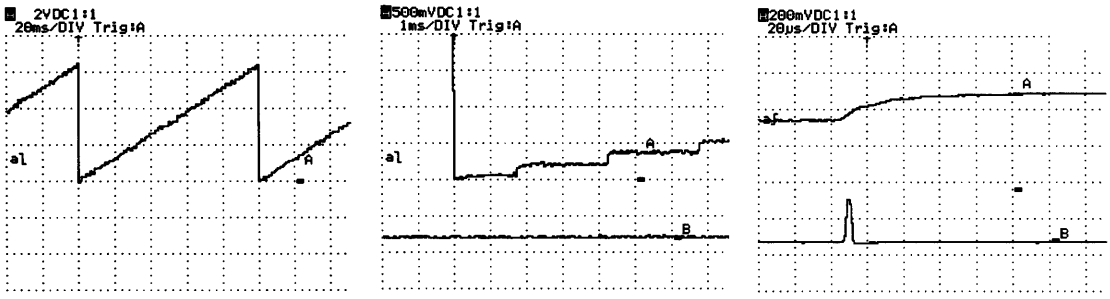

Figure 2-5: SME electrometer output voltage waveforms using strip ion chamber array. Time base and voltage gain values are shown for each channel. Channel B (right-hand image) is the magnetron current pulse. Oscilloscope time-base/sensitivity are shown at the top-right of each image

Similar investigations were performed for EDP diodes and an RKA ionisation chamber with –200 V polarising voltage. The exponential time constant Γ governing charge settle on the electrometer for all three detectors was established for the waveforms plotted at enlarged scale. Values of time constant Γ are given in Table 2-1. On the basis of the findings, a settle time T (Figure 2-4) of 200 µs was used for all three detector types, which was approximately equal to ten time constants Γ measured for the strip ion chamber array.

Detector	Time Constant Γ (µs)
Strip ion chamber array (-300V)	20.4 ± 2
EDP-10 semiconductor diode	17.9 ± 2
RKA ionisation chamber (-200V)	25.1 ± 2

Table 2-1: Time constants for charge settle onto electrometer for various detectors

Note that a settle time T of 200 µs, in combination with a time of 650 µs to sample all 20 channels of dose data, and a reset pulse duration of 40 µs, requires approximately 900 µs. This is substantially less than the minimum duration between

radiation pulses produced by the accelerator of 2.5 ms (corresponding to 400 Hz PRF). Thus, the SME could be operated at all available PRFs of the accelerator (400 Hz, 200 Hz, 100 Hz, 50 Hz, 25 Hz and 12 Hz). The number of pulses, and hence the sample rate, were adjustable. However, on testing some constraints on the operating conditions were identified:

- the minimum integration period which could be used was 20 ms
- the integration period was limited to a multiple of 10 ms
- the minimum number of radiation pulses which could be integrated was two.

These constraints imposed no real limitations on the operation of the device except for extremely fast sampling. However, the constraints needed to be considered when choosing operating parameters. For example, the maximum sampling rate (50 Hz) could be only be achieved at PRFs 400 Hz and 200 Hz (corresponding to 8 and 4 radiation pulses per sample respectively), whilst at PRFs 50 Hz and 25 Hz the maximum rate was 25 Hz (2 pulses per sample) and 5 Hz (5 pulses per sample). The expected accelerator PRF, the number of radiation pulses/sample, the sample integration period and the settle time T were all defined in a library of prescriptions developed within the SME software.

The maximum number of radiation pulses that could be integrated before the electrometer saturated was clearly dependent on the sensitivity of the detector used and the size of the integrating capacitor. For example, in the case of the strip ion chamber array (Chapter 3) located at the accelerator's accessory tray, approximately 38 radiation pulses resulted in signal levels of full-scale deflection. For this detector the working maximum number of pulses was taken as 32, which at the highest PRF of 400 Hz provided integrated dose samples at 80 ms intervals.

During data collection, 'live' data was displayed at the PC and updated every 2.0 s. However, timing problems meant this display mode was not possible for integration periods of less than 100 ms although data collection could still be performed. The timing limitations described were in part due to limitations of the serial communications interface between the SME data acquisition module in the treatment room and the host PC at the accelerator control area.

2.4.3 Electrometer sensitivity, ADC linearity, noise level and stability

Linearity of the 12-bit ADC was confirmed by applying an adjustable voltage to a single channel of the SME through a 10 GΩ resistance. The external applied voltage was measured using a conventional digital voltmeter (DVM) (accuracy ± 0.3 %). The applied voltage was adjusted and the signal measured for a sample period of 100 ms. Bench testing of this type could be performed in the absence of an accelerator (and hence the thyratron drive voltage used for triggering/synchronisation) using a test mode of the SME data acquisition module in which an internal signal could be used to replace the accelerator test signal.

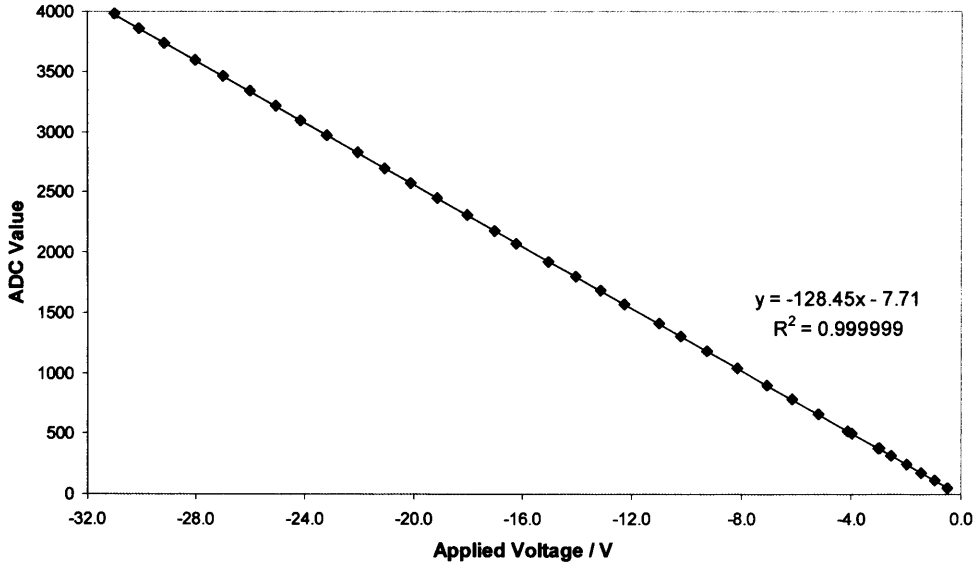

Figure 2-6: ADC Linearity. Obtained by applying an adjustable voltage to a single channel of the SME through a 10 GΩ resistance. The results of linear regression are plotted.

Figure 2-6 shows the observed ADC value plotted against the applied voltage measured with the DVM. A linear fit to the data shows excellent linearity for the ADC. Note that the signal offset observed could have been removed by the auto-zero facility which has been described. The absolute sensitivity of the channel under test (number 2) could be determined from the characteristic in Figure 2-6, the period of charge integration used for this measurement (100 ms) and the calculated input current through the 10 GΩ resistance. For this channel the sensitivity per ADC unit was calculated as $77.8 \pm 0.8 \times 10^{-15}$ C. This value was typical for all channels. The exact sensitivity of a given channel was dependent on the gain of the operational amplifier and the exact value of the integrating capacitor (tolerance ± 2.5 %).

The noise level of the ADC was assessed as part of a self-check test routinely performed by the SME at switch-on. The routine involved 30 samples of a 2.5 V reference voltage directly connected to the ADC (corresponding to an ADC level of approximately 1847 units). The routine also acted to confirm the presence of the correct reference, and the correct operation of the ADC. Standard deviations for each series of 30 samples were always less than unity under normal conditions confirming excellent system noise performance.

Figure 2-7 shows the long-term stability of the ADC and 2.5 V reference test. The mean of 30 samples of the 2.5 V reference voltage (± SD) on each occasion is plotted for measurements over 251 days. Data has been normalised to the mean value and the results of linear regression are plotted. Over the 250 day period, the drift is very small (around 0.09 %, which is approximately 1.7 ADC units). Note that although standard deviations for each series of 30 samples were less than unity under normal conditions, Figure 2-7 contains results from occasions when the system was under test

and the noise performance had been compromised by the removal of external covers which provided electrical screening.

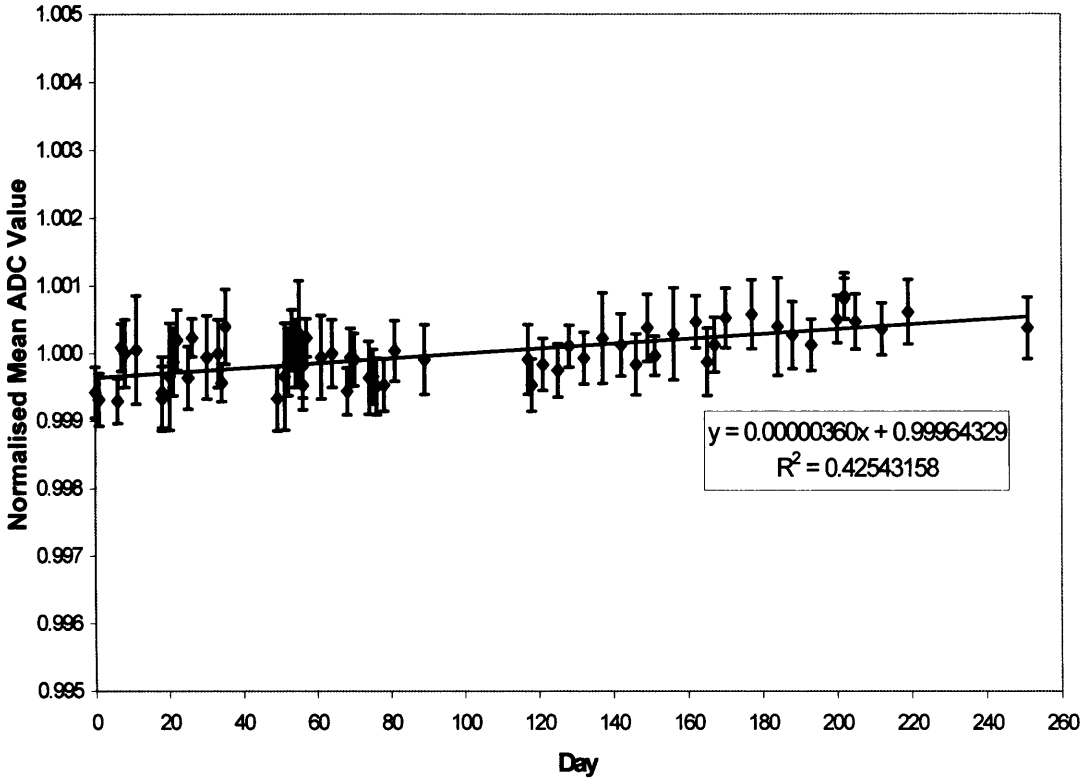

Figure 2-7: Results of ADC and 2.5V reference test over 251 days. Mean value ± SD is plotted for each test result, and the results of linear regression are also shown.

2.5 Interface to accelerator dosimetry system

2.5.1 Introduction

The execution of DMLC on an Elekta linear accelerator is based on control points that define collimator positions at cumulative fractions of the total number of MU to be delivered. However, as the signal integration period of the SME data acquisition module is locked to the accelerator dose pulse train, the SME records integrated dose signals at equal *temporal* intervals, *i.e.* data sample intervals are defined by *time* not by *accelerator MU* as in the case of DMLC. Therefore an additional

component of the electrometer system to record the number of MU delivered by the accelerator at each data sample was developed.

The issue of dose-based control of DMLC and the verification of dose delivery using a time-locked system was first discussed by Partridge *et al.* (1998) when using a fast EPID which acquired images synchronised to the accelerator dose pulse chain. The group recorded cumulative dose by digitising an analogue voltage signal representing the cumulative dose delivered during treatment. This signal was in fact provided by the accelerator as the dose signal for use by the DMLC control system. The Elekta accelerator used for DMLC in this study is of a more recent design (IMRT software version 3.1.0) and makes use of a communication port and serial link for data transfer from the accelerator to the MLC.

Recording of the accelerator's cumulative dose using the SME time-locked system described here is somewhat different from the first approach of Partridge *et al.* (1998) since in this case a direct (optically isolated) connection has been made to the accelerator's dosimetry system. Partridge and co-workers have since made a similar direct connection to the dosimetry system of their accelerator (Partridge *et al.* 2000a). Such a direct connection to the dosimetry system is of particular value since it is *fully independent* of the dose signal provided by the accelerator for use by the DMLC control system. This signal has been shown to lag behind the true dose signal (Chapter 3) and would otherwise require correction (Chapter 6).

2.5.2 Technical description and operation

The connection was made to a test point available on the accelerator's primary dosimetry system. The primary dosimetry channel was chosen in preference to the back-up channel, since the dosimetry of the accelerator is based on the primary channel.

On inspection, the test point available from the dosimetry system provided a signal which repeatedly underwent transitions, with each transition representing the measurement of one 1/64th of one monitor unit (*i.e.* 1/64th MU) on the accelerator dosimetry system. The dosimetry of the accelerator is based on counting these transitions. A typical waveform observed with an oscilloscope is shown in Figure 2-8 for the accelerator operating at 400 Hz PRF and a dose rate of approximately 500 MU min^{-1}.

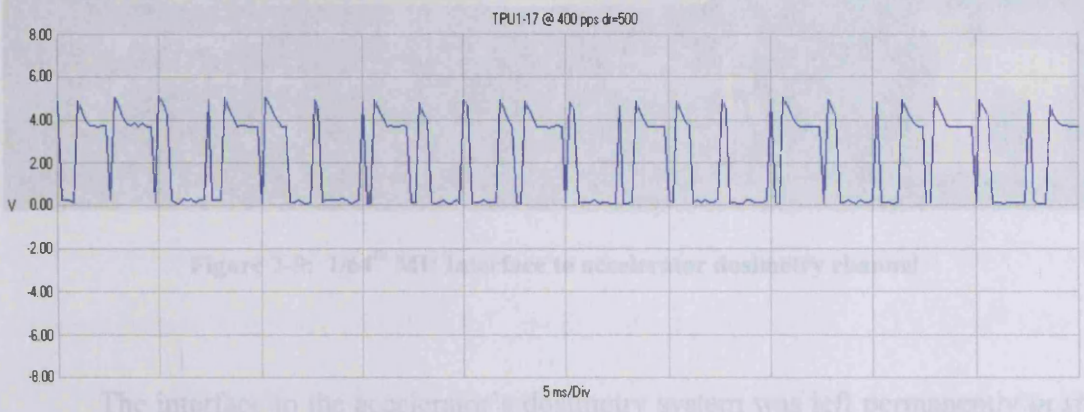

Figure 2-8: Test point waveform from dosimetry channel. The accelerator was operating at 400 Hz PRF. The dose rate was 500 MU min^{-1}. The time base was 5 ms division^{-1}.

For the signal shown in Figure 2-8 (duration 50 ms) there are 27 positive-going transitions. Based on the accelerator dose rate of 500 MU min^{-1}, a dose of 0.41 MU was delivered during this period. The corresponding number of 1/64th MU is 26.7 which agrees with the number of transitions identified.

The SME data acquisition module counted the cumulative number of transitions produced by the accelerator's dosimetry system in a 16-bit register, and recorded the cumulative value at the end of each period of signal integration together with the integrated dose signal for all 20 channels of the SME. The maximum dose which could be counted by the 16-bit register was 1024 MU (*i.e.* corresponding to 2^{16} transitions).

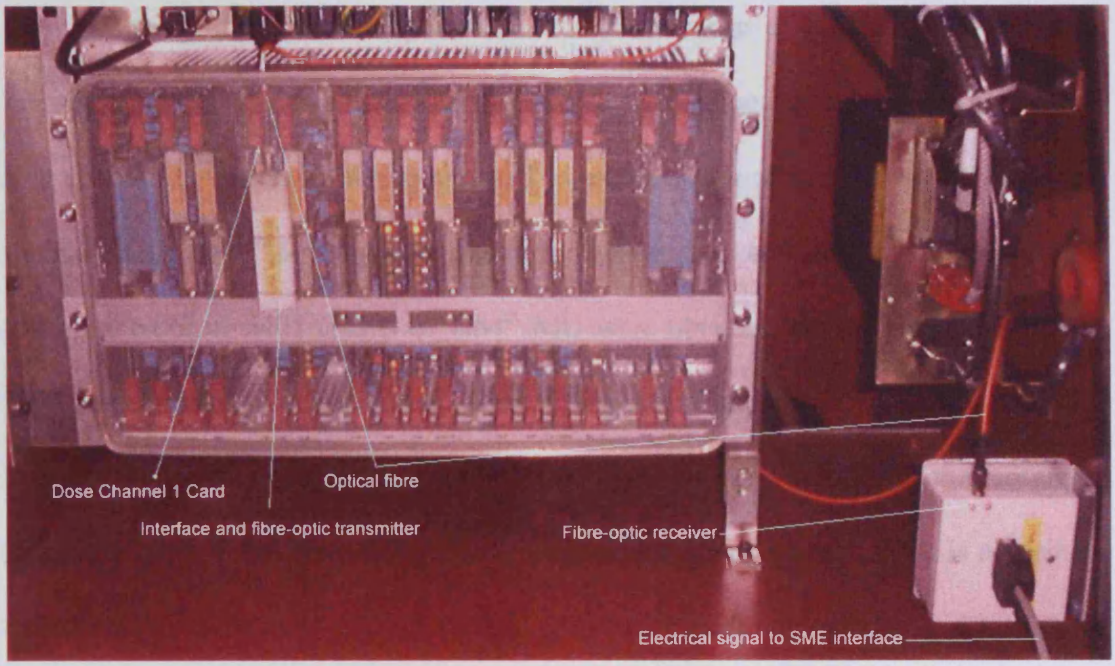

Figure 2-9: 1/64th MU Interface to accelerator dosimetry channel

The interface to the accelerator's dosimetry system was left permanently *in situ* even though the signal was only used for experimental work with the SME. In order to avoid interfering with dosimetry of the accelerator, for example by introducing spurious signals and thus affecting the accelerator's output calibration, the electrical connection to the dose card had to be optically isolated. This was achieved using fibre-optic techniques to convey the signal to a fibre-optic receiver housed within an interface unit conveniently located on the drum of the accelerator. This unit provided the electrical signal used for direct input to the SME. The use of optical fibre technology not only ensured electrical isolation of the dosimetry channel of the accelerator, but would undoubtedly have reduced electrical noise pick-up. Figure 2-9 is a photograph of the interface.

2.5.3 Performance

Testing of the dosimetry interface over the range of doses capable of being measured by the 16-bit register was performed by reading the total number of $1/64^{th}$ MU counted by the SME during repeated exposures. For all accelerator MU settings, the number of $1/64^{th}$ MU counted was never greater than one from that expected: for example, 6400 or 6401 counts of $1/64^{th}$ MU were obtained for the case of 100 MU. This was observed for all operating PRFs of the accelerator.

The delivery of a single $1/64^{th}$ MU beyond that set is a result of the fact that a single accelerator radiation pulse represents greater than $1/64^{th}$ MU. This is evident by calculating the dose as a fraction of 1 MU delivered by a single radiation pulse from the observed dose rate knowing the accelerator PRF: when operating at 400 Hz PRF the accelerator dose rate was 515 MU min^{-1}, giving a dose per pulse of 1.37 x $1/64^{th}$ MU.

The observed accuracy of the accelerator in controlling dose delivery also demonstrates the ability of the accelerator dosimetry system to terminate radiation exposure in a time interval *less* than the interval between radiation pulse (*i.e.* 2.5 ms in case of 400Hz PRF).

The interface also allowed 'leakage' of the monitor chamber and the electrometer of the dose channel to be readily quantified. During radiation-off, typically 45 x $1/64^{th}$ MU were be counted in a period of 5 minutes. This represented a leakage rate of approximately 0.14 MU min^{-1}, which was well within manufacturer's specification for the accelerator (maximum 0.2 MU min^{-1}). Leakage at this rate was observed both immediately post-irradiation and after reset of the accelerator dosimetry system.

Figure 2-10 shows a typical recording of 1/64th MU counted during dose delivery. A dose of 100 MU was delivered in this case and the accelerator PRF was 400 Hz. The number of 1/64th MU delivered during each SME integration period of 100 ms (corresponding to 40 radiation pulses) was obtained from the cumulative value stored for each integration period. The 19.0 s of data shown cover the entire 100 MU delivery. Single 1/64th MU increments attributable to leakage are evident at times 0.5 s and 5.7 s. Clearly beam-start is well resolved at a time just after 6.5 s. During steady-state irradiation the mean number of 1/64th MU per sample interval was 55.13 (S.D. 0.45), calculated for the data after time 10.0 s. This corresponds to a dose rate of 516 MU min^{-1}, which is consistent with the accelerator dose rate observed during the measurement.

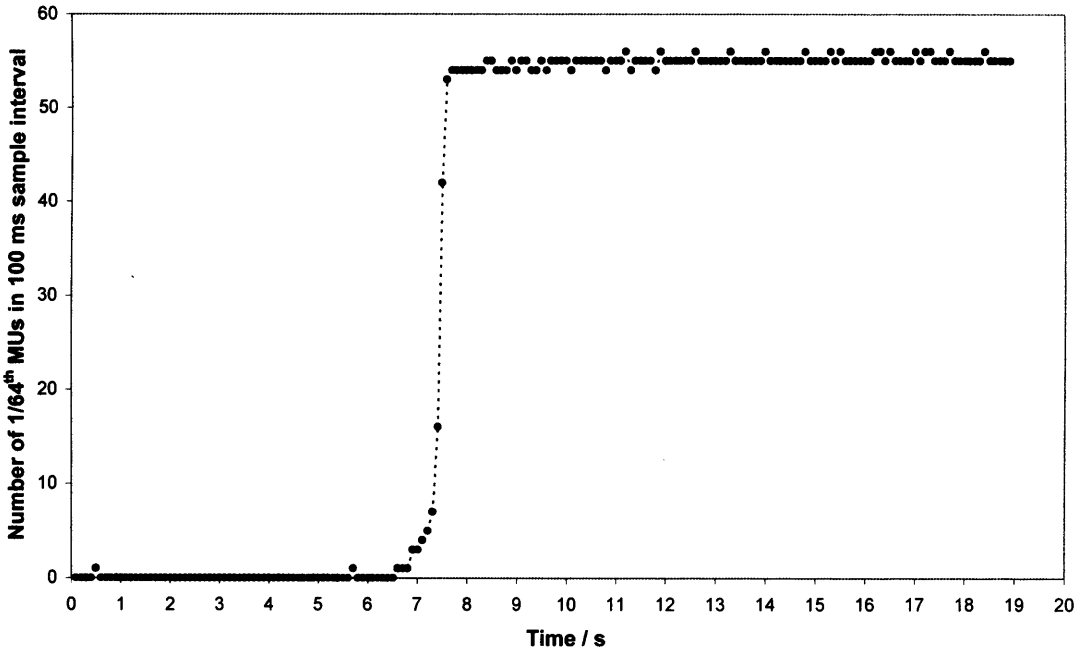

Figure 2-10: Number of 1/64th MU recorded by SME during delivery of 100 MU at 400 Hz PRF. The sample interval was 100 ms (40 radiation pulses).

2.6 High tension supply for ion chamber applications

The SME provided a high tension supply via a BNC connector for use as a polarising voltage with ionisation chamber detectors including the strip ionisation chamber array (Chapter 3). The supply was negative polarity to provide a negative signal compatible with the input polarity of the SME electrometers (configured for use with commercial semiconductor diode detectors).

Short and long–term stability of the high tension supply was considered. The voltage was measured directly using a DVM for several hours following power-on of the SME. Measurements were made on several occasions over a six-month period during which time the strip ionisation chamber array was under investigation. The results are shown in Figure 2-11.

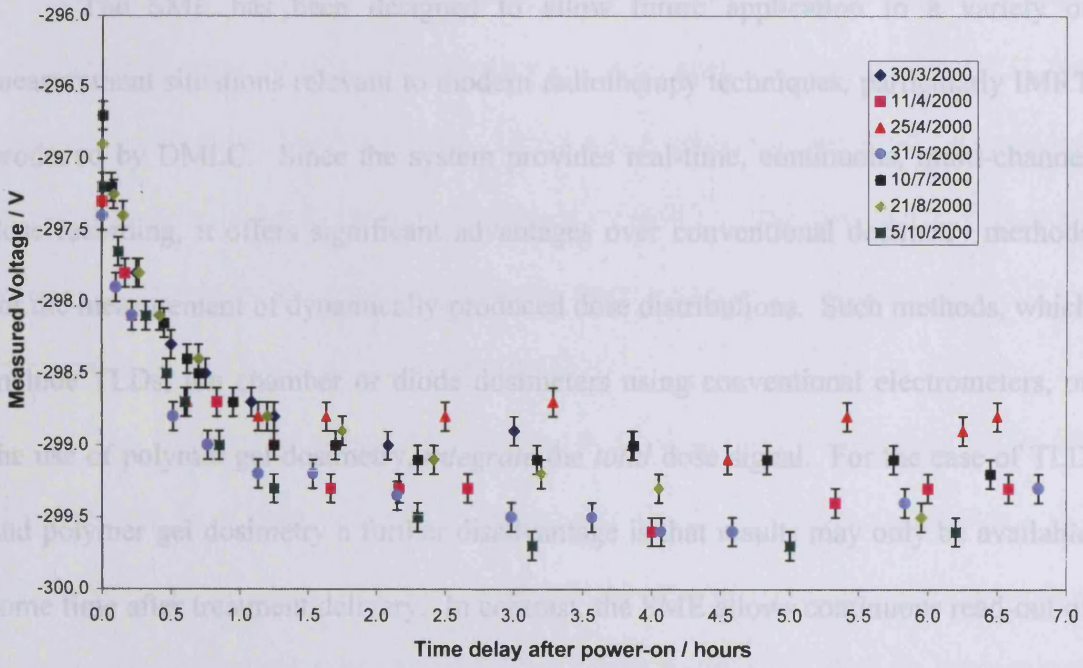

Figure 2-11: Stability of SME high voltage supply following power-on. Measurements were conducted over a six-month period.

Clearly, the voltage stabilises after approximately 1.5 hours, during which time the voltage changes by approximately –2.0 V. From typical charge-voltage characteristics measured for the strip ion chamber array (Chapter 3) this results in a very small change in collected charge (less than 0.01 %). It was therefore concluded that no warm-up period was necessary for the high voltage supply since the observed voltage change would have no measurable effect on the collected charge.

The data also shows no identifiable long-term drift in the voltage supplied by the SME. The mean 'stable' voltage (averaged from data measured at least 1.5 hours following power-on) on the seven occasions over the six-month period was 299.1 ± 0.2V.

2.7 Future applications of SME

The SME has been designed to allow future application to a variety of measurement situations relevant to modern radiotherapy techniques, particularly IMRT produced by DMLC. Since the system provides real-time, continuous, multi-channel dose recording, it offers significant advantages over conventional dosimetry methods for the measurement of dynamically-produced dose distributions. Such methods, which include TLDs, ion chamber or diode dosimeters using conventional electrometers, or the use of polymer gel dosimetry, *integrate* the *total* dose signal. For the case of TLD and polymer gel dosimetry a further disadvantage is that results may only be available some time after treatment delivery. In contrast, the SME allows continuous read-out of dose signals from up to 20 detectors with high temporal resolution, which could ultimately be performed on-line, together with simultaneously recording of cumulative

accelerator MU. There are potential applications in both pre-treatment and real-time verification.

The SME could be applied to pre-treatment verification studies of dynamic dose delivery using multiple point dose detectors in a phantom. Since the device provides continuous read-out of dose delivery, it allows correlation of dose delivered to a detector at any moment during the DMLC sequence against that intended. This may allow confirmation of dose delivered against that modelled within the IMRT planning system, including correct dose modelling of the MLC delivery system and correct execution by the MLC delivery system. This type of approach to IMRT verification has been reported by Low *et al.* (1998b). They used a phantom containing film and multiple point integrating detectors (ion chamber and TLD) but were only able to consider the *total* integrated dose at the *end* of the sequence. More recently, Agazaryan *et al.* (2000) have reported continuous read-out of dose delivery using a phantom containing 15 commercial diode detectors and a commercial electrometer (IVD, Sun Nuclear Corporation, Melbourne, FL, USA) which integrated the diode signals, and recorded dose every 2.0 s. Phantoms designed for IMRT verification that accommodate multiple detectors for this purpose are becoming commercially available (IMRT 3D QA Phantom™, Med-Tec Inc. Orange City, IL, USA).

The SME is also suitable for real-time dosimetric verification since the electrometers have been designed to be suitable for direct patient connection. This allows the use of diode detectors designed for *in vivo* dosimetry for continuous measurement of patient dose delivery. This may be of value both in conventional radiotherapy and IMRT in order to investigate the effect of intra-fraction patient motion on dose delivery. This includes effects of respiration, or other patient or internal organ

motion, which is of concern particularly for IMRT, since the dose distribution is delivered over an extended time (*e.g.* Chui 1999).

Further applications of the SME include the quality assurance of the accelerator radiation beam, particularly during beam-start: with suitable detectors the SME allows assessment of beam flatness, output and energy continuously during beam-start with adjustable and if desired, high temporal resolution.

Chapter 3: Development and application of a strip ionisation chamber array

3.1 Introduction

This chapter describes the design and performance of an ion chamber array under investigation for real-time verification of DMLC on a linear accelerator. The chamber array, located at the beam aperture of the accelerator, is used with the synchronised multi-channel electrometer (SME, Chapter 2). The suitability of the configuration for the verification of dynamic wedge and DMLC treatment will also be considered in this chapter.

There are a few reports of custom-built ionisation chambers for the purpose of dose measurement or monitoring during external beam radiotherapy. Galbraith *et al.* (1990) implemented a custom-built ionisation chamber as part of a dose rate trip on a dual mode accelerator. A single wire mounted on insulating supports within the accelerator's secondary collimator and maintained at a negative potential formed the chamber. Paliwal *et al.* (1996) reported the use of a large area transmission ion chamber that mounted below the accessory tray of an accelerator for assessing the consistency of dose delivery in conventional static field radiotherapy. They used a commercial dose-area product meter (140 x 140 mm) aligned with the radiation beam central axis and mounted perpendicular to the beam direction. Paliwal *et al.* investigated the ability of the system to detect changes in treatment parameters including correct blocks, wedge, field size and MU. In the case of field size, the signal from the system (normalised to 100 % at 10.0 x 10.0 cm) increased from 16 % to 410 % between the extreme field sizes 4.0 x 4.0 cm and 20.0 x 20.0 cm. The relationship between chamber signal and collimator position for a dynamic wedge was also simulated by manual positioning of the moving collimator. For a group of four patients

undergoing consecutive measurements over ten days of treatment, deviations were observed to be within a ± 3 % limit. The chamber did not impede normal working practice due to its optical transparency, and did not introduce significant attenuation (< 0.3 %) or a significant rise in surface dose (+ 3.4 %). Paliwal *et al.* concluded that the chamber could be used to measure the consistency of delivered dose and was sensitive to small changes in MU, field size and accessories. They also proposed use of the device to monitor dynamically generated dose distributions. However, the device was limited to identifying any deviation from the *first* treatment, and this was only possible *after* a treatment was complete. The authors also admitted that the system could not itself prevent errors from happening.

Partridge *et al.* (1999a) used a large-area ionisation chamber (200 x 200 x 12 mm) mounted onto the accessory tray of their accelerator to measure the temporal variation of the accelerator's output. The data was used to remove the effect of output fluctuations on the scanning CsI/photodiode EPID developed at the Royal Marsden Hospital (Sutton, UK) used for thickness measurements (Symonds-Tayler *et al.* 1997). Chamber signal was acquired with image data by direct connection of the signal to an electrometer channel corresponding to the edge of the array.

Kerr *et al.* (1997, 2000) reported the use of a single strip ionisation chamber for on-line monitoring of dynamic wedge treatments at Kingston Regional Cancer Centre (Ontario, Canada). The authors highlighted that for dynamic wedge treatments there is an underlying assumption that the delivery system performs reproducibly following commissioning and in the time interval between routine quality assurance. The reported system was designed as a convenient means of assessing reproducibility of dynamic wedge dose delivery independently from the control system of their Varian 2100C/D accelerator. The prototype consisted of a single strip ion chamber formed by

copper tape (0.3 x 16.0 cm) with a 2.0 mm air gap built on an accessory tray. The strip was orientated parallel to the direction of collimator motion. A 300 V polarising voltage was used and the instantaneous current from the collecting plate was measured at a rate of up to 4 Hz by a pico-ameter to produce a waveform showing the variation of chamber current with time. Kerr *et al.* (2000) proposed that the strip chamber could be made thin enough so as to be indistinguishable from the field centre cross-hairs, and as such could be left in place for all treatments. For Co-60 irradiation (*i.e.* constant dose rate) the chamber current was observed to remain constant within fluctuations of approximately 0.4 %, which was considered to be the noise level in the digital signal. Pre- and post-irradiation leakage was stable at approximately 1 % of the beam-on signal. Measurements of a 6 MV static beam from their accelerator showed significant, non-reproducible transient fluctuations in the raw chamber current equivalent in range to approximately 30 % of the mean signal level. However, the total charge collected was reproducible to within 0.1 %. Kerr *et al.* (2000) demonstrated that these transients were not a result of electrical noise and attributed them to normal fluctuations in the dose rate of their accelerator. For dynamic wedges the current/time waveform showed two phases: after a rise in current at beam-start, the current remained constant during the open portion of the field where the collimators were stationary; then, following a momentary interruption in dose rate (and hence reduction in chamber current), the current rose to a level (which was a function of accelerator dose rate) from which it fell as the moving collimator reduced the irradiated length of the ion chamber. Kerr *et al.* (2000) recorded the current/time waveform for four available wedge angles whilst keeping field size, dose rate and number of monitor units constant. For all wedge angles the level of instantaneous current in the static phase was constant, but the duration of this phase differed, as did the waveform during collimator motion. It was

concluded that the chamber could identify the use of an incorrect wedge angle. The system was also able to detect an error in field size since the current during the static phase was proportional to the length of chamber exposed and hence field size. Additionally, the relative duration of the dynamic phase changed with wedge angle. On introducing a moving average filter to reduce transients in the signal associated with dose rate fluctuations, two successive measurements showed instantaneous differences in signal of up to 4 % of the maximum. On this basis Kerr *et al.* (2000) suggested that the minimum deviation which could be detected was 7 - 8 %, *i.e.* approximately twice the level of normal fluctuations. The authors stressed that since the current/time waveform was a function both of dose rate and collimator position, differences in the signal waveform only indirectly suggested incorrect beam profile delivery and as a result it may not be possible to quantify any error in the resulting dose distribution. However, they proposed that an error in dose rate was unlikely to counteract an error in collimator position. Kerr *et al.* (2000) also proposed that on-line assessment of treatment reproducibility would be possible by correlating the current waveform being measured against previous measurements of the same treatment sequence.

The strip ion chamber described in this present work is of similar design to that described by Kerr *et al.* (2000). However, use of the device with the SME allows comparison of recorded signals against accelerator *MU* as opposed to *time* as in the case of Kerr *et al.* (2000), which is necessary for verification of dynamic delivery using a dose-based control system. Sample rates for the SME are also much faster than the maximum of 4 Hz used by Kerr *et al.* (2000). The chamber developed also has improved leakage performance and the multiple element design allows extension of its application from a single moving collimator (*i.e.* dynamic wedge) to evaluation for DMLC verification in which leaves move independently.

It should be noted that Scanditronix-Wellhöfer (Schwarzenbruck, Germany) are developing a device based on a metal/phosphor plate and amorphous silicon photodiode array. The device is of very similar design to the flat-panel portal imaging devices under development currently, which will be considered in Chapter 7 with regard to their application to verification. The Scanditronix-Wellhöfer device, which is not commercially available at present, is also intended to be mounted at the beam aperture of the accelerator for verification of IMRT (R Plompen, Scanditronix-Wellhöfer, Personal Communication, 2000). A prototype (ADAS 128) based on a 128 x 128 pixel matrix (9.6 x 9.6 cm) has been used for MVCT (Groh *et al.* 1998). Paul *et al.* (1998) have reported work in progress to characterise the device for its application for dynamic treatments.

3.2 Description of strip ionisation chamber array

The ion chamber array was mounted on a modified accessory tray of the Elekta SL15*i*. The array comprised 20 parallel plate chambers constructed from two opposed epoxy glass boards (1.6 mm thick) of the type intended for printed circuit board production which had copper cladding (35 μm) on the innermost sides only. The polarising and collecting plates of the chamber were formed from isolated regions of copper created using a computer-controlled milling machine to produce insulating tracks of 1.0 mm width and 0.5 mm depth through the copper cladding into the board. For practical reasons the boards were limited to 170 x 170 mm, thus limiting plate area. The dimensions of the polarising and collecting plates shown in Figure 3-1.

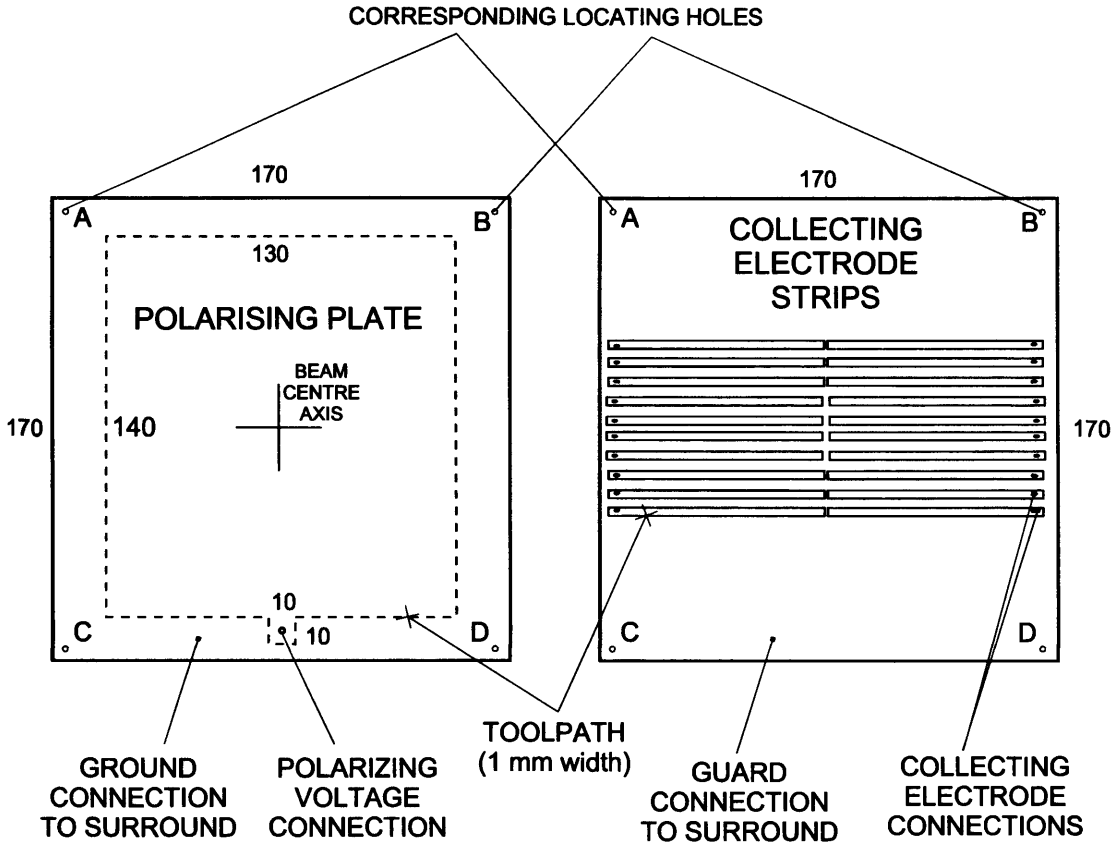

Figure 3-1: Geometry of the polarising and collecting plates. Dimensions shown in mm. The 1.0 mm wide tool path was used to create 'islands' in the copper cladding as drawn. The polarising and collecting plates were aligned using corresponding locating holes through each board (shown as A-D) which ensured alignment of the plate areas.

The array had twenty collecting plates formed from elongated strips (80.0 x 3.0 mm) arranged in two opposing banks with ten plates located either side of central axis (Figure 3-1, right). The chamber was placed in the accessory tray (68.2 cm from source) such that the collecting plates were parallel to the direction of leaf motion. The centre of each was aligned with the projection of the first five MLC leaves (10 mm wide at isocentre) either side of central axis, covering two banks of ten leaves in total.

The polarising plates extended 65 mm either side of central axis in the direction of leaf travel (and thus projected a sensitive length for each chamber pair of approximately 190.0 mm at isocentre). This meant that the maximum field width (in the direction of leaf movement) which could be accommodated by the present chamber

was 190.0 mm at isocentre, with a dimension of 100.0 mm for the field length (based on ten leaves being shadowed in the orthogonal direction).

A guard electrode was connected to the copper cladding surrounding each collecting electrode, which included a region of width 1.0 mm passing perpendicular to the strip direction through central axis. The width of this guard, in addition to the 1.0 mm width of the tool-path which formed each collecting electrode, meant that there was a 3.0 mm width between collecting electrodes across central axis. The use of guarding surrounding each chamber was intended to avoid leakage currents from the polarising electrode reaching the collecting electrodes, and to define the collecting volume of each ion chamber (Boag 1966).

The plates were aligned via locating holes in each corner positioned relative to the electrode area (as shown in Figure 3-1). Nylon bolts, washers and nuts were used and these acted as insulating support pillars. Nylon washers at each corner were used as 'spacers' between the plates to provide a plate separation at each corner of 0.83 ± 0.01 mm. The chamber was mounted using the insulating pillars within an outer enclosure providing electrical screening. The top and bottom of the enclosure were made from copper clad board (220.0 x 235.0 mm) with the copper cladding facing inwards in contact with square section aluminium bars forming the sides of the enclosure, thus completing the construction and ensuring electrical continuity. The depth of the electrical screening enclosure was 25.0 mm. A cross-section of the ion chamber within the enclosure is shown in Figure 3-2. The insulating support pillars on which the chamber was constructed protruded through the lower enclosure plate and located into recesses machined into the accessory tray allowing correct chamber alignment with the radiation central axis and MLC leaf banks. The accessory tray holder was modified in order to rigidly clamp the accessory tray and overcome relative movement within the

accessory tray holder (maximum 1.5 mm) observed for this tray and those used clinically (*e.g.* customised shielding).

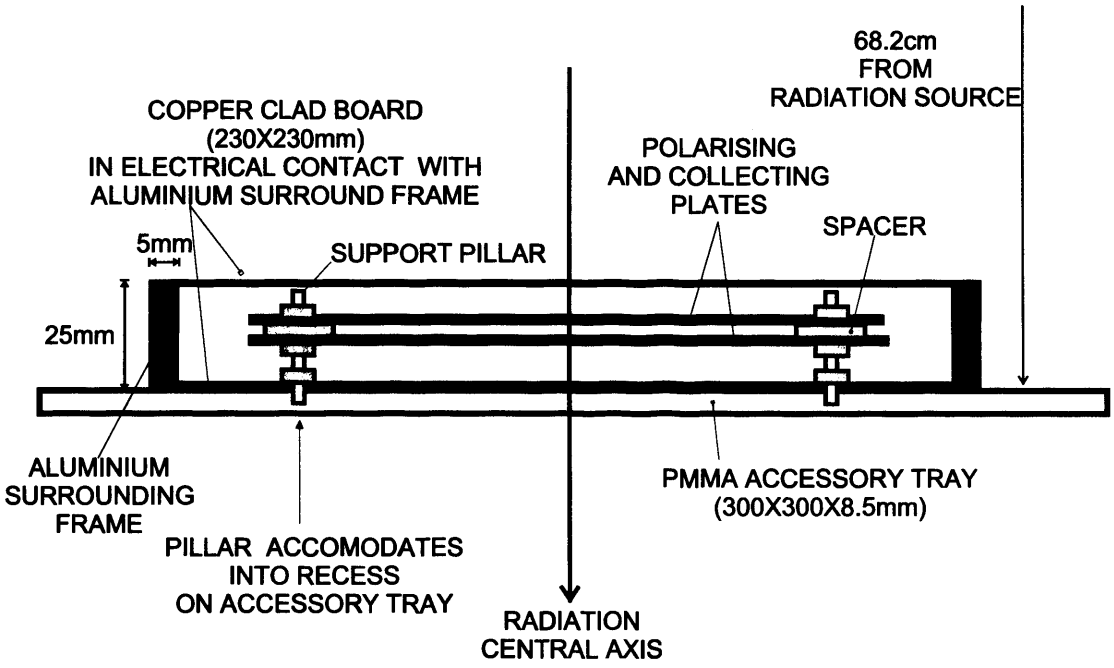

Figure 3-2: Cross-section showing location of ion chamber within electrical screening enclosure. The location of the structure onto the accessory tray of the accelerator is also shown.

Electrical connection to the polarising and collecting plates was achieved from the non-clad side by feeding the centre core of each connecting cable through holes in the epoxy board. Miniature coaxial cable (diameter 3.0 mm) was used to reduce cable bulk. The cable was also chosen for its low microphonic (triboelectric) noise performance.

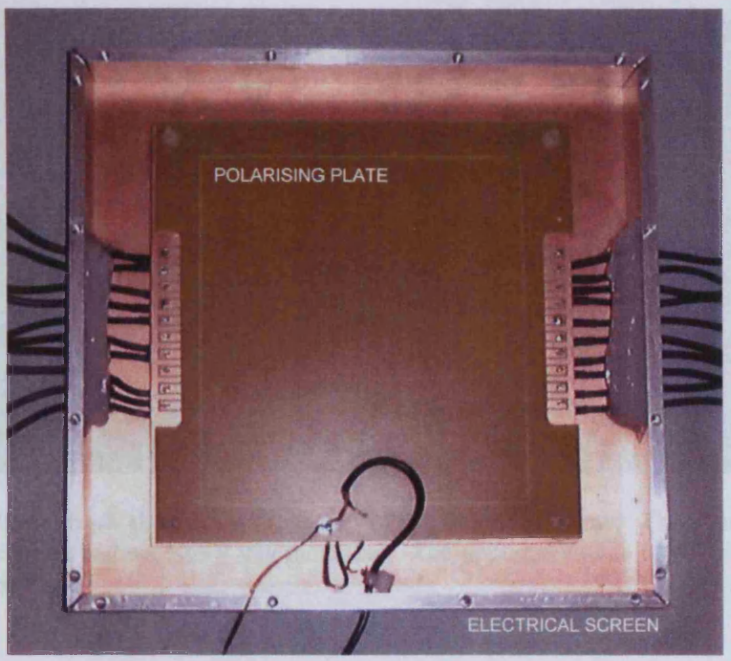

Figure 3-3(a): Photograph showing internal construction of ion chamber. The top plate of the electrical screening enclosure has been removed to show the polarising plate overlying the collecting plates, and the construction of the surrounding electrical screen.

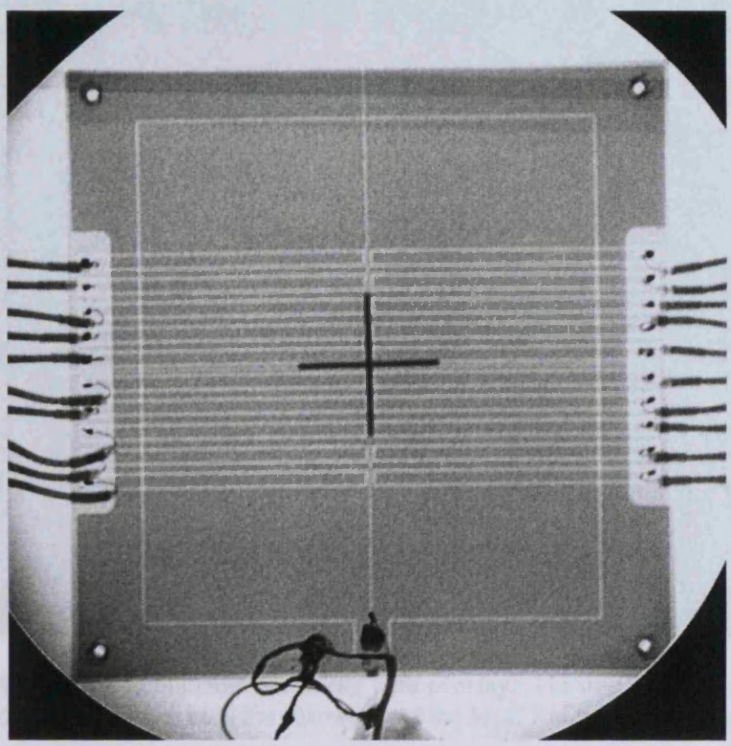

Figure 3-3(b): Radiograph of ion chamber taken on radiotherapy simulator. The alignment of collecting and polarising plates is visible. The central cross-wires are the simulator field centre. The chamber was imaged whilst mounted on the modified accessory tray which is scribed with major field axes. These were aligned to the simulator cross-wires and are visible on the image. Clearly the image shows good alignment of the chambers with the field centre indicated on the accessory tray.

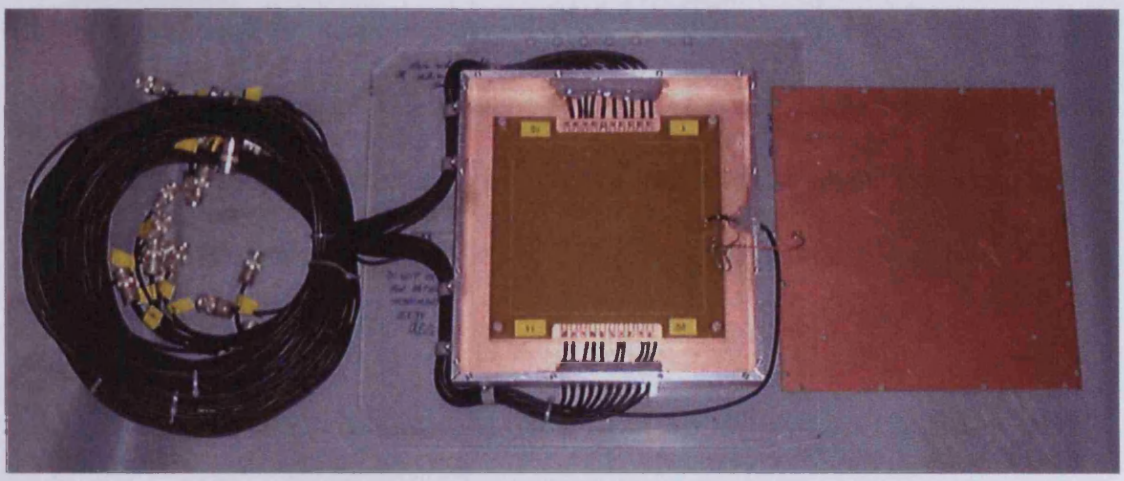

Figure 3-4(a): Photograph showing components of ion chamber array. The complete assembly is shown including cabling and accessory tray mounting. The uppermost plate of the electrical screening enclosure lies to the right.

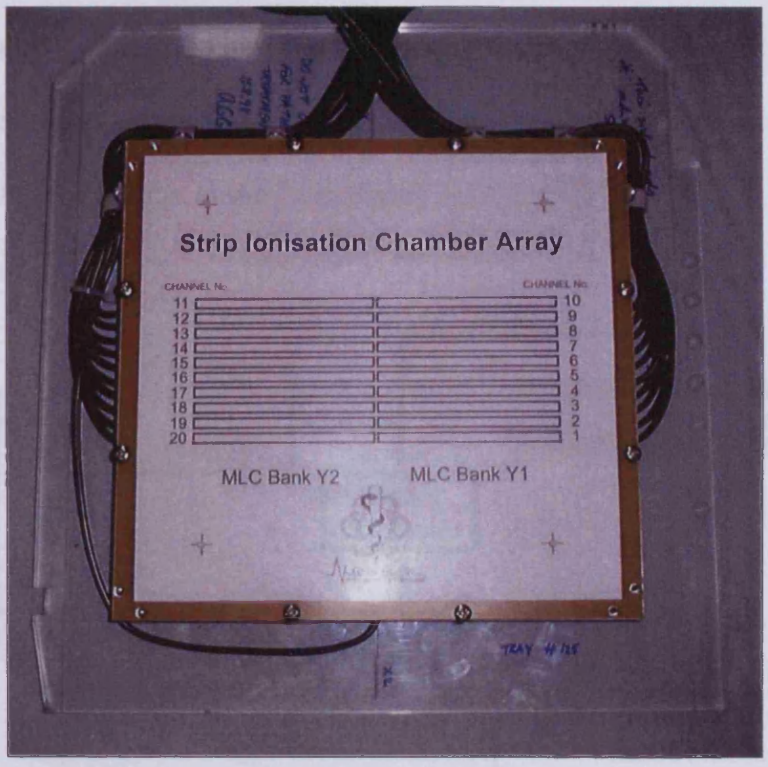

Figure 3-4(b): Photograph of ion chamber array with overlay. The overlay gives a visual indication of the location and identification of each ion chamber, and the MLC leaf bank orientation.

Figure 3-3(a) shows a photograph of the final arrangement (with the top plate of the electrical screening enclosure removed), and Figure 3-3(b) is a radiograph of the system showing plate alignment taken with the chamber mounted on the modified accessory tray. Figure 3-4(a) shows a photograph of the complete assembly including

cabling mounted on the accessory tray. Figure 3-4(b) shows the ion chamber with an overlay which located onto the four support pillars (Figure 3-2) which protrude outside the electrical screening enclosure. The overlay indicated externally the location and identification of each chamber, and the MLC leaf bank orientation.

3.3 Experimental characterisation of strip ionisation chamber array

Various fundamental characteristics of the strip ion chamber array were studied including chamber sensitivity, reproducibility and leakage. This was performed using a conventional electrometer (Therados RDM2A, Therados, Uppsala, Sweden) operating in charge mode, and an adjustable polarising voltage (Keithley 246, Keithley Instruments Inc., Cleveland, Ohio, USA). The arrangement, detailing collecting and polarising plate connections, is shown in Figure 3-5.

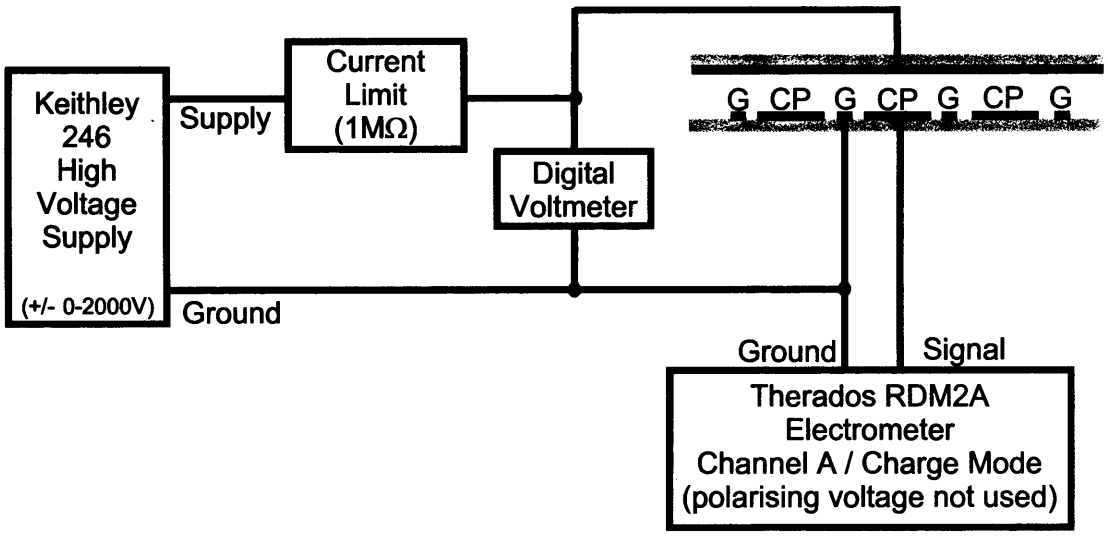

Figure 3-5: Electrometer and polarising voltage connections for experimental characterisation of the strip ion chamber array. The cross-section of the chamber indicates collecting plates (CP) interleaved with the electrically continuous surrounding guard (G).

Connection could be made to any of the twenty collecting plates. It should be noted that the 1 MΩ current-limiting safety resistor connected to the output of the

polarising supply formed a potential divider with the input impedance of the digital voltmeter (Fluke 77 Series II, Fluke Corporation, Everett, WA, USA) which has a nominal value of 10 MΩ. This resulted in the polarising voltage being approximately $10/11^{ths}$ of the voltage provided by the supply.

3.3.1 Chamber sensitivity and leakage

Based on the chamber dimensions described and the plate separation afforded by the nylon washers acting as spacers at the support pillars (0.83 ± 0.01 mm) (Figure 3-2) the sensitive volume of the chamber was approximately 0.16 cm^3. Unfortunately the copper clad board used for plate construction bowed following removal of the tracks described, resulting in increased separation at the centre of the array (maximum 1.2 mm). This made the actual chamber volume larger than that estimated simply from geometry. Comparison at 6 MV against an NE2570 Farmer-type ion chamber (0.6 cm^3) suggested that the sensitivity of a single collecting plate was approximately 60 % of the Farmer. This indicates that the active volume of each chamber was somewhat greater then expected even accounting for the bowing. This was thought to be attributable to the construction of the collecting plates since isolation of each 3.0 mm wide collecting plate on the copper clad surface of the epoxy glass board was achieved by a removing a track of 1.0 mm width. This created an insulating region of substantial relative width to which no guard connection was made. This would allow an electric field pattern wider than the width of the collecting plate, and thus giving rise to an enlarged active volume (Boag 1966).

Leakage currents were very small (<0.05 %) during all measurement occasions and as such could be ignored. Furthermore, testing with the SME showed no leakage signal on applying polarising voltage, confirming the excellent leakage properties of the chamber, which can be attributed to the design of the collecting plates/guard.

3.3.2 Stabilisation and reproducibility of chamber response

The stabilisation and reproducibility of the chamber response was assessed during several sequences of exposures. Data was measured using two of the available collecting plates (numbers 5 and 11, see overlay Figure 3-4(b)) with the chamber located at the accessory tray using doses of approximately 2.2 Gy (100 MU). Figure 3-6 shows the measured response normalised to the mean value calculated for the repeated stable measurements. All data was measured using a polarising voltage of 272.2 V.

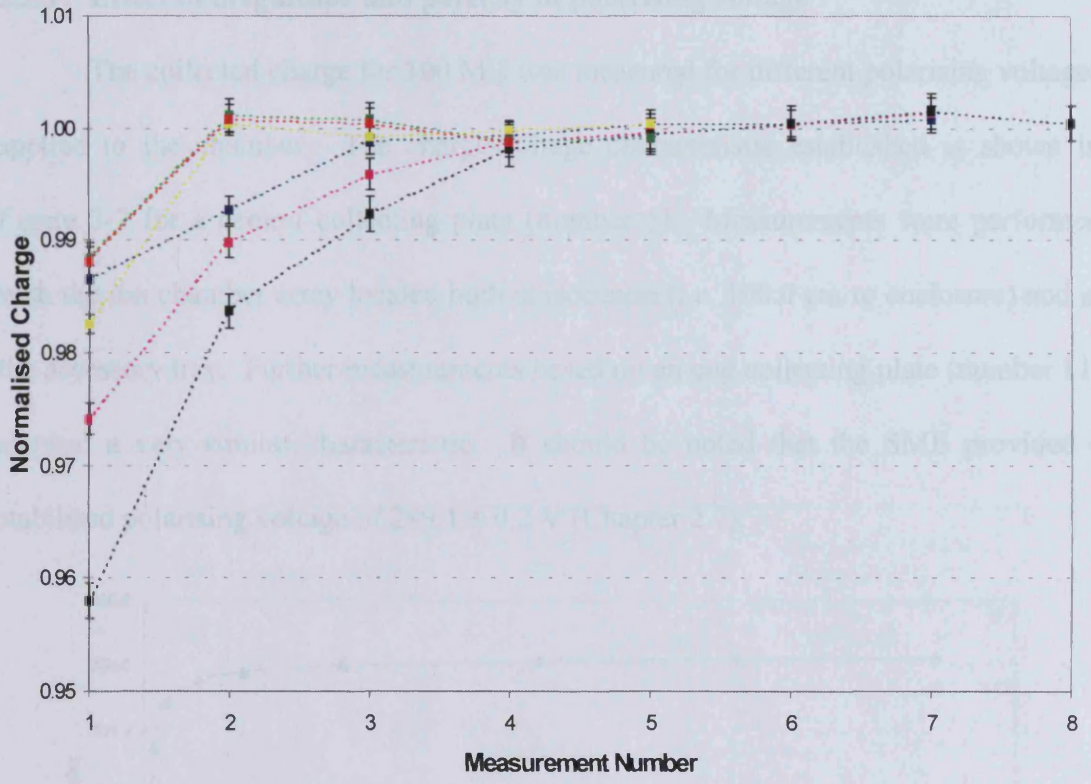

Figure 3-6: Stabilisation and reproducibility of strip ion chamber response on several occasions (3-5 days between each occasion) . Readings are shown normalised to the mean of the stable readings and were measured for two collecting plates in sequences of 2.2 Gy irradiations in which the array was located on the accessory tray.

Clearly the chamber exhibits good reproducibility (typically < 0.1 % SD) following one, and in some cases two, previous exposures for which the observed response was lower in all cases. In fact the mean reduction in response evident for the first measurement in each series was 2.0 % (SD 1.2 %). Based on these observations it

was concluded that a pre-irradiation dose to the entire array of approximately 4.0 Gy was advisable to ensure stabilised response. This finding is a common observation for the first few readings taken with an ionisation chamber; the cause is not well understood, but is thought to be associated with charge built up on insulators not protected by the guard (Johansson *et al.* 1987; Johansson, Private Communication, 2000). A phenomenon of similar magnitude was observed for repeated exposures using the SME. Additionally, it was observed that exposures made after an interval of 1.5 hours or more following initial irradiation showed a similar effect.

3.3.3 Effect of magnitude and polarity of polarising voltage

The collected charge for 100 MU was measured for different polarising voltages applied to the chamber. The charge-voltage characteristic established is shown in Figure 3-7 for a central collecting plate (number 5). Measurements were performed with the ion chamber array located both at isocentre (*i.e.* 100.0 cm to enclosure) and at the accessory tray. Further measurements based on an end collecting plate (number 11) showed a very similar characteristic. It should be noted that the SME provided a stabilised polarising voltage of 299.1 ± 0.2 V (Chapter 2.7).

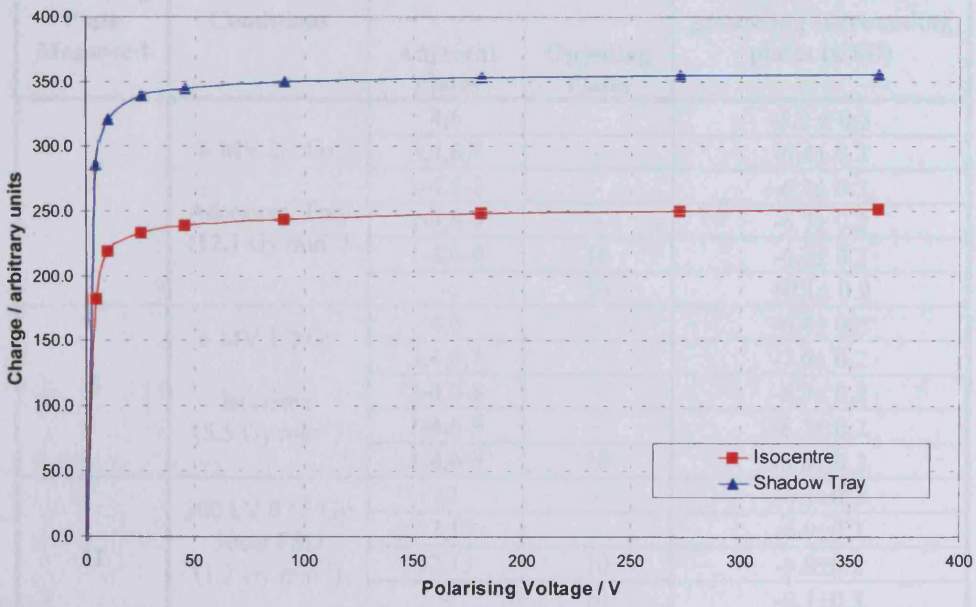

Figure 3-7: Typical charge-voltage characteristic for strip ion chamber array. This data was measured for collecting plate 5 at isocentre and accessory tray.

The effect of reversing the polarity of the polarising voltage was also considered for both collecting plates numbers 5 and 11. Measurements were made for an absolute value of polarising voltage of 272.2 V with the chamber array located at the accessory tray. The ratio of chamber readings for both polarities was 1.0045 ± 0.022 and 1.0068 ± 0.0014 (collecting plates 5 and 11 respectively). Clearly the chamber exhibits only a small polarity effect which is comparable with reported values for commercial ionisation chambers of parallel plate design (Mattsson *et al.* 1981, Nisbet and Thwaites 1998).

3.3.4 Effect of grounding adjacent collecting plates

During experiments in which charge was measured from a single collecting plate, it was observed that electrical connection of the surrounding collecting plates to the electrometer input ground had an effect on the magnitude of charge measured. Data obtained in measurements using a polarising voltage of 272.2 V for a central plate (number 5) and an end plate (number 11) under different irradiation conditions is shown in Table 3-1.

Collecting Plate Measured	Irradiation Conditions	Surrounding Plates Grounded		Change in charge collected (%) on grounding surrounding plates (± SD)
		Adjacent Plates	Opposing Plates	
5	6 MV 2.2 Gy Accessory Tray (12.1 Gy min^{-1})	4,6	-	-5.2 ± 0.3
		3,4,6,7	-	-6.4± 0.2
		2-4,6-8	-	-6.7± 0.2
		1-4,6-9	-	-6.7± 0.2
		1-4,6-9	16	-6.5± 0.2
		-	16	+0.1± 0.2
5	6 MV 1.0 Gy Isocentre (5.5 Gy min^{-1})	4,6	-	-6.4± 0.2
		3,4,6,7	-	-7.6± 0.2
		2-4,6-8	-	-8.9± 0.2
		1-4,6-9	-	-8.7± 0.2
		1-4,6-9	16	-8.8± 0.2
11	300 kV 0.55 Gy 50cm FSD (1.2 Gy min^{-1})	12	-	-6.1±0.2
		12,13	-	-6.9±0.3
		12,13	10	-6.8±0.2
		-	10	-0.1±0.3

Table 3-1: Effect of grounding surrounding collecting plates on measured charge

The identification of each collecting plate is shown in the overlay (Figure 3-4(b)). From the data it is clear that on grounding the collecting plates surrounding the plate under test the level of collected charge declined by the order of several percent. However, no additional effect was observed when grounding plates beyond two adjacent on both sides to the plate under test (*i.e.* plates 2-4 and 6-8 in the case of collecting plate 5). It is also clear that grounding the opposing plate had no effect (plate 16 in the case of collecting plate 5, and plate 10 in the case of collecting plate 11). The underlying cause is believed to be a change in the effective collecting volume associated with changes in the electrical potential of regions surrounding a collecting plate (*i.e.* adjacent collecting plates) (Boag 1966). Although the guard was intended to define the collecting volumes, its relatively small width compared to the size of adjacent collecting plates was thought to have been insufficient to overcome the effect of changes in potential of adjacent collecting plates when not grounded.

On the basis of these findings, all measurements to characterise the ionisation chamber based on measurements for a single collecting plate using the RDM2A electrometer were made with the two collecting plates adjacent on both sides to the plate under test grounded to remove any possible effect. It should be noted that during operation of the strip chamber array with the SME all collecting plates are effectively grounded since the electrometer inputs are virtual ground. The lack of grounding of surrounding collecting plates was also observed to reduce the sharpness of the charge-voltage characteristic (Figure 3-7). This is associated with the introduction of regions of reduced electric field strength, and hence increased recombination (Boag 1966).

3.3.5 Longitudinal variation in chamber response

As has been discussed previously, the separation of the polarising and collecting plates was fixed at 0.83 ± 0.01 mm by spacers located at the extreme corners of the

construction, and increased to approximately 1.2 mm towards the centre of the chamber due to bowing of the plates. Previous work on a prototype ionisation chamber had confirmed that signal levels for a given pair of parallel plate electrodes forming an ionisation chamber was proportional to collecting volume of the chamber and hence to the plate separation. The variation in plate separation along the length of each chamber introduced variation in local sensitivity along the length of each strip chamber (*i.e.* longitudinally).

Measurements were performed using a 10.0 mm wide radiation field orientated perpendicular to the axis of the strip chambers at 100.0 cm SSD with the chamber lying on the customised accessory tray. A polarising voltage of 299.6 V was used (matched to that from the SME). Integrated charge was measured from collecting plates 5 and 11 (corresponding to central and end strip chambers respectively, Figure 3-4(b)) for fixed accelerator exposures at various positions along the length of the strip. Figure 3-8 shows the sensitivity measured with the centre of the 10.0 mm wide field placed at distances 10.0, 20.0, 30.0, 40.0, 50.0 and 60.0 mm off-axis, normalised to the mean sensitivity for all measurement on each of the collecting plates.

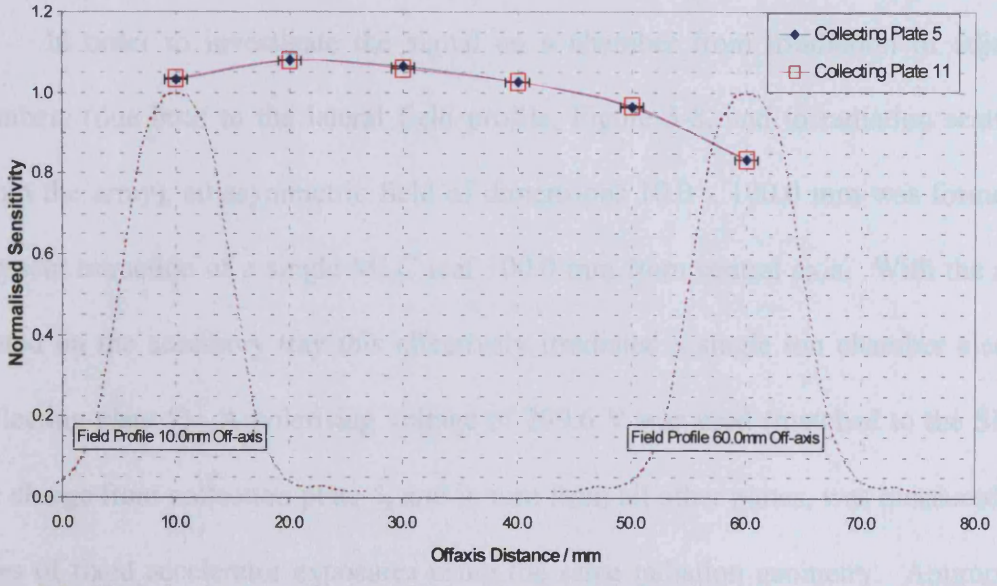

Figure 3-8: Variation in normalised sensitivity of collecting plates 5 and 11. The dose profile for the 10.0 mm wide field used is also shown at off-axis locations 10.0 and 60.0mm.

Clearly in Figure 3-8 non-uniform sensitivity is evident off-axis: between 20.0 mm and 50.0 mm there is an 11.2 % decrease in sensitivity which could be attributed to reducing plate separation or changes in electric field strength. The measured sensitivities at 10.0 and 60.0mm off-axis are reduced due to the limited dimension of the ion chamber strip and polarising plate. The field profile is indicated at these locations (taken from the TMS planning system (Helax AB, Uppsala, Sweden)).

In an attempt to reduce longitudinal variation in sensitivity, four additional spacers, identical to those at each corner, were placed either side of both banks of the collecting plates. Repeat measurements showed that the additional spacers reduced the overall sensitivity of the chamber (by reducing the collecting volume), but had little effect on the longitudinal variation in sensitivity. The reason for this lack of improvement was unclear but may have been associated with distortion remaining in the chamber, and non-uniform electrical field produced by the polarising plate. It was concluded that correction for longitudinal sensitivity variation may be required in the application of the chamber to DMLC verification (Chapter 3.5) and the original construction was retained.

3.3.6 Chamber 'cross-talk'

In order to investigate the signal on a chamber from irradiation of adjacent chambers (due both to the lateral field profile, Figure 3-8, and to radiation scattered within the array), an asymmetric field of dimensions 10.0 x 100.0 mm was formed to represent retraction of a single MLC leaf 100.0 mm from central axis. With the array located on the accessory tray this effectively irradiated a single ion chamber element (collecting plate 5). A polarising voltage of 299.6 V was used (matched to the SME). The charge from collection plate 5, and in turn from all other plates, was measured in a series of fixed accelerator exposures using the same radiation geometry. Appropriate

grounding of plates adjacent to the one under assessment was made (Chapter 3.3.4). The normalised charge collected from each plate is plotted against the charge measured for plate 5 in Figure 3-9.

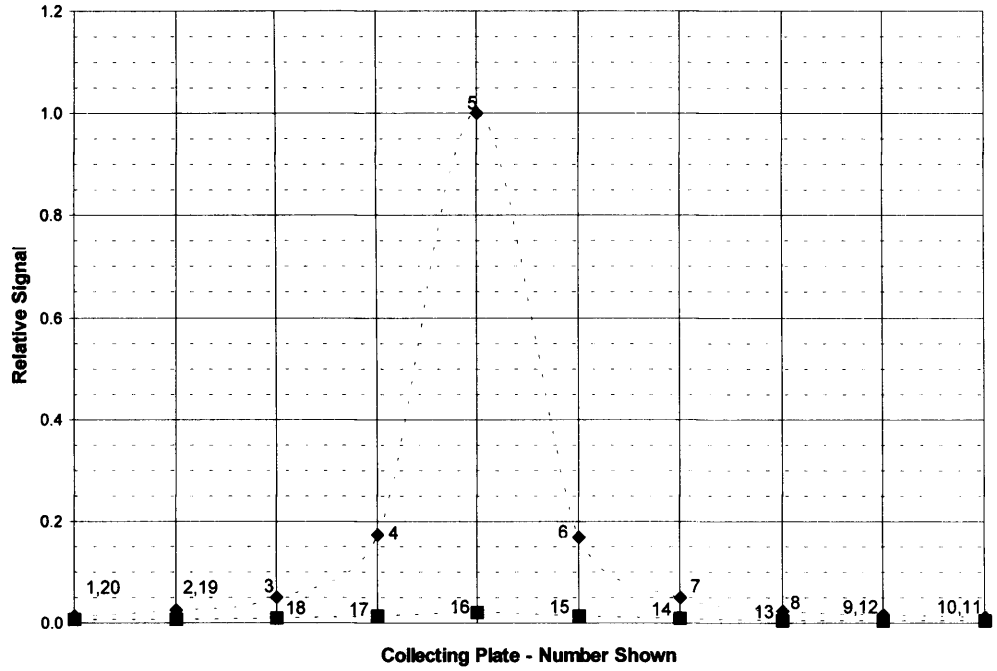

Figure 3-9: Normalised charge collected from all plates when irradiating plate 5 using 10.0 x 100.0 mm field. Plate numbers are indicated next to each data point (Figure 3-4(b)).

3.3.7 Transmission factor and surface dose measurement

The transmission of the ion chamber array and customised accessory tray was measured using a Farmer-type ion chamber positioned on field centre (5.0 cm deep in WT1 (Radiation Physics, St Bartholomew's Hospital, London, UK) at 95.0 cm SSD) and a field size of 10.0 x 10.0 cm (Table 3-2).

Component	Transmission Factor
Customised Accessory Tray	0.962 ± 0.001
Customised Accessory Tray + Ion Chamber Array	0.913 ± 0.001

Table 3-2: Measured transmission factors for ion chamber array and accessory tray

Loss of skin sparing was also measured using a parallel plate chamber (NACP, Scanditronix Medical AB, Uppsala, Sweden) which has a 0.5 mm graphite front window and a distance of 2.0 mm between the outer surface and the lower (collecting) electrode, giving a collecting volume 1.5 mm deep. Measurements were made at 6 MV with the chamber flush to the surface of WT1 phantom (100.0 cm SSD), and compared with measurements with the chamber under 15.0 mm depth WT1 (D_{max}) (Table 3-3).

Ion Chamber Array	Measured Surface Dose (%)
Omitted	38.5 ± 0.4
In place	41.4 ± 0.1

Table 3-3: Effect of ion chamber array on surface dose

According to the data, the introduction of the ion chamber array increases surface dose by 2.9 ± 0.4 % (expressed as a percentage of that measured at D_{max}).

3.4 Performance of SME and strip ion chamber array for dosimetry of static fields

In all measurements of static and dynamic fields that follow (Chapter 3.4 and Chapter 3.5 respectively) the strip ion chamber array was used with the twenty channel SME described in Chapter 2. This included use of the high tension supply provided by the SME for the chamber polarising voltage.

3.4.1 Stabilisation and reproducibility of chamber response

Measurements of the reproducibility of chamber response were performed with the SME by making repeated exposures on several occasions. The total dose signal for each measurement channel was obtained by summing the dose signal recorded by the

SME during each sample period. In each series it was often observed that the first summed dose signal was reduced in comparison to those following. This had been observed in experimental characterisation of the chamber (Chapter 3.3.2), and confirmed that the array required pre-irradiation. Discounting this initial reading, the standard deviation on repeated exposures was less than 0.2 % for all channels.

3.4.2 Long term sensitivity drift

The sensitivity of the strip ionisation chamber array was assessed over a period of 130 days using a fixed geometry at 6 MV. The chamber array was located at the accessory tray and an isocentre field size of 30.0 x 30.0 cm was used (which was larger than chamber array). Variation in accelerator output was measured using a Farmer-type ion chamber (5.0cm depth WT1, 95.0 cm SDD). The accelerator was operated at 400 Hz PRF, and the SME was used with an integration period of 80 ms (corresponding to 32 radiation pulses), which gave signal levels approximately 85 % of full-scale deflection for the SME electrometers.

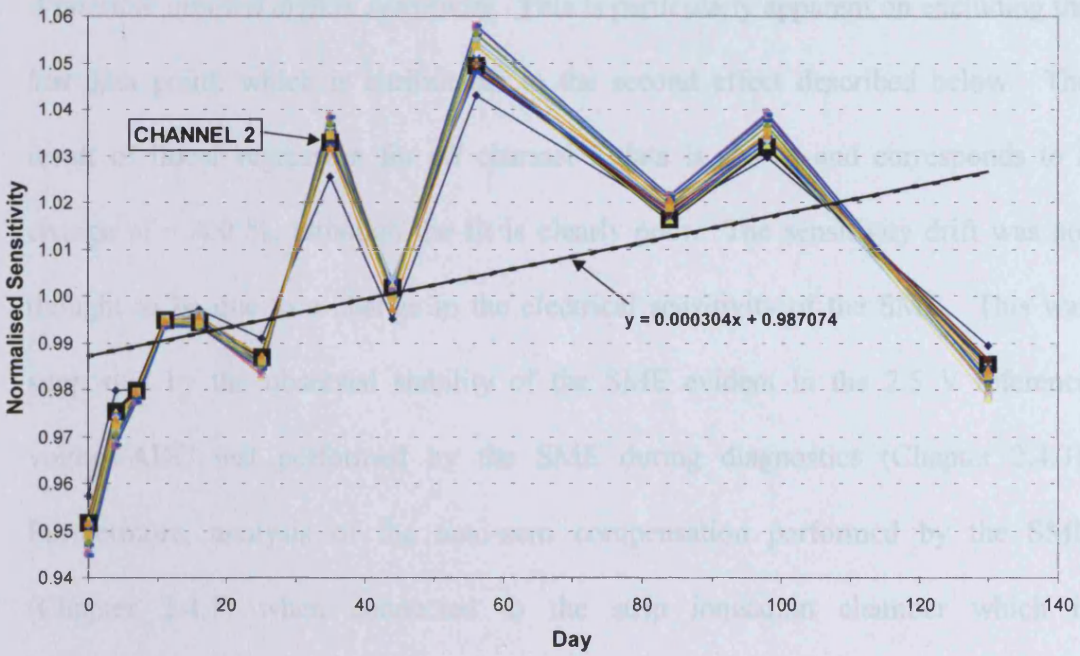

Figure 3-10: Sensitivity of strip chamber array over 130 days. Data for all twenty channels is shown corrected for variation in accelerator output. No temperature or pressure corrections have been applied (both strip ionisation chamber array and reference chamber unsealed). The result of linear regression for Channel 2 data is shown.

Figure 3-10 shows the sensitivity of all measurement channels on each occasion (corrected for changes in accelerator output), normalised to the mean for each channel. No correction for temperature or pressure on each measurement occasion has been included, based on the assumption that both the Farmer-type chamber and the chamber array are unsealed, and therefore would have identical corrections for atmospheric conditions.

It should be noted that no account has been taken of changes in the off-axis dose distribution. However, this was observed to be stable over the measurement period: routine quality control of the beam profile on eight occasions showed deviations ≤ 1.0 %. The data for each channel on each occasion is the mean for several exposures for which standard deviations were less than 0.2 %. Clearly the chamber shows significant variation in sensitivity. Therefore, all chamber signal data presented for dynamic measurements (Chapter 3.5) was normalised to an open field signal. Figure 3-10 shows two distinct effects:

1. *A possible upward drift in sensitivity.* This is particularly apparent on excluding the *last* data point, which is attributable to the second effect described below. The result of linear regression for *all* channel 2 data is shown and corresponds to a change of + 4.0 %, although the fit is clearly poor. The sensitivity drift was not thought to be due to a change in the electrical sensitivity of the SME. This was supported by the observed stability of the SME evident in the 2.5 V reference voltage/ADC test performed by the SME during diagnostics (Chapter 2.4.3). Furthermore, analysis of the auto-zero compensation performed by the SME (Chapter 2.4.1) when connected to the strip ionisation chamber which is automatically logged suggested stable electrometer sensitivity (maximum SD 0.6 %). The sensitivity drift is therefore a property of the strip ionisation chamber

array. It was postulated that this might be associated with either radiation damage or ongoing exposure to environmental conditions causing some change in the properties of the epoxy glass board, although the mechanism was not understood.

2. *An apparently random fluctuation in sensitivity* is also evident in Figure 3-10. All channels follow the fluctuations on each occasion. On investigation it was found that the sensitivity variation correlated with negative absolute temperature which has been plotted in Figure 3-11 (right-hand axis) against the sensitivity of channel 2 of the strip ionisation chamber array corrected for the sensitivity drift evident in Figure 3-10. The explanation for the correlation of sensitivity with negative absolute temperature was thought to be associated with changes in separation of the upper and lower boards forming the chamber with temperature (*i.e.* bowing). It was postulated that such separation changes could occur due to dissimilar temperature expansion characteristics of the component layers of the boards (*i.e.* epoxy glass and copper cladding), which might have been exaggerated by the creation of insulating tracks. The bowing might be reduced by fixing the plates at additional points to the ones in the corners.

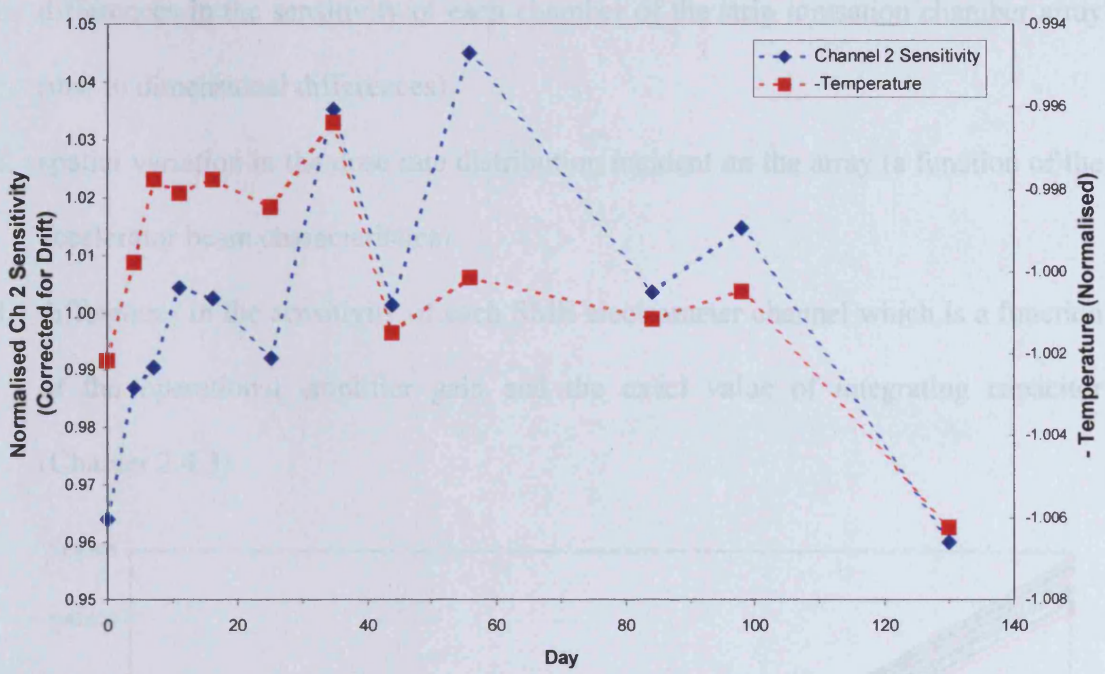

Figure 3-11: Correlation of chamber sensitivity with negative absolute temperature. The sensitivity of channel 2 has been corrected to the sensitivity drift evident in Figure 3-10 using the result of linear regression, and normalised to the mean of all values. Negative absolute temperature values have also been normalised to the mean value, and are plotted on the right-hand axis.

3.4.3 Linearity with accelerator MU

To assess linearity with delivered dose, further irradiations at 400 Hz PRF were performed for a range of accelerator MU settings using an integration period of 100 ms (corresponding to 40 radiation pulses per sample). Current limitations on the memory available within the SME meant that a maximum of 512 data samples could be acquired, corresponding to approximately 51 s of data collection and hence an upper limit on the total number of MU which could be used (approximately 380 MU).

The mean total dose signal acquired for each measurement channel in three exposures at each accelerator setting is shown in Figure 3-12, and the response of all measurement channels is very linear. From the observed gradients the sensitivity of the system lies in the range 4,000-4,5000 ADC units MU^{-1}. However, as the signal from a strip chamber depends on the length irradiated, these values are for irradiation of the entire length of each strip chamber. The difference in the sensitivity or gradient of each channel is associated with:

1. differences in the sensitivity of each chamber of the strip ionisation chamber array (due to dimensional differences)
2. spatial variation in the dose rate distribution incident on the array (a function of the accelerator beam characteristics)
3. differences in the sensitivity of each SME electrometer channel which is a function of the operational amplifier gain and the exact value of integrating capacitor (Chapter 2.4.3).

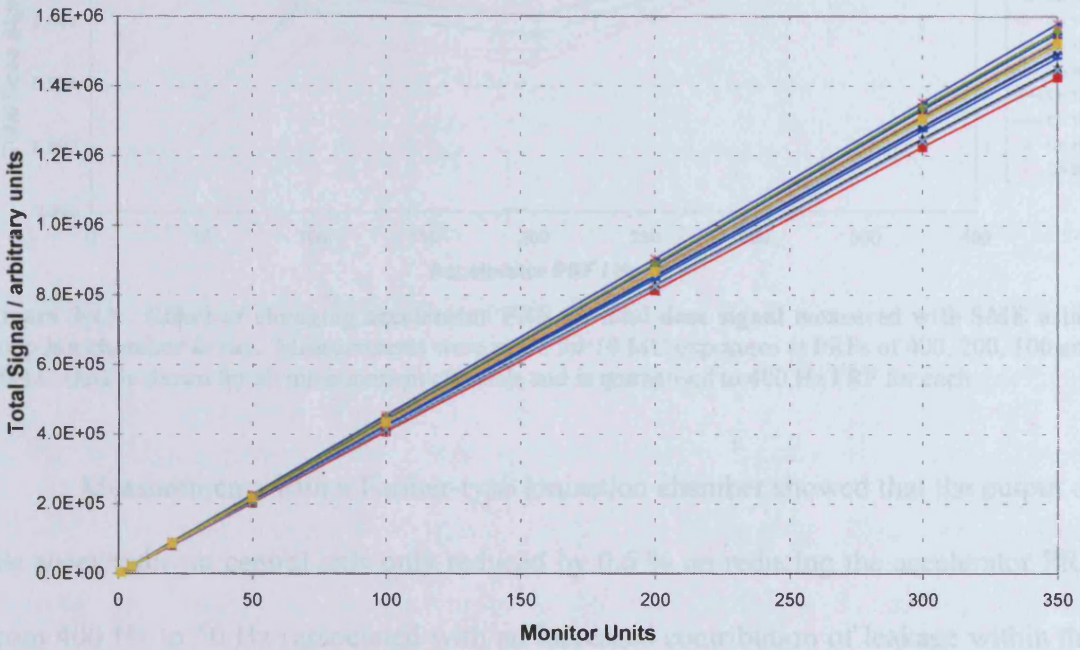

Figure 3-12: Linearity of total dose signal from the strip ionisation chamber with accelerator MU. Data is plotted for all twenty measurement channels of the SME and corresponding elements of the strip ion chamber array. Standard deviations for the repeated measurements at each MU setting are too small to be shown.

3.4.4 Effect of accelerator PRF

In order to confirm that operation of the accelerator at different PRFs had no effect on measurement of dose signal, a series of 10 MU exposures were given to the strip ion chamber array whilst operating the accelerator at PRFs of 400, 200, 100 and 50 Hz. The lowest PRF used was the minimum required clinically, and an exposure of only 10 MU was used to avoid excessive beam time at reduced PRF. For each PRF the

integration period was adjusted in order to keep the number of dose pulses fixed at 40 (*e.g.* 800 ms at 50 Hz).

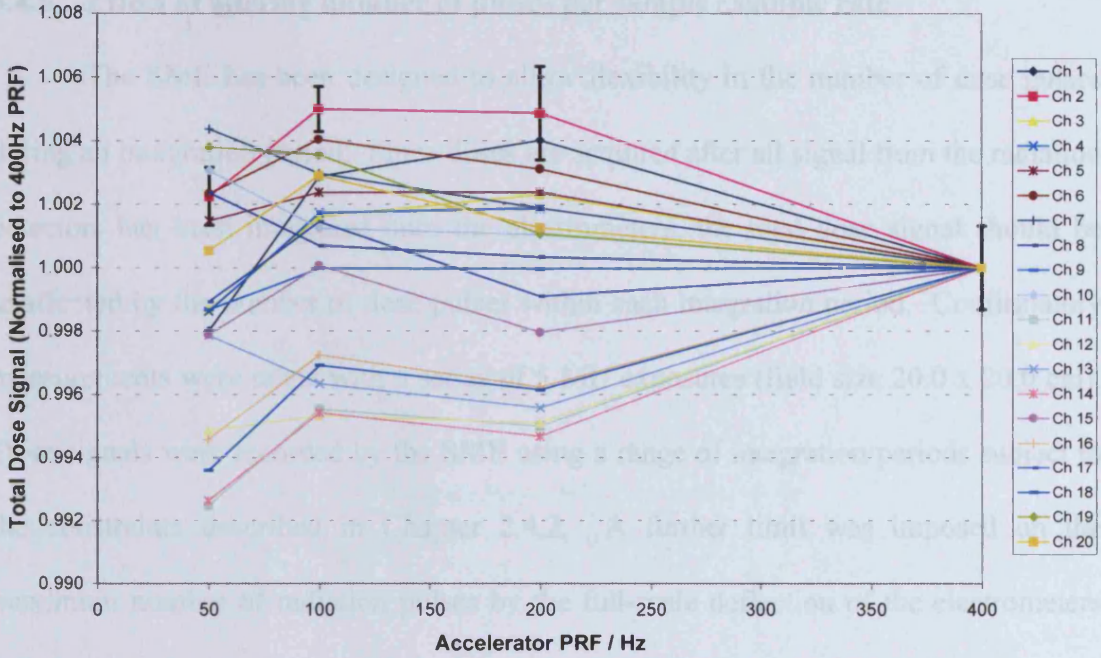

Figure 3-13: Effect of changing accelerator PRF on total dose signal measured with SME using strip ion chamber array. Measurements were made for 10 MU exposures at PRFs of 400, 200, 100 and 50Hz. Data is shown for all measurement channels and is normalised to 400 Hz PRF for each.

Measurements with a Farmer-type ionisation chamber showed that the output of the accelerator on central axis only reduced by 0.6 % on reducing the accelerator PRF from 400 Hz to 50 Hz (associated with an increased contribution of leakage within the accelerator dosimetry system). Additionally, studies of the effect of PRF on the dose rate profile of the accelerator reported in Chapter 5, showed changes of at most 2 % along major axes for a much larger field (40.0 x 40.0 cm compared to 20.0 x 20.0 cm for this case). Thus, no correction was made to dose measurements with the strip ion chamber array for change in output or dose rate profile when reducing PRF. The total dose signal measured for each channel, normalised to the signal at 400 Hz PRF, is plotted in Figure 3-13. For clarity standard deviations (based on repeat measurements) are only shown for Channel 2, but these were typical. Clearly there is only a small

change in the total dose signal measured for all channels over this range of PRFs, which is anticipated for the mode of operation of the SME.

3.4.5 Effect of altering number of pulses per sample / sample rate

The SME has been designed to allow flexibility in the number of dose pulses during an integration period. Since doses are acquired after all signal from the radiation detectors has been integrated onto the electrometers, the total dose signal should be unaffected by the number of dose pulses within each integration period. Confirmatory measurements were made with a series of 5 MU exposures (field size 20.0 x 20.0 cm). Dose signals were recorded by the SME using a range of integration periods subject to the constraints described in Chapter 2.4.2. A further limit was imposed on the maximum number of radiation pulses by the full-scale deflection of the electrometers (45 radiation pulses at the time of measuring this data). The accelerator was operated at 100 Hz PRF in order to increase the time interval between pulses and allow SME operation at the minimum sample period corresponding to 2 radiation pulses (*i.e.* 20 ms period). Measurements were made using the following integration periods (corresponding number of radiation pulse shown in parentheses): 20 ms (2 pulses), 40 ms (4 pulses), 100 ms (10 pulses), 200 ms (20 pulses) and 400 ms (40 pulses). It should be noted that the duration of the exposure was also limited by the maximum number of data samples possible with the SME (currently 512) which corresponded to approximately 10.0 s of data collection for the highest sampling rate (50 Hz).

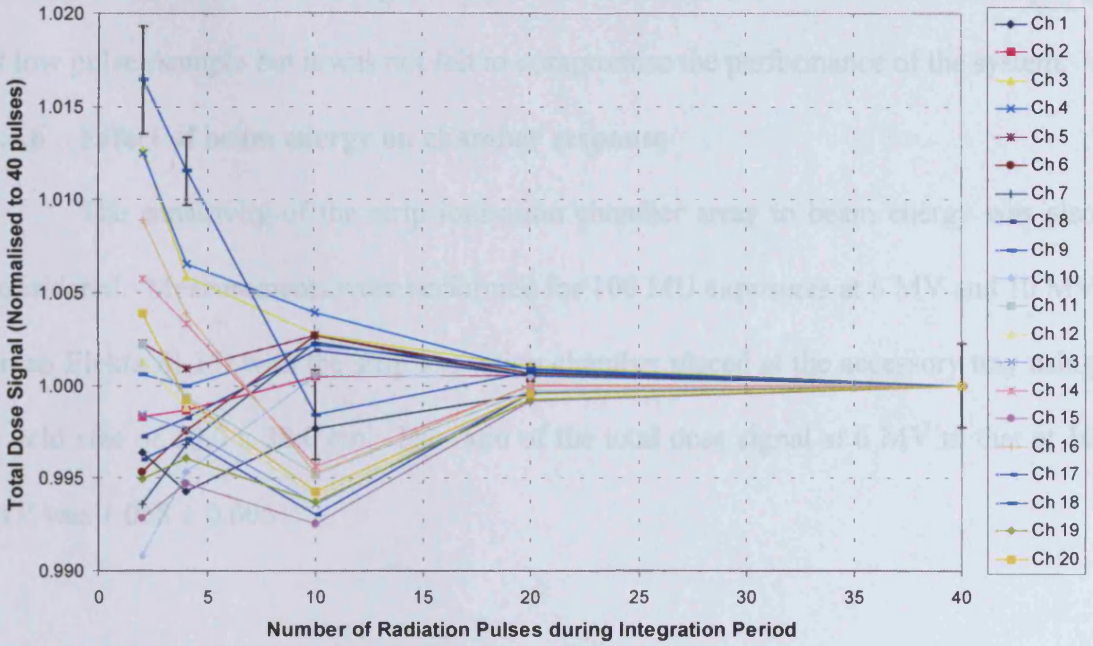

Figure 3-14: Effect of changing number of radiation pulses on total dose signal measured. Measurement were made for a 5MU exposure at 100Hz PRF using 2, 4, 10, 20 and 40 radiation pulses during each integration period.

The results for all channels, normalised to the dose signal for 40 radiation pulses (*i.e.* 400 ms integration period), are plotted in Figure 3-14. Standard deviations, based on repeat measurements, are only shown for Channel 18 for the sake of clarity, but were typical for all channels. The data clearly shows only a small change in total dose signal on reducing the number of radiation pulses during an integration period. For 20 pulses the normalised doses for all channels are within ± 0.1 %, for 10 pulses normalised doses fall in the range + 0.4 % to – 0.7 %, for 4 pulses the range is + 1.2 % to – 0.6 %, and for 2 pulses the range increases to + 1.6 % to – 0.9 %. Thus over the range 2 - 40 pulses the total dose differs by at most 1.6 %. The change on reducing the number of pulses is not systematic in nature, with the effect being different across the range of channels at each number of radiation pulses integrated. Careful inspection of the raw data confirmed no difference in the performance of the auto-zero for input bias current despite the large range of integration periods used (20 ms to 400 ms). The underlying

cause remained unclear, although it may be due to an artefact related to dose sampling at low pulses/sample but it was not felt to compromise the performance of the system.

3.4.6 Effect of beam energy on chamber response

The sensitivity of the strip ionisation chamber array to beam energy was also considered. Measurements were performed for 100 MU exposures at 6 MV and 10 MV on an Elekta SL15*i* with the strip ionisation chamber placed at the accessory tray using a field size of 30.0 x 30.0 cm. The ratio of the total dose signal at 6 MV to that at 10 MV was 1.058 ± 0.006.

3.5 Performance of SME and strip ion chamber array for dosimetry of dynamic fields

3.5.1 Dynamic wedge intensity modulation

3.5.1.1 Measurements of dynamic wedge treatment

The ability of the strip ionisation chamber array and the SME to perform collimator position verification for dynamic wedge delivery was considered. A beam with a wedged profile was delivered with an accelerator dose of 50 MU while operating the accelerator at 50 HZ PRF. For the Elekta DMLC system, movements are defined by a series of control points (maximum 300) each corresponding to an absolute fraction of total dose delivered (defined with a resolution of 0.1 %). At each control point, the position of each MLC leaf and the rectilinear collimators are defined (subject to general geometric constraints placed on the MLC). The dynamic control software calculates the desired position of the MLCs and collimators and executes movement between sequential control points (of which there is a minimum of 2) in a linear fashion with the total dose fraction delivered by the accelerator.

The wedge studied was defined by 56 control points, which are plotted in Figure 3-15. Initially, the collimator opening is a minimum, with the Y2 collimator 100.0 mm from central axis. The Y1 collimator bank moves at a progressively increasing rate to 100.0 mm from central axis to form the wedged dose gradient. The final collimator opening is 200.0 mm, and the field width is fixed at 200.0 mm.

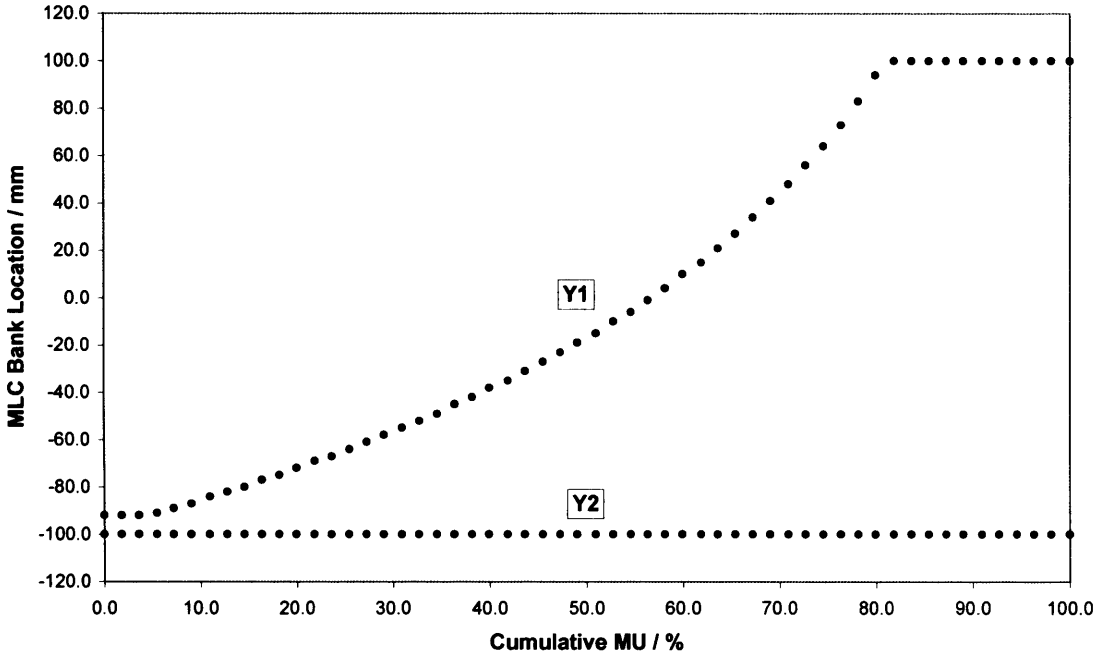

Figure 3-15: Control points defining collimator movement for dynamic wedge. The sequence contains 56 control points which specify collimator position as a fraction of cumulative accelerator MU.

The signal from the strip ionisation chamber array was recorded with the SME for the dynamic wedge using a 200 ms sample period (corresponding to 10 radiation pulses at 50 Hz PRF). Signals for channels 6 and 15 (which correspond to two opposing strips in the centre of the chamber, Figure 3-4(b)) are plotted in Figure 3-16 against cumulative accelerator dose, together with the sum of signals from both chambers.

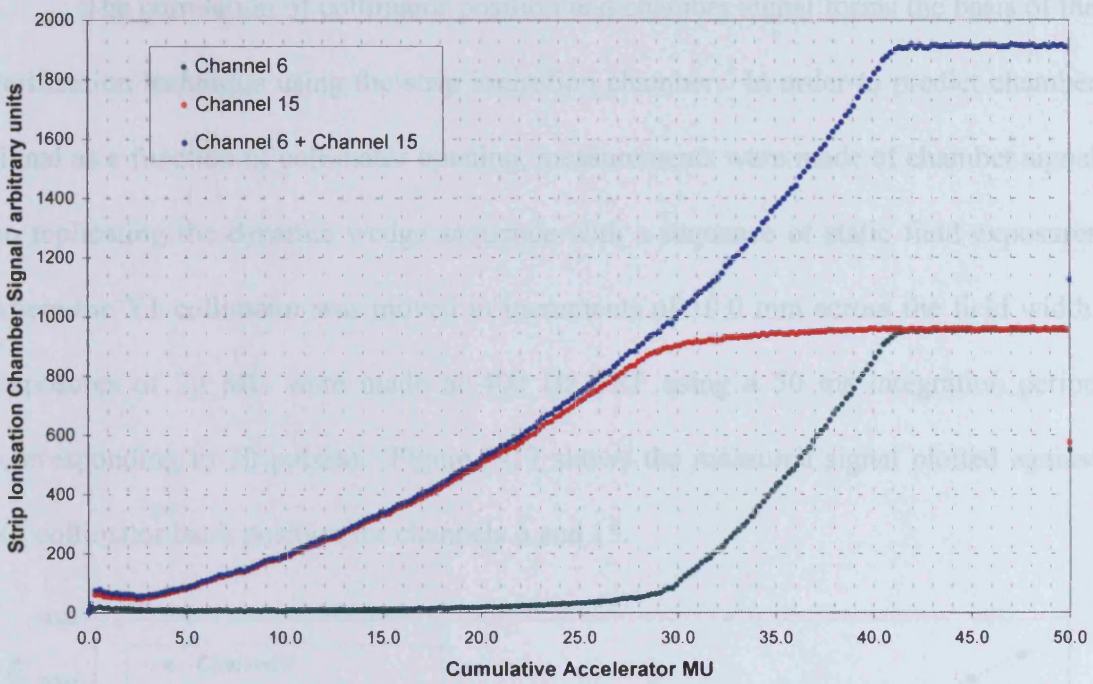

Figure 3-16: Signals from channels 6 and 15 of strip ionisation chamber array recorded by the SME during dynamic wedge. Chamber signals are plotted against cumulative accelerator dose. The SME integration period was 200 ms (*i.e.* 10 pulses at 50 Hz PRF).

Various phases are apparent and correlate with the collimator movement described by Figure 3-15:

1. Initially both collimators are stationary and form a small opening over chamber 15, which exhibits a signal level greater than chamber 6.
2. As collimator bank Y1 moves the length of chamber 15 irradiated increases, corresponding to a monotonic increase in signal from that channel from approximately 5 % of cumulative dose (*i.e.* 2.5 MU) as chamber 15 becomes progressively more uncovered.
3. At approximately 55 % of cumulative dose (*i.e.* 27.5 MU) the Y1 collimator bank passes over central axis. Beyond this, signal from chamber 6 begins to increase, as signal from channel 15 reaches a maximum.
4. At approximately 82 % of cumulative dose (i.e. 41 MU) the Y1 collimator bank reaches its final position.

The correlation of collimator position and chamber signal forms the basis of the verification technique using the strip ionisation chamber. In order to predict chamber signal as a function of collimator opening, measurements were made of chamber signal on replicating the dynamic wedge sequence with a sequence of static field exposures where the Y1 collimator was moved in increments of 10.0 mm across the field width. Exposures of 20 MU were made at 400 Hz PRF using a 50 ms integration period (corresponding to 20 pulses). Figure 3-17 shows the measured signal plotted against Y1 collimator bank position for channels 6 and 15.

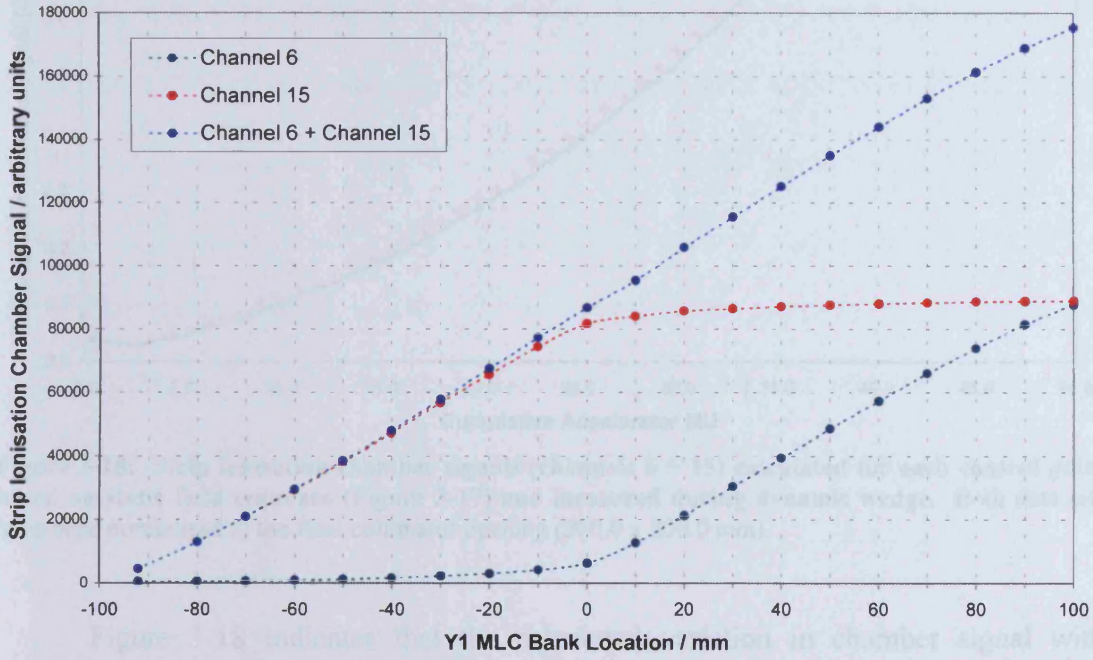

Figure 3-17: Signals from channels 6 and 15 of strip ionisation chamber array recorded for different Y1 collimator bank locations. Chamber signals are the mean for 20 MU exposures.

From Figure 3-17 it is clear that when collimator bank Y1 < 0.0 mm different lengths of channel 15 are being irradiated, and that when Y1 > 0.0 mm different lengths of channel 6 being irradiated. From the total signal for the opposing ionisation chamber strips (*i.e.* channel 6 + channel 15) for each Y1 collimator position, it was possible to interpolate signals at intermediate collimator positions. This was performed at each collimator position specified by the control points defining the wedge (Figure 3-15).

The calculated chamber signals at each control point, normalised to the final field size of 200.0 x 200.0 mm, are shown against cumulative accelerator dose in Figure 3-18. Also shown, again normalised to the final field size, is the total signal for the channels plotted against the accelerator dose recorded by the SME during the dynamic wedge delivery (Figure 3-16).

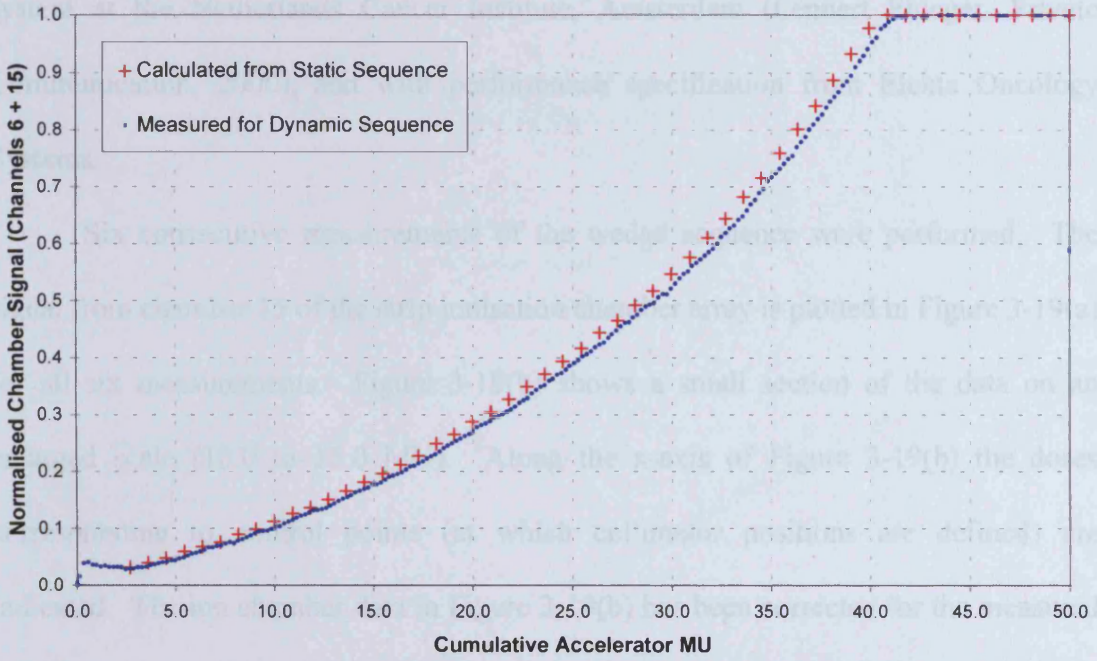

Figure 3-18: Strip ionisation chamber signals (channels 6 + 15) calculated for each control point based on static field sequence (Figure 3-17) and measured during dynamic wedge. Both data sets have been normalised to the final collimator opening (200.0 x 200.0 mm).

Figure 3-18 indicates that the calculated variation in chamber signal with accelerator dose (based on the static field data) is followed closely by the variation in chamber signal recorded by the SME during delivery of the dynamic wedge. However, there is a systematic deviation between the two data sets such that a given normalised chamber signal is reached some dose later than that based on calculation from static field data. This corresponds to the horizontal distance (i.e. number of accelerator MU) between the two data sets. This was calculated for every control point during the curved portion of the data (corresponding to motion of the Y1 collimator bank) which gave a mean value of 0.71 ± 0.09 MU. Based on the measured accelerator dose rate of

63.4 MU min^{-1} this corresponds to a time of 0.67 ± 0.08 s. This time lag is a function of the Elekta DMLC system (version 3.10, Elekta SL*i* Javelin research release). The time lag is associated with lag in communication of the accelerator MU value to the MLC, and a further latency inherent in the DMLC control system. The combined lag of 0.67 ± 0.08 s measured here agrees with measurements on the Elekta SL*i* DMLC system at the Netherlands Cancer Institute, Amsterdam (Lennert Ploeger, Private Communication, 2000), and with performance specification from Elekta Oncology Systems.

Six consecutive measurements of the wedge sequence were performed. The signal from chamber 15 of the strip ionisation chamber array is plotted in Figure 3-19(a) for all six measurements. Figure 3-19(b) shows a small section of the data on an enlarged scale (10.0 to 15.0 MU). Along the x-axis of Figure 3-19(b) the doses corresponding to control points (at which collimator positions are defined) are indicated. The ion chamber data in Figure 3-19(b) has been corrected for the measured lag of the system *i.e.* doses corresponding to each data point have been incremented by 0.71 MU.

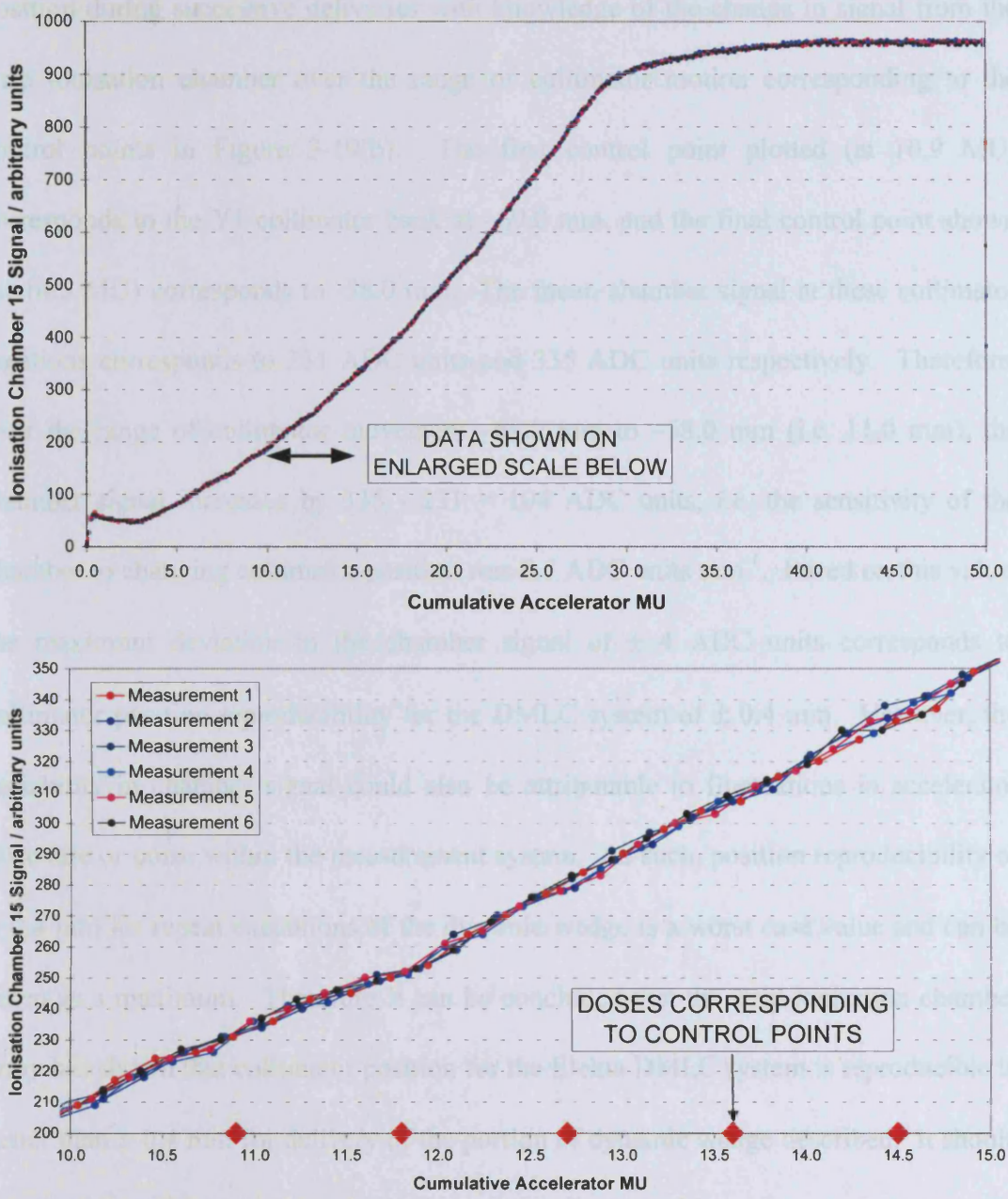

Figure 3-19(a) and (b): Six consecutive measurements of dynamic wedge delivery using strip ionisation chamber array. Figure 3-19(b) shows a portion of the data on an enlarged scale (10.0 to 15.0 MU) together with the doses corresponding to control points. The ion chamber data in Figure 3-19(b) has been corrected for the accelerator MU lag.

Figure 3-19(b) clearly demonstrates the reproducibility of the chamber signal during successive deliveries of the wedge: at any accelerator dose the maximum deviation in the chamber signal for the repeat measurement is ± 4 ADC units from the mean (for all points below 27.5 MU when the Y1 collimator passes over central axis, Figure 3-15). Based on this, it is possible to estimate the reproducibility of collimator

position during successive deliveries with knowledge of the change in signal from the strip ionisation chamber over the range of collimator motion corresponding to the control points in Figure 3-19(b). The first control point plotted (at 10.9 MU) corresponds to the Y1 collimator bank at –69.0 mm, and the final control point shown (at 14.5 MU) corresponds to -58.0 mm. The mean chamber signal at these collimator positions corresponds to 231 ADC units and 335 ADC units respectively. Therefore, over the range of collimator movement –69.0 mm to –58.0 mm (i.e. 11.0 mm), the chamber signal increases by 335 - 231 = 104 ADC units, *i.e.* the sensitivity of the chamber to changing collimator position was 9.5 ADC units mm^{-1}. Based on this value, the maximum deviation in the chamber signal of ± 4 ADC units corresponds to collimator position reproducibility for the DMLC system of ± 0.4 mm. However, the variability in chamber signal could also be attributable to fluctuations in accelerator dose rate or noise within the measurement system. As such, position reproducibility of ± 0.4 mm for repeat executions of the dynamic wedge is a worst case value and can be taken as a maximum. Therefore it can be concluded that the strip ionisation chamber array has shown that collimator position for the Elekta DMLC system is reproducible to better than ± 0.4 mm for delivery of the portion of dynamic wedge described. It should be noted that this parameter is likely to be a function of accelerator dose rate, the number of control points for the dynamic sequence and the leaf speed/acceleration for a particular DMLC prescription. Between the two control points considered in Figure 3-19(b) the collimator bank moved 11.0 mm, during which time 14.5 - 10.9 MU = 3.6 MU were delivered at a dose rate of 63.4 MU min^{-1}, which required 3.4 s. Therefore the mean collimator speed in this case was 11.0/3.4 mm s^{-1} = 3.2 mm s^{-1} and in fact the maximum leaf speed for the data below 27.5 MU in Figure 3-19(b) was 5.8 mm s^{-1}.

Budgell *et al.* (2000) has also recently confirmed the precision of leaf positioning for the Elekta DMLC system in measurements of the effect of fixed errors in leaf position on dose delivery: for constant leaf velocities in the range 1.3 – 3.3 mm s^{-1} excellent agreement between predicted and measured dose errors was found, from which Budgell concluded that there was little variation of leaf position from that predicted. It is interesting to note that the maximum positional reproducibility of ± 0.4 mm estimated in this present work for the Elekta MLC operating in dynamic mode, is comparable with reported reproducibility of field edge positioning in repeat settings of a 10.0 x 10.0 cm static field (Jordan and Williams 1994). Their measurements, on one of the original production Elekta MLCs, demonstrated positional reproducibility of 0.23 mm root mean square (RMS) (0.75 mm maximum) for gantry 0° (MLC motion horizontal), and 0.12 mm RMS (0.4 mm maximum) at gantry 90° (MLC motion vertical). Maximum differences between field edge positions resulting from approaching the field size by opening or closing the collimator were 0.4 mm and 0.1 mm respectively.

For the repeat dynamic wedge deliveries, the total chamber signal (summed for all integration periods) was also observed to be very reproducible: standard deviations for all measurement channels were never more than 0.2 %.

The reproducibility of the instantaneous chamber signal for the strip ionisation chamber measured using the SME for delivery of a dynamic wedge using the Elekta DMLC system is much improved compared to repeated delivery of a Varian dynamic wedge: measurements using a single strip chamber by Kerr *et al.* (2000) (considered at the beginning of this chapter) demonstrated fluctuations of up to 4 % of the maximum after filtering. This may have been attributable to the method of sampling chamber current employed by Kerr *et al.* (2000) which is believed to be asynchronous to the

accelerator dose pulse train, unlike the SME. Furthermore, on a Varian accelerator the dose pulse train is dynamically controlled to achieve the required dose rate (Hamish Porter, Western General Hospital, Edinburgh, Private Communication, 2000) which will result in dose rate fluctuations. This is supported by the observed fluctuation in instantaneous (unfiltered) chamber current observed by Kerr *et al.* (2000) of up to 30 % for static fields.

3.5.1.2 Modelling of dynamic wedge treatment

It has been demonstrated that collimator position during the delivery of a dynamic wedge test case can be verified based on calculated chamber signals from data obtained for static field irradiation of the chamber. However, the static fields chosen were such as to encompass the range of collimator movement for the dynamic wedge. For the approach to be applied to a wide range of wedge sequences (*e.g.* a range of symmetric and asymmetric wedge field widths) it would be desirable to be able to model chamber signal based on the prescribed control point geometry. This would avoid any requirement for a series of static field irradiations covering every possible field width.

For the dynamic wedge considered the chamber signal was calculated at control points based simply on the length of strip ionisation chamber irradiated. The calculation ignored 'contaminating' chamber signal associated with radiation scattering within the strip ionisation chamber or transmission through the collimators. The longitudinal variation in chamber sensitivity has also been omitted, together with off-axis dose rate variation and any effect of leaf end penumbra. Figure 3-20 shows the normalised signal for the central ionisation chambers 6 + 15 (summed), together with the calculated signal at every control point from the static field data (from Figure 3-18). The measured chamber signal for the dynamic sequence (also from Figure 3-18),

corrected for the accelerator MU lag, is also shown and clearly overlies the calculated signal from static field data.

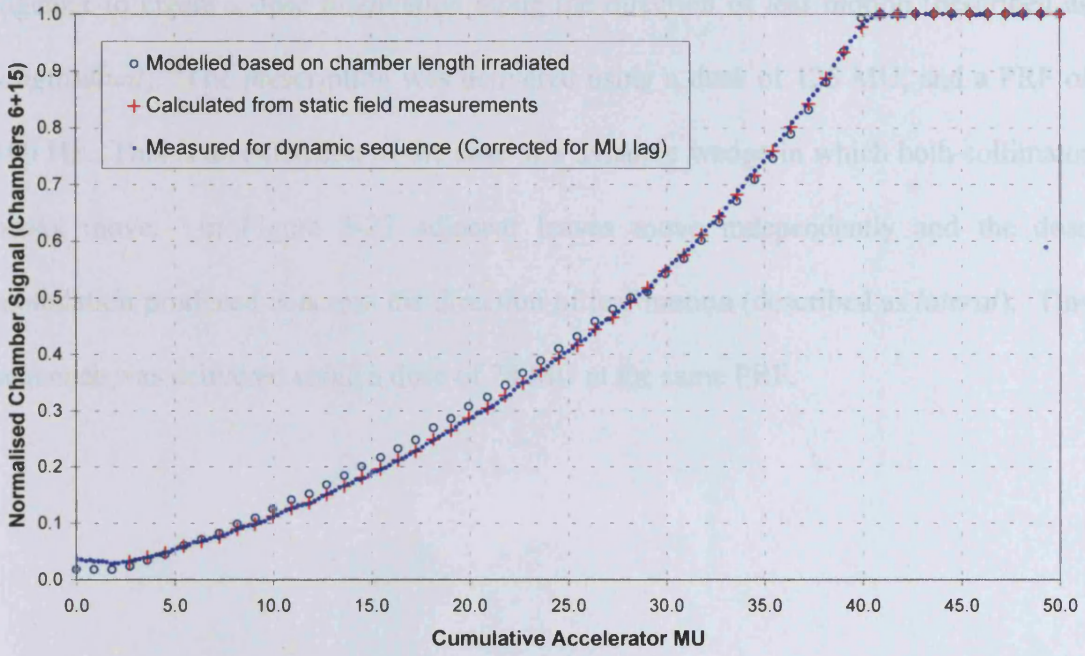

Figure 3-20: Strip ionisation chamber signals (chamber 6 + 15 summed) modelled for each control point based on chamber length irradiated, calculated for each control point based on static field data, and measured during dynamic sequence. All data sets have been normalised to the final collimator opening 200.0 x 200.0 mm).

There is remarkably good agreement between chamber signal calculated from static field measurement and that modelled simply from irradiated length of the strip ionisation chamber. The maximum deviation for all control points is 2.1 % (mean 0.6 %, SD 1.1 %). The concept of modelling the chamber signal based on irradiated chamber length will be extended to other dynamic sequences in which the leaves move independently in Chapter 3.5.2.

3.5.2 Sinusoidal intensity modulations

Two DMLC sequences that created sinusoidal dose modulations were considered for both modelling and measurement of strip ionisation chamber signals during dose delivery. Meyer *et al.* (2000) have studied these modulations in a comparison of compensator and MLC-produced IMBs. The leaf positions at each of 26 control points defining the sequences is shown in Figure 3-21 and 3-22. To aid

interpretation of the sequences, a grey-scale image indicating the resultant dose distributions for each sequence are also shown. In Figure 3-21 the leaf banks move together to create a dose modulation along the direction of leaf motion (described as *longitudinal*). The prescription was delivered using a dose of 125 MU, and a PRF of 100 Hz. This is an extension of the case of a dynamic wedge in which both collimator banks move. In Figure 3-22 adjacent leaves move independently and the dose modulation produced is across the direction of leaf motion (described as *lateral*). This sequence was delivered using a dose of 74 MU at the same PRF.

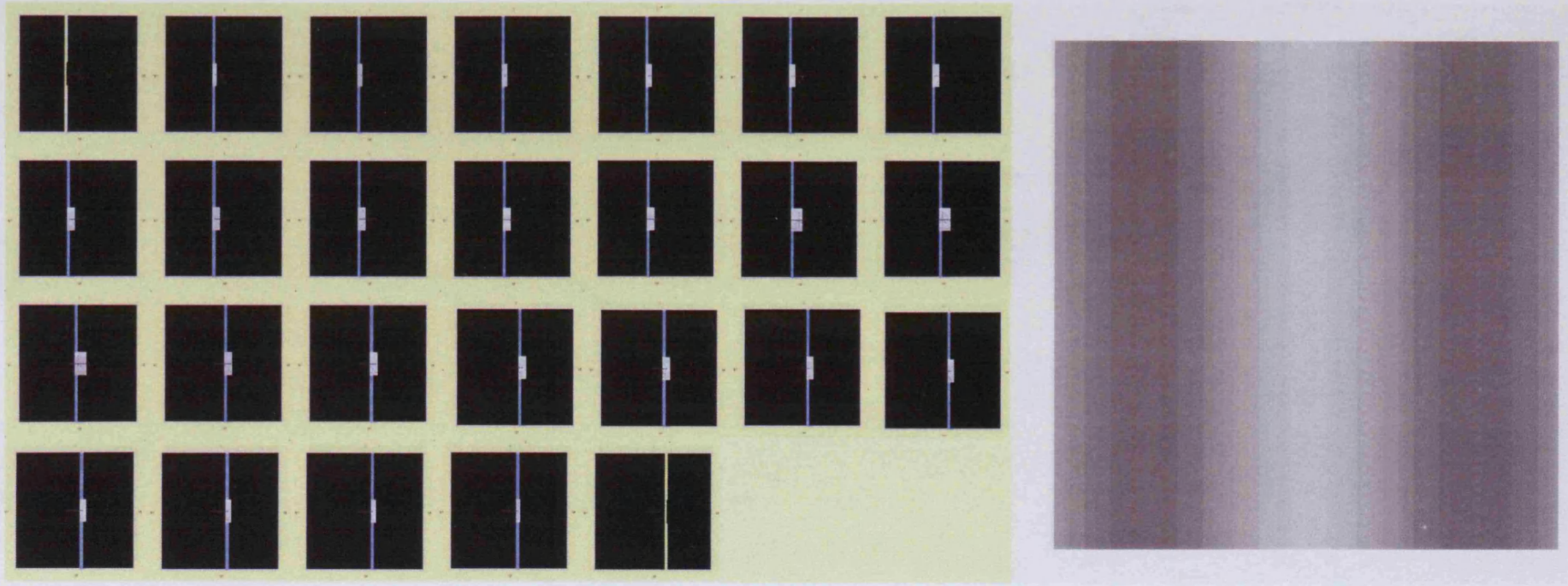

Figure 3-21: Longitudinal sinusoidal dose modulation produced by DMLC. The leaf positions at the 26 control points are shown on the left (starting top-left). The right-hand image is a grey-scale representation of the resulting dose distribution (dark corresponds to high dose). Delivered using a dose of 125 MU, and PRF of 100 Hz.

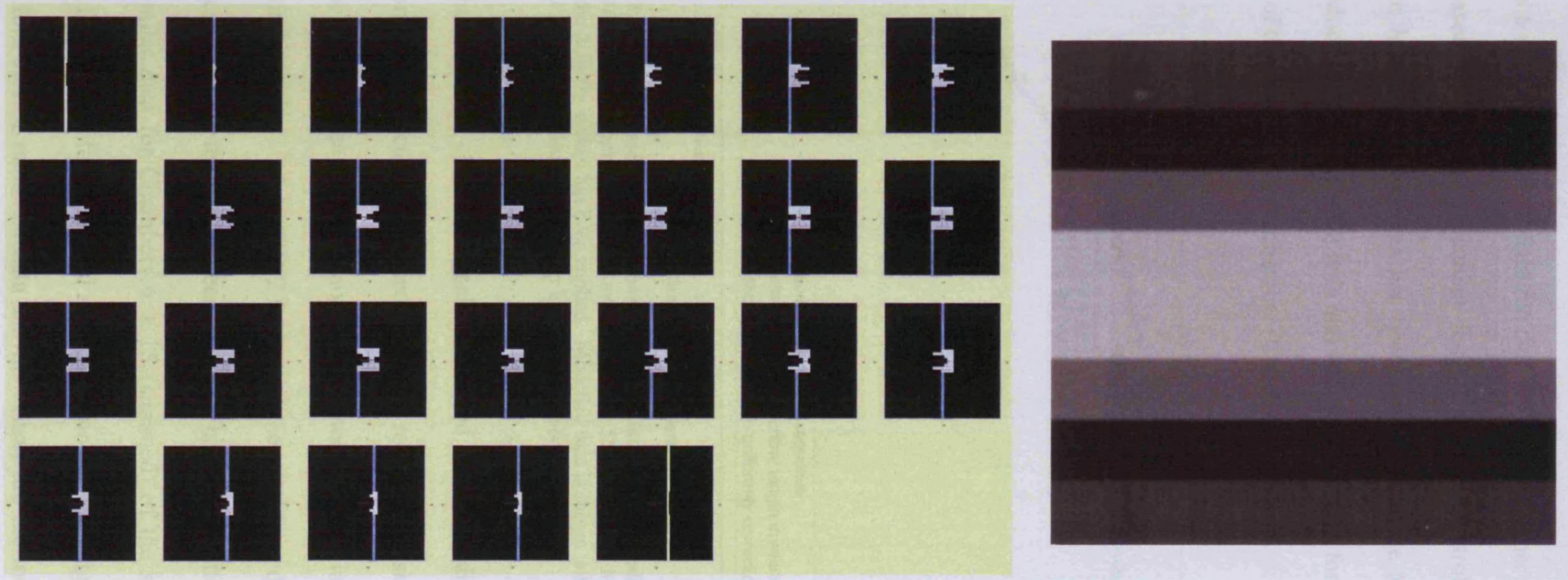

Figure 3-22: Lateral sinusoidal dose modulation produced by DMLC. The leaf positions at the 26 control points are shown on the left (starting top-left). The right-hand image is a grey-scale representation of the resulting dose distribution (dark corresponds to high dose). Delivered using a dose of 74 MU and a PRF of 100 Hz. (Images in Figures 3-21 and 3-22 courtesy of SG Hunt, Leicester Royal Infirmary, using 'Dynamic Therapy File Viewer' package).

Figure 3-23 shows the results for the longitudinal modulation (Figure 3-21) for Chambers 6 + 15 (summed). Measured data is shown, together with modelled chamber signal (based on irradiated chamber length) at each control point plotted against accelerator MU. Measured data has been corrected for the MU lag in the delivery system. Modelled data is shown with and without correction for longitudinal sensitivity variation of the strip ionisation chamber (Chapter 3.3.5).

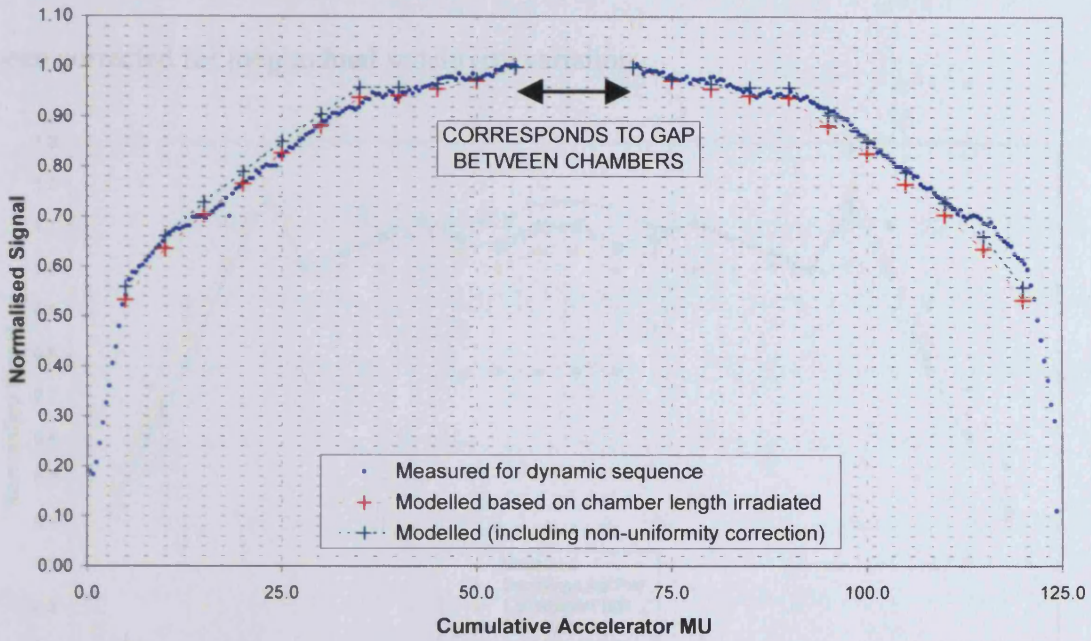

Figure 3-23: Measured and modelled chamber signal data for longitudinal sinusoidal modulation (Figure 3-21). Data is normalised to the mean signals at 55 MU and 70 MU, and a correction for the MU lag of the delivery system has been applied. Modelled data is shown with and without correction for longitudinal sensitivity variation of the strip ionisation chamber.

The calculated chamber signal is increased at off-axis distances by applying the non-uniformity correction (corresponding to reduced sensitivity off-axis). The agreement between measured and modelled chamber signal is in general good, with the mean deviation being –1.7 % (SD 2.6 %), and the maximum deviation being –7.7 %. Data corresponding to the gap between chambers has been omitted.

Similar data for Chambers 6 + 15 (summed) of the strip ionisation array is shown in Figure 3-24 for the lateral sinusoidal modulation (Figure 3-22). In this case there are four sets of modelled data shown. These are the modelled chamber signal

based on the length of chamber irradiated by the overlying MLC leaf pair, together in turn with additional components based on the corresponding aperture created by adjacent leaf pairs. These clearly contribute to signal on Chamber 5 and 16 by virtue of the lateral field profile and radiation scattered within the array (Chapter 3.3.6). The contribution of signals from the 1st, 2nd and 3rd adjacent leaf pair apertures was 17.0, 5.0 and 2.3 % respectively, which was based on measurement (Chapter 3.3.6). All data has been normalised to chamber signals at 17.8 and 65.8 MU, and the modelled data has been corrected for longitudinal sensitivity variation.

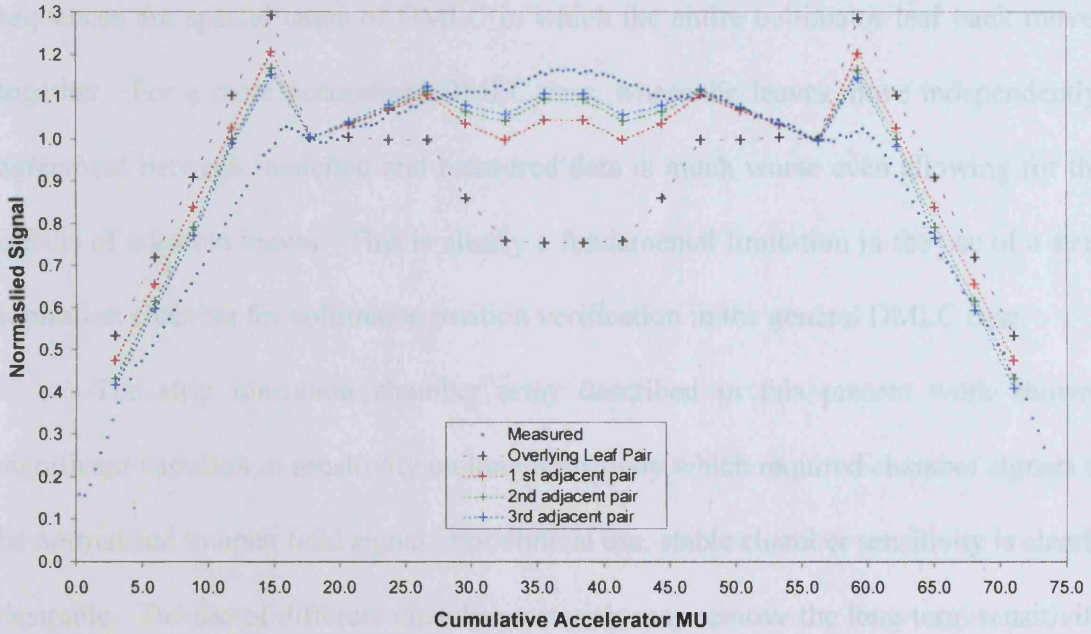

Figure 3-24: Measured and modelled chamber signal data for lateral sinusoidal modulation (Figure 3-22). Data is normalised to the mean signals at 17.8 MU and 68.5 MU, and a correction for the MU lag of the delivery system has been applied. Modelled data, which includes correction for longitudinal sensitivity variation of the strip ionisation chamber, is shown including contribution to chamber signal associated with the opening of up to three adjacent leaf pairs.

It is clear that on introducing components due to the aperture created by adjacent leaf pairs, the modelled chamber signal becomes progressively closer to that measured, although the change diminishes and beyond the 3rd leaf pair (the most extreme plotted) the signal from adjacent leaf pairs falls to below 1.6 %. However, on accounting for three leaf pairs on either side, the measured and modelled chamber signals still do not agree well (maximum deviation 13.0 %, mean –3.6 %, SD 6.5 %).

3.6 Discussion

Clearly there is good agreement between the measured and modelled data for both the dynamic wedge and longitudinal sinusoidal modulation, allowing use of the strip ionisation chamber array and SME for collimator position verification in these types of DMLC based on predicted chamber signal from measured or modelled data. For the dynamic wedge data presented the array has also allowed characterisation of the Elekta DMLC system, specifically accelerator MU lag and collimator position reproducibility. However, with regard to collimator position verification, these sequences are special cases of DMLC in which the entire collimator leaf bank moves together. For a more generalised DMLC case, where the leaves move independently, agreement between modelled and measured data is much worse even allowing for the effects of adjacent leaves. This is clearly a fundamental limitation in the use of a strip ionisation chamber for collimator position verification in the general DMLC case.

The strip ionisation chamber array described in this present work showed significant variation in sensitivity on long term study which required chamber signals to be normalised to open field signal. For clinical use, stable chamber sensitivity is clearly desirable. The use of different chamber materials may remove the long-term sensitivity change, which was postulated to be associated with radiation damage or environmental exposure. The construction of accelerator monitor chambers, generally carbon or metal on a thin substrate of mica or plastic foil (Greene and Williams 1997), is likely to be suitable. It would also be desirable to overcome temperature dependence of sensitivity, which for the chamber described here may be possible by redesigning chamber construction to include extra spacers to rigidly define plate separation.

Chapter 4. Characteristics of Gd_2O_2S:Tb phosphor as a detector for dosimetry of dynamically produced dose distributions

4.1 Introduction

Chapters 4-7 consider the application of a tube camera-based EPID to verification of IMRT. This chapter investigates the characteristics of the x-ray phosphor terbium doped gadolinium oxysulphide (Gd_2O_2S:Tb) used in camera-based EPIDs, which are relevant to the dosimetry of dynamically produced radiotherapy dose distributions.

The phosphor forms an optical image from radiation transmitted through the patient, which is viewed indirectly by a video camera. The three commercial accelerator-mounted EPIDs of this type all use a Gd_2O_2S:Tb phosphor screen (Visser *et al.* 1990, Munro *et al.* 1990, Shalev *et al.* 1989), namely: *i*View™ (Elekta Oncology Systems, Crawley, UK; formerly SRI-100™, Philips Medical Systems), Theraview™ (Cablon Medical BV, Leusden, The Netherlands) and Beamview PLUS™ (Siemens Medical Systems, Concord, California, USA). In addition Wellhöfer Dosimetrie (Schwarzenbruck, Germany) manufacture an imaging system, intended for quality assurance of treatment machines, which uses the same phosphor. The material has also been used in custom-built imaging devices for proton beam dosimetry (Boon *et al.* 1998, Boon *et al.* 2000). It is also used as the x-ray detector in flat panel amorphous silicon photodetector arrays currently being introduced for portal imaging (Antonuk *et al.* 1998) and being applied to dosimetry (El-Mohri *et al.* 1999).

The phosphor was originally developed for use at diagnostic x-ray energies. However, despite its extensive use in EPIDs, there is little data on the luminescent properties of the phosphor under megavoltage photon irradiation from a linear accelerator. Such irradiation is pulsed at repetition frequencies (PRFs) of typically a

few hundred Hz and is characterised by high instantaneous dose rates associated with small duty cycles. These parameters vary with accelerator type, and may vary between beam energies from a particular accelerator. Knowledge of the luminescent properties of the phosphor is important since systems based on the material have been used for quantitative dose measurement (*e.g.* Heijmen *et al.* 1995, Pasma *et al.* 1998), and for the verification of dynamically produced dose distributions both in this present work and by others (Ma *et al.* 1997, Pasma *et al.* 1999b). In particular, for assessment of integrated dose distributions produced by DMLC, any residual signal from the phosphor associated with long-lived luminescence (or afterglow) must be quantified.

This chapter presents a review of reported properties of Gd_2O_2S:Tb and describes the use of a photomultiplier tube for the direct measurement of Gd_2O_2S:Tb luminescence when irradiated by a 6MV photon beam from a linear accelerator. The form of the observed luminescent decay under steady state irradiation was investigated, and using the SME (Chapter 2) the temporal variation of the optical signal and dose rate incident on the phosphor were studied at beam-start. Measurements were also performed following termination of a radiation exposure to investigate the existence of residual signal from the phosphor. The electrometer was also used to investigate any effect of accelerator PRF on the response of the phosphor.

4.2 Reported properties of Gd_2O_2S:Tb

Luminescence can be divided into two distinct components (Mainprize & Yaffe 1998): *primary luminescence*, which occurs immediately after irradiation and is described by luminescent lifetimes in the range of nanoseconds to microseconds, and an *afterglow* component which can continue for a long time after primary luminescence. The afterglow phenomenon occurs because of the existence of trapping centres causing delay in radiative recombination.

Data published for the luminescent decay of Gd_2O_2S:Tb following pulsed and prolonged stimulation with radiation of different forms is summarised in Table 1. Swank (1974) also reported a value of 0.4 ms for the decay time in measurements using Am-241 (59.6 keV γ-rays). Yaffe (Private Communication 1999) has suggested that the primary luminescent decay characteristic of Gd_2O_2S:Tb when irradiated with high energy x-rays is likely to be similar to that observed for 28 kVp x-rays (Mainprize & Yaffe 1998, Table 1). However, data for afterglow from the phosphor following kilovoltage stimulation cannot be assumed for megavoltage therapy applications, due to significant differences in the magnitude of delivered doses and instantaneous dose rates. Indeed, afterglow at therapy dose levels is suggested by the observation of luminescence for many minutes following Co-60 irradiation to 10 Gy (Berzins *et al.* 1983 (Table 1)). Furthermore, afterglow is acknowledged to be a function of the intensity and duration of the incident radiation beam (Sandel *et al.* 1986, Shepherd *et al.* 1995) and there is clearly a marked difference in the radiation beam intensity (*i.e.* instantaneous dose rate) under both conditions: for kilovoltage fluoroscopy, dose rates are typically around 1 μ Gy s^{-1} (MJ Dunn, Private Communication, 2000), compared to typical megavoltage therapy instantaneous dose rates of around 20 Gy s^{-1}. As a result, the existence of optical signal from the phosphor at times much greater than suggested by luminescent decay times for Gd_2O_2S:Tb reported by Shepherd *et al.* (1995) and Mainprize & Yaffe (1998) for kilovoltage exposures must be considered in megavoltage therapy applications such as EPIDs, particularly in their use for DMLC verification.

X-ray Source	Detector	Pulsed Radiation		Prolonged Radiation		Reference
		Exposure Duration	Decay Characteristic	Exposure Duration	Decay Characteristic	
0.6 MeV	PD	3 ns	2.9 % after 2 ms	Observed luminescence for minutes following 10Gy Cobalt-60		Berzins *et al.* (1983)
20-30 kVp	PMT	60 μs	2 % after 2 ms	15 s	0.03 % after 10s	Moy *et al.* (1993)
8 keV	PMT	17 ms	τ: 0.7 ms	10 s	Decay to 0.1 % ≈ 1 s	Shepherd *et al.* (1995)
80 kV_p	PD	10 ms	50 % after 0.6 ms 10 % after 1.5 ms 1 % after 2.4 ms	-	-	Rudin *et al.* (1998); Rudin (Private Comm. 2000)
28 kV_p	PMT	500 μs 3 s between pulses	τ: 0.184-0.196 ms (0.249±0.005) τ: 0.556-0.560 ms (0.751±0.002)	500ms pulsed 3s between pulses	Decay to 0.1 % ≈ 1 s	Mainprize & Yaffe (1998)

Table 4-1: Reported luminescent decay characteristics of Gd_2O_2S:Tb. PMT detector is a photomultiplier tube. PD is a photodiode. τ is the calculated exponential lifetime. For the data reported by Mainprize & Yaffe (1998), 90% confidence intervals are quoted, with the values in parentheses referring to the relative contribution of each component.

It is also possible that accelerator PRF may have an effect on afterglow. There are no reports of the effect of PRF on phosphor response except that reported by Leong (1986) who used a different phosphor (believed to be zinc cadmium sulphide, based on composition data given Berzins *et al.* 1983), and did not observe any effect in measurements using a prototype custom-built camera-based EPID. It is useful therefore to consider any effect of accelerator PRF on Gd_2O_2S:Tb luminescence.

Several authors have reported the emission wavelength of Gd_2O_2S:Tb to be approximately 545 nm (Berzins *et al.* 1983, Moy *et al.* 1993, Blasse & Grabmaier 1994, Shepherd *et al.* 1995, Althof *et al.* 1996). Additionally, Berzins *et al.* (1983)

demonstrated Gd_2O_2S:Tb to have a significantly greater relative sensitivity (to 1.25 MeV γ-rays) than a range of other commercially available phosphors.

Published data confirms that Gd_2O_2S:Tb is not susceptible to long-term radiation damage. Antonuk *et al.* (1990) reported that the sensitivity of a Gd_2O_2S:Tb screen remained relatively constant over irradiation to 10 kGy with Co-60, and Boon *et al.* (1998) did not observe any effect on a screen which had received 900 Gy (50 % protons, 50 % photons).

4.3 Direct measurement of luminescence

4.3.1 Experimental arrangement

A 6 MV photon beam from an Elekta SL15*i* linear accelerator was used. When operating at 400 Hz PRF the accelerator delivered approximately 5.0 Gy min^{-1} to isocentre. The duration of the radiation pulse was approximately 3 μs, and the accelerator was operated at PRFs of 25, 50, 100, 200 and 400 Hz for this study.

The experimental arrangement is shown in Figure 4-1. All measurements were performed on the phosphor screen integral to the commercial Theraview EPID. The screen is commercially available (Lanex Fast, Eastman Kodak Company, Rochester, NY, USA) and is bonded to a 2 mm thick copper plate. The metal/phosphor screen and mirror of the EPID are constructed in a rigid elbow assembly which is detachable from the accelerator. For these measurements the screen/mirror detector assembly was placed with the screen horizontal on an open section of the treatment couch, and an under-couch beam used. The mirror allowed the optical detector to be removed from the primary beam. A collimator opening of 25.0 x 25.0 cm at isocentre was used, which projected to the entire dimension of the phosphor screen (approximately 40.0 x 40.0 cm) at the source-detector distance (SDD) of 160.0 cm. This represented a clinically realistic SDD for the EPID. Additionally 14.7 g cm^{-2} of water equivalent

attenuator was placed at the accelerator shadow tray (68.0 cm SSD). The dose rate to the phosphor screen was measured as 1.2 Gy min^{-1} for an accelerator PRF of 400 Hz.

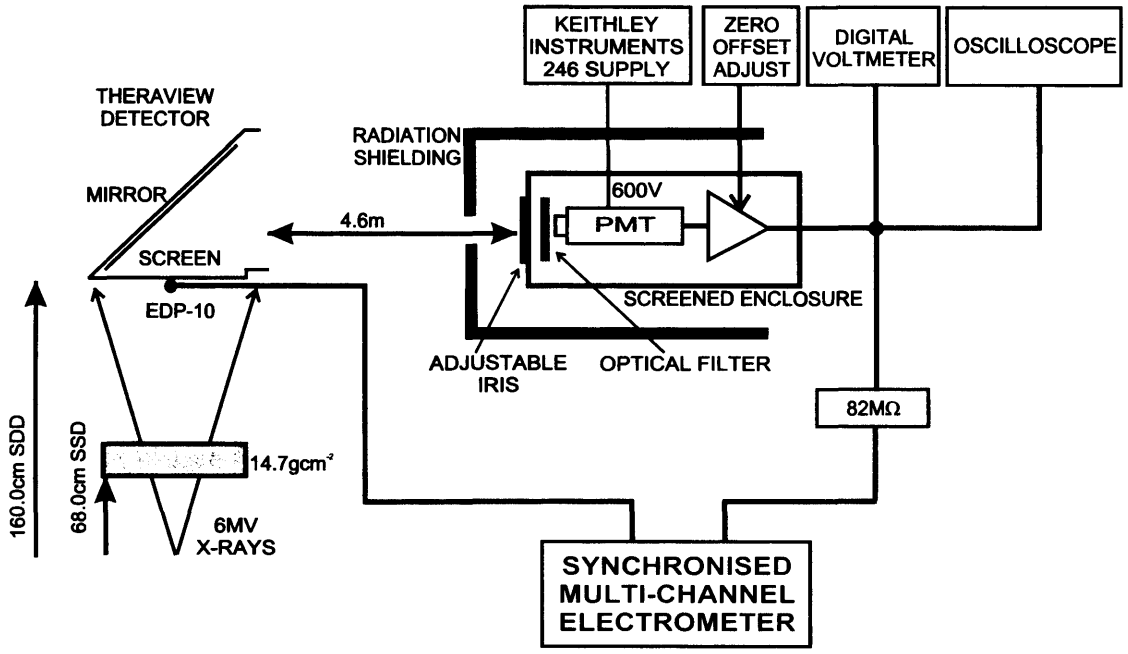

Figure 4-1: Arrangement for studying luminescent signal using photomultiplier tube (PMT) and amplifier, oscilloscope and Synchronised Multi-channel Electrometer (SME). One electrometer channel was connected to a semiconductor diode (EDP-10) placed on the incident surface of the phosphor screen, and a second channel connected to the signal obtained from the photomultiplier tube amplifier.

The photomultiplier tube (PMT) (Hamamatsu R928, Hamamatsu Photonics Ltd., Japan) was operated at 600 V from a stabilised supply (Keithley 246 High Voltage Supply, Keithley Instruments Inc., Cleveland, OH, USA). The PMT was housed in a screened enclosure with its output connected to an ultra-low bias current operational amplifier (OPA 129, Burr-Brown Corporation, Tucson, AZ, USA), also housed within the same enclosure, to provide peak signal levels of around 2.0 V. Frequency limitation associated with any cable capacitance was not of concern due to the low input impedance of the amplifier. Measurements of the response of the PMT and amplifier to a pulsed light source showed that the system had a rise time (10-90 %) of 6 μs, which is approximately two orders of magnitude faster than the reported luminescent decay time of Gd_2O_2S:Tb (Table 4-1), and thus adequate for this study. Measurements were

performed with the treatment room in darkness. It was possible to partially offset any DC signal from the PMT system associated with remaining ambient light (*e.g.* from status indicators on the equipment in use) by means of an offset adjustment at the amplifier output. Due to the high sensitivity of such devices, the PMT was placed 4.6 m from the phosphor screen/mirror. Additionally an optical filter (formed by exposed radiographic film with an optical density of 1.17) was also used to further reduce illumination of the PMT. An adjustable iris, which could be fully closed, was mounted on the PMT enclosure in-line with the sensitive aperture of the PMT. By completely closing the iris it was possible to quantify the contribution to measured signal associated with ambient light (assessed with the radiation beam off), and the additional component due to irradiation of the PMT (assessed with radiation beam on). Customised lead shielding was placed around the enclosure to reduce the contribution to the measured signal due to direct interaction of radiation with the PMT structure.

4.3.2 Measurement of luminescent decay using oscilloscope

A digitising storage oscilloscope (Fluke 99 ScopeMeter; Fluke Corporation, Everett, WA, USA) was used to study the luminescent decay following a radiation pulse whilst the phosphor was under continuous irradiation (Figure 4-1). The magnetron current pulse waveform was used for oscilloscope triggering. Measurements were performed to establish the timing of the luminescent signal following the magnetron current pulse, and to view the form of the entire luminescent signal up to and including the signal associated with the 'next' radiation pulse.

Signal averaging (128 samples) was performed by the oscilloscope. The oscilloscope also had the facility to transfer waveforms to a computer for display and analysis. Signals were observed with the accelerator operating at PRFs in the range 25 Hz-400 Hz.

4.3.3 Measurement of luminescent signal during beam-start and termination using SME

The SME (Chapter 2) was used to assess the temporal variation of the dose rate incident on the phosphor screen and the optical signal from the phosphor (Figure 4-1). An EDP-10 semiconductor diode detector (Scanditronix Medical AB, Uppsala, Sweden) measured the radiation incident on the phosphor screen, and the optical signal provided by the PMT was connected to a second channel of the electrometer via a series resistance (82 MΩ) acting as voltage-to-current converter (Figure 4-1). It should be noted that measurement of the radiation incident on the phosphor using a single point dose detector was considered valid: previous measurements had shown that the relative spatial distribution of radiation dose delivered by the accelerator did not vary significantly during beam-start. Due to its robustness, an EDP-10 semiconductor diode was used to assess dose rate from the accelerator in preference to an ionisation chamber. However, measurements with the SME have shown that the dose rate measured during beam-start by a semiconductor diode and a 0.12 cm^3 RK ionisation chamber (Scanditronix Medical AB, Uppsala, Sweden) were identical.

Measurements were made at beam-start to confirm linearity of the optical signal with incident dose rate. The accelerator was operated at 400 Hz PRF and an integration period of 50 ms was used (corresponding to 20 radiation pulses) to provide good temporal resolution. In order to identify any long-lived optical signal, the SME system was used to record dose rate and the optical signal following beam termination. However, as synchronisation and triggering of the SME were controlled via an interface to the thyratron drive voltage, which ceases at beam termination, it was necessary to artificially terminate the beam whilst maintaining this signal to ensure that the SME continued to acquire following beam termination. This was achieved by software control of the accelerator's gun current from its beam-on value to a stand-by level. This

achieved beam-off whilst ensuring continuation of SME acquisition. The beam-off transition was difficult to achieve reproducibly and lasted between 0.6 - 1.0 s (which was limited by the software control system and thermal lag of the gun filament). An estimate of the dose delivered to the phosphor screen at beam termination was derived from the number of MU registered by the accelerator.

4.3.4 Effect of accelerator PRF on phosphor response

The SME was also used to integrate the total optical signal for a series of 30 MU exposures, made using the arrangement in Figure 4-1, whilst operating the accelerator at PRFs of 25, 50, 100, 200 and 400 Hz. SME integration periods were chosen for each PRF such that 20 radiation pulses were integrated for each period. The EDP-10 diode was used to measure the dose for each exposure. Again, it should be noted that measurement of the dose incident on the phosphor using a single point dose detector was considered valid, as previous measurements had also shown that the spatial distribution of radiation dose did not vary significantly whilst operating the accelerator at different PRFs.

4.4 Results

4.4.1 Measurement of luminescent decay using oscilloscope

Using the oscilloscope to study the magnetron current and the optical signal from the phosphor, an obvious delay was apparent in the rise of the optical signal after the rise in magnetron current. This is a function of the operation of the Elekta accelerator, since the radiation pulse (approximately 3 μs in duration) occurs after a small time delay (estimated at 1 μs) following the rise in the magnetron current. Figure 4-2 (left trace) shows the luminescent decay for around 900 μs after the radiation pulse for an accelerator PRF of 400 Hz. Measurements at reduced PRF showed very similar

waveforms. The signal measured with the optical iris closed is also plotted in Figure 4-2 (right trace). The signal with the iris closed was attributed to direct radiation interaction with the PMT structure. It was confirmed that this signal was not associated with electrical interference from the magnetron since on manipulation of the accelerator gun current to stand-by (and thus terminating radiation exposure whilst maintaining magnetron operation), the signal was observed to disappear. However, the signal was only present during and immediately following the radiation pulse and as a result did not interfere with observation of the luminescent signal over a longer time-period. Quantification of the contribution of this signal to the integrated optical signal from the phosphor is presented in Chapter 4.4.2.1.

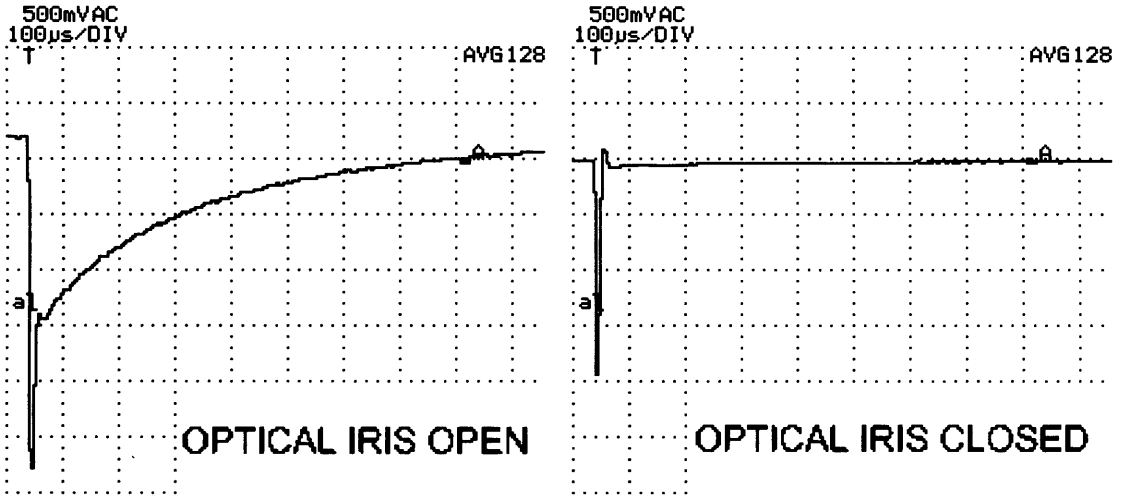

Figure 4-2: Luminescent signal with optical iris open (left-hand trace) and closed (right-hand trace). Waveforms were obtained from a digitising oscilloscope using an average of 128 waveforms, a time-base of 100 µs division^{-1} and a sensitivity of 500 mV division^{-1}. The accelerator PRF was 400Hz.

Figure 4-3 shows the results of subtraction of the signal measured with the iris closed from the signal measured with the iris open. Data was acquired using a reduced oscilloscope time-base to enable two consecutive radiation pulses to be captured (accelerator PRF 400 Hz). Clearly the two luminescent pulses are 2.5 ms apart which is in agreement with that expected from the accelerator PRF. The luminescent decay following each pulse reaches a steady-level, and the decay observed is very consistent

with luminescent lifetime data reported for the phosphor. For comparison, the data from Mainprize and Yaffe (1998) given in Table 4-1 has been plotted for the luminescence following the first radiation pulse shown.

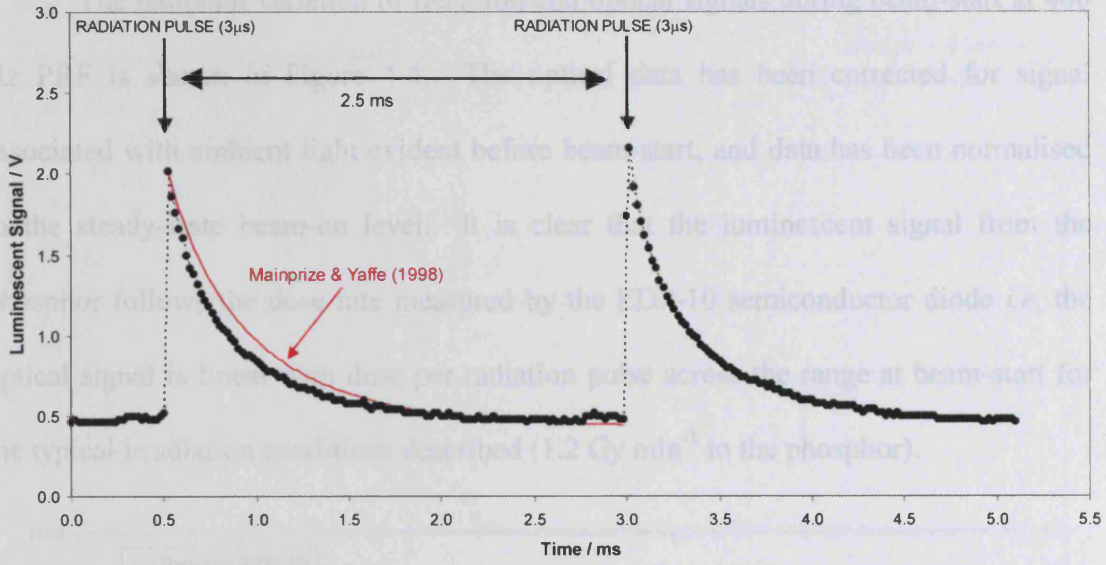

Figure 4-3: Luminescent signals following two consecutive radiation pulses captured by oscilloscope (using 128 waveform average). The data plotted is the difference between the signal measured with the iris open and the signal measured with the iris closed. Data from Mainprize and Yaffe (1998) for the dominant decay lifetime of Gd_2O_2S:Tb (558 μs) has been plotted for the luminescence following the first radiation pulse shown.

4.4.2 Measurement of luminescent signal using SME

4.4.2.1 Quantification of radiation-induced signal

Measurements of the same accelerator exposure were repeated with the optical iris open and closed to assess the magnitude of the radiation-induced component. Signals captured for each integration period were added to give total (integrated) signals for each exposure. The total signal in the case of the open iris was corrected for the contribution from ambient light which could not be fully removed electrically using the output offset adjustment described. The correction was based on the mean signal level measured before the radiation exposure.

Measurement of radiation-induced signal was performed on several occasions, and in all cases the contribution of radiation-induced signal (measured with iris closed)

to the total signal (measured with the iris open) was less than 1 %. Therefore, in the data which follows no correction for this signal has been made.

4.4.2.2 Luminescent signal during beam-start

The temporal variation of radiation and optical signals during beam-start at 400 Hz PRF is shown in Figure 4-4. The optical data has been corrected for signal associated with ambient light evident before beam-start, and data has been normalised to the steady-state beam-on level. It is clear that the luminescent signal from the phosphor follows the dose rate measured by the EDP-10 semiconductor diode *i.e.* the optical signal is linear with dose per radiation pulse across the range at beam-start for the typical irradiation conditions described (1.2 Gy min^{-1} to the phosphor).

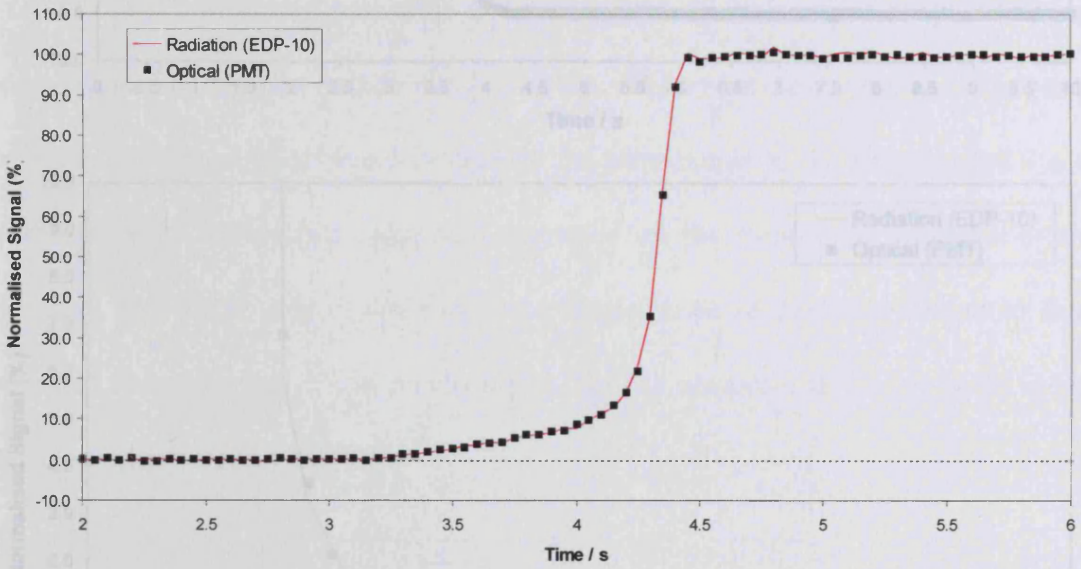

Figure 4-4: Temporal variation of radiation and optical signals during beam-start at 400 Hz PRF. The optical data has been corrected for ambient light. Data has been normalised to the steady-state beam-on level.

4.4.2.3 Luminescent signal during beam termination

The temporal variation in optical and radiation signals during termination of the radiation beam (by manipulation of accelerator gun current) is shown in Figure 4-5. The total dose delivered to the phosphor screen was estimated as 1.4 Gy for the data shown. Figure 4-5(b) shows the data plotted on an expanded scale. Signals have been expressed as a percentage of those measured over 20 data samples (*i.e.* a period of 1.0

s) before termination. The optical data has been corrected for ambient light based on the mean optical signal measured over 20 data samples (period 1.0 s) at a time of 20.0 s following beam-off.

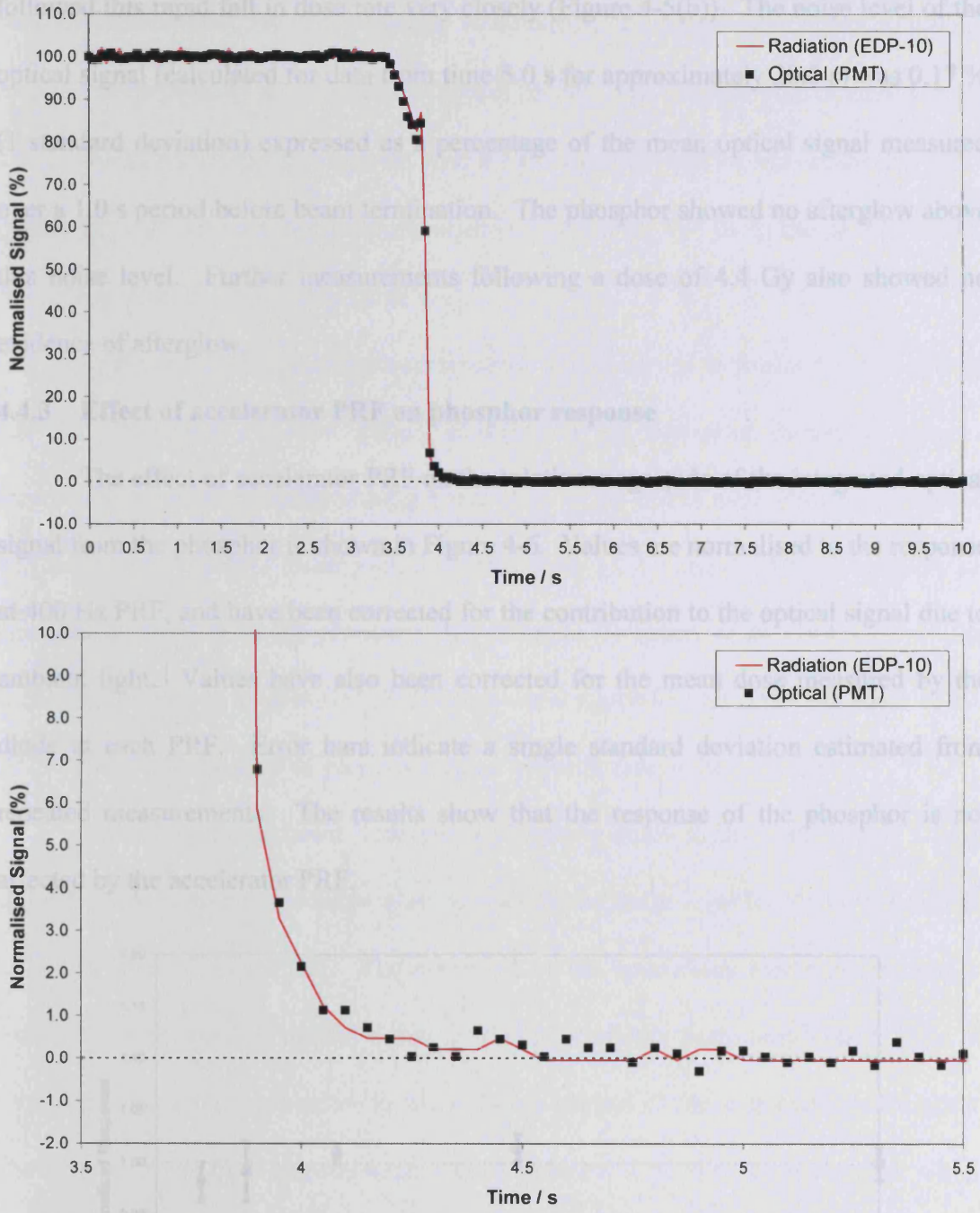

Figure 4-5 (a) and (b): Temporal variation of radiation and optical signals during beam termination. Signals have been expressed as a percentage of those measured over 20 data samples (i.e. a period of 1.0 s) before termination. The optical data has been corrected for ambient light based on the mean optical signal measured over 20 data samples (period 1.0 s) at a time of 20.0 s following beam-off. Measurements were made operating the accelerator at 400 Hz PRF, following a dose of 1.4 Gy to the phosphor. Figure 4-5(b) shows the data plotted on an expanded scale.

The initial decrease in dose rate to approximately 85 % of that before manipulation of gun current was relatively slow (400 ms duration). The dose rate then fell rapidly to below 1 % in a further 300 ms. The optical signal from the phosphor followed this rapid fall in dose rate very closely (Figure 4-5(b)). The noise level of the optical signal (calculated for data from time 5.0 s for approximately 20.0 s) was 0.17 % (1 standard deviation) expressed as a percentage of the mean optical signal measured over a 1.0 s period before beam termination. The phosphor showed no afterglow above this noise level. Further measurements following a dose of 4.4 Gy also showed no evidence of afterglow.

4.4.3 Effect of accelerator PRF on phosphor response

The effect of accelerator PRF on the relative magnitude of the integrated optical signal from the phosphor is shown in Figure 4-6. Values are normalised to the response at 400 Hz PRF, and have been corrected for the contribution to the optical signal due to ambient light. Values have also been corrected for the mean dose measured by the diode at each PRF. Error bars indicate a single standard deviation estimated from repeated measurements. The results show that the response of the phosphor is not affected by the accelerator PRF.

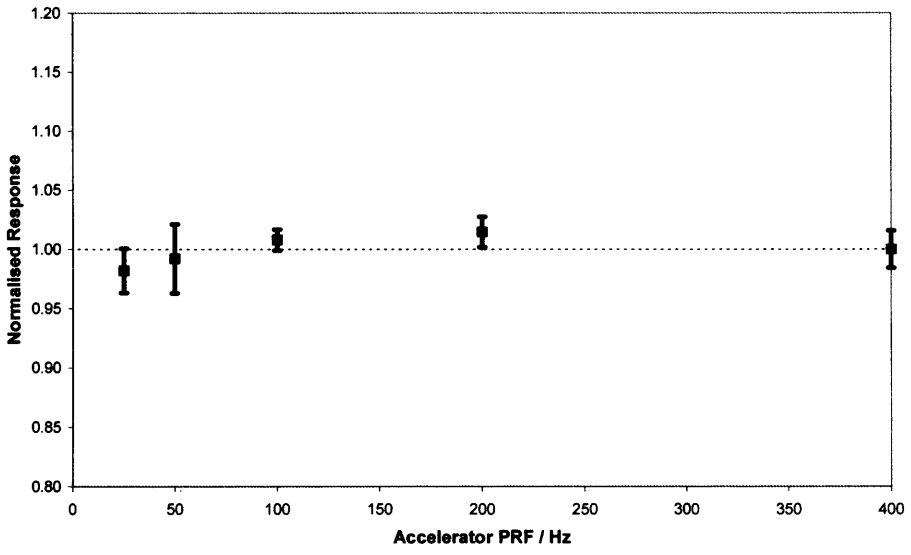

Figure 4-6. Effect of accelerator PRF on the response of the phosphor. The integrated optical signal is plotted normalised to 400Hz for each PRF. The response has been corrected for the dose measured by the diode at each PRF.

4.5. Discussion

Direct measurement of the luminescence of Gd_2O_2S:Tb phosphor under irradiation with 6 MV x-rays from a linear accelerator has been achieved using a photomultiplier tube. By using a digital oscilloscope, the luminescent signal following each radiation pulse of the accelerator (approximately 3 μs duration) has been observed. The decay characteristic is consistent with the findings reported by Mainprize and Yaffe (1998) (who observed a dominant exponential lifetime of 558 μs in the case of pulsed irradiation with 28 kV_p x-rays, Table 4-1).

Using the SME, phosphor luminescence was observed to follow the rise in dose rate (*i.e.* dose per radiation pulse) incident on the phosphor measured using a semiconductor diode detector during beam-start. This direct measurement confirmed that the optical signal is linear with dose rate up to 1.2 Gy min^{-1}. This is certainly an anticipated property of the phosphor: for example, Heijmen *et al.* (1995) varied the incident dose rate to an SRI-100 EPID using water equivalent absorber thickness of 10-29 cm and found the ratio of grey scale value to portal dose to be constant.

Measurements at beam termination following doses to the phosphor of 1.4 Gy and 4.4 Gy showed no detectable afterglow above the noise level for the optical signal, estimated as 0.17 % (1 SD). The operation of the specialised electrometer used to record the dose rate and optical signal limited how rapidly beam termination could be achieved, since it was necessary to use software control of the accelerator gun current. The dose rate fell from approximately 85 % to below 1 % in a 300 ms period, which represents a change in dose rate at least as fast as that encountered in DMLC. For example, taking a 20 to 80 % penumbra width of 5.0 mm for the MLC, and the maximum leaf speed of the Elekta MLC of 20.0 mm s^{-1}, the dose rate to a point under a moving leaf would change from 20 to 80 % in 250 ms. The measurement demonstrates

that afterglow from Gd_2O_2S:Tb phosphor is not a limitation for its application to DMLC verification.

The response of the phosphor was observed to be independent of accelerator PRF (25-400 Hz). This is consistent with reported observations of Leong (1986) who used a different phosphor (zinc cadmium sulphide, Berzins *et al.* 1983) in a custom-built camera-based EPID. Leong observed a linear dependence of image intensity on dose rate, by altering accelerator PRF using fixed frame duration. The independence of phosphor response from accelerator PRF is particularly important for dosimetric applications of an imaging system using the phosphor. It is not therefore necessary to account for differences in PRF between EPID calibration and patient treatment. This is particularly important for DMLC, since accelerators may be required to operate in this mode at PRFs below those normally used due to constraints of the DMLC control system.

The use of a PMT and electrometer to measure the response of the phosphor may itself be a useful technique for dosimetry studies of metal/phosphor screens. A conventional integrating electrometer could be used to assess the integrated optical signal rather than the specialised device described here. Munro *et al.* (2000a, 2000b) have recently described such a system based on a photodiode and light pipe. Such techniques have the advantage of omitting any effect of the camera from the measurement, and thus give direct read out.

Chapter 5. Dosimetry properties of a tube camera-based electronic portal imaging device

5.1 Introduction

The application of EPIDs to dosimetry has been considered using either in-house imaging systems, most notably those developed by the Royal Marsden Hospital (Sutton, UK) (Symonds-Tayler *et al.* 1997, Mosleh-Shirazi *et al.* 1998b), or commercially available EPIDs. Of the four EPIDs commercially available at present, dosimetric studies have been reported on two: namely, the liquid ion chamber matrix (PortalVision™, Varian Associates, Palo Alto, CA, USA) (Meertens *et al* . 1995, van Herk & Meertens 1988), and the camera-based system SRI-100™ (Elekta Oncology Systems, Crawley, UK; formerly the Philips Medical Systems) (Visser *et al.* 1990). The other two systems are both camera-based, namely Beamview PLUS™ (Siemens Medical Systems, Concord, California, USA) (Shalev *et al.* 1989) and Theraview™ (Cablon Medical BV, Leusden, The Netherlands; formerly InfiMed Inc. Liverpool, NY, USA) (Munro *et al.* 1990). A free-standing camera-based system is also commercially available (PORTpro™, Eliav-Medical Imaging Systems, Haifa, Israel). To date, little information has been reported on the non-imaging application of these latter systems, with the exception of some work that is believed to have been done with the Siemens device (Rajapakshe *et al.* 1996, Rajapakshe 1998).

This chapter describes an investigation of the dosimetric properties of the Theraview™ EPID, which are principally related to the characteristics of the tube camera used in this EPID. As such the EPID has significantly different characteristics to those reported in the literature for the SRI-100, which uses a charge-coupled device (CCD) camera. Such a study is a pre-requisite to dosimetric application of a portal imaging system. This work was the first reported study in the literature of this EPID

(Glendinning and Bonnett 2000a). Recently a further study has been reported on this device with broadly similar findings (Partridge *et al.* 2000a).

5.2 Description and operation of the Theraview EPID

The detector in the Theraview system consists of a 2 mm thick copper plate bonded to a 400 mg cm^{-2} Gd_2O_2S:Tb screen. A 2.2 mm thick cover (high impact polystyrene, density 1.04 g cm^{-3}) is mounted over the detector so that the phosphor screen lies approximately 4 mm below the physical surface of the detector. The maximum field of view of the system is 40.0 x 40.0 cm (approximately 28.0 x 28.0 cm at isocentre).

The detector plate and 45° angled mirror form part of a detachable detector arm or 'elbow'. The detector is aligned with a large field of view lens which forms an image of the light emitted from the screen on the pick-up tube (Plumbicon) of a Video-Optics Inc. camera (VO 1519, Los Gatos, CA, USA) mounted horizontally on the gantry.

The camera operates in a non-standard mode known as camera target integration (Munro *et al.* 1990). The target of the camera accumulates light collected by the lens from the phosphor for an adjustable integration period. This is achieved by switching off the electron beam which scans the camera target in a process known as *'blanking'*. Prior to acquisition, the camera target is being scanned continuously, and beam blanking is triggered when the video signal rises above a threshold level (*i.e.* when the radiation comes on). Following the period of camera target integration, a non-interlaced progressive scanning pattern is used to read out a single frame of video at the frame rate of 30 Hz. Camera target integration is beneficial in terms of reduced noise in the imaging system, since the contribution of noise from the TV camera is reduced (Munro

et al. 1990). A detailed investigation of camera target blanking is presented in Chapter 6, where the signal is used to trigger recording of accelerator MU during portal imaging.

In the 'Single Image' mode, read-out of the camera target is performed at the end of the radiation exposure. This is initiated by a beam-off signal via an interface to the accelerator. In the alternative 'Treatment Loop' mode the EPID captures a series of discrete images, each produced by separate periods of camera target integration (0.25-3.00 s duration). The camera target is read out at the end of each integration period and each frame of video forms a separate image. The system does not perform frame addition - each image is formed from a single frame of video. The modes of camera operation used for image acquisition are summarised in Table 5-1.

Acquisition Mode	Camera Target Integration	Image Acquisition Rate
Single Image	Integrates for duration of exposure (maximum 19.0 s)	-
Double Exposure Set-up Image	Integrates for duration of open & closed field exposures	-
Single Treatment Loop	Sequence of discrete images acquired. Camera target integration period: 0.25-3.00 s	Default: one image every second. Minimum: one image every three seconds. Limit: 40 images.
Multiple Treatment Loop	Acquires a sequence of up to 10 Single Treatment Loops	

Table 5-1: Theraview EPID image acquisition modes and imaging parameters

The operation of the camera is controlled by a modified camera control unit (CCU) (Chapter 6) which is configured to provide suitable fixed video signal gain and apply a correction to the video signal for spatial non-uniformity (termed '*shading correction*'). The CCU is directly interfaced to an 8-bit (512 x 512 pixel) video acquisition and control card housed in a Sun Microsystems SPARCstation5™ (Palo

Alto, CA, USA). All measurements presented in this work have been made using version 2.0 and 2.3 of the commercial software.

5.3 Dosimetric properties

Various characteristics of the device pertinent to dosimetric applications were investigated. Measurements were made using an Elekta SL15*i* accelerator with 6 MV x-rays. All dosimetric studies were performed using the clinical acquisition modes described in Table 5-1, and the CCU was powered on for at least one hour prior to commencement, which was shown to be sufficiently long to achieve system stability (Chapter 5.3.4).

5.3.1 Dose response studies: 'Single' image mode

To study the dose response characteristic against an ionisation chamber (IC), the EPID was modified to include fixation points at each corner, to allow a double-layer structure of Perspex (polymethyl methacrylate or PMMA, density 1.185 g cm^{-3} (Thwaites *et al.* 1996)) to be securely mounted against the surface of the detector plate (Figure 5-1). The Perspex structure was machined to accommodate a 0.6 cm^3 NE2581 Farmer-type IC (NE Technologies Ltd., Reading, UK) centrally within the system field of view. This acted as dose reference. An additional Perspex plate was used to place the geometric centre of the IC at a depth of 1.7 g cm^{-2}. Taking into account the effective point of measurement, this gave a depth for the IC matched to the depth of dose maximum in water for the 6 MV beam (15 mm).

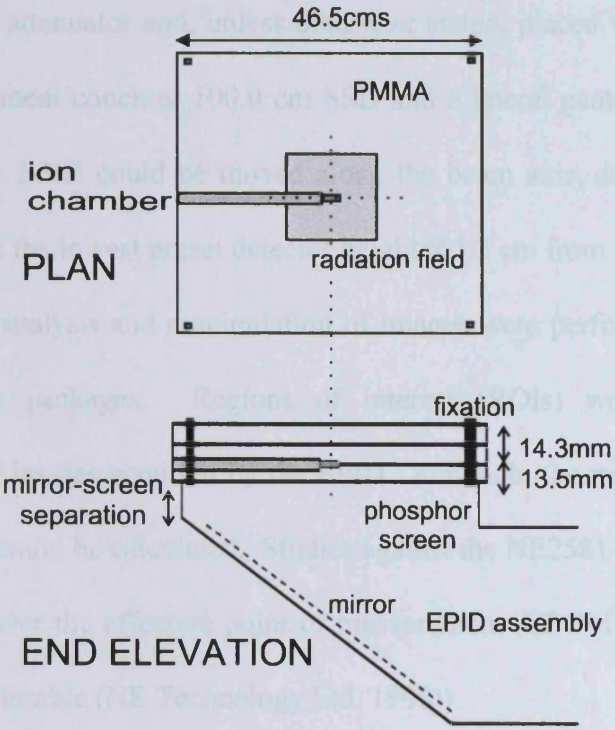

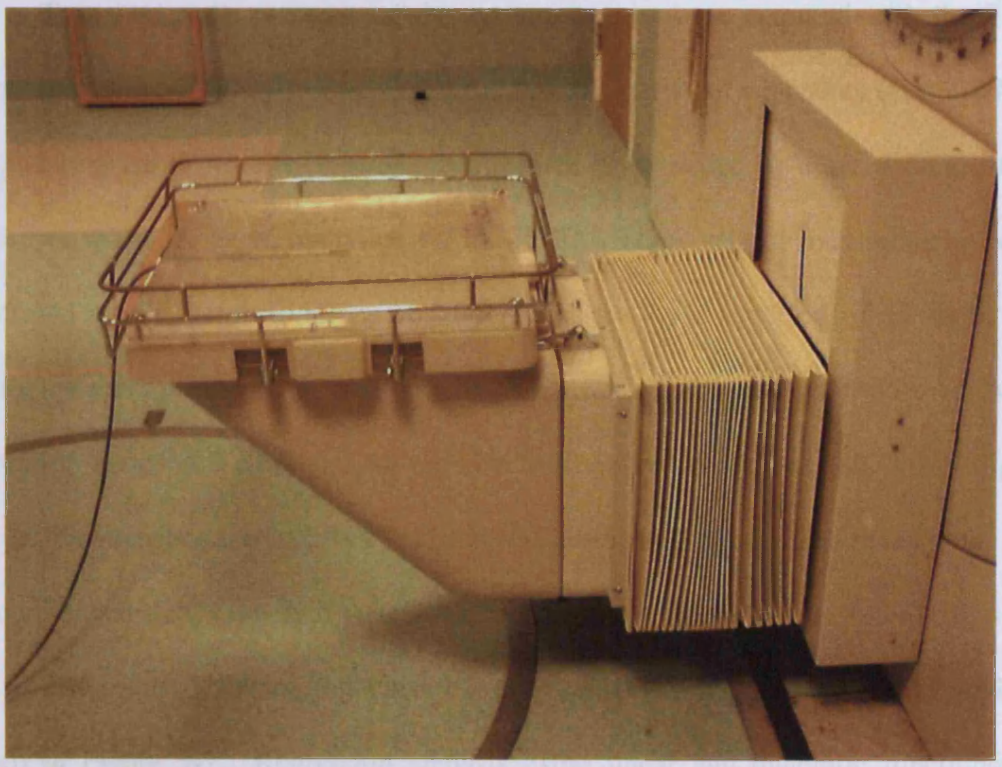

Figure 5-1: Ionisation chamber holder mounted onto EPID (drawing not to scale)

For this study and the majority of others in this chapter, a fixed accelerator geometry and a 10.0 x 10.0 cm field size was used. Sheets of Perspex and WT1 (Radiation Physics, St Bartholomew's Hospital, London, UK) phantom material (15.9 g

cm^{-2}) were used as attenuator and, unless otherwise stated, placed vertically on a solid portion of the treatment couch at 100.0 cm SSD and a lateral gantry angle used. The detector arm of the EPID could be moved along the beam axis, and unless otherwise stated was placed at the lowest preset detector height (65.2 cm from isocentre).

Dosimetric analysis and manipulation of images were performed off-line using several proprietary packages. Regions of interest (ROIs) were established for dosimetric study of images acquired by the EPID. For each, the mean pixel value and standard deviation could be calculated. Studies against the NE2581 IC used a fixed 4x4 pixel ROI placed over the effective point of measurement (EPOM) of the IC (13 mm from the tip of the thimble (NE Technology Ltd. 1990)).

To measure the response of the system, images were acquired with the EPID operating in 'Single' image mode (Table 5-1) using a series of exposures from 2-8 MU. The imaging sequence was immediately followed or preceded by a series of identical exposures made to the IC mounted on the EPID. Three sets of measurements were performed on the same EPID on separate occasions over a period of 17 days. IC readings were corrected for temperature and pressure, the absorbed dose to water calibration factor at 6 MV applied, together with an inverse square law term, to give dose at the phosphor screen. ROI analysis was performed to provide a mean value and standard deviation for repeated exposure.

The results from the three sets of measurements are extremely similar and are shown in Figure 5-2. Regression analysis using linear and quadratic functions are plotted (r^2=0.9955 and 0.9996 respectively). The response is sub-linear and best described by the quadratic function. This is believed to be primarily due to the transfer characteristic (gamma) of the camera tube (Plumbicon XQ 2172, Philips Components,

Slatersville, RI, USA) of 0.95 ± 0.05, but may also be a function of any non-linearity in the video amplification or acquisition process.

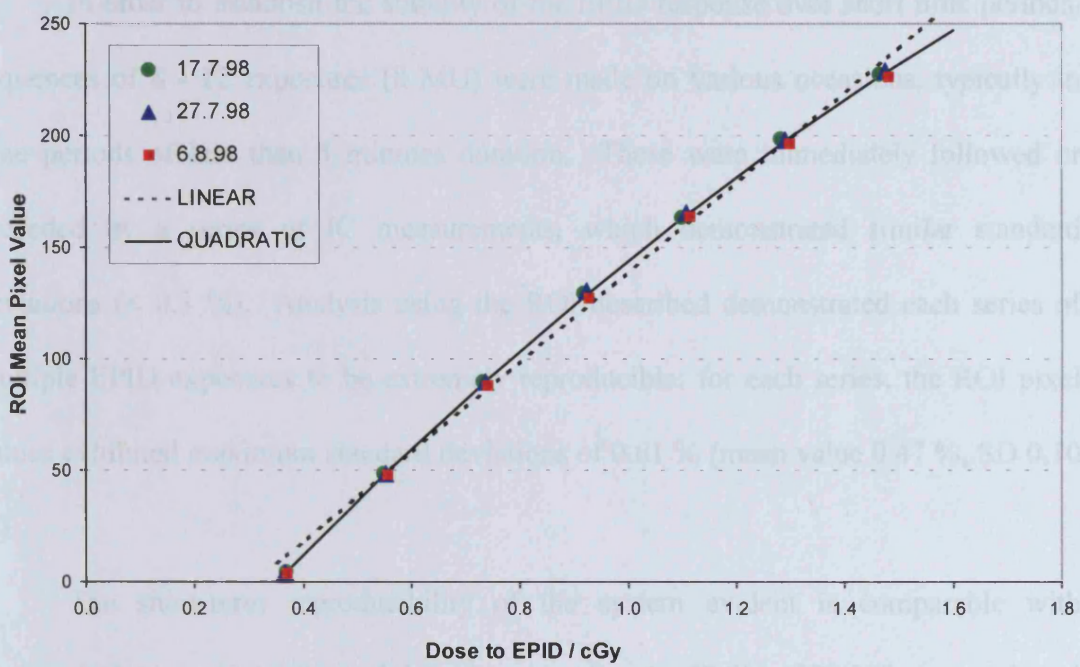

Figure 5-2: Dose response of a Theraview EPID. The dose to the EPID at each MU setting was observed to be extremely repeatable (standard deviations typically < 0.3 %, maximum 0.5 %). Standard deviations for each set of ROI mean pixel values were less than 1.5 grey scale units over the full grey scale range. Standard deviations are thus too small to be shown in both cases.

Figure 5-2 shows an obvious dose threshold for the EPID of around 0.35 cGy. At doses to the detector higher than 1.6 cGy, the system saturated. The sensitivity of the system is a function of the level of video signal gain in the CCU, and the f-number of the lens used (equal to the ratio of the focal length to the lens diameter), since the collection efficiency of the lens has a reciprocal dependence on the square of the f-number (Swindell 1991). In adjustments to the Theraview system studied, increasing the video signal gain was observed to increase the sensitivity of the system by translating the dose response curve to reduced dose levels.

5.3.2 Temporal changes in dose response

5.3.2.1 Central axis short-term stability

In order to establish the stability of the EPID response over short time periods, sequences of 8 - 12 exposures (8 MU) were made on various occasions, typically in time periods of less than 5 minutes duration. These were immediately followed or preceded by a series of IC measurements, which demonstrated similar standard deviations (< 0.3 %). Analysis using the ROI described demonstrated each series of multiple EPID exposures to be extremely reproducible: for each series, the ROI pixel values exhibited maximum standard deviations of 0.61 % (mean value 0.47 %, SD 0.10 %).

The short-term reproducibility of the system evident is comparable with observed short-term stability of dose response for the Philips SRI-100 camera-based EPID: for the Philips system a standard deviation of better than 0.5 % (Dirkx *et al.* 1995) and a range of ±0.5 % (Kirby & Williams 1995) have been reported.

Studies of the same Theraview EPID made 18 – 24 months later showed significantly reduced reproducibility for repeated exposures. The effect was also observed for a second system, and was thought to be associated with increased variability in the dose level at which the EPID triggered. An investigation of this is presented in Chapter 7.3.2.

5.3.2.2 Central axis long-term stability

A study of long-term drift in the dose response of the system during initial work with this EPID consisted of several series of exposures (8 MU) using the 'Single' image mode. Variation in accelerator output was corrected for by IC measurement. Measurements were repeated over a 68 day period on a total of 14 occasions during which no adjustments were made to the imaging system.

Figure 5-3(a) shows the ratio of the mean ROI pixel value to the ion chamber reading, corrected for temperature and pressure, calculated for each session over the 68 day measurement period and normalised to the first session. The data clearly demonstrates a decrease in the sensitivity of the EPID. The result of linear regression is plotted and indicates a sensitivity reduction of 0.04 % day^{-1}.

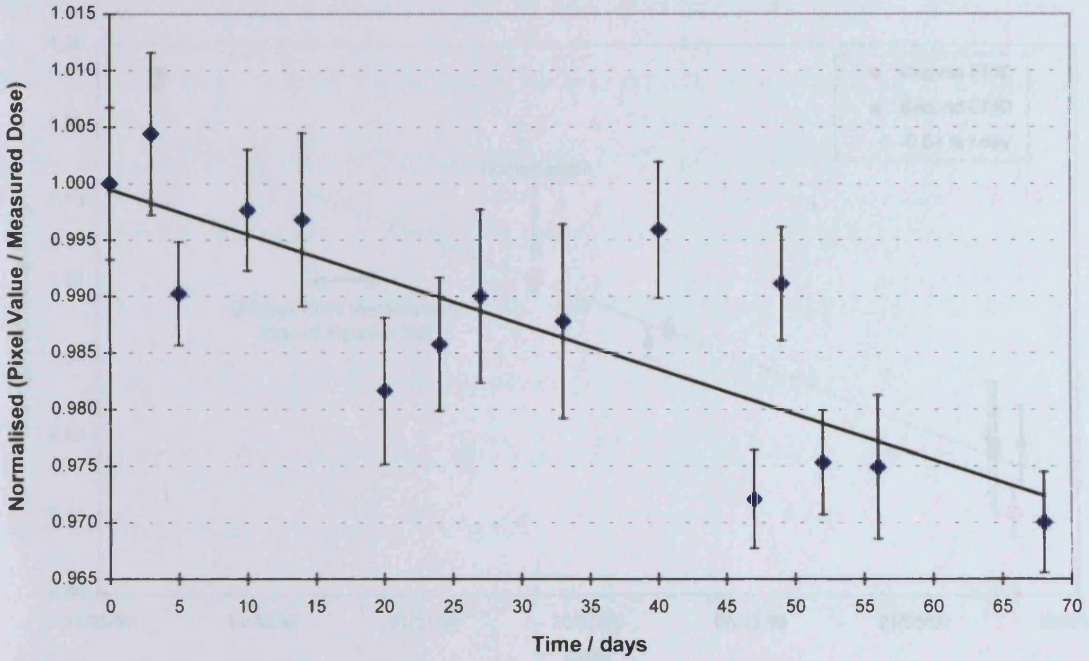

Figure 5-3(a): Normalised sensitivity of an EPID over 68-day period. The result of linear regression is also plotted (-0.04 % day^{-1}).

Further sensitivity data obtained from routine quality control checks of this and a second EPID is shown in Figure 5-3(b). The measurements cover a period of 2 years 10 months, during which time no adjustments were made to *either* system. Data from the original Theraview studied (Figure 5-3(a)) and the second EPID have both been normalised on a date approximately in the middle of the time period shown when both systems underwent routine quality control (18/3/99). The trend-line plotted indicates a decline of 0.04 % day^{-1} (from Figure 5-3(a)), again normalised on 18/3/99). The ten-

week time period during which the data shown in Figure 5-3(a) was obtained is also indicated (approximately 6/98 – 9/98).

The significantly increased standard deviations shown for measurements in the last month of data plotted in Figure 5-3(b) should be noted. This is evident for both systems studied and is believed to be attributable to increased variability in the dose at which the EPID triggered (which is considered in detail in Chapter 7.3.2).

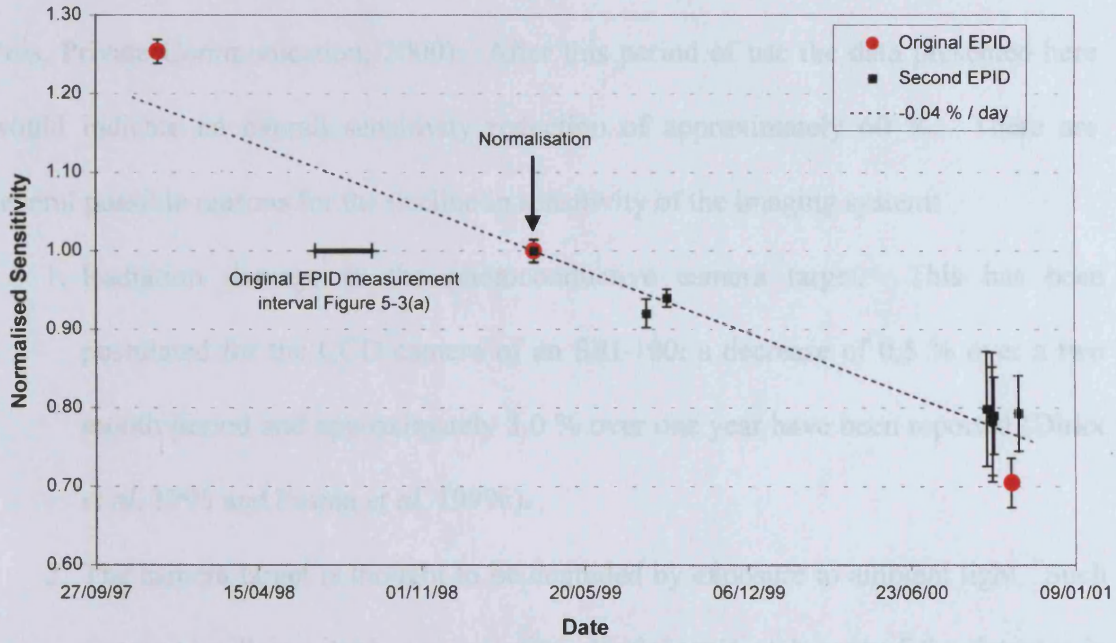

Figure 5-3(b): Sensitivity of two EPIDs observed during routine quality control over a period of 2 years and 10 months. Data is shown for the EPID studied in Figure 5-3(a) (labelled 'Original EPID'), and for a second EPID, both normalised on 18/3/99. The dotted line indicates sensitivity loss of 0.04 % day^{-1} (from the trend-line in Figure 5-3(a)), also normalised on 18/3/99. The ten-week period during which the data in Figure 5-3(a) was collected is indicated.

It is clear from Figure 5-3(b) that both Theraview systems show very similar sensitivity degradation with time. Furthermore, the sensitivity loss is very consistent with the decrease of 0.04% day^{-1} observed on the first system (Figure 5-3(a)). It should be noted that Partridge *et al.* (2000a) have also presented some data on long-term stability over approximately 75 days, which did not show the gradual reduction observed here due to random errors on their data.

For dosimetric applications of this device, correction for sensitivity drift may be necessary. However, the observed sensitivity change is predictable, and for dosimetric applications of the EPID such as patient dosimetry or machine quality assurance (*e.g.* the daily measurement of accelerator output) the system would require reasonably infrequent re-calibration.

Although the exact mode of camera failure is unclear, the manufacturers have indicated an anticipated camera lifetime in this application of around 4 years (van der Pols, Private Communication, 2000). After this period of use the data presented here would indicate an overall sensitivity reduction of approximately 60 %. There are several possible reasons for the decline in sensitivity of the imaging system:

1. Radiation damage to the photoconductive camera target. This has been postulated for the CCD camera of an SRI-100: a decrease of 0.5 % over a two month period and approximately 3.0 % over one year have been reported (Dirkx *et al.* 1995 and Pasma *et al.* 1999c).
2. The camera target is thought to be degraded by exposure to ambient light. Such exposure will inevitably occur during attachment/detachment of the detector in clinical use.
3. The reduction may also be attributable to systematic drift of internal signals within the camera, particularly the beam current, which typically declines over time due to ageing of the cathode filament resulting in a decline in the level of the video signal.
4. The level of optical input to the camera may decline. Although the efficiency of phosphor screen is known not to decrease with accumulated dose (reported data has been reviewed in Chapter 4), radiation damage of the optical lens causing discolouration may attenuate optical signal. No data is available as to the

radiation hardness of this component. However, Lutz (Private Communication, 1999) has stated that the *lens and objective* of the BIS (Wellhöfer Dosimetrie, Schwarzenbruck, Germany), which is of similar design to the EPID and uses a Gd_2O_2S:Tb phosphor as the radiation detector, suffers a 50 % reduction in transmission at approximately 200 Gy.

5. A further cause may be drift in the ADC of the video acquisition and control card.

5.3.2.3 Off-axis long-term stability

The relative off-axis response of the system was also considered over the ten-week period using the same 8 MU images (10.0 x 10.0 cm field). Further ROIs were located 50 pixels from the central ROI (approximately 41 mm at detector level) along the axes of the image matrix in the gun-target (GT or inplane) and ceiling-floor (crossplane) directions. The mean ROI pixel value for each session was corrected for variation in the central axis value.

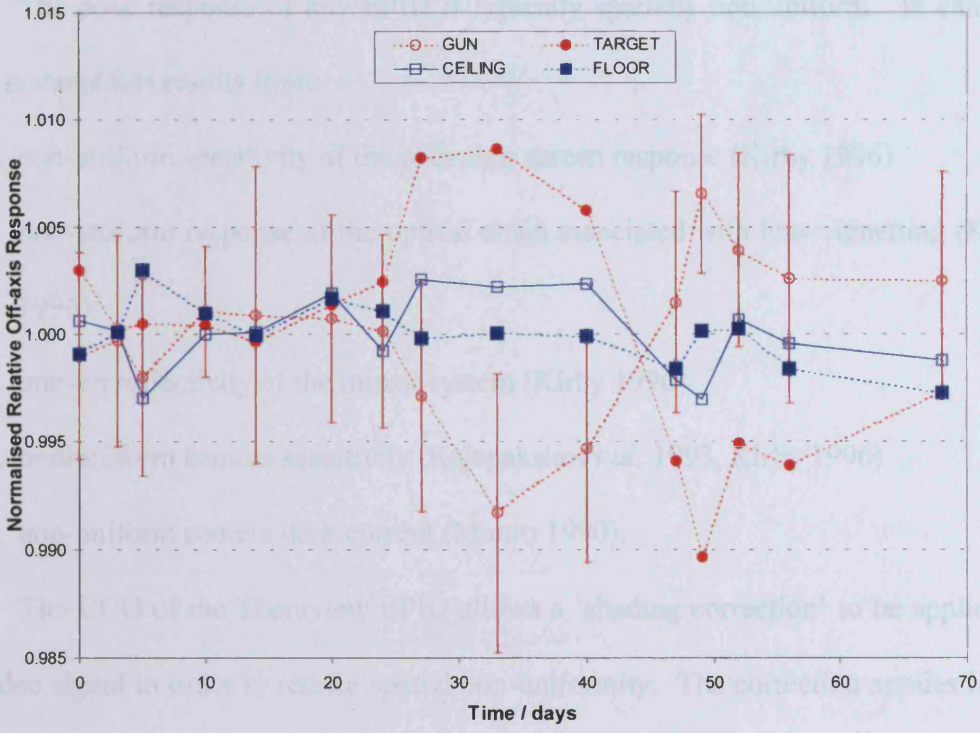

Figure 5-4: Reproducibility of off-axis response

Figure 5-4 shows the data normalised to the mean response for each ROI over the measurement period. For clarity, error bars (1 SD) are only shown for the ROI orientated towards the gun, but these are typical. Figure 5-4 shows that the changes in relative response of the EPID are small (maximum SD 0.56 %) indicating that the off-axis response of the system is stable. Better stability for the SRI-100 has been reported by Heijmen *et al.* (1995) who accounted for variations in the incident beam profile and observed day-to-day changes of less than 0.2 % (1 SD). No account has been made of variations in the beam profile of the accelerator for the Theraview data. However, this was observed to be stable over the period: in six measurements of the beam profile as part of routine quality control, maximum variations of ± 0.9 % (crossplane) and ± 1.5 % (inplane) were observed. Furthermore, Figure 5-4 shows greatest deviation in the inplane axis which is known to have undergone minor flatness adjustment during this period.

5.3.3 Spatial uniformity of dose response

The dose response of any EPID is typically spatially non-uniform. In camera-based systems this results from:

1. non-uniform sensitivity of the phosphor screen response (Kirby 1996)
2. non-uniform response of the optical chain associated with lens vignetting (Kirby 1996)
3. uneven reflectivity of the mirror system (Kirby 1996)
4. non-uniform camera sensitivity (Rajapakshe *et al.* 1993, Kirby 1996)
5. non-uniform camera dark current (Munro 1990).

The CCU of the Theraview EPID allows a 'shading correction' to be applied to the video signal in order to reduce spatial non-uniformity. The correction applies linear and parabolic modulation to the video signal at line and field rates to compensate for

variations in image non-uniformity across the field of view (known as shading). However, despite use of the correction, all three local systems showed considerable non-uniformity, and on occasions this was significant for clinical imaging.

Non-uniformity was assessed along major axis profiles through the centre of the image matrix. The incident dose rate profile of a steady-state beam was assessed using a linear ion chamber array (Victoreen 7000-2 Therapy Beam Analyser, Victoreen Inc., Cleveland, Ohio, USA). Measurements were made under the standard scatter conditions used locally for assessment of radiation field flatness (which placed the detector at a depth of approximately 5 g cm^{-2}, with a similar depth of back-scatter material). A field size of 35 x 10 cm^2 was used, with the larger opening orientated along both cardinal axes in turn. The ion chamber array was located such that the ion chambers were at the same SDD as the phosphor screen of the EPID (150.0 cm).

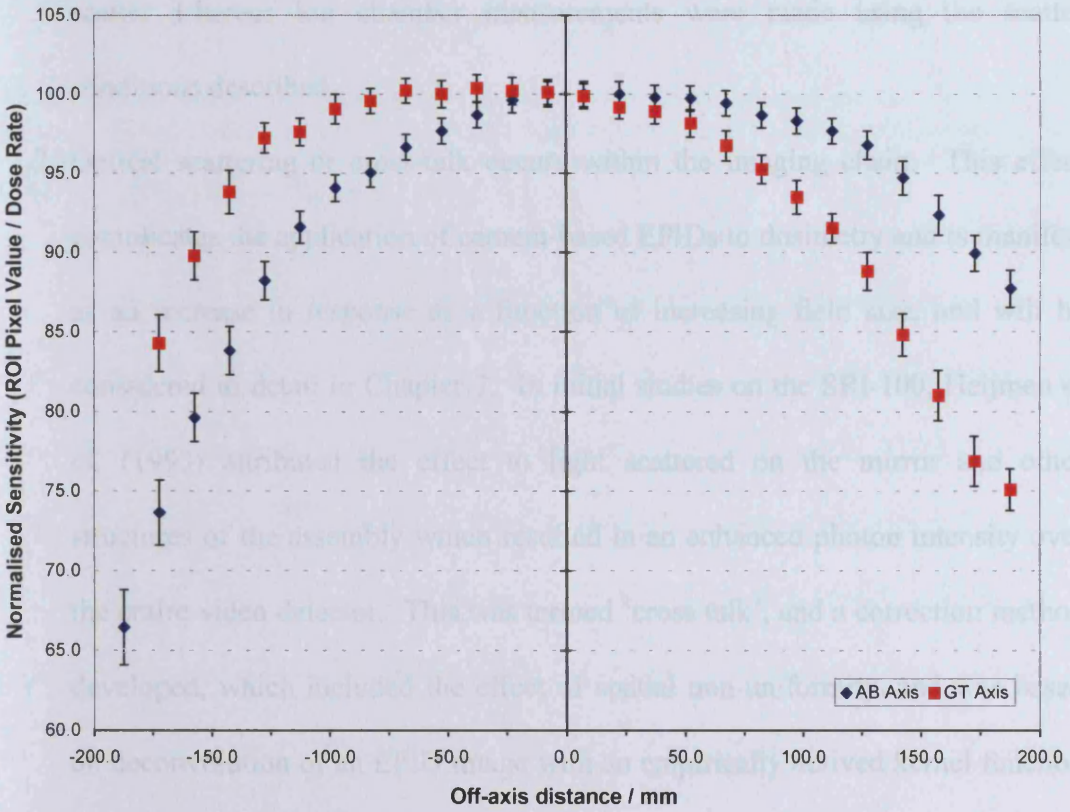

Figure 5-5: Major axis sensitivity profiles for a Theraview EPID. AB and GT refer to the crossplane and inplane axes of the accelerator. Uncertainties are based on the sum of the percentage standard deviation of the pixel values in each ROI, and an estimated uncertainty of ± 0.2 % for measured dose rates based on observed measurement reproducibility with the ion chamber array.

Theraview images of the steady-state beam were acquired using the 'Single Treatment Loop' facility (Table 5-1). Following pixel size calibration, ROIs of the appropriate dimensions were established within the image matrix at the calculated location of each corresponding ion chamber. The array contained 30 chambers which were 8.5 x 21.0 mm in cross-section and located at 15 mm separation. The ratio of the mean pixel value in each ROI to the dose rate measured by each corresponding ion chamber of the array was determined. The normalised results are shown in Figure 5-5.

Figure 5-5 clearly demonstrates spatial non-uniformity with a circular symmetry. This was typical for all three systems and was thought to be primarily a result of lens vignetting. However, the exact interpretation of this data requires caution since:

1. The phantom scatter conditions differ for the ion chamber array and EPID: the EPID effectively has 2.02 g cm^{-2} 'build-up' material, and effectively no back-scatter whereas ion chamber measurements were made using the scatter conditions described.
2. Optical scattering or cross-talk occurs within the imaging chain. This effect complicates the application of camera-based EPIDs to dosimetry and is manifest as an increase in response as a function of increasing field size, and will be considered in detail in Chapter 7. In initial studies on the SRI-100, Heijmen *et al.* (1995) attributed the effect to light scattered on the mirror and other structures of the assembly which resulted in an enhanced photon intensity over the entire video detector. This was termed 'cross talk', and a correction method developed, which included the effect of spatial non-uniformity, and was based on deconvolution of an EPID image with an empirically derived kernel function describing optical 'cross-talk' (Heijmen *et al.* 1995, Pasma *et al.* 1998). Subsequently, Munro *et al.* (1998) have termed the effect 'glare'. They

proposed that the effect is attributable not only to light scattered from the mirror and walls of the EPID, but also to light reflected by the mirror *back* to the surface of the phosphor screen, which can then be *re-emitted* (Figure 5-6).

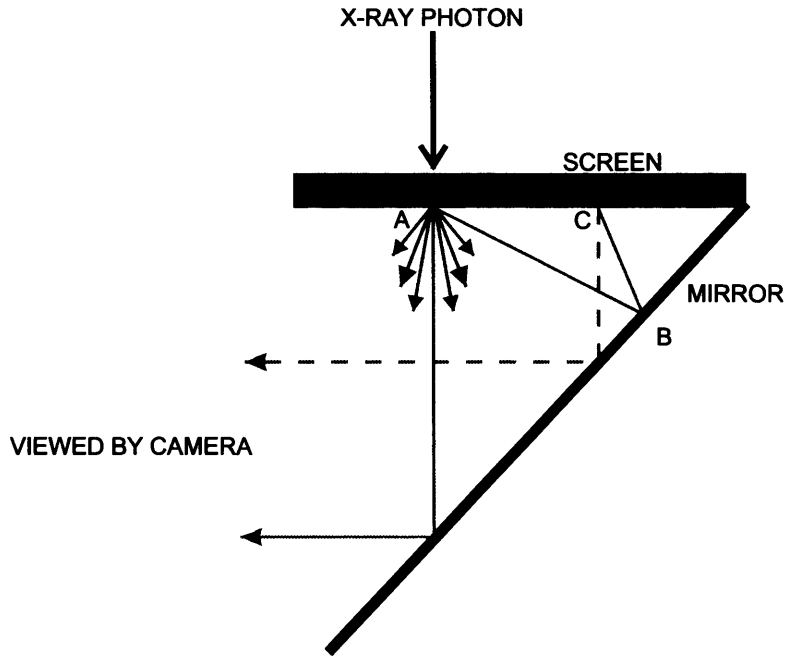

Figure 5-6: Illustrating optical scattering between phosphor screen and mirror. Incident x-ray photons at A produce light that is emitted directly towards camera, and at higher emission angles, light that is reflected by the mirror (B) back onto the phosphor screen (C) which acts as a reflector itself. From Munro *et al.* (1998) and Partridge *et al.* (1999b).

For both the SRI-100 and PortalVision, the spatial non-uniformity correction for clinical imaging is reported in the literature, and is based on a normalised image of an open radiation field directly irradiating the detector (*e.g.* Visser *et al.* 1990, Yin *et al.* 1994). However, normalisation to an in-air open field flood image is not sufficient for two-dimensional dosimetric measurements, since the non-uniform profile of a megavoltage beam in-air will quantitatively affect the correction applied to the image matrix (*e.g.* Essers *et al.* 1995, Parsaei *et al.* 1998, Curtin-Savard & Podgorsak 1999). Various approaches reported to overcome this difficulty are considered in Chapter 7, where a correction method for spatial non-uniformity to allow two-dimensional dose measurement with the Theraview EPID is presented. This includes evaluation of a

purely physical means of reducing optical cross talk recently proposed by Partridge *et al.* (1999b).

5.3.4 System warm-up characteristics

The variation in sensitivity of an EPID following power-on of the camera system was assessed by making repeated exposures (8 MU) under the fixed geometry described for the reproducibility studies (Chapter 5.3.2).

Images were acquired using the 'Single' image mode (Table 5-1). The CCU had been switched off for just under 3.5 hours. Following power-on of the CCU a series of exposures were made (at approximately 35 s intervals) for 6 minutes, followed by exposures approximately every 2 minutes for around one hour. A further series of exposures were made at 1.5 hours from power-on of the CCU. The temporal change in ROI mean pixel values is shown in Figure 5-7, normalised to the mean value for the repeated exposures at 90 minutes. The maximum uncertainty in the time of each exposure after power-on of the CCU was estimated as ± 5 s. The uncertainty in the normalised response is expressed as one standard deviation calculated from ROI analysis of each image.

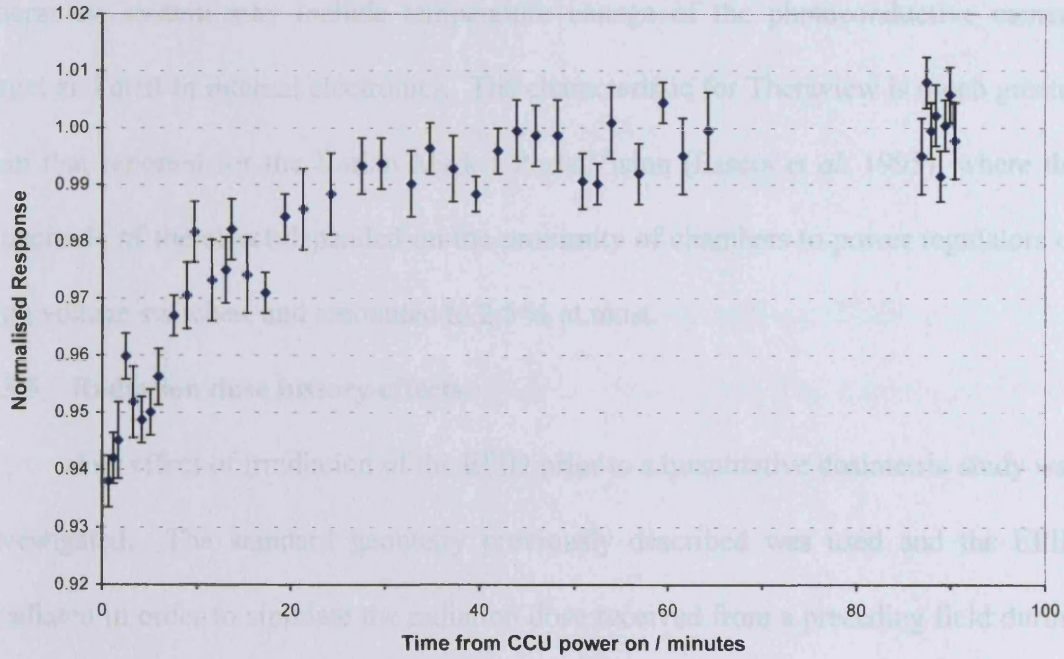

Figure 5-7: Warm-up characteristic of EPID.

The response is clearly stable at around 40 minutes following power-on of the CCU. The increase in pixel value (*i.e.* sensitivity) for this system is almost 7 % following a period of 3.5 hours during which the CCU had been switched off. Measurements on a second EPID system for which the power to the CCU had been switched off overnight revealed a similar characteristic: the second system took a similar time to reach stability, and demonstrated a larger (12 %) enhancement in sensitivity. Further analysis using off-axis ROIs (previously described) was applied to every third image in the sequence in Figure 5-7 and showed no obvious spatial variation in the warm-up characteristic.

On the basis of the observed characteristic, a time period of one hour was taken as the minimum required following power-on of the CCU prior to performing any dosimetric measurements with the system, in order to allow the sensitivity to stabilise. It should be noted that warm-up characteristics have not been reported or quantified for camera-based systems, despite warm-up of components in a video-based portal imaging system being identified as a source of temporal variation of image pixel value (Rajapakshe *et al.* 1993). The underlying causes of the observed characteristic for the Theraview system may include temperature change of the photoconductive camera target and drift in internal electronics. The characteristic for Theraview is much greater than that reported for the Varian Mark I PortalVision (Essers *et al.* 1995), where the magnitude of the effect depended on the proximity of chambers to power regulators or high voltage switches, and amounted to 2.5 % at most.

5.3.5 Radiation dose history effects

Any effect of irradiation of the EPID prior to a quantitative dosimetric study was investigated. The standard geometry previously described was used and the EPID irradiated in order to simulate the radiation dose received from a preceding field during

which time the system was not set to acquire. Following the pre-irradiation dose delivery, a series of repeated exposures (8 MU) were acquired using the 'Single' image mode as rapidly as possible. The time interval between termination of the pre-irradiation dose and acquisition of each image was noted.

Figure 5-8 shows the result of measurements on three separate occasions following a dose of 1.9 Gy to the detector. The mean pixel value for each ROI, normalised to the mean of the last four values in each sequence, is plotted against the time from termination of the pre-irradiation dose delivery. The maximum uncertainty estimated in the time delay (± 5 s) and the standard deviation for each ROI are shown.

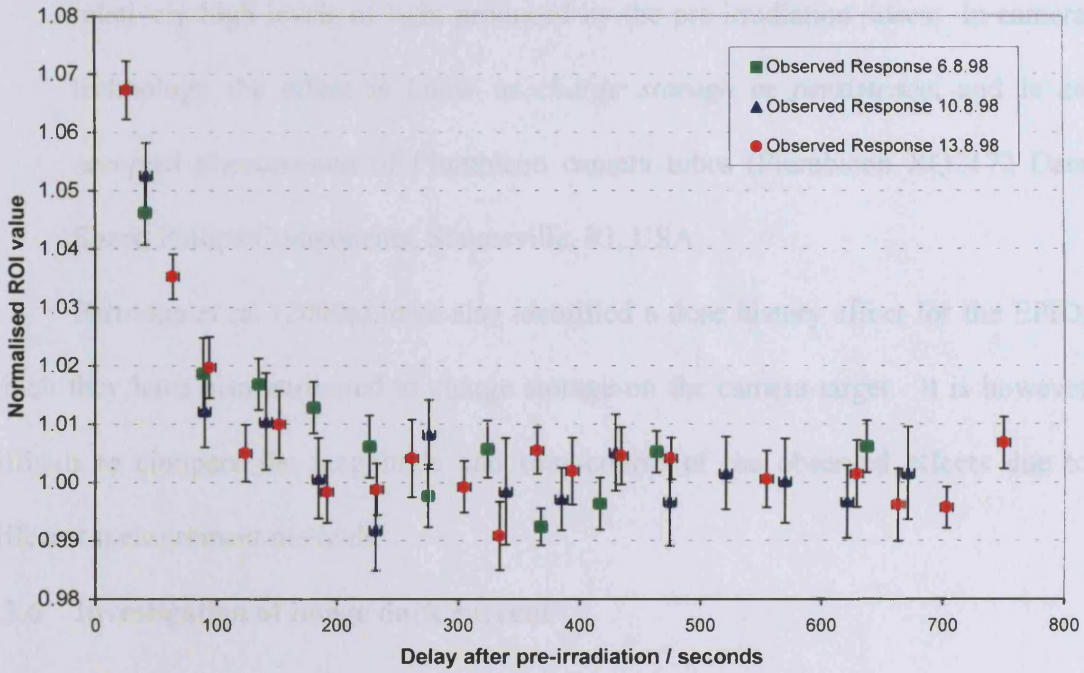

Figure 5-8: Effect of pre-irradiation on EPID response.

The three sets of data, measured over a period of one week, show a consistent pattern in which there was a clear enhancement in the response of the EPID which reduced with time. The maximum enhancement was observed at around 7 % for the most rapidly acquired image (26 s delay, 13/8/98). The reduction in pixel value with time could be described adequately by a half-life of about 40.0 s. The experiment was

repeated with a smaller 0.19 Gy pre-irradiation exposure and the effect reduced to around 3 %.

There are two potential causes underlying the effect:

1. Afterglow from Gd_2O_2S:Tb. However, the measurements presented in Chapter 4 have shown no detectable afterglow from Gd_2O_2S:Tb after exposure to doses as large as 4.4 Gy.
2. High levels of charge on the camera target may not be fully removed by the read-out process, thus creating a 'ghost' image evident as increased pixel value in a subsequent image. The effect could occur following exposure to the relatively high levels of light produced by the pre-irradiation doses. In camera technology the effect is know as *charge storage* or *persistence*, and is an accepted phenomenon of Plumbicon camera tubes (Plumbicon XQ2172 Data Sheet, Philips Components, Slatersville, RI, USA).

Partridge *et al.* (2000a) have also identified a dose history effect for the EPID, which they have also attributed to charge storage on the camera target. It is however difficult to compare the magnitude and time-course of the observed effects due to different measurement methods.

5.3.6 Investigation of image dark current

The Theraview image acquisition system does not perform dark current subtraction. As a result, accumulation of dark current has been identified as a potential problem with the mode of camera operation, since the useful dynamic range will be reduced (Munro *et al.* 1990). For quantitative work with such a system it is necessary to investigate the magnitude of any dark current contribution. As the system does not perform dark current subtraction, and it is not possible to force the system to acquire a dark current image directly due to the trigger mechanism (which is discussed fully in

Chapter 7.3) it was necessary to measure dark current indirectly. This was achieved by a novel approach in which images were acquired using accelerator exposures of a fixed magnitude (MU), but delivered using a range of accelerator PRFs, which has the effect of altering the exposure time. Images were acquired using the 'Single' imaging mode using the standard geometry described. A series of repeated exposures were made at each PRF and analysed using the central ROI to give a mean pixel value for each PRF. Variations in accelerator output with PRF (<1.0 %) were removed based on IC measurements. Exposures of 6 MU were made at 400, 200, 100, 50 and 25 Hz PRF, and exposures of 8 MU were made at 400, 200 and 100 Hz PRF. The response, normalised to the 400 Hz PRF data, is presented against the exposure duration relative to 400 Hz (based on the actual PRF compared to the normal PRF setting of 400 Hz) in Figure 5-9.

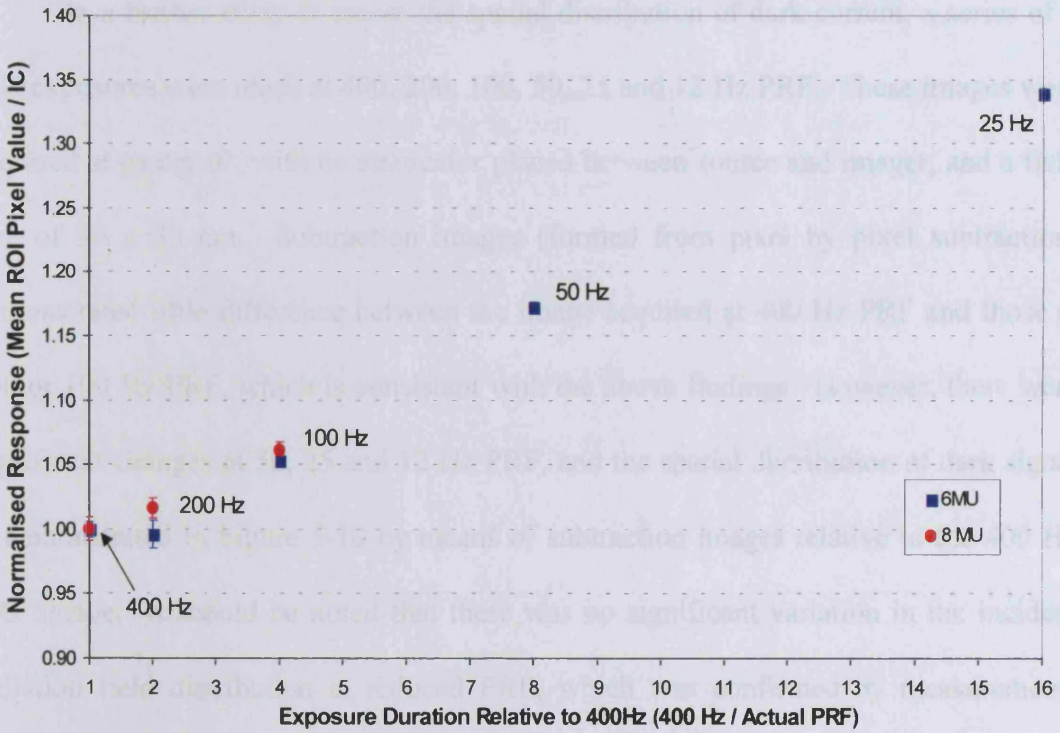

Figure 5-9: Response of EPID at different accelerator PRFs for exposures of 6 and 8 MU as a function of relative exposure duration. Expressed relative to the normal operating PRF of 400Hz. Uncertainties, expressed as one standard deviation, indicate the sum of the percentage uncertainties in each series of ROI values and IC readings.

The results clearly show a significant increase in pixel value on reducing accelerator PRF. Indeed, saturation prevented 8 MU exposures being given below 100 Hz, and at 6 MU the limit was 25 Hz. An additional limit was imposed by the maximum (19 s) integration period of the EPID in this mode (Table 5-1). The observed characteristic is a direct result of the contribution of dark current to the image since reducing the accelerator PRF extends the exposure time, and as a result images contain a larger dark current component. The calculated relative exposure duration is not strictly valid because although dose rate changes linearly with PRF, the simple ratio neglects any variations in dose rate during beam-start. However, the investigation allows semi-quantitative assessment of dark current levels. For example, on extending the exposure duration nominally by a factor of four (*i.e.* using 100 Hz PRF), the additional contribution of dark current is just over 6 %.

In a further study to assess the spatial distribution of dark current, a series of 3 MU exposures were made at 400, 200, 100, 50, 25 and 12 Hz PRF. These images were acquired at gantry 0°, with no attenuator placed between source and imager, and a field size of 30 x 30 cm. Subtraction images (formed from pixel by pixel subtraction) demonstrated little difference between the image acquired at 400 Hz PRF and those at 200 or 100 Hz PRF, which is consistent with the above findings. However, there were significant changes at 50, 25 and 12 Hz PRF, and the spatial distribution of dark signal is demonstrated in Figure 5-10 by means of subtraction images relative to the 400 Hz PRF image. It should be noted that there was no significant variation in the incident radiation field distribution at reduced PRF, which was confirmed by measurements using the linear ion chamber array: profiles of incident dose rate along major axes were acquired for the accelerator operating at 12 – 400 Hz PRF, and within the field of view

of the EPID, the profiles at reduced PRF compared to 400 Hz were within ± 1.2 % (inplane), and within -1.3 and +2.0 % (crossplane).

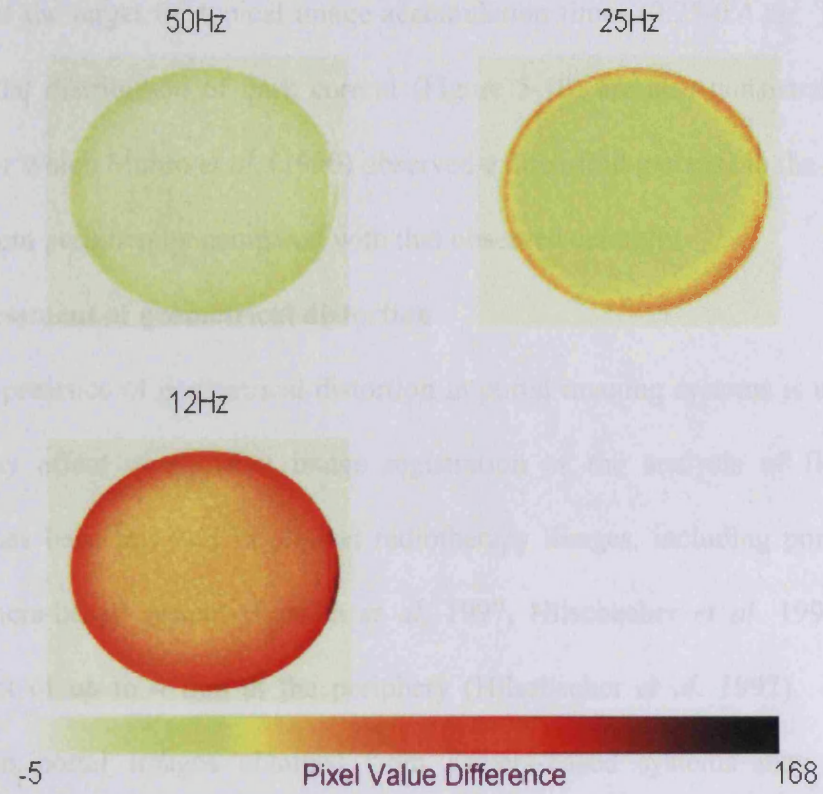

Figure 5-10: Subtraction images formed from images acquired at different accelerator PRFs (compared to 400 Hz) showing spatial distribution of dark current. It should be noted that the irregularity evident as a line structure on the right-hand side of all three images was caused by incorrect video camera alignment (lateral displacement) at the time of image acquisition.

The subtraction images in Figure 5-10 clearly demonstrate spatially non-uniform dark current which increases significantly towards the periphery of the field of view, and a more uniform distribution within the central region of the image.

It is clear from Figure 5-9 that dark currents become significant on increasing the period of camera target integration, which is of particular concern when imaging with low dose rates (associated with reduced PRF or large attenuator thickness). Although it is difficult to quantify the contribution of dark current from the above data, the effect should be considered in dosimetric applications of the device. It should also be remembered that dark currents are likely to increase during the lifetime of the camera and regular re-assessment should be considered. The findings are consistent with

results for the prototype reported by Munro *et al.* (1990). For the device Munro *et al.* (1990) studied, dark currents were less than 2 % of the maximum level of video signal over most of the target for typical image accumulation times (0.25-0.4 s). The results for the spatial distribution of dark current (Figure 5-10) are also consistent with the prototype for which Munro *et al.* (1990) observed a three-fold increase in the magnitude of dark current peripherally compared with that observed centrally.

5.3.7 Assessment of geometrical distortion

The presence of geometrical distortion in portal imaging systems is undesirable since it may affect quantitative image registration or the analysis of field shape. Distortion has been reported in clinical radiotherapy images, including portal images from a camera-based system (Luchka *et al.* 1997, Hilsebecher *et al.* 1997), with a displacement of up to 4 mm at the periphery (Hilsebecher *et al.* 1997). Geometric distortion in portal images obtained from camera-based systems may also have significant consequences for dosimetric application of such devices, effectively resulting in spatial mis-registration of collimator position or dose delivered.

Geometric distortion of a Theraview EPID was assessed using images of a regular grid transmission phantom mounted onto the exterior of the EPID. The phantom comprised a series of straight brass rods of square cross-section (3.2 mm) located rigidly at 50.8 mm separation in a sheet of Perspex. Images of the grid were acquired using suitable exposure parameters and a field size larger than the active area of the detector (Figure 5-11). Visual inspection showed no distortion in the images of the grid within an estimated uncertainty of ± 2 pixels (± 1 mm).

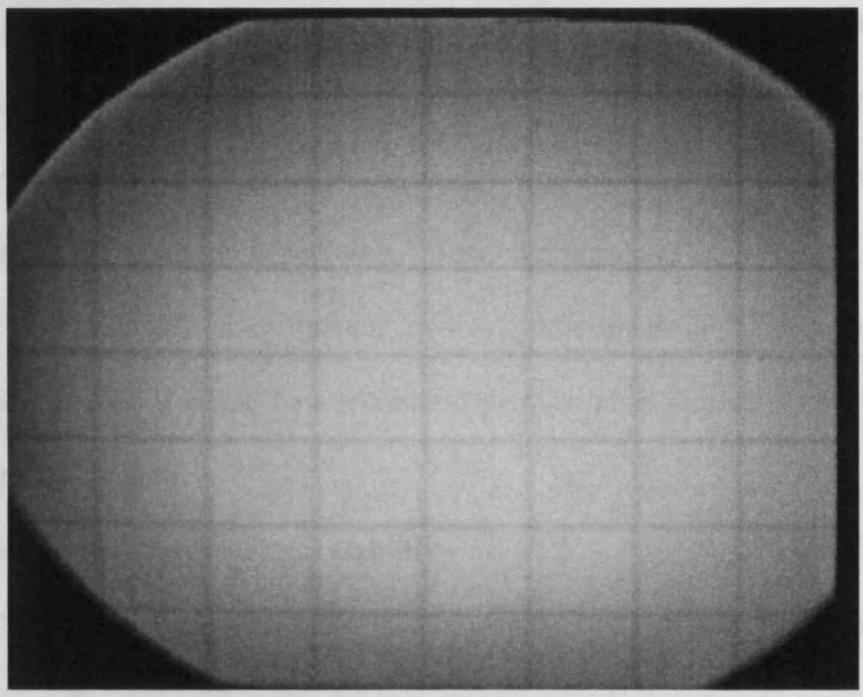

Figure 5-11: Image of a regular grid transmission phantom used to assess geometric distortion.

There is little reported data for observed geometric distortion in camera-based EPIDs. The commercial camera-based BIS (Wellhöfer Dosimetrie, Schwarzenbruck, Germany), which is of similar design to the EPID, exhibited no geometric distortion along its major axes, since the pixel location of an imaged field edge was shown to be linearly dependent on the field size (Ma *et al.* 1997). In their recent study of Theraview, Partridge *et al.* (2000a) reported assessment of geometric distortion using a regular transmission phantom and an automatic analysis routine at cardinal gantry angles. They found a rigid body rotation of 1.2 ± 0.4° independent of gantry angle, and similar geometric distortion to that found here, with a value of 0.5 mm given for the central 10.0 x 10.0 cm of the field of view, and less than 1 mm over the remaining field of view.

It should be noted that routine monthly quality control of pixel size calibration for the Theraview EPID, which involved measurement of a 100.0 mm test object, has shown errors in the measured dimension of 2-4 mm (2-4 %) in both image directions on

all three available EPIDs. The drift in size calibration is thought to be attributable to change in the horizontal and vertical scan rates within the tube camera (which is an inherent problem with tube cameras), and as such would affect pixel size calibration for images taken for dosimetric purposes. Such discrepancies have continued to be observed despite regular re-calibration involving adjustment of the scan rates. For dosimetric purposes it would be advisable to perform pixel size calibration on every measurement occasion.

5.3.8 Assessment of mechanical stability

The positional reproducibility of the imaging system's detector assembly, and any motion associated with gantry rotation, directly affects the imaging geometry since the detected field shifts within the image matrix. The actual motion of an imager is complex since it may undergo translations and rotations both in and out of the image plane, and the observed image displacement may be in the opposite direction to that expected from the sag of the arm (Kirby 1995).

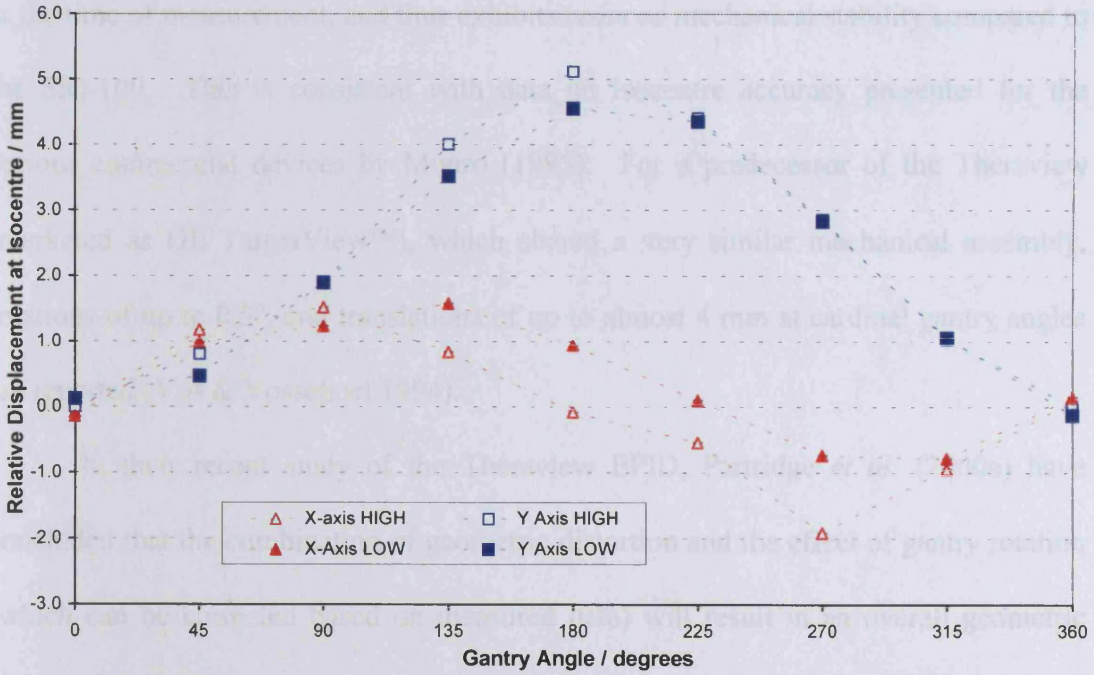

Figure 5-12: Displacement of isocentrically located ball bearing with gantry rotation. Measured at extremes of SDD: HIGH (139.8 cm), LOW (165.2 cm). X and Y axes correspond to accelerator crossplane (AB) and inplane (GT) axes respectively.

The stability of a Theraview EPID on rotation of the accelerator gantry was assessed by imaging an isocentrically mounted steel ball bearing (5.5 mm diameter) at 45° gantry angles at extremes of SDD (165.2 cm and 139.8 cm). For each projection the centre of the ball was found from horizontal and vertical profiles (3 pixels width) following a method reported by Roback & Gerbi (1995), although this present work considered both crossplane and inplane directions. Displacement of the ball at each gantry angle (relative to gantry 0°) was calculated at isocentre distance (Figure 5-12).

The maximum displacement was along the inplane axis at gantry 180° (associated with droop of the EPID) and amounted to approximately 5 mm. Displacement in the orthogonal image direction of up to 1.5 mm was observed for lateral gantry angles. The magnitude and gantry dependence of the displacements is very similar to that reported for an SRI-100 about 4 years in age by Kirby (1995). However, Kirby (1995) also reported reduced movement for a second SRI-100 only a few months old (maximum 2 mm). The Theraview unit studied was around 1 year old at the time of measurement, and thus exhibits *reduced* mechanical stability compared to the SRI-100. This is consistent with data on isocentre accuracy presented for the various commercial devices by Munro (1995). For a predecessor of the Theraview (marketed as GE TargetView™), which shared a very similar mechanical assembly, rotations of up to 0.5°, and translations of up to almost 4 mm at cardinal gantry angles are reported (Vos & Vossepoel 1994).

In their recent study of the Theraview EPID, Partridge *et al.* (2000a) have concluded that the combination of geometric distortion and the effect of gantry rotation (which can be corrected based on measured data) will result in an overall geometric accuracy for the Theraview system of around ±2 mm. This is likely to be the case for the system studied here, but based on the observed variation in pixel size calibration it

would be advisable to perform rigorous quality control of the geometric calibration of the system.

5.4 Summary

A review of the operation and characteristics of the tube camera EPID Theraview™ pertinent to dosimetry has been presented. The dose response of the system demonstrates a non-linear characteristic thought to be a function primarily of the transfer characteristic (gamma) of the tube camera. The sensitivity of two systems has been observed to decrease at a rate of 0.04 % day^{-1}, and although initially the device showed good reproducibility (0.5 % SD), this was observed to have degraded significantly two years later. However, the relative sensitivity off-axis was observed to be stable (maximum SD 0.56 % over 10 weeks). The system also shows significant spatial non-uniformity and a prolonged 'warm-up' characteristic (40 minutes) during which time its sensitivity is not stable. The tube camera also suffers from charge storage (or persistence) following previous irradiation, and exhibits spatially non-uniform dark current. Based on observed geometric distortion and the effect of gantry rotation, the geometric accuracy of the system was estimated as ± 2 mm.

Chapter 6. Application of a tube camera-based electronic portal imaging device to collimator position verification during dynamic multileaf collimation

6.1 Introduction

There are two approaches to verification of DMLC using EPIDs. The first approach, which is the subject of this chapter, is to perform geometric verification of DMLC by measuring or 'tracking' collimator and leaf positions during dynamic dose delivery. The second uses the EPID to investigate the integrated dose distribution delivered by the DMLC sequence, which is the subject of Chapter 7.

Partridge *et al.* (2000b) have recently reported the comparison of three different EPIDs applied to leaf tracking in DMLC, namely:

(i) The CCD camera-based system developed at Royal Marsden Hospital (Sutton, UK) which was based on a reticulated CsI:Tl scintillator array (Mosleh-Shirazi *et al.* 1998b). Partridge *et al.* (1998) described the implementation in which the accelerator was operated at 25 Hz PRF. Single frames were formed from each radiation pulse and images were formed at 1.6 s intervals from averages of 40 frames. The accelerator dose was also recorded with each image by digitising an analogue voltage representing cumulative MU. As discussed in Chapter 2, this signal was used by the system controlling the DMLC motion and was thus not completely independent. They established that the leaf position in each portal image corresponded to half the intensity level for leaf speeds and offsets of interest using penumbra modelling and measurement. They showed that within the measurement resolution of their system, prescribed DMLC sequences were followed correctly.

(ii) An implementation of the Elekta SRI-100 at the Christie Hospital (Manchester, UK) reported by James *et al.* (2000) in which eight snap-shot images were acquired at equally spaced MU intervals by means of an external trigger circuit which monitored accelerator MU. During delivery the images formed were compared visually with a template overlay, allowing manual interruption should a discrepancy be identified. Images were also analysed off-line using an edge detection algorithm.

(iii) A method to overcome motion distortion developed for the Varian PortalVision matrix ion chamber at The Netherlands Cancer Institute (Amsterdam) to allow field shape verification for dynamic beams: Smitsmans *et al.* (2000) have described the approach, which involved digitising accelerator MU with each line of the image and calculating the expected field edge from the DMLC prescription, which could be shown as an overlay on the image.

Partridge *et al.* (2000b) concluded that all three systems had similar performance and showed an overall accuracy for measured collimator position against prescribed of ± 1.0 mm.

Having reported the dosimetric and geometric properties of the Theraview EPID in Chapter 5, this chapter describes the use of this EPID for collimator position verification in dynamic treatments.

Partridge *et al.* (2000a) have also reported an approach for collimator position verification using this EPID. In their implementation a "dose display board" was mounted at one edge of the camera's field of view. The board consisted of light emitting diodes (LEDs) acting as decade counters. The LEDs provided a real-time indication of the number of $1/64^{th}$ MU delivered by their Elekta accelerator, which could be altered by an adjustable division factor. The LED display was captured as part

of each image allowing, the accelerator MU during each period of image formation to be identified from automatic inspection of the image with the help of marker LEDs to aid alignment. For the minimum camera integration period (0.25 s) the lowest decade could not be resolved, resulting in a dose resolution of ± 1.25 MU for a dose rate of 200 MU min^{-1}.

A different approach to leaf tracking using the commercial Theraview EPID is described here. The approach is based on an isolated interface to the camera control unit (CCU) used to trigger recording by the SME (Chapter 2) of the accelerator $1/64^{th}$ MU value, and has no effect on the normal operation of the EPID.

6.2 Materials and Methods

6.2.1 Overview of camera operation

The operation of the Theraview EPID tube camera has been outlined in Chapter 5, together with the image acquisition modes (Table 5-1). As discussed, images are formed by light integration onto the camera target by cutting off the electron beam that reads out the target (blanking). The first frame of video read after un-blanking the camera is digitised to form an image. The read-out process is itself destructive since it removes the charge distribution that has built up on the target.

The camera and CCU of the EPID are operated in an external control mode. Via a direct connection to the CCU, a video acquisition and control card within the Theraview workstation provides frame/line synchronisation pulses, and the beam blanking control signal to control camera target integration. Typical beam blanking control signals were obtained using a storage oscilloscope for both 'Single' and 'Treatment Loop' modes of image acquisition (Table 5-1), and are shown annotated in Figure 6-1. For all measurements presented, Theraview version 2.3 software was used.

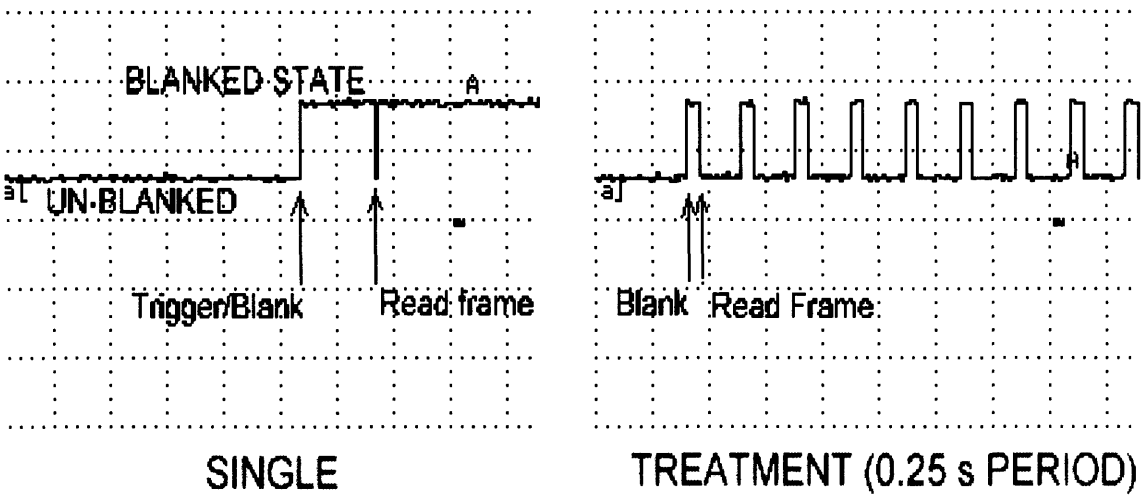

Figure 6-1: Beam blanking control signal for 'Single' (left) and 'Treatment' (right) modes of image acquisition. The oscilloscope time-base was 1.0 s division^{-1} in both cases. The camera target integrates light when the control signal is at the upper voltage level (the *blanked* state), and the target is read when the control signal is at the lower voltage level (the *un-blanked* state). For the Treatment mode the integration period set was 0.25 s, with one image acquired every 1.0 s.

For the Single mode of image acquisition (Figure 6-1, left), the camera target is in the blanked state when the trigger mechanism, which is based on sensing video signal against a threshold (Chapter 7.3), identifies initiation of the radiation beam. The charge distribution on the target is subsequently read when the beam is un-blanked (for a period of one frame), which is initiated by the video acquisition and control card following termination of accelerator exposure. For the Treatment Loop mode of image acquisition (Figure 6-1, right) the beam blank control signal undergoes repeated transition between the blanked and un-blanked states to form repeated periods of camera target integration, which results in a series of discrete images.

6.2.2 Recording accelerator MU during portal imaging

A technique was developed which allowed the number of 1/64th MU delivered by the Elekta SL15*i* to be identified every time the beam blanking control signal underwent a state change (*i.e.* blanking at the beginning of target integration or un-blanking at frame read). This allowed assessment of the number of 1/64th MU

delivered by the accelerator at the beginning and end of each period of image integration.

The beam blanking control signal was obtained via an isolated interface inserted between the CCU and the video acquisition and control card (Figure 6-2). The connection to the beam blanking control signal was optically isolated in order to provide ground isolation for the measurement system, and to protect the CCU and video acquisition and control card from any extraneous signals. On testing the interface it was observed to have no effect on the operation or timing of the Theraview imaging system. It was therefore left permanently *in situ* during normal imaging, allowing use at any time.

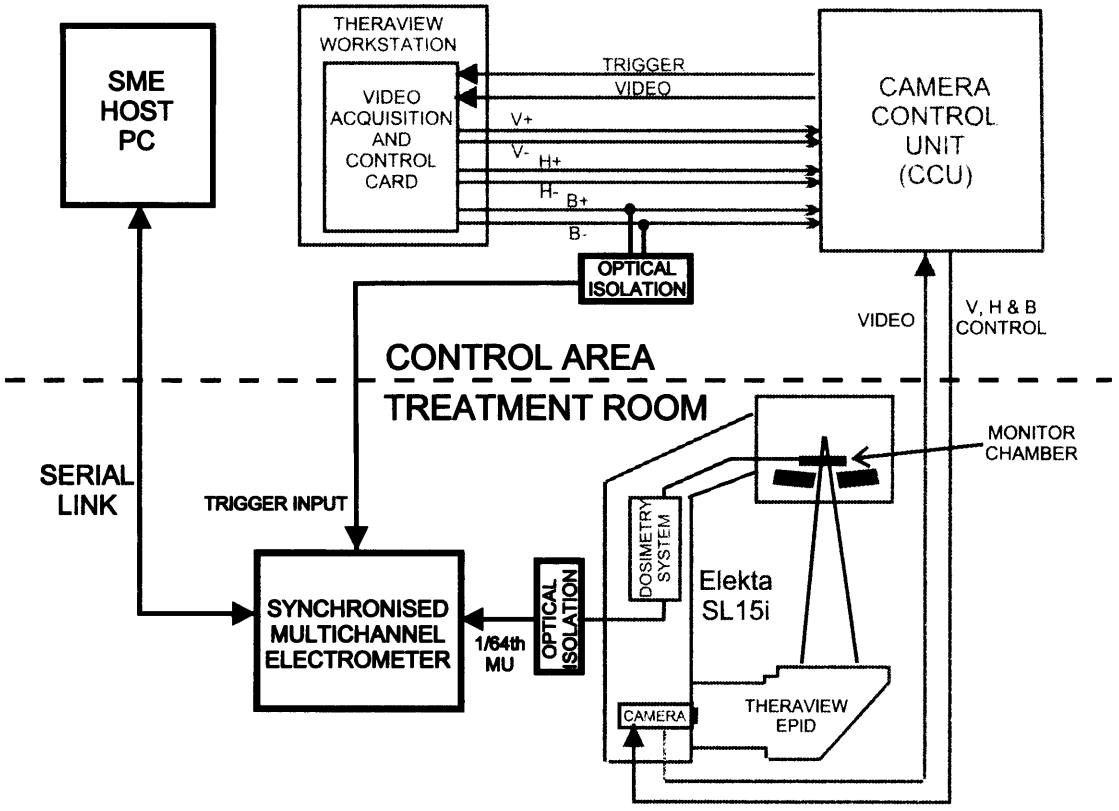

Figure 6-2: Interface to Theraview camera beam blanking control signal. All locally developed hardware is shown in darker print. The differentially driven control signals from the video acquisition and control card in the Theraview workstation are shown. V +/- and H +/- are frame and line synchronisation pulses, and B +/- is beam blanking.

The beam blanking control signal derived from the interface was connected to the 'trigger' input of the SME (Chapter 2) available for this purpose (Figure 6-2). This was achieved via a line driver, which took the signal from the treatment control area (where the CCU was located) to the SME (which was located in the treatment room as shown in Figure 6-2).

As discussed in Chapter 2.5, the SME continuously counts the cumulative $1/64^{th}$ MU value into a 16-bit dose register via an optically isolated interface to the accelerator dosimetry system providing $1/64^{th}$ MU pulses. An option was available within the SME software to read the cumulative accelerator $1/64^{th}$ MU value when a change in the status of the trigger was identified by means of the following software routine. During a repeating 10 ms time interval (provided by an available software timer), the status of the trigger was read at approximately 30 μs intervals. The dominant state for each 10 ms interval was identified and compared to the status of the *previous* 10 ms interval, in order to identify a *change* in status of the beam blanking control signal. On identifying a change in status, the SME stored the cumulative $1/64^{th}$ MU value held in the 16-bit dose register.

Following completion of the accelerator exposure, the $1/64^{th}$ MU data could be saved off-line to an ASCII file at the SME host PC. This file indicates the date and time of measurement, and the control signal transitions identified along with their corresponding $1/64^{th}$ MU values.

In addition to leaf tracking, the beam blanking control signal interface allowed assessment of the accelerator $1/64^{th}$ MU at which the EPID triggered under different geometries, which is of concern with this EPID for its application to dosimetry (Chapter 7.3). It was also possible to assess trigger reproducibility and long-term stability (Chapter 7.3).

6.2.3 DMLC example prescription

A 20.0 x 20.0 cm dynamic wedge formed by moving MLC leaves was used as a test prescription. The same prescription has been studied with the strip ionisation chamber array (Chapter 3.5.1). The sequence was delivered with 6 MV x-rays on the Elekta SL15*i* at 50 Hz PRF and a dose of 50 MU. The Theraview EPID was used to acquire a series of Treatment Loop images using a set integration period of 0.25 s, with images acquired at one second intervals. Measurements were performed at the minimum SDD (139.8 cm) with no attenuator present.

A leaf pair adjacent to the central axis was considered in this test case. An image of a static 10.0 x 10.0 cm field was taken in order to establish isocentre and pixel size. The leaf position in each image was identified using a maximum gradient edge detection algorithm (James *et al.* 2000).

6.3 Results

6.3.1 Recording accelerator MU during portal imaging

The software approach described, which is based on considering the status of the beam blanking control signal over 10 ms time intervals, was used in order to avoid multiple recording of accelerator $1/64^{th}$ MU following a transition of the signal. This was necessary to overcome spurious triggering associated with ringing introduced to the beam blanking control signal by the camera interface and cabling to the SME (*i.e.* the approach provided software *'de-bounce'*). Additionally, the approach removed erroneous $1/64^{th}$ MU recording associated with occasional, spurious signals of approximately 500 μs in duration identified on the trigger signal. However, the assessment of trigger status weighted over 10 ms intervals introduced potential software delay between a change in the status of the beam blanking control signal and recording

of the accelerator 1/64th MU. This occurs because the system completes a 10 ms interval before any decision on a change in status is made. The worst case delay was estimated as 15 ms based on 1½ intervals of 10 ms duration, corresponding to a transition mid-way during a 10 ms interval which may not be identified until the end of the following 10 ms interval. For the test case (50 Hz PRF), a 15 ms delay may introduce one further dose pulse (delivering approximately 0.022 MU) to the cumulative 1/64th MU value recorded. This results in a dosimetric error of up to 2/64th MU (*i.e.* 0.031 MU).

6.3.2 DMLC example prescription

The sequence of images acquired is shown in Figure 6-3. The maximum number of images acquired in such a sequence is 40, which is a limitation of the Theraview software used (version 2.3). Delivery of the entire prescription required a sequence of 48 images, and as a result the first eight images were over-written and are not available.

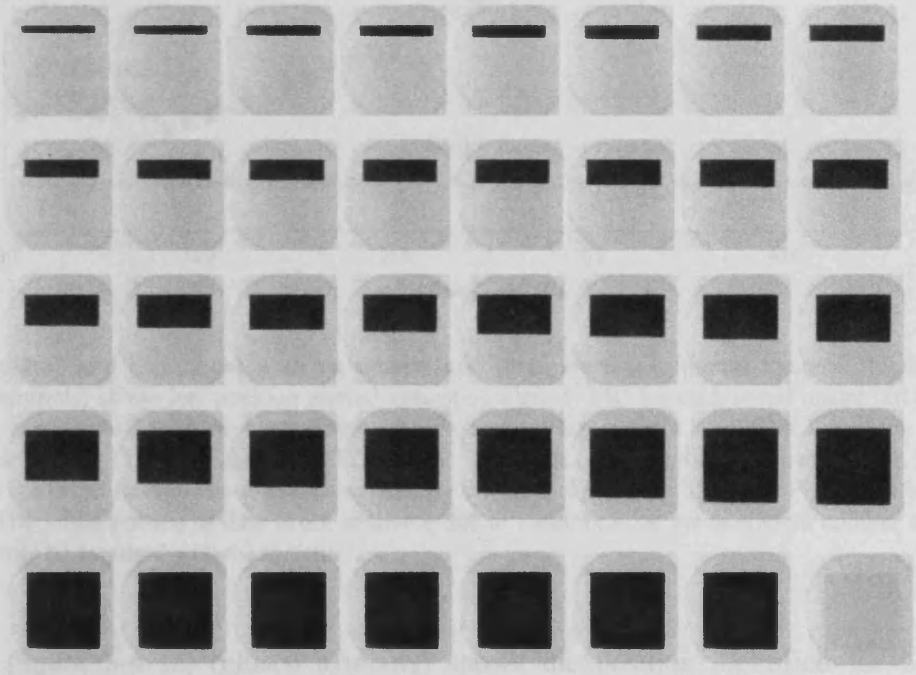

Figure 6-3: Sequence of Theraview images captured for a dynamic wedge using a 0.25 s integration period. The first image is top-left and images are shown in rows. The uppermost collimator is stationary and the lower moving. The final field size is 20.0 x 20.0 cm.

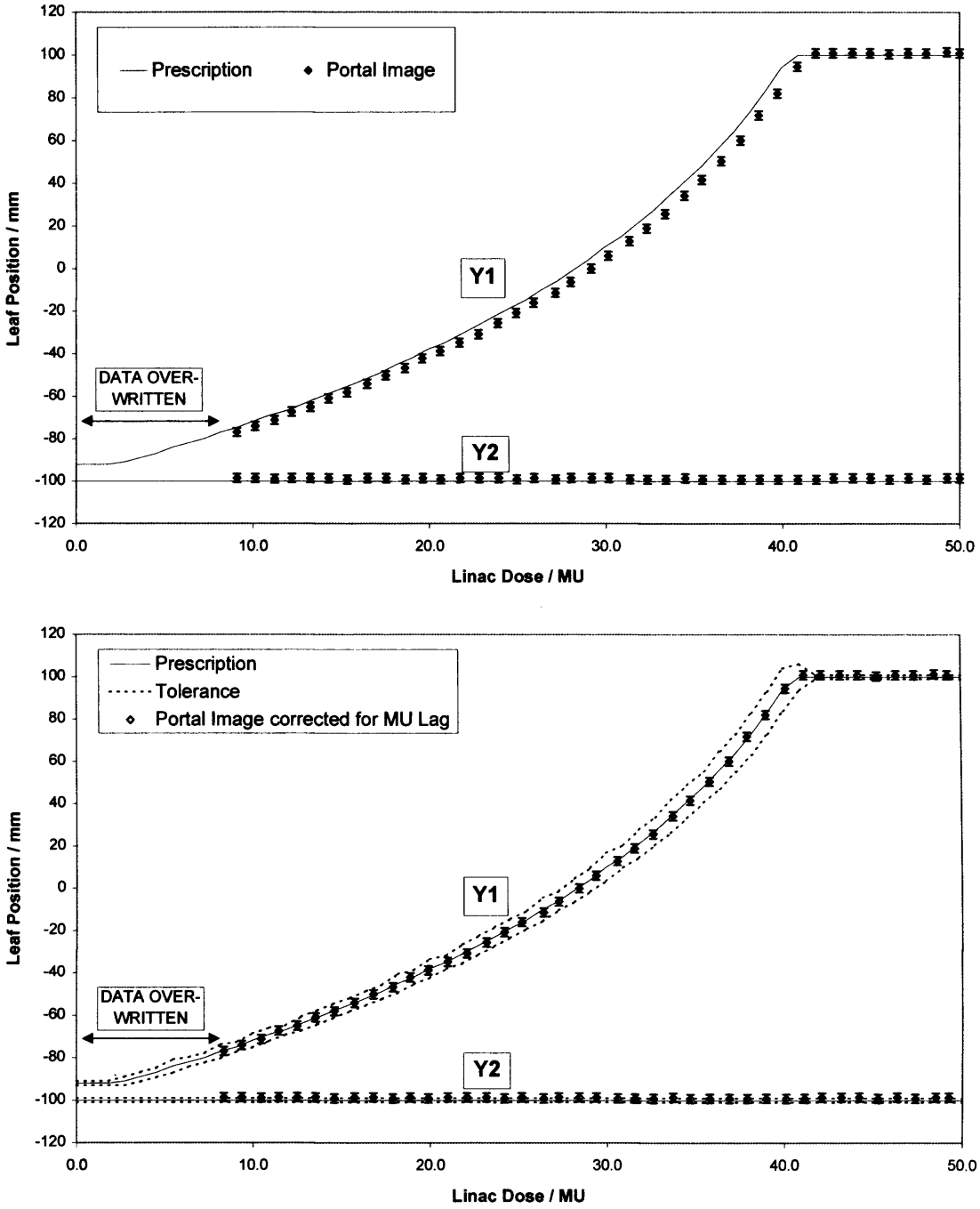

Figure 6-4(a) and (b): Leaf position determined from electronic portal images. Figure 6-4(a) (closed symbols) shows leaf position plotted against accelerator MU for each portal image. In Figure 6-4(b) the accelerator MU have been corrected for observed lag in the Elekta DMLC system. Data is shown for moving (Y1) and stationary (Y2) leaves. The DMLC prescription is shown in both Figure 6-4(a) and (b) (solid lines). The tolerance applied by the control system is shown in Figure 6-4(b) (dotted lines). The initial portion of data is not available due to constraints on the maximum number of images which could be acquired with the system.

Figure 6-4 (a) (closed symbols) shows the position identified for both the moving and stationary leaves (Y1 and Y2 receptively) plotted against accelerator MU for each image, based on a mean value of MU read at the beginning and end of each

period of image formation. The expected leaf positions from the DMLC prescription for the wedge are also plotted (solid lines). Leaf positions below 9 MU are not available due to limitations in the maximum number of images that could be acquired. The geometric accuracy, estimated as ± 2 mm (Chapter 5), is shown for each leaf position identified. The maximum dosimetric error of 0.031 MU (*i.e.* $2/64^{th}$ MU) is too small to be shown.

Figure 6-4(a) shows a systematic lag (or displacement) of the measured leaf position relative to that prescribed. The effect is more evident as leaf speed increases (*i.e.* as the Y1 leaf approaches its final position) and amounts to up to 10 mm. This is a function of the lag in the Elekta DMLC system, which has been quantified using the strip ionisation chamber array as 0.67 ± 0.08 s (Chapter 3.5.1.1). In Figure 6-4(b) (open symbols) the MU corresponding to each data point has been corrected for the MU delivered in the lag period (calculated as 0.73 MU based on an observed dose rate of 65.5 MU min^{-1}). The tolerance applied by the DMLC control system is also shown in Figure 6-4(b) (dotted lines). This is based on a tolerance for static fields of 1 mm, and for dynamic fields a tolerance of 2 - 10 mm is based on a maximum dose error of 2 %. On introducing the correction for lag there is agreement to within ± 2 mm between the prescribed and measured leaf positions.

6.4 Discussion

The approach presented here to identify accelerator MU corresponding to a sequence of portal images acquired using the commercial Theraview EPID differs from the approach of Partridge *et al.* (2000a), who used a dose display within the field of view of the EPID. Although the approach of Partridge *et al.* (2000a) is suitable for implementation with other camera-based EPIDs, finite camera acquisition periods may

place some dose resolution limitations for high accelerator dose rates or long integration periods. This is the case both for systems which perform camera target integration (such as Theraview) or for those which perform frame addition (such as the SRI-100). The approach described in this work offers improved resolution of accelerator MU, but clearly requires knowledge of camera operation and may not be suitable for all camera systems or operating software. The approach also avoids reduction of the EPID's field of view associated with a dose display, and in addition the approach does not require modification of the commercial imaging system.

The technique described also provides accelerator $1/64^{th}$ MU values directly, *i.e.* it does not require interpretation of images encoded with this information (as in the case of Partridge *et al.* 2000a). Furthermore, the approach does not require modification of the commercial hardware since the optically isolated interface simply locates in-line between the video acquisition and control card in the Theraview workstation and the CCU.

A maximum software delay of 15 ms was estimated between a change in the status of the camera control signal and recording the accelerator $1/64^{th}$ MU value. This is associated with the need to remove multiple recording of accelerator $1/64^{th}$ MU following a transition of the beam blanking control signal (*i.e.* 'de-bounce') based on an available 10 ms. A shorter timer was not possible due to limitations of the present SME system, but this could be improved by implementation of this 'de-bounce' function in hardware should this be considered necessary. For the 50 Hz test case, the delay introduces a dosimetric error of up to $2/64^{th}$ MU (*i.e.* 0.031 MU). For the highest PRF available on the accelerator (400 Hz), the maximum delay corresponds to only $10/64^{th}$ MU (*i.e.* 0.16 MU). However, implementation of de-bounce in hardware would also allow simultaneous multi-channel electrometer operation of the SME whilst

recording MU data using the trigger input described with *no additional latency*. In the current implementation it was not possible to operate the multi-channel dose signal collection mode of the SME simultaneously with recording of accelerator $1/64^{th}$ MU, triggered by the beam blanking control signal, due to additional software delay of variable magnitude (estimated maximum 80 ms).

The 16-bit dose register of the SME, which counts the cumulative accelerator $1/64^{th}$ MU, imposes a maximum number of $1/64^{th}$ MU of $2^{16} = 65{,}536$ (*i.e.* 1024 MU). This is not a limitation for clinical DMLC cases. The maximum number of images that could be acquired for the implementation of Theraview software used was only 40, which led to omission of some data from the test case studied. For clinical implementation it would be necessary to increase the number of images which could be acquired by the commercial system.

For application to on-line verification, the prescribed collimator position (based on recorded $1/64^{th}$ MU) would require overlaying on each image. James *et al.* (2000) have presented this approach for the SRI-100 using a limited number of images.

It is interesting to note a horizontal banding artefact evident in the images acquired at 50 Hz PRF. Figure 6-5 shows an image from the sequence in Figure 6-3. The image has been enhanced using the histogram equalisation facility of the commercial Theraview software, and clearly demonstrates horizontal banding. In the un-enhanced image there is a transition in pixel values of approximately 2 % between the band regions.

Figure 6-5: Horizontal banding artefact on a portal image acquired at 50 Hz PRF. The image shown is the penultimate one of the sequence in Figure 6-3 and has been enhanced to show the artefact.

The artefact is due to the pulsed nature of the radiation source (and hence the pulsed nature of light emission from the phosphor) in combination with read-out of the camera target *during* irradiation. The phenomenon is not evident for Single image mode in which the camera target is read out *after* irradiation. However, for Treatment Loop mode, which has been used to image the dynamic sequence presented, radiation pulses occur during camera read-out (duration 33.3 ms). In the case of 50 Hz PRF, pulses occur every 20 ms which results in 1 or 2 radiation pulses being delivered during every read-out period. As the target is read out, radiation pulses result in charge on areas of the camera target already read at that moment. This contributes to the following frame. Similarly, as a frame is being read, regions towards the end of the target receive additional charge due to further pulses. The combined effect is step changes in the charge levels on the camera target resulting in a banding artefact, which

appears to move systematically from one image to the next due to image acquisition and PRF being asynchronous. The effect is not evident at 400 Hz PRF, but becomes increasingly evident at reduced PRF, since the number of pulses per image reduces. This results in the banding fluctuations becoming more pronounced, and in addition the time between pulses (and hence distance between bands) becomes greater. The artefact has also been described by Rajapakshe *et al.* (1993) and observed in clinical use of a Siemens EPID (Girouard *et al.* 1998).

In conclusion, a method for recording accelerator MU during the acquisition of portal images by the commercial camera-based Theraview EPID has been presented. The approach uses a customised, optically isolated interface to the beam blanking camera control signal as a trigger to record the number of MU delivered by the accelerator at the beginning and end of each period of image formation. The method of recording accelerator MU allows application of the EPID to the verification of collimator position in DMLC. This has been demonstrated using a dynamic wedge test prescription. The current implementation has a maximum delay of 15 ms between a change in the status of the camera control signal and recording of the accelerator MU value. This could be improved with implementation in hardware. The customised interface had no effect on the operation of the commercial EPID, and could therefore be left permanently *in situ* during normal clinical use. The technique described uses a specific camera-based EPID and accelerator, although the general principle of using an EPID control signal to trigger recording of accelerator MU may be applicable to other EPIDs/accelerators with suitable knowledge of the accelerator dosimetry system.

Chapter 7. Application of a tube camera-based electronic portal imaging device to integrated dose measurement during dynamic multileaf collimation

7.1 Introduction

EPIDs are also being considered for measurement of the integrated dose distribution delivered by a DMLC. The group in Rotterdam has extended their work on portal dosimetry with the SRI-100 (Heijmen *et al.* 1995) to DMLC verification (Pasma *et al.* 1998, 1999b). Studies using the PortalVision system to verify multiple-static field IMRT have also been reported by Curtin-Savard & Podgorsak (1999) in Quebec (Canada). Images were acquired of each segment, and once converted to dose distributions, were added by weighting with appropriate MU values. Measurements were performed behind sheets of phantom material placed directly on the imager, and compared to treatment planning system calculations (Varian Cadplan). Beam profile measurements using a diode array agreed to within ±2 mm for isodoses in steep dose gradients and within ±2 % elsewhere. Similar work in progress in Denmark is reported by Murmann *et al.* (1999). Studies of DMLC have also been performed with the Mark I PortalVision (Chang *et al.* 1998, 2000) where the slow (9.0 s) acquisition time was overcome by increasing MU nine-fold, and thus reducing leaf speeds by this factor. In this way, an acquisition rate of one image per second was simulated. Images were summed and converted to a dose distribution from which profiles were considered. Following point-by-point subtraction against the intended profile, a standard deviation was calculated as a 'goodness of match' parameter. For uniform phantom studies of prostate treatments, the average standard deviation was 3.3 % compared to values of >5.0 % for a 3.0 mm isocentre displacement, 24 % for incorrect use of asymmetric jaws

and 27 % for a frozen leaf. Chang *et al.* (2000) concluded that a 'pass' level for this parameter could be set and used as the basis for pre-treatment quality assurance.

The use of the Theraview EPID for measurement of integrated dose distributions from the summation of images acquired during dose delivery is the subject of this chapter. Having considered the basic properties of the Theraview EPID relevant to dosimetry applications in Chapter 5, and confirmed the absence of afterglow from the phosphor at therapy dose levels in Chapter 4, this chapter considers the suitability of the Theraview system for dose integration during DMLC. This includes an evaluation of the system for dose integration, study of the mechanism of triggering image acquisition and its suitability for such applications, correction for non-ideal optical transport within the imaging chain and correction for spatial non-uniformity. Finally, dose measurements are compared with ionisation chamber data for static and DMLC fields.

7.2 Characteristics of a tube camera for dose integration

7.2.1 'Latent' image correction

The Theraview EPID used for this work exhibited a fixed, spatially non-uniform background image on which acquired images were superimposed. The background image was termed a 'latent' image and was evident for all images acquired with the system. The latent image could be acquired using the 'Single' image mode by interrupting the accelerator prior to delivery of any radiation. This forced the EPID to acquire a single frame of video in the absence of any radiation signal.

Repeated latent images were observed to be extremely reproducible. After a period of 115 days, the difference in pixel values between two latent images formed from the mean of several images was 0.6 ± 0.1 (± SD). Such stability allowed

correction of all dosimetry images acquired with the system by subtraction of a mean latent image, Figure 7-1.

The existence of the latent image was thought to be attributable to a spatially variant background video level (which represents the absolute black level of the camera). This is likely to be attributable to properties and limitations of the imaging system (camera target, camera and CCU).

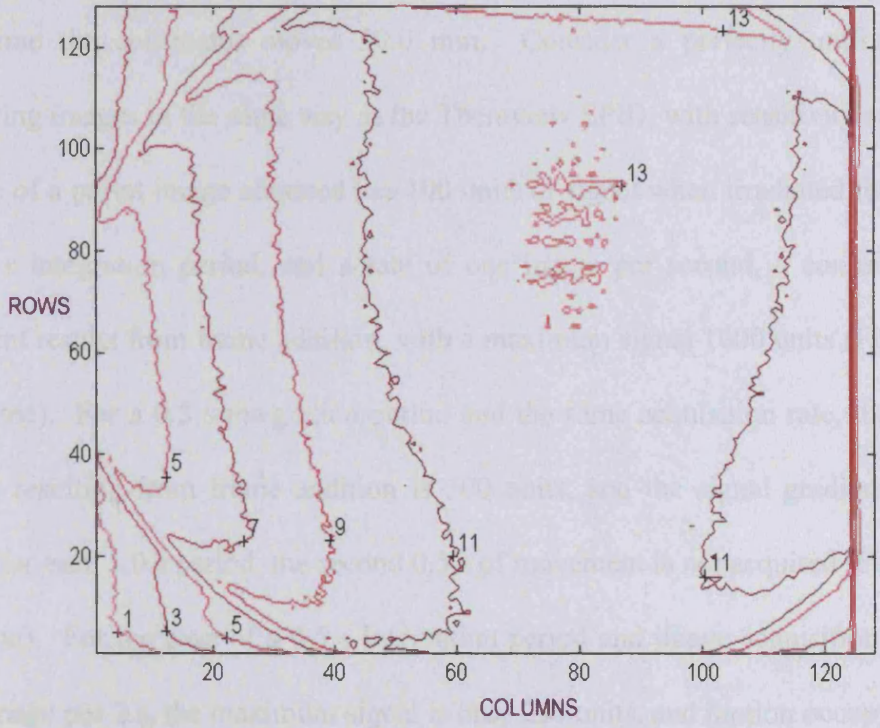

Figure 7-1: Mean 'latent' image plotted as contours of equal pixel value. The original 512 x 512 image matrix has been reduced to 128 x 128 for clarity.

7.2.2 Limitations on duty cycle

The operation of the tube camera has been described in Chapters 5 and 6, together with a description of the image acquisition modes (Table 5-1). The limited dose range below pixel saturation evident from the dose response studies (Chapter 5) imposes a limitation, dependent on incident dose rate, on the maximum integration period which can be used in Treatment Loop imaging. Often this may require an

integration period less than the time interval between images for typical patient thickness, PRFs and SDDs. Consequently, a series of images acquired using this mode will not always be contiguous in time (*i.e.* the duty cycle will be less than 100 %), so that integration of the entire dose delivered cannot be achieved by frame addition.

The effect of duty cycles less than 100 % on the result of frame addition for a dynamic prescription can be assessed by modelling. Consider the case of a dynamic wedge moving at 5.0 mm s^{-1} whilst acquiring images over a period of 10.0 s. During this time the collimator moves 50.0 mm. Consider a perfectly uniform detector acquiring images in the same way as the Theraview EPID, with sensitivity such that any region of a portal image obtained has 100 units of signal when irradiated for 1.0 s. For a 1.0 s integration period, and a rate of one image per second, a continuous signal gradient results from frame addition, with a maximum signal 1000 units (Figure 7-2(a), blue line). For a 0.5 s integration period and the same acquisition rate, the maximum signal resulting from frame addition is 500 units, and the signal gradient is stepped since for each 1.0 s period, the second 0.5 s of movement is not acquired (Figure 7-2(a), red line). For the case of a 0.5 s integration period and image acquisition at a rate of one image per 2 s, the maximum signal is only 250 units, and motion occupying 1.5 s is omitted from each imaging cycle (Figure 7-2(a), green line). Figure 7-2(b) shows the effect of normalising the curves to the maximum signal level.

Although the exact effect of reduced integration periods or reduced acquisition rates will clearly depend on the collimator speeds involved and the number of frames added, Figure 7-2 clearly demonstrates deviations from the true gradient, which cannot be avoided with this approach. In their application of the Theraview EPID to DMLC verification by integrated dose measurement, Partridge *et al.* (2000a) recommend operating the EPID at the maximum acquisition rate (*i.e.* one image per second), and

have described the effect of reduced integration periods as a 'sampling error'. Chang *et al.* (2000) confirmed that sampling is also of concern for PortalVision, although an acquisition rate of one image per second is sufficient to reconstruct dose profiles under normal treatment conditions (200-300 MU min^{-1}, 100-150 MU). However, they state that it is unlikely to be sufficient for fast moving leaves (20-30 mm s^{-1}) or steep dose gradients (*e.g.* penumbra).

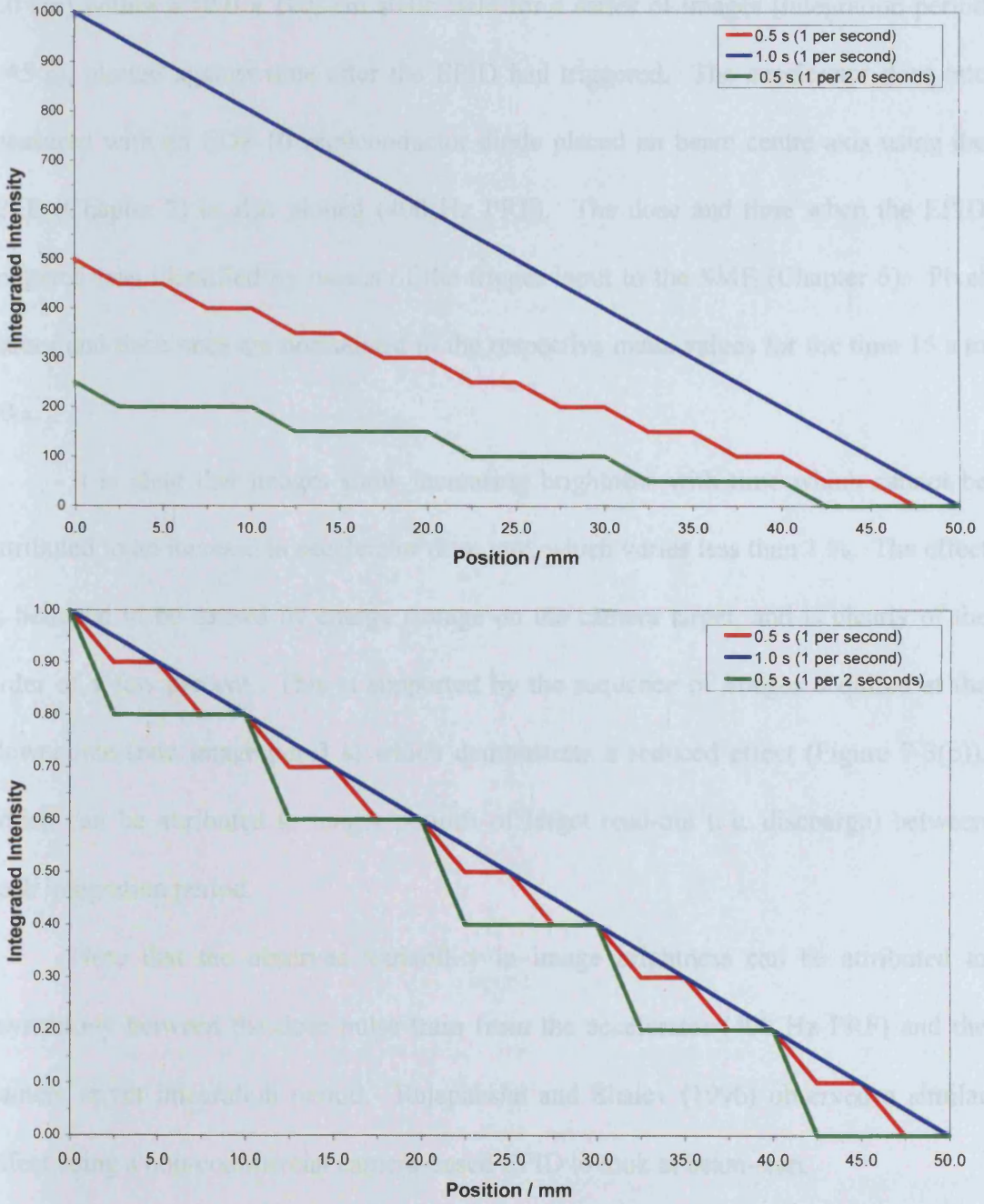

Figure 7-2(a) and (b): Modelled effect of integration period and acquisition rate on intensity profile resulting from frame addition for test case of a 5 mm s^{-1} dynamic wedge. Figure 7-2(b) shows the data normalised to the maximum signal intensity in each case.

7.2.3 Effect of charge storage on camera target

The effects of charge storage on the target of the tube camera, identified for 'Single' images in Chapter 5, have also been observed in 'Treatment Loop' images acquired during continuous irradiation, and this must be considered for DMLC imaging.

7.2.3.1 Static fields

Figure 7-3(a) shows the normalised mean pixel value for a central ROI (1.0 x 1.0 cm) within a 10.0 x 10.0 cm static field for a series of images (integration period 0.45 s), plotted against time after the EPID had triggered. The accelerator dose rate measured with an EDP-10 semiconductor diode placed on beam centre axis using the SME (Chapter 2) is also plotted (400 Hz PRF). The dose and time when the EPID triggered was identified by means of the trigger input to the SME (Chapter 6). Pixel values and dose rates are normalised to the respective mean values for the time 15 s to 20 s.

It is clear that images show increasing brightness with time which cannot be attributed to an increase in accelerator dose rate, which varies less than 1 %. The effect is believed to be caused by charge storage on the camera target, and is clearly of the order of a few percent. This is supported by the sequence of images acquired at the slower rate (one image per 3 s) which demonstrate a reduced effect (Figure 7-3(b)), which can be attributed to longer periods of target read-out (*i.e.* discharge) between each integration period.

Note that the observed variability in image brightness can be attributed to asynchrony between the dose pulse train from the accelerator (400 Hz PRF) and the camera target integration period. Rajapakshe and Shalev (1996) observed a similar effect using a non-commercial camera-based EPID to look at beam-start.

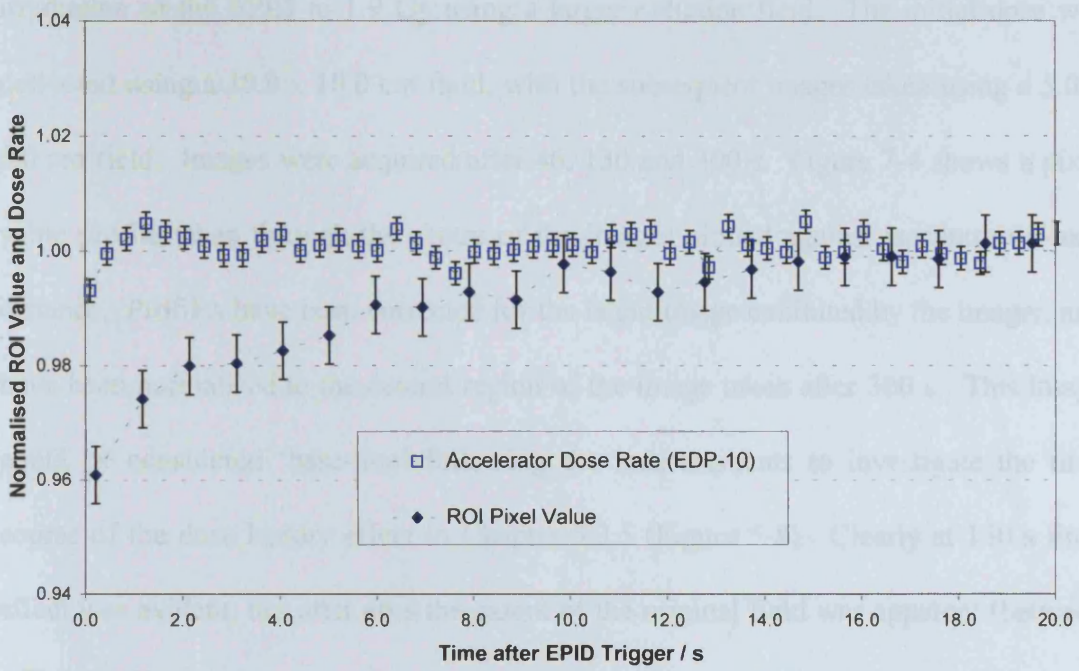

Figure 7-3(a): Normalised pixel values and accelerator dose rate during 20.0 s of data collection. The integration period was 0.45 s. The dose and time at which the EPID triggered was measured using the EPID trigger input facility of the SME. ROI values are plotted against the time representing the middle of each integration period. The accelerator dose rate was measured by an EDP-10 diode using the SME. Data sets are normalised to the period 15 to 20 s.

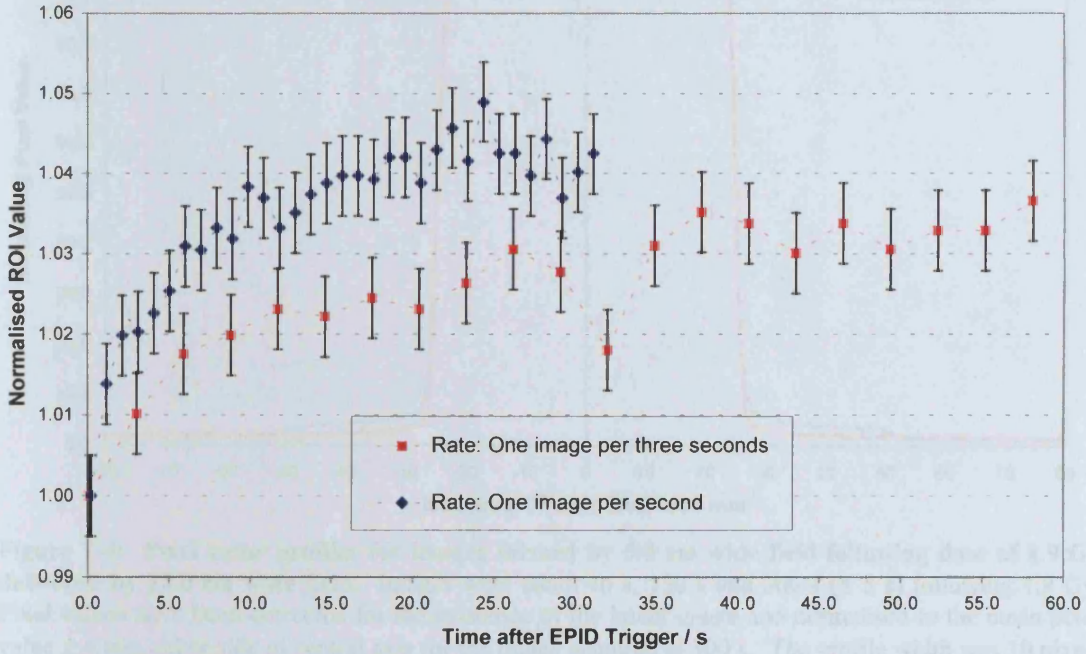

Figure 7-3(b): Effect of acquisition rate on normalised pixel values. Data shown in Figure 7-3(a) are plotted as "Rate: One image per second". A second series of images acquired at a rate of one image per 3 s is also plotted over almost 60 s. Data sets are normalised to the first image acquired in each sequence.

The existence of charge storage on the camera target introducing image lag was further demonstrated by acquiring a 'Single' image of a radiation field following

irradiation of the EPID to 1.9 Gy using a larger radiation field. The initial dose was delivered using a 10.0 x 10.0 cm field, with the subsequent images taken using a 5.0 x 5.0 cm field. Images were acquired after 46, 130 and 300 s. Figure 7-4 shows a pixel value profile taken through the centre of the images plotted against isocentre off-axis distance. Profiles have been corrected for the latent image exhibited by the imager, and have been normalised to the central region of the image taken after 300 s. This image could be considered 'base-line' following the measurements to investigate the time course of the dose history effect in Chapter 5.3.5 (Figure 5-8). Clearly at 130 s little effect was evident, but after 46 s the extent of the original field was apparent (between ±50 mm off-axis).

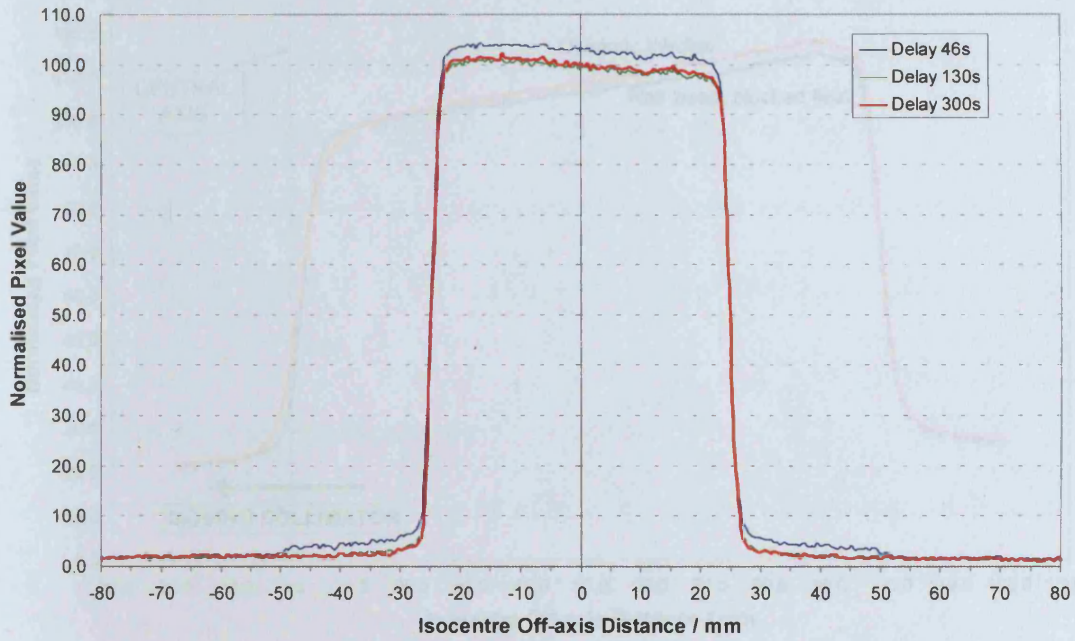

Figure 7-4: Pixel value profiles for images formed by 5.0 cm wide field following dose of 1.9 Gy delivered by 10.0 cm wide field. Images were taken 46 s, 130 s and 300 s (± 5 s) following 1.9 Gy. Pixel values have been corrected for the existence of the latent image and normalised to the mean pixel value ± 4 mm either side of central axis for the image acquired at 300 s. The profile width was 10 pixels (approximately 5 mm).

For the profile data shown, within ± 23 mm either side of central-axis (*i.e.* within the 5.0 cm field), pixel values for the image at 46 s are enhanced by a mean value of 2.8 ± 0.3 %. Within the regions between 26 mm and 50 mm off-axis (*i.e.* in

the region between the 5.0 and 10.0 cm wide fields), pixel values are enhanced by a mean value of 2.2 ± 0.4 %. The magnitude of this effect is consistent with the effect reported in Chapter 5.3.5.

7.2.3.2 Dynamic wedge field

The effect of charge storage on the camera target was also studied using a sequence of images acquired during delivery of the dynamic wedge studied for collimator position verification in Chapter 6. The accelerator dose rate was 68 MU min^{-1}, and a total dose of 50 MU was delivered. The EPID was at 139.8 cm SDD, and 6.0 g cm^{-2} of water equivalent attenuator (PMMA) were placed at 100.0 cm SSD. An integration period of 1.0 s was used, with one image being acquired each second.

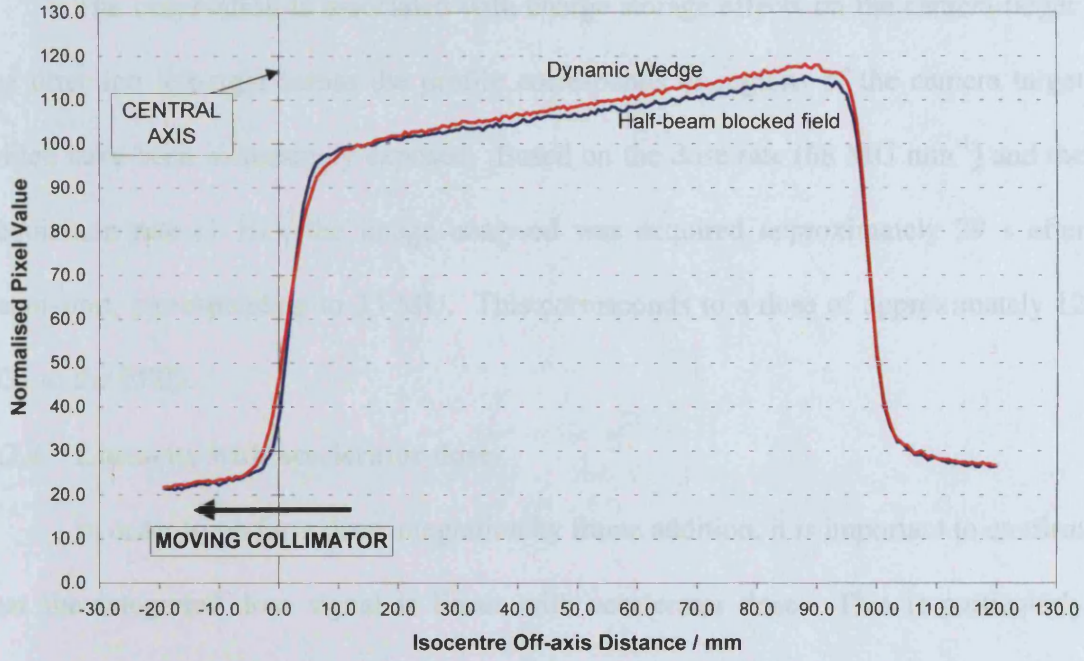

Figure 7-5: Pixel value profiles for images of dynamic wedge and half-beam blocked field. The moving collimator (corresponds to the left-hand field edge) was moving from right to left. Images have been corrected for the existence of the latent image, and are normalised to the off-axis distance +15mm.

An image from the sequence acquired corresponding closely to that created by a half-beam blocked field was considered (*i.e.* an image where the moving collimator was aligned to central axis). Following a delay of a few minutes after delivery of the dynamic wedge, images of the corresponding half-beam blocked field were acquired

using the same accelerator and EPID parameters. Figure 7-5 shows pixel value profiles drawn through the centre of the detector field of view in the direction parallel to collimator motion.

The pixel value profiles in Figure 7-5 have been corrected for the existence of the latent image, and normalised at the off-axis distance + 15 mm. Clearly the dynamic wedge appears to show a greater dose rate increase off axis than the half-beam blocked field. The difference between the profiles increases with off-axis distance, and in the region 80.0 - 90.0 mm off-axis the mean increase is 2.5 ± 0.3 %. If such an image sequence were used for frame addition in order to use the images for the measurement of a dose profile, a corresponding error would result in the measured wedge gradient.

The observation is associated with charge storage effects on the camera target: the direction left-right across the profile corresponds to regions of the camera target which have been increasingly exposed. Based on the dose rate (68 MU min^{-1}) and the acquisition rate (1 Hz), the image analysed was acquired approximately 29 s after beam-start, corresponding to 33 MU. This corresponds to a dose of approximately 12 cGy to the EPID.

7.2.4 Linearity with accelerator dose

In order to perform dose integration by frame addition, it is important to confirm that the integrated dose signal is linear with accelerator dose. This is particularly important because of the contribution of charge storage effects to the apparent dose signal when performing frame addition for dose integration.

In order to assess the linearity of the total dose signal against the accelerator MU setting, a series of exposures were made over the range 5–300 MU and captured using the 'Treatment Loop' imaging mode. The SDD was 165.2 cm, and 35.9 g cm^{-2} of water equivalent phantom (PMMA and WT1) was placed at 100 cm SSD. The field size was

5.0 x 5.0 cm, and a camera target integration period of 1.00 s was used. This gave pixel values of approximately 145 which was well below the saturation level evident for the system (which was presented in Figure 7-15). A maximum number of 38 images were acquired for the 300 MU exposure. ROI analysis was performed using the ROI described in Chapter 7.2.3. ROI values were summed for all images acquired for each exposure, and corrected for the latent image. Figure 7-6 shows the total ROI value plotted against accelerator MU.

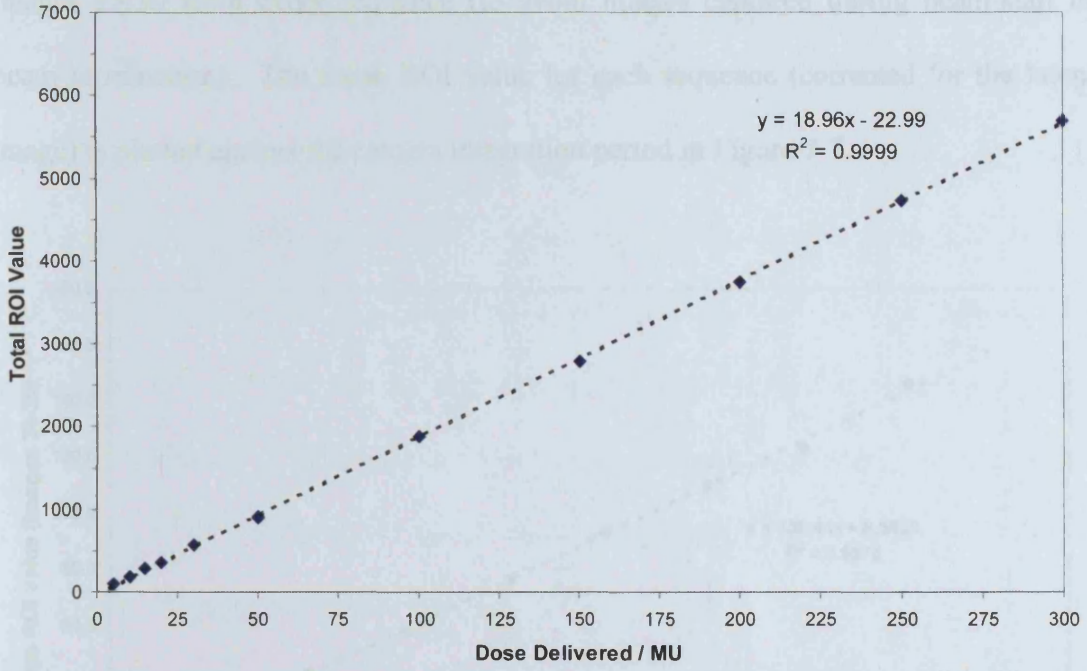

Figure 7-6: ROI values summed for sequences of images acquired for exposures of 5 - 300 MU. Uncertainties are too small to be shown (SD 0.7 % and 0.2 % respectively for repeat exposures of 20 and 50 MU).

The observed characteristic is clearly very linear, *i.e.* the integrated image formed by frame addition is linear with delivered dose. Close inspection of each sequence of images confirmed that they all exhibited the characteristics of charge storage (Figure 7-3). Repeat exposures made for 20 MU and 50 MU showed the total ROI value to be very reproducible, with standard deviations of 0.7 % and 0.2 % respectively.

7.2.5 Effect of adjusting camera target integration period

Further measurements were performed using the same geometry as in the previous section (Chapter 7.2.4) for a series of 300 MU exposures in which 'Treatment Loop' images were acquired using a range of integration periods (0.25, 0.37, 0.50, 0.62, 0.75, 0.87 and 1.00 s). This covered the range of possible integration periods for an image rate of 1 Hz, and gave pixel values well below saturation (Figure 7-15).

Each image sequence comprised 38 images. ROI analysis was performed on images 25-30 from every sequence (to avoid images captured during beam-start or beam termination). The mean ROI value for each sequence (corrected for the latent image) is plotted against the camera integration period in Figure 7-7.

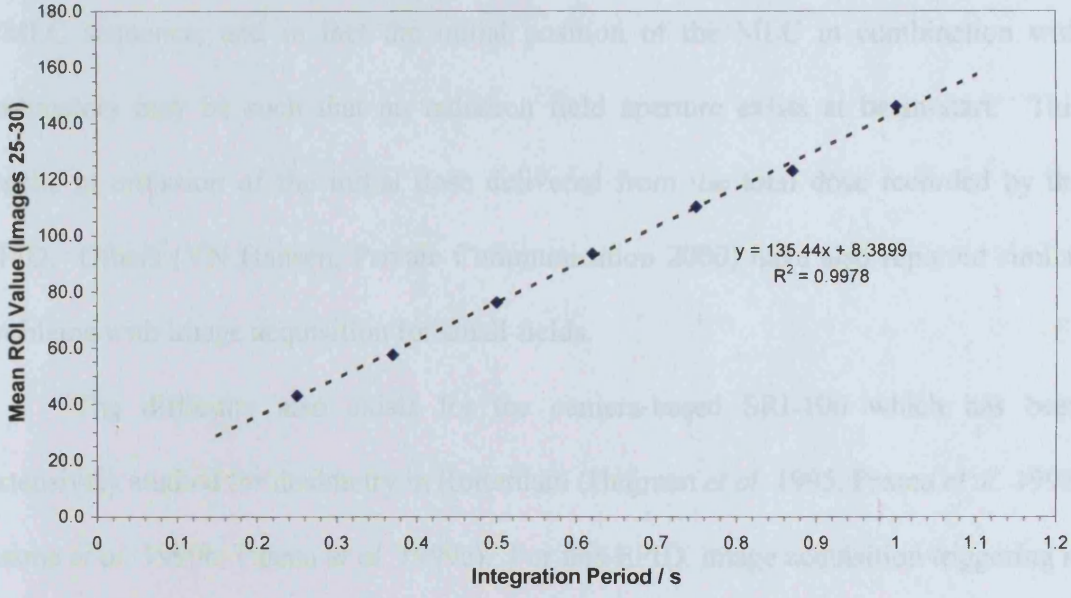

Figure 7-7: Mean ROI values for images acquired with camera target integration periods of 0.25-1.00 s. Standard deviations, at most 0.4 %, are too small to be shown.

Clearly image brightness increases linearly with integration period, which corresponds to a linear increase in pixel value with dose delivered during the integration period (assuming no changes in dose rate between the repeated exposures).

7.3 Controlling image acquisition for dose integration

7.3.1 Introduction

In order to use an EPID to derive the integrated dose distribution delivered by a DMLC sequence, image acquisition must begin sufficiently early to ensure that the entire irradiation sequence is captured in order to allow assessment of the *total* dose distribution. For the Theraview EPID, configured for an Elekta linear accelerator, image acquisition is initiated by transition of the video signal originating from a central region of the camera's field of view over a threshold (Chapter 5). However, in studies of the application of this EPID to the verification of DMLC, the device has been observed to trigger unreliably when the initial irradiated region is small and displaced from the central region. Such radiation geometries are common at the beginning of a DMLC sequence, and in fact the initial position of the MLC in combination with collimators may be such that no radiation field aperture exists at beam-start. This results in omission of the initial dose delivered from the total dose recorded by the EPID. Others (VN Hansen, Private Communication 2000) have also reported similar problems with image acquisition for small fields.

The difficulty also exists for the camera-based SRI-100 which has been extensively studied for dosimetry in Rotterdam (Heijmen *et al.* 1995, Pasma *et al.* 1998, Pasma *et al.* 1999b, Pasma *et al.* 1999c). For this EPID, image acquisition triggering is achieved by a similar mechanism to that for the Theraview EPID. To overcome the associated problem in the application of the SRI-100 to integrated dose measurements of DMLC, Pasma *et al.* (1998, 1999b) have reported starting acquisition manually. Manual control of image acquisition is also required for the BIS 700 (Wellhöfer Dosimetrie) (R Plompen, Private Communication 2000) used by Ma *et al.* (1997) for verification of the integrated dose distribution produced by DMLC. However, for the

implementation of such techniques it is desirable for image capture to be fully automated. In addition manual override may not always be possible, which is the case for the Theraview EPID.

One approach to initiating image acquisition is by direct connection to the dosimetry system of the accelerator. The camera-based EPID marketed by Elekta (*i*View™) has this modification (MC Kirby, Private Communication 2000). This clearly allows image acquisition to be achieved reliably even in the case of no radiation aperture at beam-start. The method proposed here is an alternative approach to ensure that all of the radiation delivered by the accelerator is captured by the EPID. The proposed approach is completely *independent* of the accelerator, having the advantage of not requiring connection to the accelerator dosimetry system.

7.3.2 Effect of field size on image acquisition triggering

Using the external trigger input of the SME it was possible to assess the accelerator dose, in $1/64^{th}$ MU, when image acquisition of the Theraview EPID was triggered. This facility of the SME, which has been described in Chapter 6, allowed recording of the cumulative accelerator $1/64^{th}$ MU value as the camera target was blanked.

Figure 7-8 shows the mean accelerator dose (±SD) at triggering for field sizes 5.0 x 5.0, 10.0 x 10.0 and 20.0 x 20.0 cm. Measurements were performed at 400 Hz PRF, with 165.2 cm SDD and 20.0 cm water equivalent plastic (WT1) at 100.0 cm SSD. Measurements were also repeated after introducing a light control screen immediately behind the phosphor screen. This screen has been evaluated as a means of reducing optical scatter in dosimetry measurements with the EPID (Chapter 7.5).

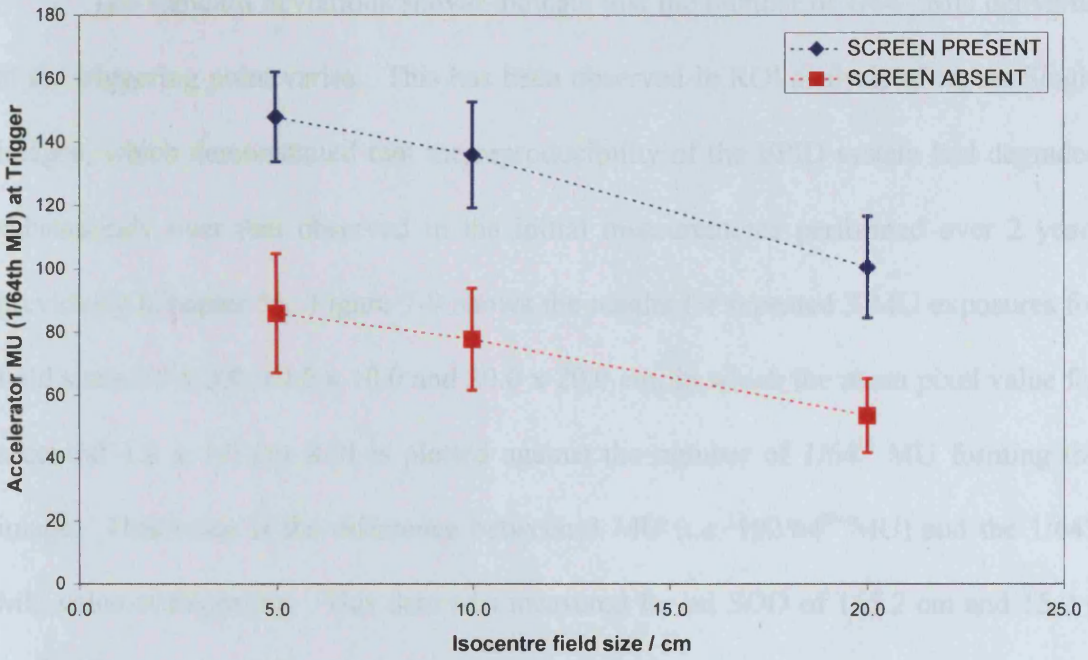

Figure 7-8: Effect of field size and light control screen on accelerator MU at triggering of image acquisition. The field sizes shown correspond to square fields.

Figure 7-8 clearly shows that as the field size reduces, larger doses are delivered before the EPID triggers, *i.e.* on reducing field size triggering is delayed. This is to be expected since the amplitude of video signal (on which the trigger mechanism is based) will reduce with field size due to both output factor dependency *and* reduced optical scattering. On introducing the light control screen, triggering is delayed further. The existence of trigger delay when using the screen has been identified in integrated dose measurements of a dynamic sequence (Chapter 7.5).

It should be noted that the delay between a change in status of the beam blanking control signal of the EPID camera and recording accelerator $1/64^{th}$ MU has been estimated at 15 ms maximum (Chapter 6). For the data in Figure 7-8 this corresponds at most to 0.13 MU (based on the variation in $1/64^{th}$ MU recorded with the SME during beam-start). This is smaller than the standard deviations based on repeat measurements at each field size (0.18 – 0.30 MU), which are indicated by the error bars shown in Figure 7-8.

The standard deviations shown indicate that the number of 1/64th MU delivered at the triggering point varies. This has been observed in ROI analysis of repeat Single images, which demonstrated that the reproducibility of the EPID system had degraded substantially over that observed in the initial measurements performed over 2 years previously (Chapter 5). Figure 7-9 shows the results for repeated 3 MU exposures for field sizes 3.0 x 3.0, 10.0 x 10.0 and 20.0 x 20.0 cm, in which the mean pixel value for a central 1.0 x 1.0 cm ROI is plotted against the number of 1/64th MU forming the image. This value is the difference between 3 MU (*i.e.* 192/64th MU) and the 1/64th MU value at triggering. This data was measured for an SDD of 165.2 cm and 15.9 g cm^{-2} attenuator (at 100.0 cm SSD).

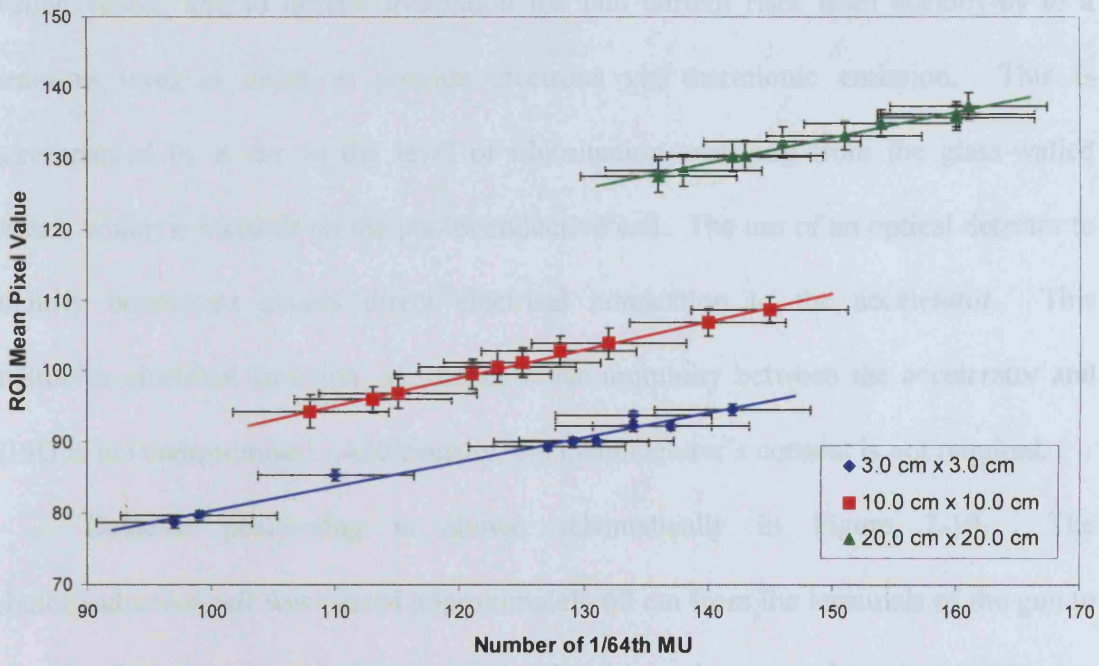

Figure 7-9: Plot of ROI mean pixel value against number of 1/64th MU for repeat 3 MU exposures. Data is shown for field sizes 3.0 x 3.0, 10.0 x 10.0 and 20.0 x 20.0 cm.

There is considerable variability in the pixel value for 3 MU exposures of a given field size. However, in each case there is very good correlation between pixel value and the dose delivered *after* image acquisition was triggered. It was therefore concluded that the increased variability in pixel value for a sequence of repeat

exposures was associated with increased variability in triggering of image acquisition. The phenomenon was observed on two EPID systems, and was thought to be associated with camera degradation causing increased video noise, to which the trigger mechanism is susceptible.

7.3.3 Proposed method for controlling image acquisition

7.3.3.1 Materials and Methods

The proposed means of detecting beam-start (and thus initiating portal image acquisition) is based on the use of a simple photoconductive cell (ORP-12, Silonex Inc., Plattsburgh, NY, USA) placed near the electron gun of the Elekta SL15*i* accelerator (Figure 7-10). For the Elekta linac the electron gun is conveniently housed in a glass-walled vessel, and to initiate irradiation the gun current rises from standby-by to a beam-on level in order to provide electrons via thermionic emission. This is accompanied by a rise in the level of illumination emerging from the glass-walled vessel, which is incident on the photoconductive cell. The use of an optical detector to identify beam-start avoids direct electrical connection to the accelerator. This maintains electrical isolation, and hence noise immunity between the accelerator and EPID is not compromised. Additionally, the manufacturer's consent is not required.

Detector positioning is shown schematically in Figure 7-10. The photoconductive cell was placed approximately 60 cm from the terminals of the gun to provide adequate separation for electrical safety (since the exposed terminals of the gun are pulsed at –37 kV during each radiation pulse).

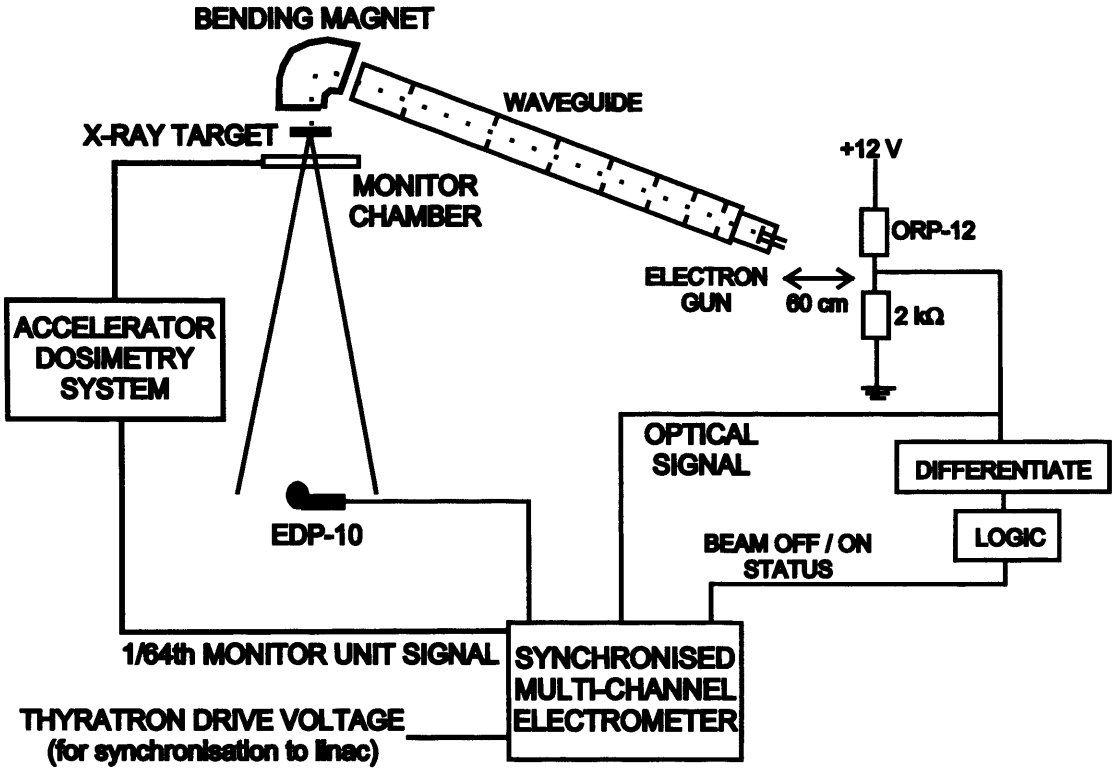

Figure 7-10: Arrangement for recording beam-start of the Elekta SL15*i* linear accelerator. Electron gun, photoconductive cell, beam on/off status circuit, EDP-10 semiconductor diode and SME are shown.

The resistance of the photoconductive cell decreases markedly on illumination with visible light: in darkness its resistance is in excess of 1 MΩ, whilst under normal illumination this decreases to a few 100 Ω. The device was placed in series with a 2 kΩ load resistance, and the light dependent output voltage from the mid-point of the resistor chain provided a direct optical signal. The signal was differentiated to identify beam-on and beam-off transitions, which were used by a simple logic circuit to produce a beam on/off status signal reflecting the emission status of the gun.

In order to assess the timing of the optical signal transition derived from the accelerator gun in relation to the rise in dose rate of the accelerator, measurements of the temporal variation of the signals were performed using three electrometer channels of the SME (Chapter 2). The direct optical signal was recorded by one channel of the SME via a series resistor (10 GΩ, Welwyn 3811, Welwyn Components Ltd.) acting as a

voltage-to-current converter. The beam on/off status signal was recorded in an identical manner by a second SME channel. The dose rate of the accelerator was recorded on a further channel using an EDP-10 semiconductor diode detector placed on beam centre-axis at 120 cm SDD. The SME connection to the dosimetry channel of the Elekta accelerator was also used to provide $1/64^{th}$ MU values at the end of each signal integration period. It was thus possible to simultaneously record the temporal variation of the optical signal from the photoconductive cell, the beam on/off status signal derived, and the dose rate from the accelerator (measured both by the EDP-10 detector and in $1/64^{th}$ MU by the dosimetry system of the accelerator). The geometry, together with an outline of connections to the photoconductive cell and derivation of the beam status signal, are shown in Figure 7-10.

Measurements were performed for 6 MV x-rays from the Elekta SL15*i*. The isocentre field size was 10.0 x 10.0 cm and the isocentre dose rate was approximately 5.5 Gy min^{-1} (400 Hz PRF).

The accelerator equipment room is separate from the treatment room. Repeated measurements were performed with the equipment room in darkness (the normal condition) whilst operating the accelerator at the normal PRF of 400 Hz. This allowed assessment of the magnitude and reproducibility of the optical signal transition in relation to the rise in dose rate at beam-start. To investigate the effect of ambient lighting on the optical signal, measurements at 400 Hz PRF were repeated with the equipment room lighting on. For all measurements at 400 Hz PRF the SME was operated with a signal integration period of 50 ms (corresponding to 20 radiation pulses), which was adequate to resolve beam-start.

Measurements were performed at 50, 100 and 200 Hz PRF in order to identify any effect of accelerator PRF on the temporal variation of beam-start. Signal integration periods for the SME were similar to those used at 400 Hz PRF.

Finally, the transition of the beam on/off signal was studied at beam termination. As discussed in Chapter 4.3.3, to maintain data capture the SME must continue to receive the thyratron drive voltage from the accelerator test point (used for synchronisation). Therefore, to continue data recording during beam-off, software control of the accelerator gun current was used in an identical approach.

7.3.3.2 Results

Figure 7-11 shows a typical recording of the optical signal, beam on/off status and dose rate during beam-start of the Elekta SL15*i*. Data has been normalised to the steady-state irradiation levels, and the optical signal has been corrected for the background signal level present before beam-start (due to residual ambient light).

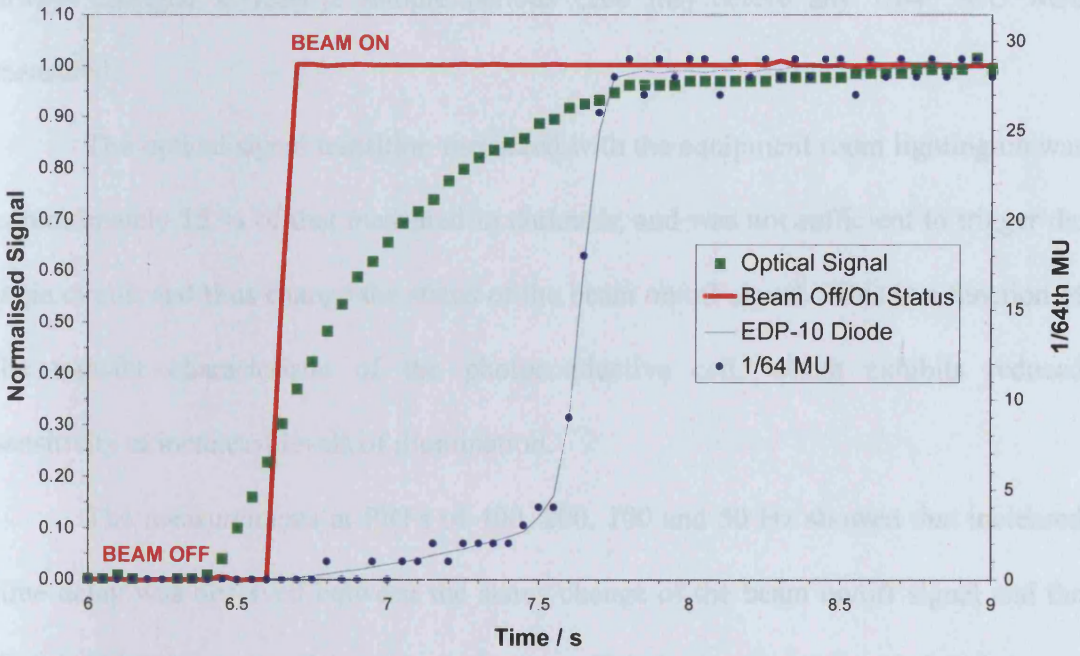

Figure 7-11: Optical signal, beam on/off status and dose rate during beam-start of the Elekta SL15*i*. The optical signal and dose rate (measured by the EDP-10 diode) are normalised to levels at steady-state irradiation and plotted on the left-hand axis. The dose measured during each integration period (50 ms duration) by the accelerator dosimetry system is shown in 1/64th MU on the right-hand axis. The optical signal due to residual ambient light which was present before the beam-start transition has been subtracted from data plotted.

Figure 7-11 also shows the number of 1/64th MU measured by the accelerator dosimetry system during each 50 ms integration period (right-hand axis). It is apparent that the dosimetry channel of the accelerator follows the instantaneous dose rate recorded by the diode very closely, which is to be expected.

Clearly the transition in the optical signal is in advance of beam-start. For the data shown the beam on/off status signal changes 2 sample periods (*i.e.* 100 ms) in advance of beam-start (*i.e.* 100 ms before the first 1/64th MU is counted by the accelerator dosimetry channel). Note that the slope of the beam on/off status signal is caused by the limited sample rate of the SME (compared to the speed of the logic). Repeated measurements showed no obvious change in the form of the optical and radiation signals, although the separation of the 50% level optical and diode signals did vary, particularly in the first few exposures of a sequence, but never by more than ±50 ms about its mean. However, in these repeated measurements the beam on/off status always changed at least 2 sample periods (100 ms) before any 1/64th MU were measured.

The optical signal transition measured with the equipment room lighting on was approximately 15 % of that measured in darkness, and was not sufficient to trigger the logic circuit and thus change the status of the beam on/off signal. This is a function of the transfer characteristic of the photoconductive cell, which exhibits reduced sensitivity at increased levels of illumination.

The measurements at PRFs of 400, 200, 100 and 50 Hz showed that increased time delay was observed between the status change of the beam on/off signal and the first 1/64th MU measured by the accelerator. This is due to increased time between radiation pulses, since a certain number are required to produce the first 1/64th MU. A maximum delay of approximately 500 ms was observed before the first 1/64th MU was

observed in the case of 50 Hz PRF. The beam on/off status signal derived from the photoconductive cell is therefore suitable as a means of controlling image acquisition for all accelerator PRFs in the range measured.

In the experiments forcing beam termination by manipulation of the accelerator gun current, at most a single $1/64^{th}$ MU was delivered after transition of the beam on/off status signal. However, normal beam termination is achieved by interruption of the accelerator PRF, followed by reduction of the accelerator gun current to the stand-by level. Therefore at normal termination the beam on/off signal will only change state *after* all dose has been delivered. This confirms the suitability of the beam status signal to control both the beginning and end of image acquisition of the EPID.

7.3.4 Discussion

The illumination of a photodetector by the electron gun of an Elekta linear accelerator can be used as a means of identifying beam-start of the accelerator. The transition of the optical signal is in advance of the rise in dose rate at beam-start for all accelerator PRFs (50-400 Hz). By incorporating a simple trigger circuit it is possible to provide a beam on/off status signal to indicate the initiation and termination of the radiation exposure. The status signal has been shown to change at least 100 ms before any dose is measured by the accelerator dosimetry channel, and does not return to its initial state until after dose delivery is complete. Such a signal is suitable to control image acquisition in Theraview and other EPIDs, to overcome difficulties in initiating image acquisition of these systems in DMLC. The approach may also be useful for other dosimetry systems which require a beam-on or beam-off status signal.

In the configuration used, which was designed to prove the principle of the technique, no attempt was made to remove ambient light from the photodetector. Under normal conditions the accelerator equipment room was in darkness. The

existence of ambient lighting was observed to considerably reduce the sensitivity of the photodetector to the beam-start transition. However, it would be possible to reduce the effect of ambient light with simple collimation. It should also be noted that the approach is only suitable for accelerators in which there is a transition in gun current prior to irradiation, and where the electron gun can be viewed by an optical detector.

7.4 Corrections for two-dimensional dose measurements

The factors affecting spatial uniformity of dose response in camera-based EPIDs, together with the complicating effect of optical scattering (cross-talk), have been considered in Chapter 5, where typical data for the Theraview system has been presented. In order to apply such a system to two-dimensional dose measurements, a correction method must be developed. The approach developed for the Theraview EPID is presented in this section, and an evaluation of the correction method is presented in Chapter 7.5 for two-dimensional dose measurements.

7.4.1 Correction for optical scattering

7.4.1.1 Introduction

The existence of optical scattering (cross-talk) in camera-based EPIDs and its effect on dosimetry has been introduced in Chapter 5.3.3 and is illustrated in Figure 5-6. The magnitude of optical cross talk is dependent on two main factors:

1. *Screen-mirror separation.* Munro *et al.* (1998) showed that increasing the screen-mirror separation reduced the effect. On this basis, the effect for the Theraview EPID should be reduced compared to the SRI-100 studied in Rotterdam, since the minimum screen-mirror separation for Theraview is 6.6 cm, compared to 4.5 cm for the SRI-100. The separation data for the SRI-100 has been provided by Pasma (Private Communication 1999), who has confirmed

the difference between the EPIDs experimentally. Furthermore, the use of a screen-mirror separation greater than the width of the screen has allowed Boon *et al.* (1998, 2000) to completely avoid the effect in a custom-built imaging system used for proton beam dosimetry: for a 45° geometry, this completely removes optical coupling between the screen and mirror (JM Schipper, Private Communication 2000).

2. *Reflective properties of the phosphor screen.* This has been demonstrated for the system developed by Zeman *et al.* (1998) which used a solid CsI:Tl crystal: Zeman (Private Communication, 1999) has shown the effect to be less than 4 % of that when using a conventional screen.

The correction method developed in Rotterdam to overcome optical scattering was based on deconvolution of an image with an empirically derived function describing optical scattering (cross-talk) (Heijmen *et al.* 1995, Pasma *et al.* 1997, Pasma *et al.* 1998). More recently, Partridge *et al.* (1999b) have studied optical scattering in camera-based EPIDs, and proposed a purely physical means of reducing optical scatter based on the use of a light control screen, consisting of louvered slats, placed directly beneath the phosphor screen. The method was implemented and investigated for the Theraview EPID used in this study.

It is worth noting that the correction approach developed in Rotterdam has *not* been widely adopted. There are several reported applications of camera-based imaging systems which do *not* use this correction, or any other means of reducing optical scattering, such as the light control screen. For example, Rajapakshe *et al.* (1996) and Rajapakshe (1998) did not take measures to exclude optical scattering in their use of a camera-based EPID for portal dosimetry (believed to be the Siemens EPID), and the

SRI-100 has been used for MVCT without accounting for the effect (Guan & Zhu 1998). The effect has also been acknowledged for the BIS (Wellhöfer Dosimetrie) by Hahm (Private Communication, 2000), who stated that optical scattering has been eliminated from this device and does not affect the measured signal, thus allowing dosimetry, although the solution has not been reported due to commercial sensitivity. It should be noted that the BIS has a curved, transparent membrane immediately behind the phosphor screen which is intended as a dust cover, and which is not involved in optical scatter rejection (Hahm, Private Communication, 2000). However, in measurements with the BIS for verification DMLC at Stanford (California, USA), Ma *et al.* (1997) specifically stated that correction for the effect had been omitted. More recent work at Stanford reported by Chen *et al.* (2000), which used the BIS to measure the fluence distribution for DMLC sequences, appears to demonstrate effects of optical scattering similar to those observed in this present work (Chapter 7.5). Hesse *et al.* (1998) have also used the BIS for MVCT and did not consider the effect of optical transport. However, as part of their study they measured a transmission profile for an anthropomorphic phantom which agreed with a diamond detector to within a mean deviation of 0.9 %, suggesting it had little influence for the case studied.

7.4.1.2 Description and characteristics of light control screen

The light control screen used (Partridge *et al.* 1999b) consists of a series of thin opaque louvered slats embedded in a polycarbonate matrix. The screens are intended for providing privacy at visual displays by preventing viewing of a display from the side. The screen used was available commercially (PF400XL, 3M UK, Bracknell, UK) and had overall dimensions 358 mm x 292 mm. The screen Measurements to characterise the angular dependent transmission of the screen were performed in darkness using an x-ray viewing box as a 'light source' (replacing the phosphor screen).

A small source (4.0 x 4.0 cm) was created by masking off the viewing box. The light control screen could be placed directly against the surface of the viewer in the same way as it was mounted against the phosphor screen in the EPID. Using a 5.5 mm x 7.0 mm silicon photodiode detector (SEE 038, International Light, Newburyport, MA, USA), and a radiometer (IL700A Research Radiometer, International Light) the irradiance[1] from the 'source' could be measured. The photodiode detector was aligned with the centre of the 'source' and mounted 14.0 ± 0.2 cm from the surface of the light 'source' using an optical bench. The detector could be moved parallel to the surface of the light source either side of the centre (Figure 7-12).

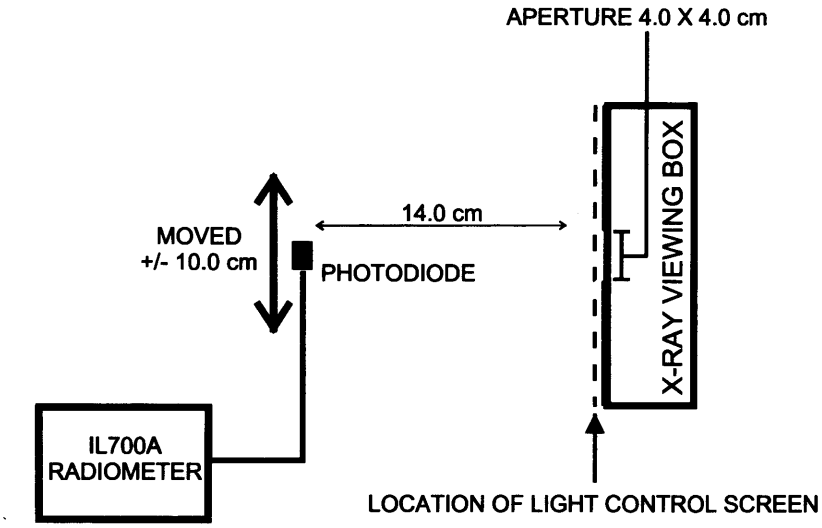

Figure 7-12: Measuring angular dependent transmission of light control screen using photodiode. A plan view is shown. The louvered slats of the screen were oriented both parallel and perpendicular to the profile direction.

Measurements were performed with the axis of the light control screen orientated both parallel and perpendicular to the profile direction in order to construct the transmission profiles, and the results are shown in Figure 7-13.

[1] Irradiance: radiant flux (*i.e.* rate of flow of radiant energy) per unit area, expressed as W m^{-2}.

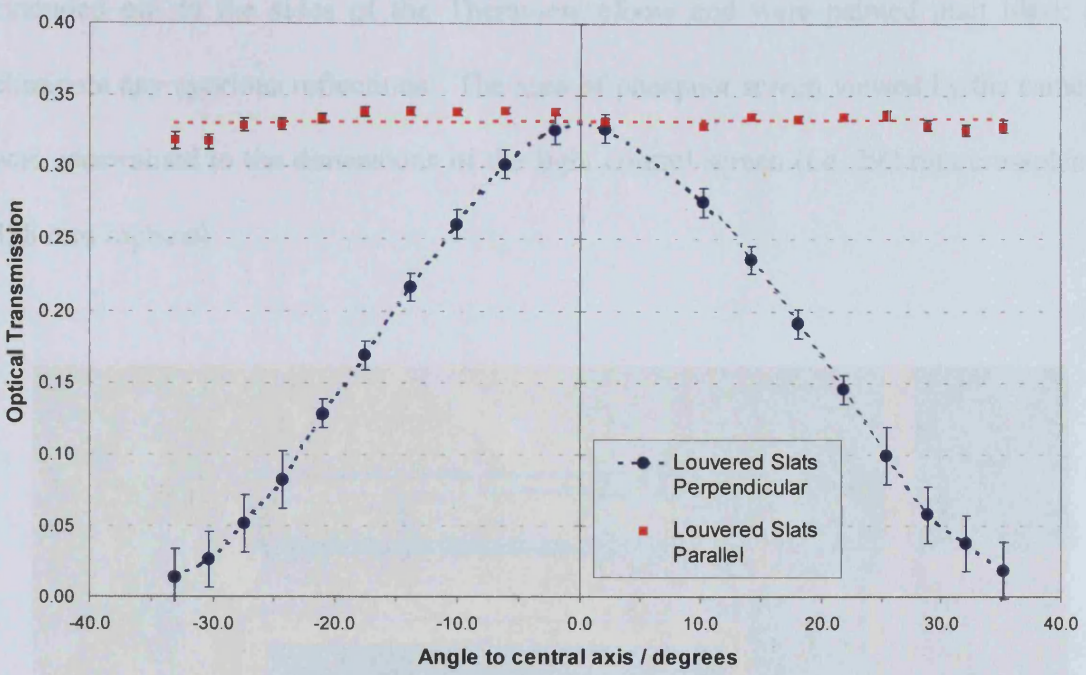

Figure 7-13: Angular dependent transmission of light control. Data is shown for the louvers of the optical control screen oriented both parallel and perpendicular to the profile direction.

Further measurements were performed with a 0.5 x 0.5 cm light source and showed very similar results. Clearly, for the case of the louvered slats perpendicular to the profile direction, the light control screen provides a marked reduction in optical transmission with increasing angle from central axis. There is little effect for the orthogonal orientation. This is clearly the effect of the light control screen when located behind the phosphor screen of the EPID and oriented to provide optical rejection along the inplane axis. It is worth noting that the screen also introduces optical attenuation: for the light source and detector used in this case, optical transmission for normal incidence was around 33 %.

The louvered slats were aligned parallel to the shorter screen dimension, which was aligned parallel to the accelerator crossplane axis. This provided optical rejection in the inplane axis. The light control screen was mounted against the phosphor screen and located symmetrically about central axis using aluminium support brackets on all four sides. A "beam's eye view" is shown in Figure 7-14. The aluminium supports

extended out to the sides of the Theraview elbow and were painted matt black to eliminate any spurious reflections. The area of phosphor screen viewed by the camera was constrained to the dimensions of the light control screen (*i.e.* 292 mm crossplane, 358 mm inplane).

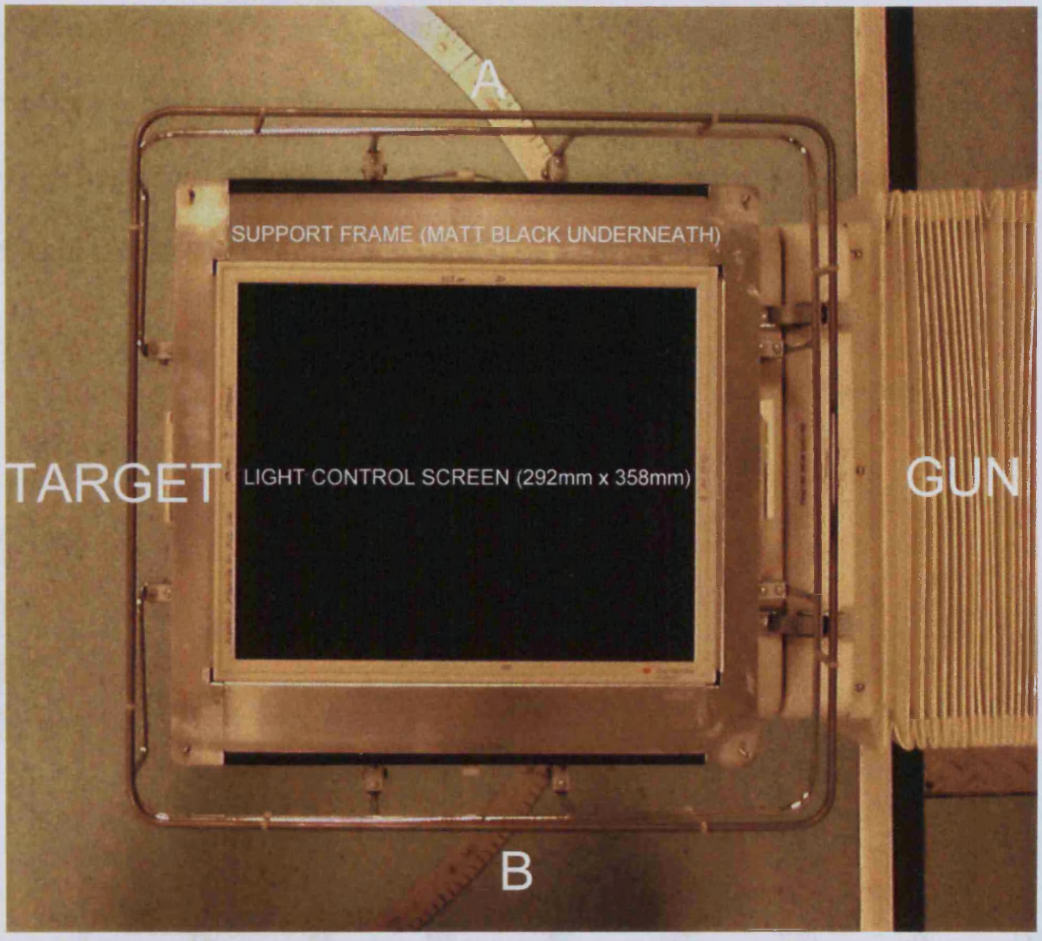

Figure 7-14: "Beam's eye view" of the light control screen mounted on Theraview EPID. The aesthetic cover, copper plate and phosphor screen have been removed showing the aluminium support frame (matt black on the underside) and light control screen. The orientation of the accelerator is marked (crossplane A-B, inplane gun-target G-T).

7.4.1.3 Effect on field size response

To investigate the effect of introducing the light control screen on field size response, the dose response of an EPID was assessed using Single image mode for a range of field sizes, with and without the light control screen in place. In Chapter 5, the dose response curve was constructed simply by plotting pixel value for an ROI against

dose measured by an ion chamber. However, the increased variability in triggering of image acquisition observed for Theraview (Chapter 7.3) compared to initial performance must be included in the construction of the dose response curves. This was achieved using the Theraview trigger input to the SME (Chapter 6) to identify accelerator 1/64th MU at triggering, and subsequently calculating the number of 1/64th MU delivered *after* triggering (as in the case of the data presented in Figure 7-9). To construct the curve this was performed for exposures of a range of MU. Results from measurements for field sizes 5.0 x 5.0, 10.0 x 10.0 and 20.0 x 20.0 cm using an SDD of 165.2 cm and 20.0 cm WT1 at 100 cm SSD are shown in Figure 7-15.

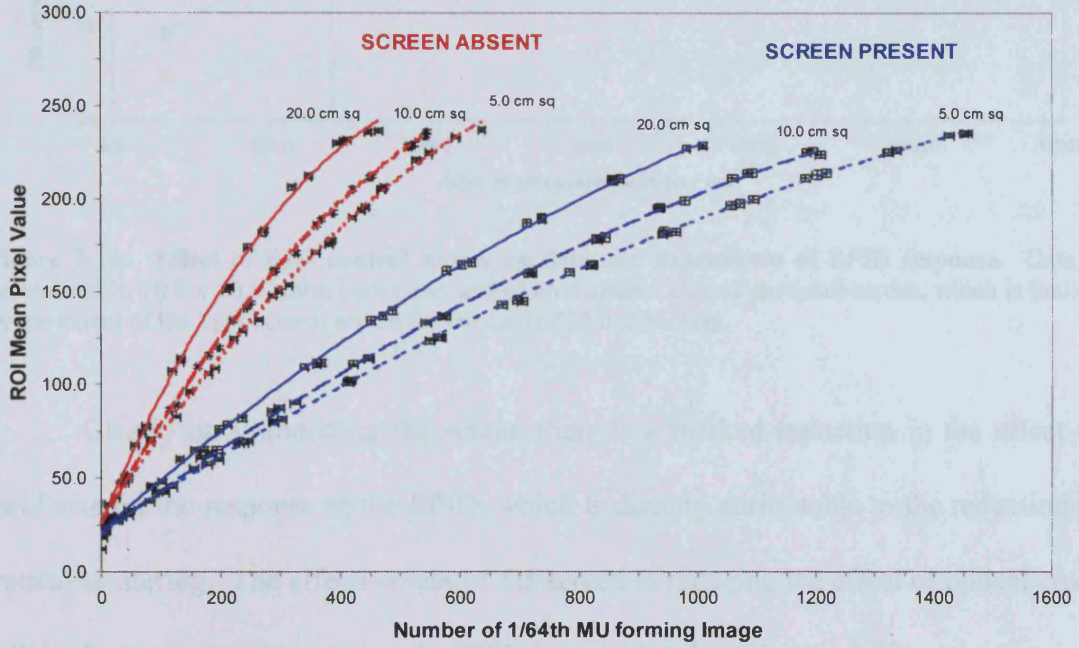

Figure 7-15: Effect of light control screen on dose response curve for different field sizes. Mean pixel value for a 1.0 x 1.0 cm ROI are plotted against the number of 1/64th MU delivered *after* the EPID triggered (i.e. the number of 1/64th MU forming each image). Results from several exposures at each MU setting are shown. Isocentre field sizes were 5.0 x 5.0, 10.0 x 10.0 and 20.0 x 20.0 cm in both cases.

The effect of the light control screen on the field size dependency of the dose response curves in Figure 7-15 was demonstrated by considering the gradient of each dose response curve. Figure 7-16 shows the gradient of each response in Figure 7-15 for all data points below a pixel value of 100 estimated by linear regression. Values,

normalised to the respective gradients for 10.0 x 10.0 cm, are shown against area of phosphor irradiated.

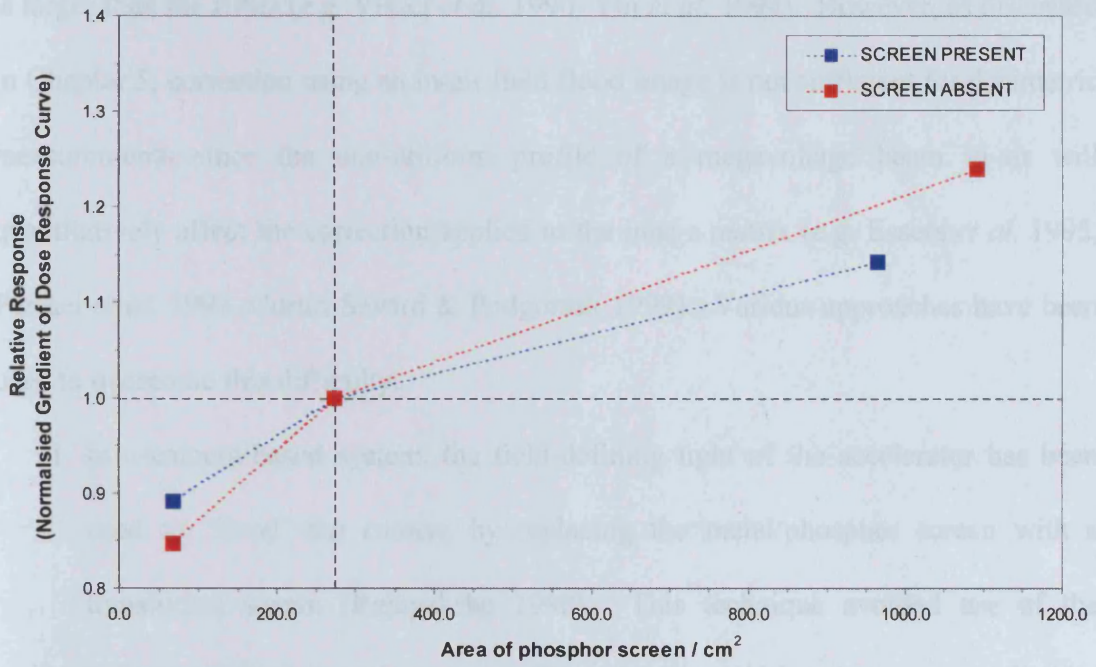

Figure 7-16: Effect of light control screen on field size dependence of EPID response. Data is normalised to 10.0 x 10.0 cm in both cases and plotted against area of phosphor screen, which is limited by the extent of the light control screen for the case of 20.0 x 20.0 cm.

Clearly on introducing the screen there is a marked reduction in the effect of field size on the response of the EPID, which is directly attributable to the reduction in optical scattering. The effectiveness of the screen in reducing the effect of optical cross talk in dose measurements using the EPID is considered in Chapter 7.5.

7.4.2 Correction for spatial non-uniformity

7.4.2.1 Introduction

As previously discussed, in order to apply an EPID to two-dimensional dose measurements a correction method for spatial non-uniformity must be developed, which in the case of camera-based EPIDs must account for optical scattering. Correction

methods to overcome the effects of spatial non-uniformity for *clinical imaging* have been reported in the literature for both the camera-based SRI-100 EPID and the matrix ion chamber (PortalVision) based on an image of an open 'flood' radiation field which is larger than the EPID (*e.g.* Visser *et al.* 1990, Yin *et al.* 1994). However, as discussed in Chapter 5, correction using an in-air field flood image is not sufficient for dosimetric measurements since the non-uniform profile of a megavoltage beam in-air will quantitatively affect the correction applied to the image matrix (*e.g.* Essers *et al.* 1995, Parsaei *et al.* 1998, Curtin-Savard & Podgorsak 1999). Various approaches have been used to overcome this difficulty:

1. In a camera-based system, the field-defining light of the accelerator has been used to 'flood' the camera by replacing the metal/phosphor screen with a translucent screen (Rajapakshe 1998). This technique avoided use of the radiation field, but neglected any effect of the metal/phosphor screen, relied on the light field being uniform, and inherently does not correctly represent optical scattering conditions that occur with the screen in place.
2. In the use of an SRI-100 for dosimetric quality control on a scanning beam accelerator, flood field calibration was omitted and only dark current correction included. Off-axis profile deviations were calculated relative to reference images, and absolute output values on-axis were only considered where an absolute calibration had been applied (Dirkx *et al.* 1995).
3. The clinical calibration protocol has also been used to study *relative* dose distributions for compensator design and verification with PortalVision (Roback & Gerbi 1995).

4. An appropriate thickness of 'beam-flattening material' has been used to achieve a 'flat' radiation beam profile for flood field calibration in which off-axis changes in dose rate could be ignored (Parsaei *et al.* 1998).
5. Off-axis changes in the dose rate for a flood field were included in calibration of PortalVision by measurement of the relative dose rate to each pixel using a scanning IC, and including this ratio in the calibration (Essers *et al.* 1995, Zhu *et al.* 1995). This is the approach adopted in this present work, which has been modified to include the light control screen for optical scatter reduction.

7.4.2.2 Method

As has been discussed in Chapter 5, the Theraview EPID does not account for any dark current and does not apply any non-uniformity correction (apart from the *shading correction* applied in the CCU). Because of the difficulty in measuring dark current directly (due to the current trigger mechanism, Chapter 5 and 7.3) no explicit correction for camera target dark current has been applied in the studies presented. However, the presence of the temporally invariant 'latent' image identified for the EPID used in this study (Chapter 7.2.1) has been corrected for by subtraction of a mean latent image (Figure 7-1).

Correction was achieved using images ('Treatment Loop') of a 6 MV steady-state 'flood' radiation field acquired with the light control screen present and absent, using integration periods of 0.25 s and 0.50 s respectively. The incident dose rate distribution along major axes was measured using an automated one-dimensional in-air scanner (RFA-300, Scanditronix Medical AB, Uppsala, Sweden) and a 0.12 cm^3 IC (RK, Scanditronix Medical AB) using a 6 MV build-up cap (diameter 30.0 mm PMMA) placed at the same SDD (146.5 cm). The IC was orientated orthogonal to the beam axis with its diameter parallel to the scan direction to optimise spatial resolution.

An isocentre field size of 30.0 x 30.0 cm was used for both imaging and IC measurement, with 20.0 cm WT1 at 100.0 cm SSD. Each IC scan took approximately 5 minutes, during which time the field flatness and symmetry error signals of the Elekta accelerator were monitored and showed deviation of no more than ± 0.2 %. Only major axis profiles have been considered in this present work, but the technique could be extended to two-dimensional correction using an empty two-dimensional plotting tank.

The relative dose rate for each pixel was calculated by linear interpolation of the IC data. The active length of the RK IC was 10.0 mm, which was taken as the profile width for each flood image (corresponding to 14 pixels). A sensitivity correction factor $S(i,j)$ was calculated for each pixel (i,j) along the major axis profiles within the flood field, based on the ratio of the interpolated dose rate $\dot{D}_{flood(i,j)}$ for pixel (i,j), the image of the flood radiation field $I_{flood}(i,j)$ and the mean latent image $I_{latent}(i,j)$:

$$S(i,j) = \frac{\dot{D}_{flood}(i,j)}{I_{flood}(i,j) - I_{latent}(i,j)} \tag{7.1}$$

which was normalised to central axis. Separate corrections, based on the same incident (measured) dose rate data, were calculated for the presence and absence of the light control screen.

7.4.2.3 Correction data

Figure 7-17 shows the normalised correction data plotted against isocentre off-axis distance. Figure 7-17(a) shows data for the crossplane (AB) axis of the accelerator, and Figure 7-17(b) shows data for the inplane (GT) axis of the accelerator. For the crossplane axis correction values for the screen present extend only to approximately ±100 mm, corresponding to the extent of the screen. Deviation between the two corrections increases off-axis, and amount to 5.5 % in opposite directions on either side of central axis. For the inplane axis there is a much greater effect on

introducing the screen, and spatial uniformity correction is significantly changed with off-axis correction factors increased by up to 50 %.

The relative off-axis response was observed to be stable in repeat measurements of the sensitivity correction on a monthly basis: comparison of two data sets acquired one month apart had a maximum local difference of 2 %, and a mean difference of 0.7 % (SD 0.7%). This is consistent with the observed stability of off-axis response (within a limited field) for the original EPID studied (Chapter 5).

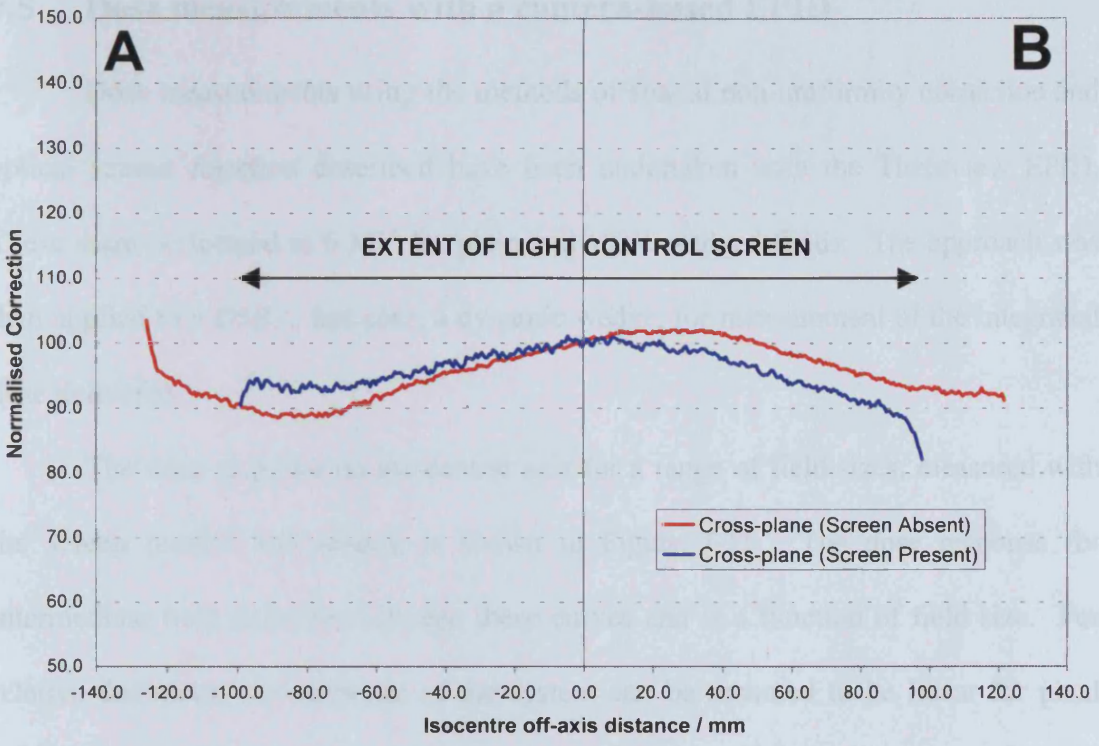

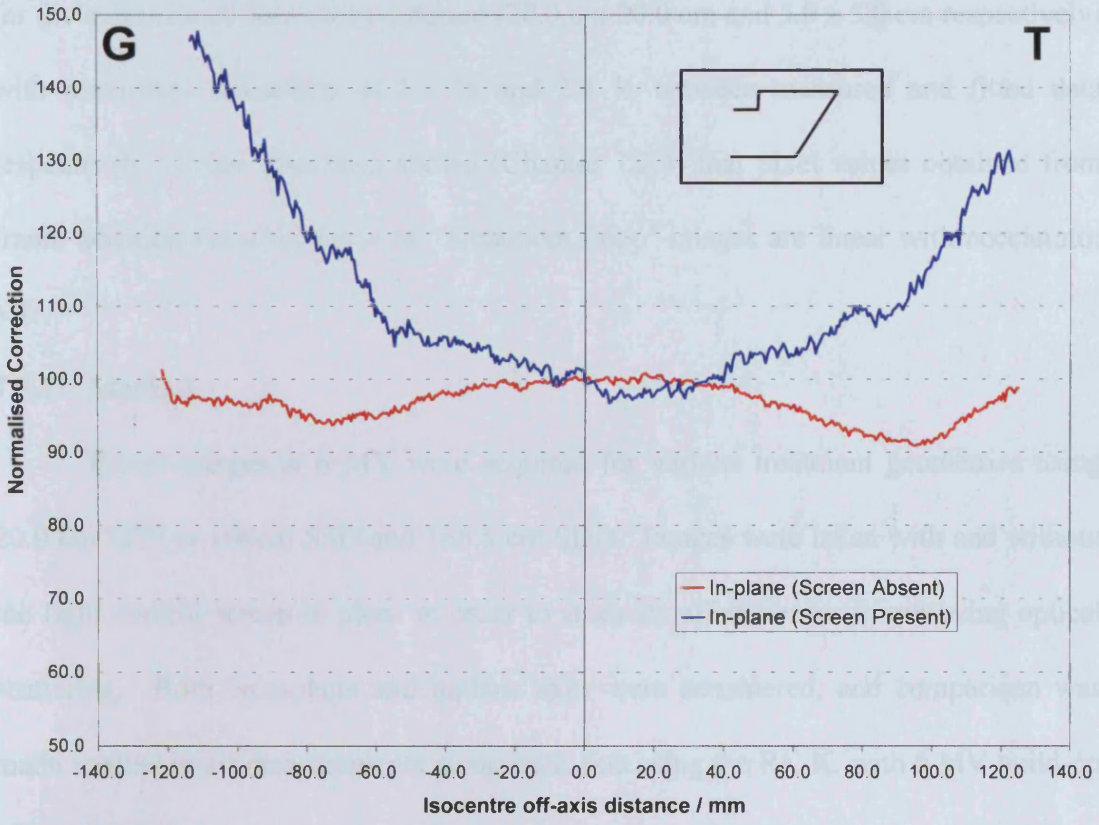

Figure 7-17 (a) and (b): Correction data for spatial non-uniformity along crossplane and inplane axes. Negative off-axis distances correspond to accelerator A (crossplane) and G (Gun, inplane) respectively, which are shown together with the orientation of the screen/mirror of the EPID. Data is show for the absence and presence of the light control screen. Values are normalised to central axis.

7.5 Dose measurements with a camera-based EPID

Dose measurements using the methods of spatial non-uniformity correction and optical scatter rejection described have been undertaken with the Theraview EPID. These were performed at 6 MV for plain and static wedged fields. The approach was then applied to a DMLC test case, a dynamic wedge, for measurement of the integrated dose delivered.

The dose response on the central axis for a range of field sizes, measured with the screen present and absent, is shown in Figure 7-15. The dose response for intermediate field sizes lies between these curves and is a function of field size. For relative dosimetry, the response of the system can be assumed to be linear for pixel values less than 200: in this range, linear regression gave r^2 values of 0.997 and 0.996 for the extremes of field size examined (20.0.0 x 20.0 cm and 5.0 x 5.0 cm respectively) with maximum deviations of 1.3 % and 3.4 % between measured and fitted data respectively. It has also been shown (Chapter 7.2.4) that pixel values obtained from frame addition for a sequence of 'Treatment Loop' images are linear with accelerator MU.

7.5.1 Method

Portal images at 6 MV were acquired for various treatment geometries using 20.0 cm WTI at 100cm SSD and 146.5 cm SDD. Images were taken with and without the light control screen in place in order to study its effectiveness in removing optical scattering. Both crossplane and inplane axes were considered, and comparison was made against in-air measurements along each axis using the RK IC with 6 MV build-up cap in an identical approach to that for the spatial non-uniformity correction. Dose profiles obtained from portal images were again averaged over the 10.0 mm length of the RK chamber's sensitive volume.

All images were corrected for the presence of the latent image described in Chapter 7.2.1. For plain and static wedge fields, images were acquired using the 'Treatment Loop' mode with a suitable integration period within the range 0.25 s to 1.00 s. This time was adjusted with field size and presence of the screen to ensure pixel values were below 200, corresponding to the most linear portion of the dose response curve. Measurements were performed for field sizes of 5.0 x 5.0, 10.0 x 10.0 and 20.0 x 20.0 cm. For the dynamic wedge field, 'Treatment Loop' images were acquired using an integration period of 1.0 s at a rate of one image per second. For all wedge fields, measurements were made with the dose gradient along both crossplane and inplane axes.

7.5.2 Results

7.5.2.1 Static plain treatment fields

Figure 7-18 (a)-(d) shows results for the crossplane axis for plain fields together with IC data. Within the 50 % field edges there is little difference for the dose profiles measured with and without the screen in place, although there is a general tendency for measurements with the screen to result in lower measured dose levels with increasing off-axis distance. The dose profiles obtained from images without the screen are in better agreement with the IC data. For the 20.0 x 20.0 cm field, deviations between EPID measurement and IC data are at most 2 %, and in general less than 1 %. Outside the 50 % field edges, agreement between EPID and IC data is better with the screen absent for 5.0 x 5.0 cm, but the opposite is true at 10.0 x 10.0 cm. Data with the screen present for 20.0 x 20.0 cm is not available due to the limited dimension of the screen crossplane.

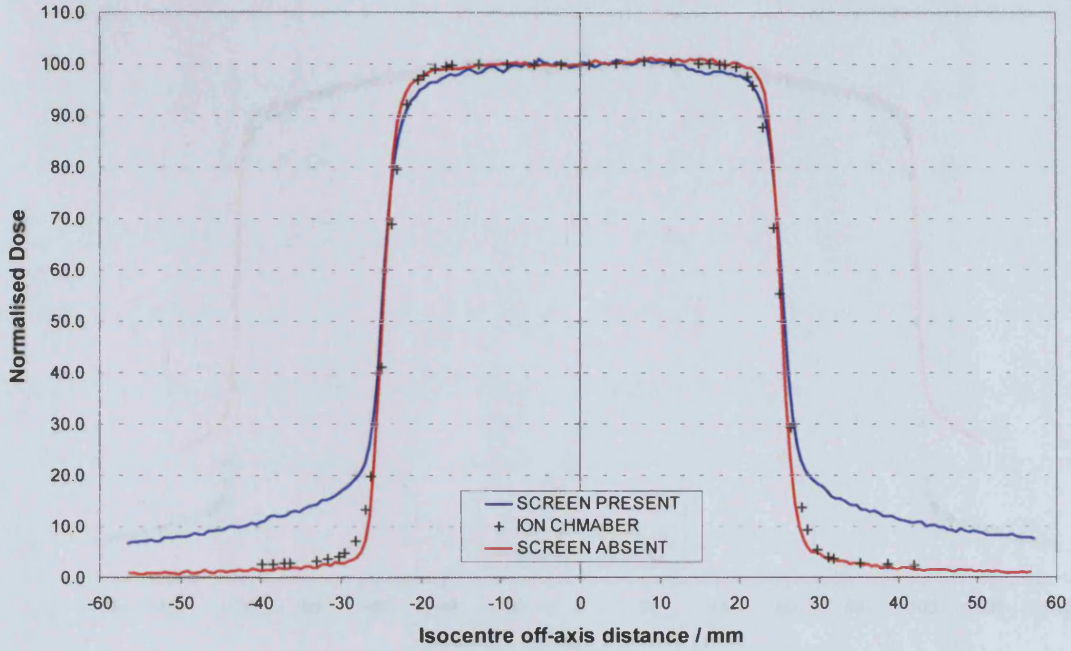

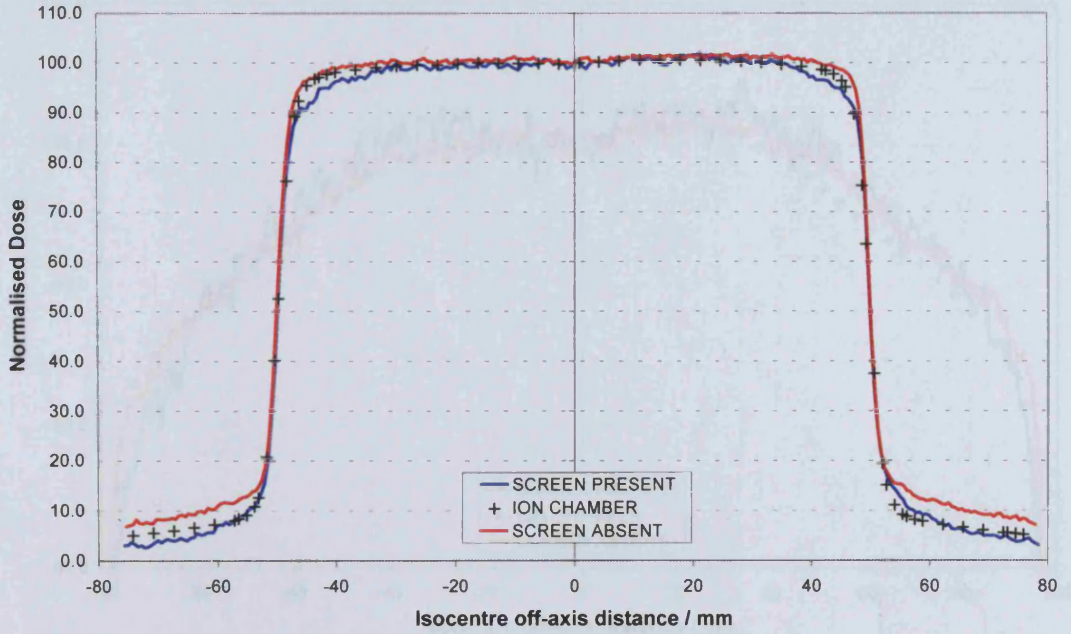

Figure 7-18 (a) and (b): Dose profiles for 5.0 x 5.0 cm and 10.0 x 10.0 cm plain fields (crossplane axis) showing effect of light control screen.

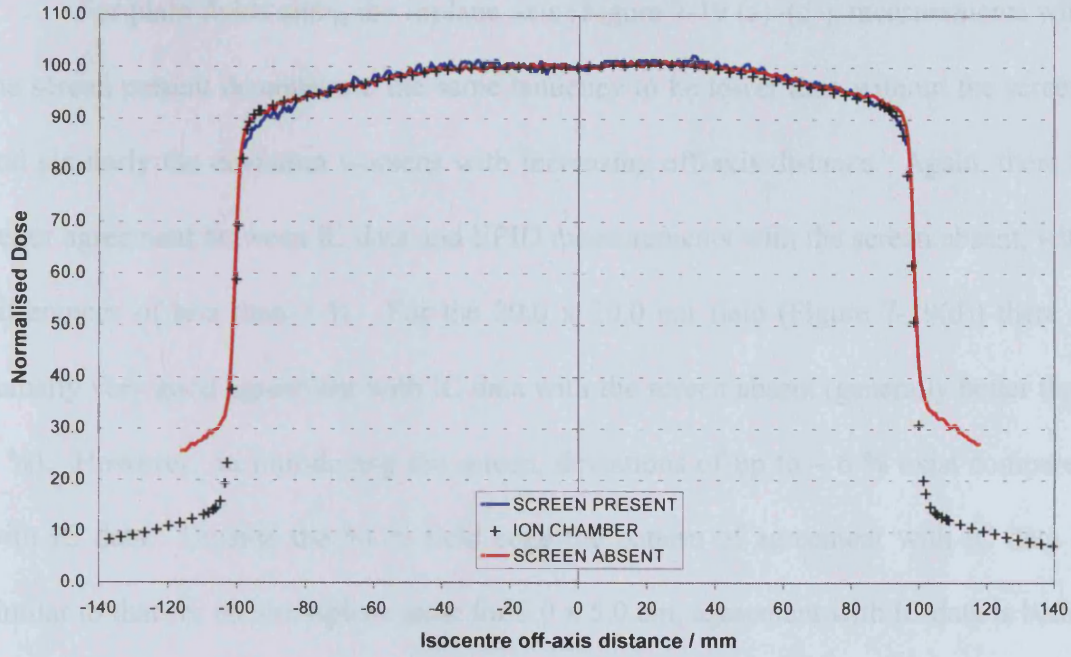

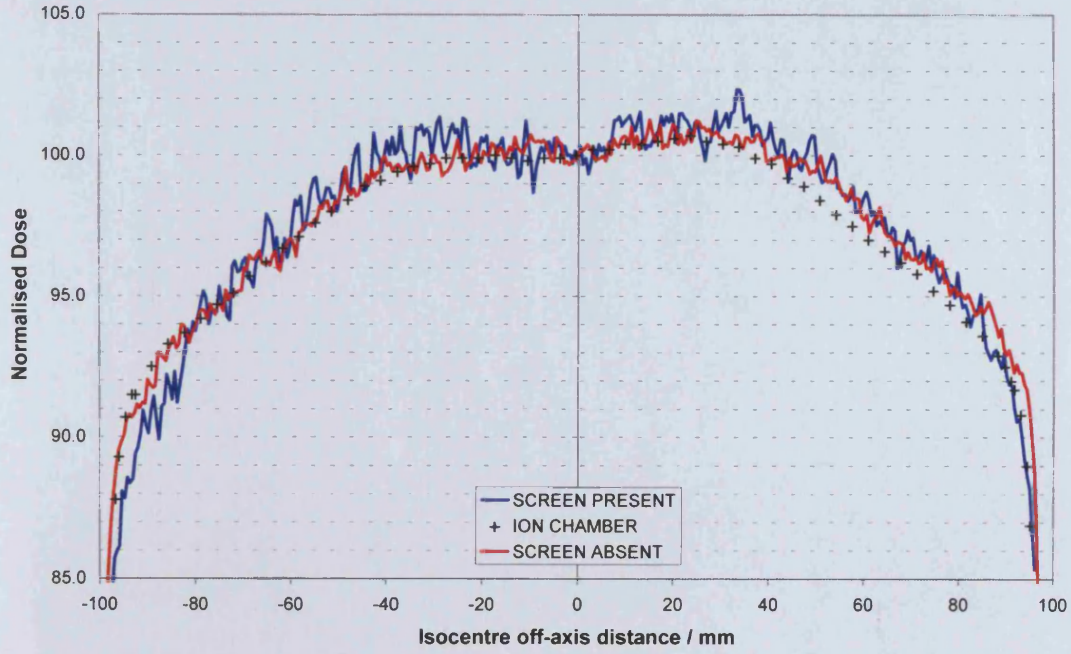

Figure 7-18 (c) and (d): Dose profiles for 20.0 x 20.0 cm plain field (crossplane axis) showing effect of light control screen. Figure 7-18 (d) is an enlargement.

For plain fields along the inplane axis (Figure 7-19 (a)–(d)), measurements with the screen present demonstrate the same tendency to be lower than without the screen, and similarly the deviation worsens with increasing off-axis distance. Again, there is better agreement between IC data and EPID measurements with the screen absent, with differences of less than 3 %. For the 20.0 x 20.0 cm field (Figure 7-19(d)) there is actually very good agreement with IC data with the screen absent (generally better than 1 %). However, on introducing the screen, deviations of up to – 6 % exist compared with IC data. Outside the 50 % field edge the pattern of agreement with IC data is similar to that for the crossplane axis: for 5.0 x 5.0 cm, agreement with IC data is better with screen absent, and the opposite is true for 10.0 x 10.0 cm.

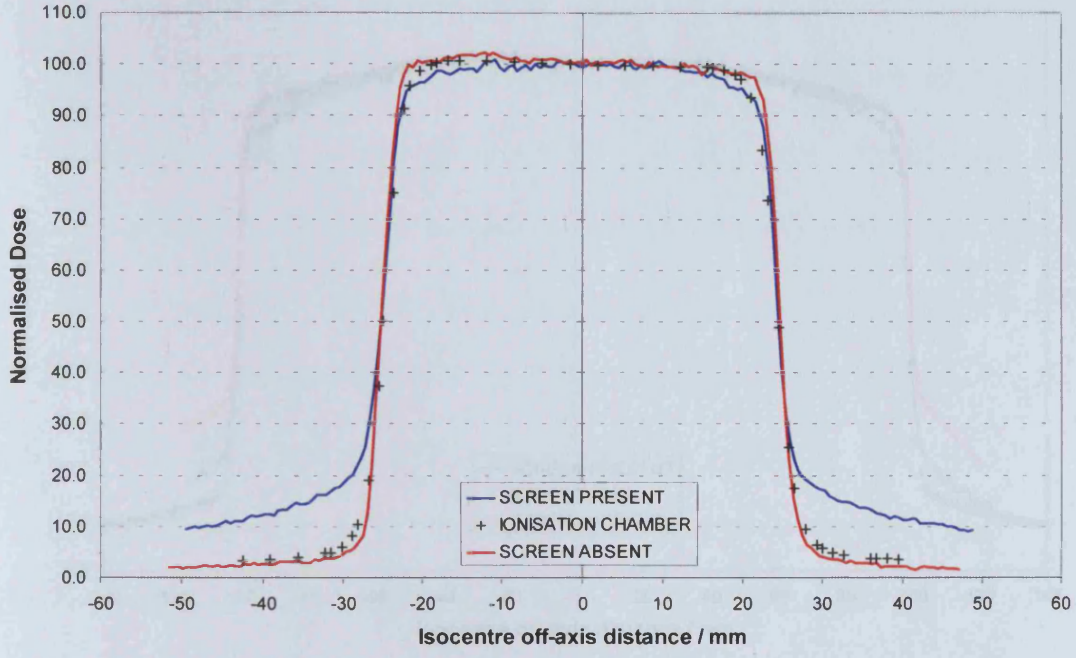

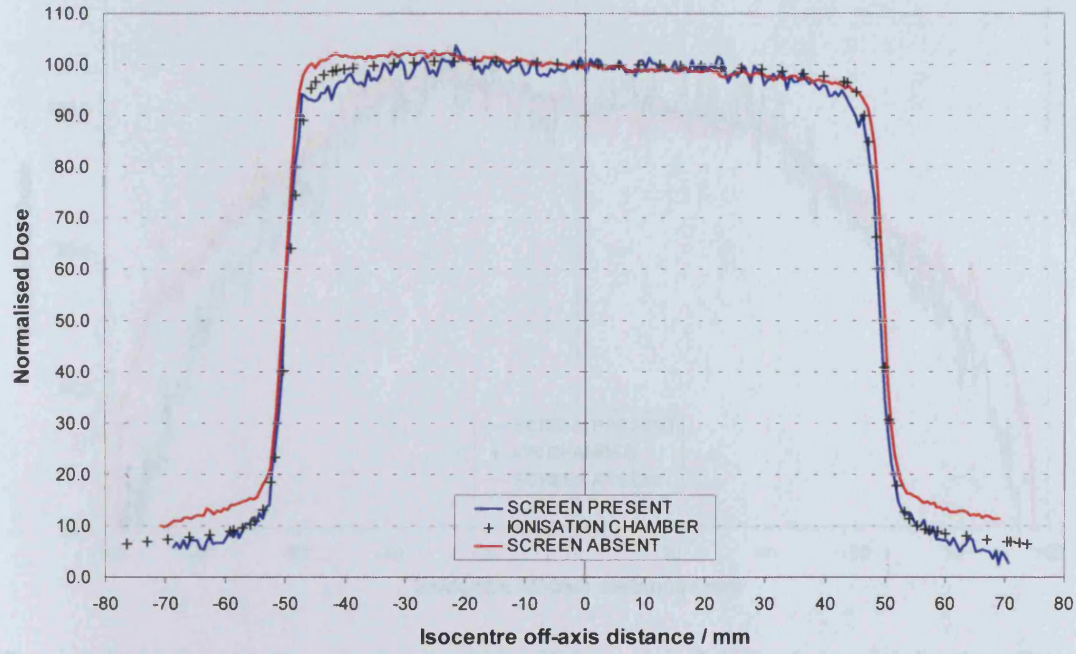

Figure 7-19 (a) and (b): Dose profiles for 5.0 x 5.0 cm and 10.0 x 10.0 cm plain fields (inplane axis) showing effect of light control screen.

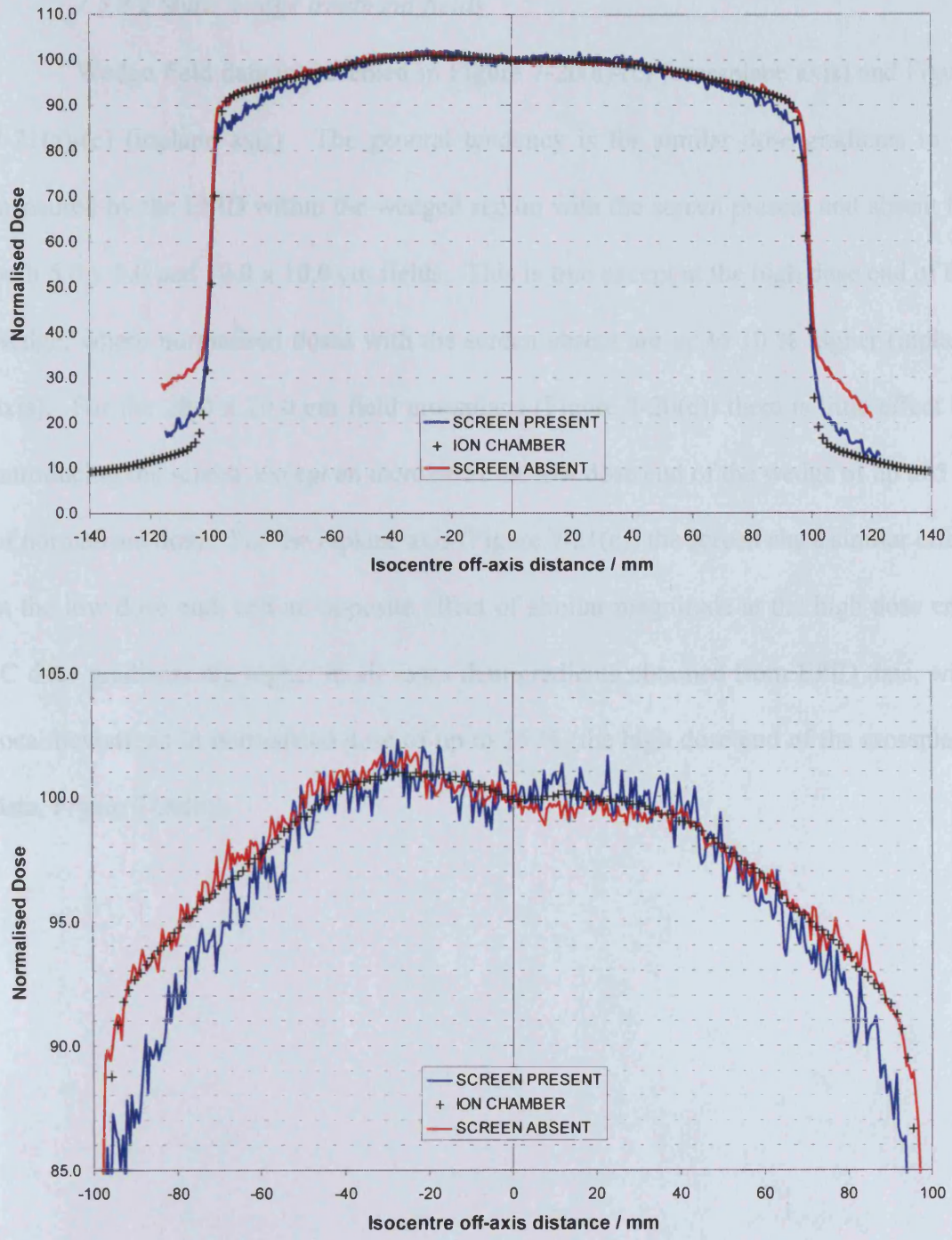

Figure 7-19 (c) and (d): Dose profiles for 20.0 x 20.0 cm plain field (inplane axis) showing effect of light control screen. Figure 7-19 (d) is an enlargement.

7.5.2.2 Static wedge treatment fields

Wedge field data is presented in Figure 7-20(a)-(c) (crossplane axis) and Figure 7-21(a)-(c) (inplane axis). The general tendency is for similar dose gradients to be measured by the EPID within the wedged region with the screen present and absent for both 5.0 x 5.0 and 10.0 x 10.0 cm fields. This is true except at the high dose end of the wedge, where normalised doses with the screen absent are up to 10 % higher (inplane axis). For the 20.0 x 20.0 cm field crossplane (Figure 7-20(c)) there is little effect on introducing the screen, except an increase at the low dose end of the wedge of up to 5 % of normalised dose. For the inplane axis (Figure 7-21(c)) the screen ahs a similar effect at the low dose end, and an opposite effect of similar magnitude at the high dose end. IC dose gradients are higher in all cases than gradients obtained from EPID data, with local deviations in normalised dose of up to 25 % (the high dose end of the crossplane data, Figure 7-20(c)).

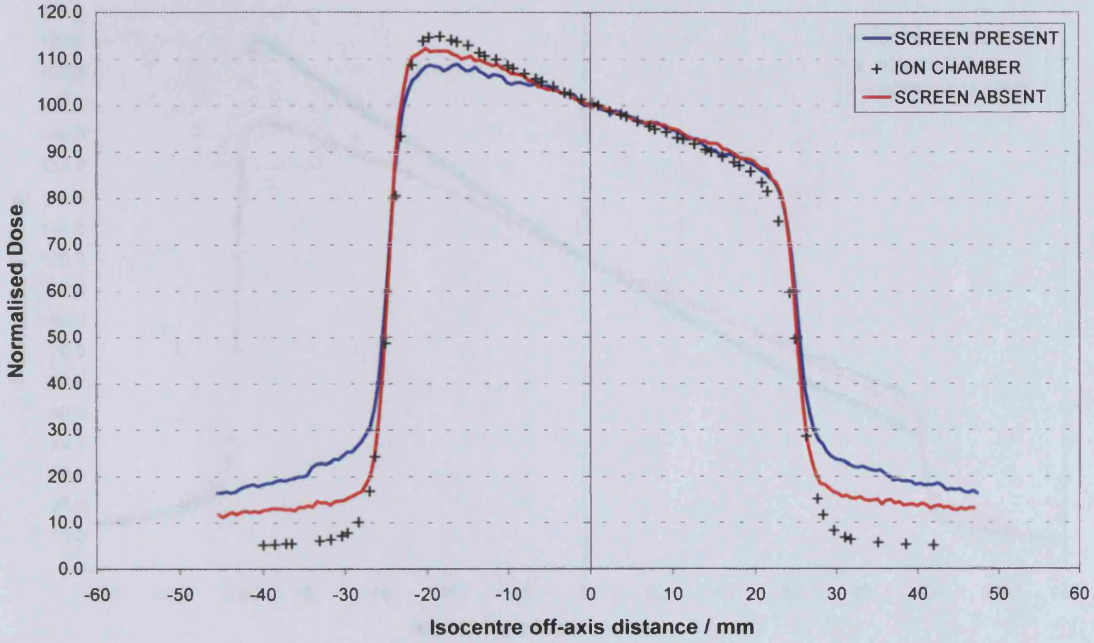

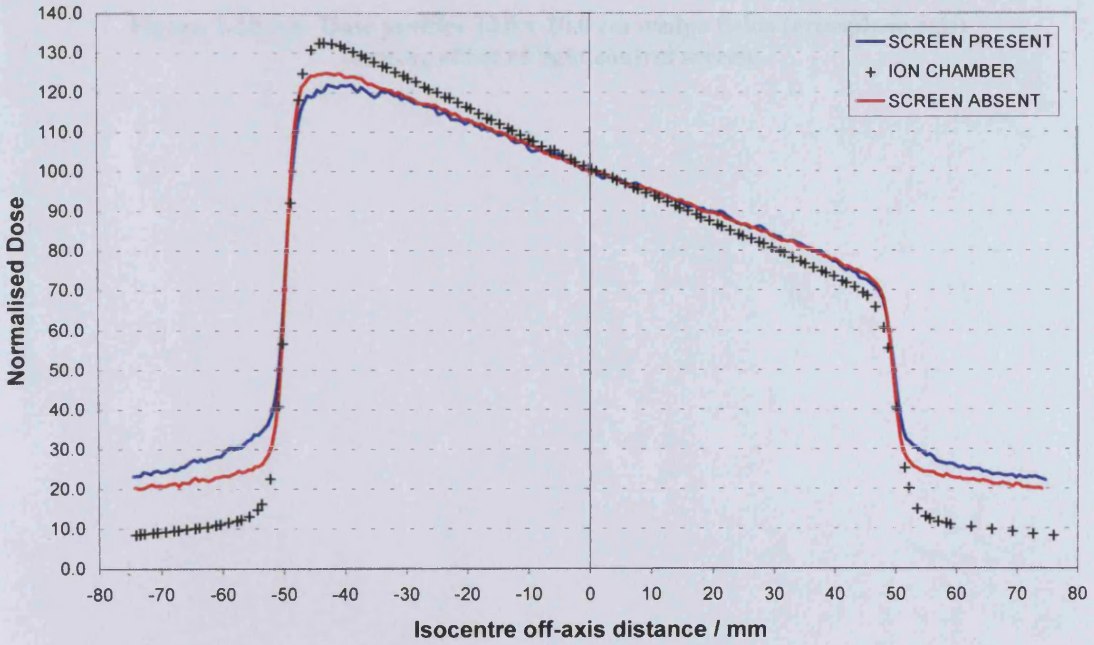

Figure 7-20 (a) and (b): Dose profiles for 5.0 x 5.0 and 10.0 x 10.0 cm wedge fields (crossplane axis) showing effect of light control screen.

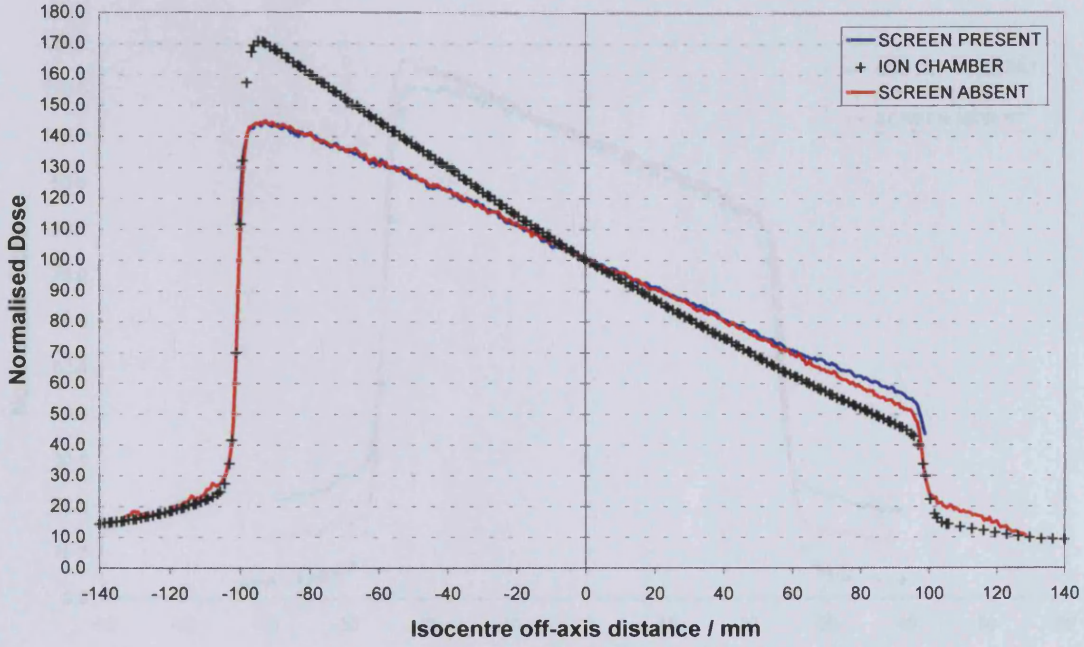

Figure 7-20 (c): Dose profiles 20.0 x 20.0 cm wedge fields (crossplane axis) showing effect of light control screen.

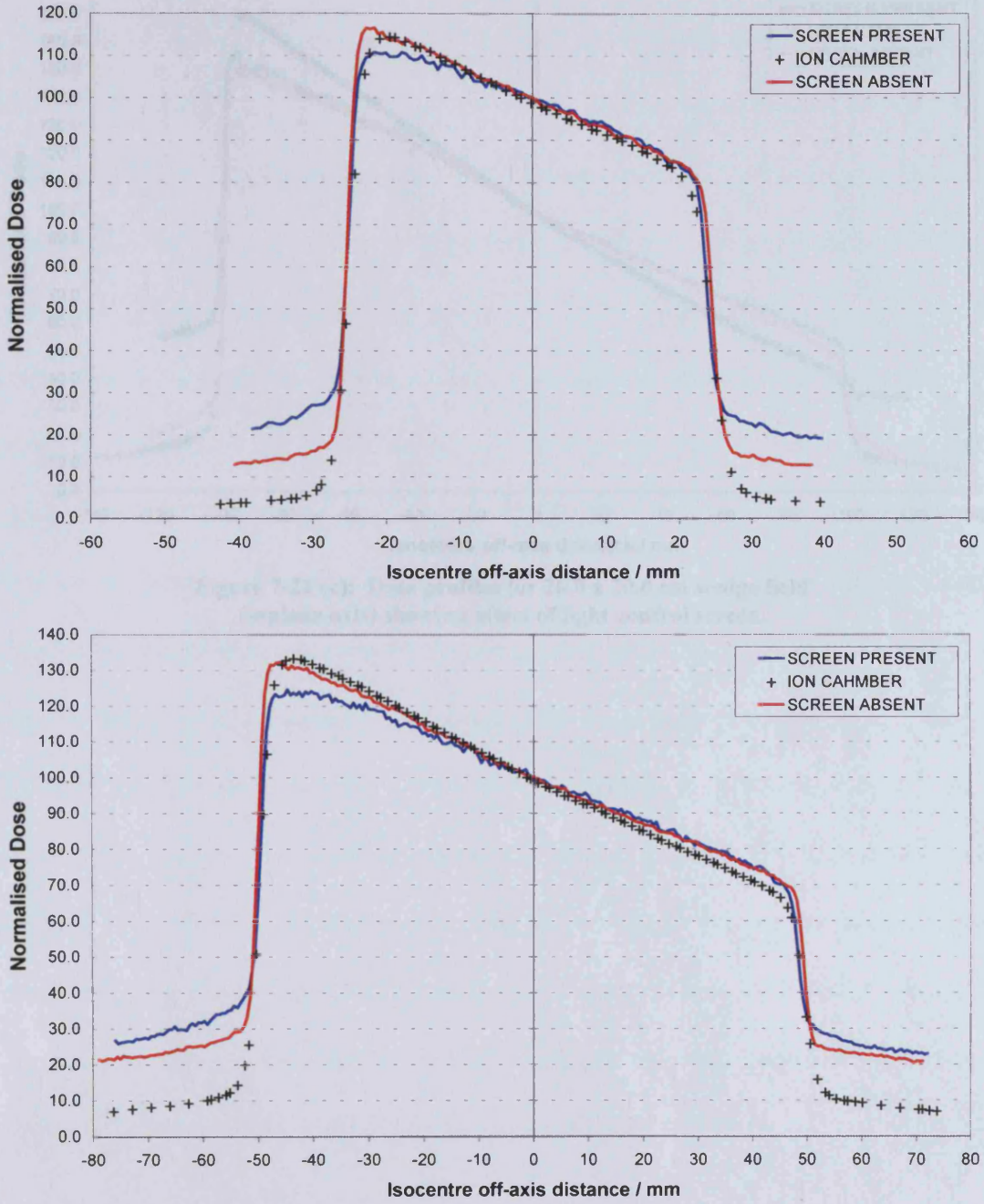

Figure 7-21 (a) and (b): Dose profiles for 5.0 x 5.0 cm and 10.0 x 10.0 cm wedge fields (inplane axis) showing effect of light control screen.

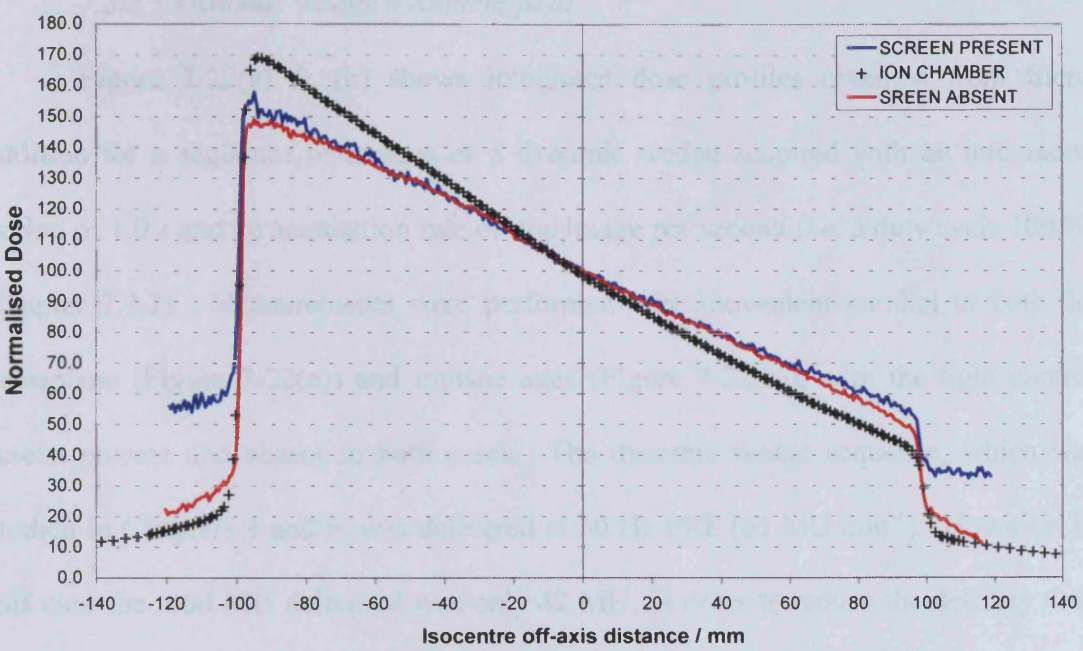

Figure 7-21 (c): Dose profiles for 20.0 x 20.0 cm wedge field (inplane axis) showing effect of light control screen.

7.5.2.3 Dynamic wedge treatment field

Figure 7-22(a) & (b) shows integrated dose profiles obtained from frame addition for a sequence of images of a dynamic wedge acquired with an integration period of 1.0 s and an acquisition rate of one image per second (*i.e.* a duty cycle 100 %, Chapter 7.2.2). Measurements were performed with movement parallel to both the crossplane (Figure 7-22(a)) and inplane axes (Figure 7-22(b)), with the light control screen present and absent in both cases. The dynamic wedge sequence, which was studied in Chapters 3 and 6, was delivered at 50 Hz PRF (65 MU min^{-1}). However, in this case the total MU delivered was only 42 MU, in order to reduce the delivery time (and hence number of images acquired by the EPID). This ensured that the entire sequence was captured, since the maximum number of images which could be acquired was limited to 40 (Chapter 6). IC measurements were again made in-air with the RK chamber (6 MV build-up cap). The one-dimensional in-air scanner was used to position the chamber at intervals along the wedge gradient for both orientations. Keeping the chamber stationary, the dose delivered by the wedge sequence was measured using a conventional integrating electrometer (Therados RDM2A, Therados, Uppsala, Sweden). Measurements were repeated at each location and showed reproducible dose delivery for the wedge sequence (SD < 0.3 %).

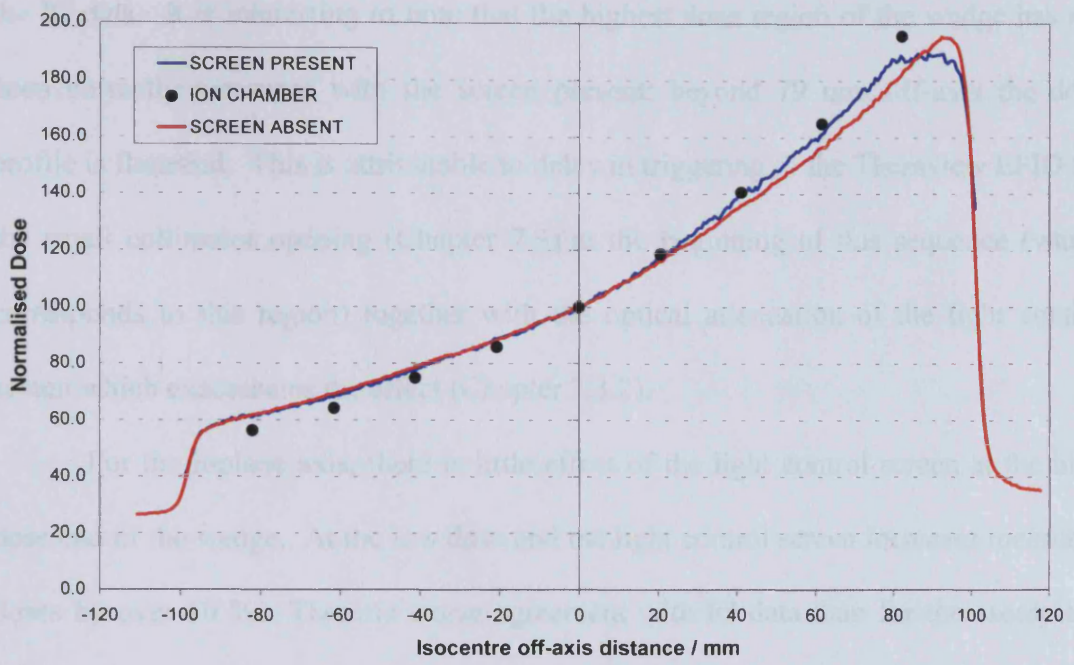

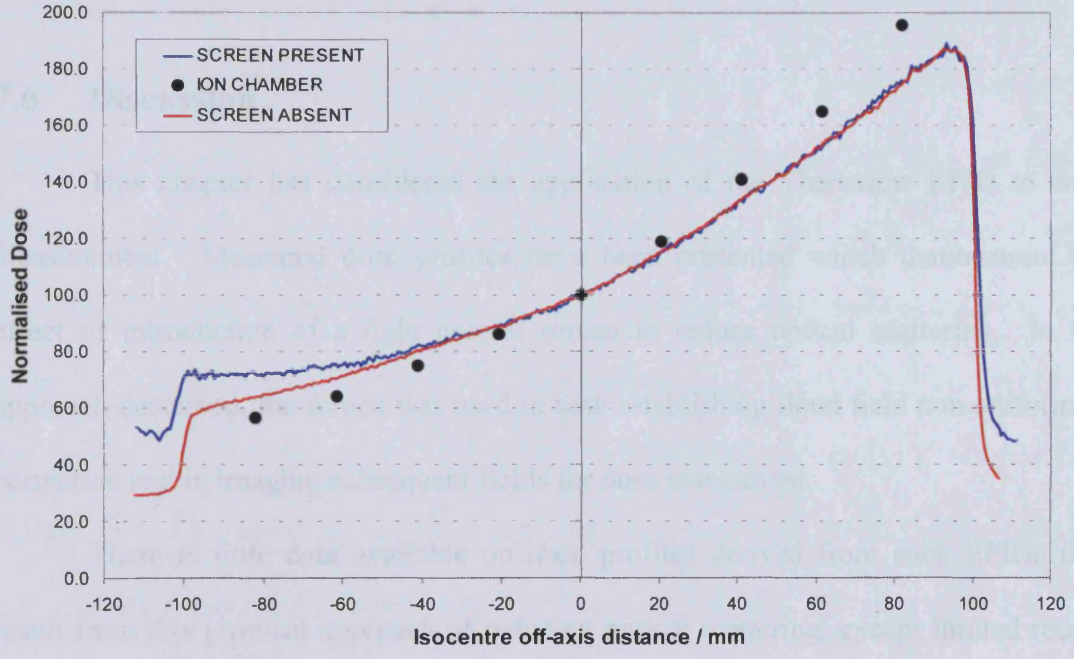

Figure 7-22 (a) and (b): Dose profiles for 20.0 x 20.0 cm dynamic wedge fields showing effect of light control screen (a) crossplane axis, (b) inplane axis. IC data is also shown.

For the crossplane axis (Figure 7-22(a)) there is little difference introduced by the screen over the low dose end of the wedge and both profiles are higher than IC data by up to a maximum of 5 % at – 82 mm off-axis. At the high dose end, introducing the screen results in measured doses up to 10 % larger, which agrees reasonably well with

the IC data. It is interesting to note that the highest dose region of the wedge has *not* been correctly measured with the screen present: beyond 79 mm off-axis the dose profile is flattened. This is attributable to delay in triggering of the Theraview EPID for the small collimator opening (Chapter 7.3) at the beginning of this sequence (which corresponds to this region) together with the optical attenuation of the light control screen which exacerbates the effect (Chapter 7.3.2).

For the inplane axis, there is little effect of the light control screen at the high dose end of the wedge. At the low dose end the light control screen increases measured doses by over 10 %. There is worse agreement with IC data than for the crossplane axis: at the high dose end the difference at 82 mm off-axis is over 20 %.

7.6 Discussion

This chapter has considered the application of the Theraview EPID to dose measurement. Measured dose profiles have been presented which demonstrate the effect of introduction of a light control screen to reduce optical scattering. In the approach described, the screen was used in both establishing flood field non-uniformity correction and in imaging subsequent fields for dose assessment.

There is little data available on *dose* profiles derived from such EPIDs that result from this physical approach of reducing optical scattering, except limited recent data reported from the Royal Marsden Hospital (Sutton, UK) using Theraview: Partridge *et al.* (2000a) showed an 'integrated intensity' image for a DMLC breast treatment acquired using an integration period of 0.25 s (one image per second), which showed agreement within 5 % with the incident fluence obtained from a planning system. However, no systematic comparison of a range of plain and wedge field sizes has been presented, as with this present work. The results presented here suggest that

the light control screen introduces only small changes to the measured two-dimensional dose data. Data on the magnitude and spatial distribution of optical scatter presented by Partridge *et al.* (1999b) suggest that the signal associated with optical scatter can be up to 15 % of the primary signal for the Theraview EPID. On introducing the screen this was reported to be reduced to a fairly uniform contribution of the order of 1 - 2 %. The observed effect of the screen on measured dose profiles in this present work appears somewhat smaller and is at most a reduction of around 5 % at extreme off-axis distances for the largest field size (20.0 cm x 20.0 cm at isocentre *e.g.* Figure 7-19(d)).

It may be that the screen used here provides less rejection at large angles to normal incidence than the one used by Partridge *et al.* (1999b), although the screens have been provided by the same manufacturer (3M UK, Bracknell, UK). Partridge *et al.* (1999b) reported that their screen had a transmission of 75 % at normal incidence, which reduced to 35 % at 15° (*i.e.* 47 % of normal incidence), and was completely extinguished by 30°. The angular dependence of the transmission of the screen used in this study has been presented in Chapter 7.4.1.2 (Figure 7-13) and is somewhat less effective. Although transmission at normal incidence in this case (33 %) was much less than in the case of Partridge *et al.* (1999b), at 15° this only reduced to 20 – 22 % (*i.e.* around 64 % of normal incidence) which is much greater than for the screen used by Partridge *et al.* (1999b). Furthermore, at 30° transmission was still around 3 - 4 % (*i.e.* around 10 % of that at normal incidence).

In this present study, dose profiles have been compared to IC measurements in-air at the same SDD as the EPID using a 6 MV build-up cap. In the case of the static plain fields the effect of the screen was small, and its introduction reduced off-axis dose below that measured by the IC, and the IC data agrees better with EPID data measured *without* the screen. However, caution must be exercised in the comparison of IC data

with that derived from the EPID which is based on a copper plate/phosphor screen detector. This is a subject of current interest due to effects of energy dependence in the copper plate/phosphor screen. This was proposed by El-Mohri *et al.* (1999) who performed relative dosimetry with a flat-panel EPID based on a amorphous silicon photodiode array, which is normally used with an overlying copper plate/phosphor screen. Dose profiles were measured with the panel 'sandwiched' in phantom material with a build-up depth of d_{max} using two detector configurations: *indirect detection*, in which a 1 mm copper plate and a Gd_2O_2S:Tb phosphor screen acted as an x-ray-to-light converter overlying the photodiode array, and an *indirect detection* configuration, in which the copper/ Gd_2O_2S:Tb was removed and the photodiodes acted as direct radiation detectors. For indirect detection the system was approximately 10 times less sensitive per unit dose, but showed better agreement between IC data measured at d_{max} in water: for a 15.0 x 15.0 cm field at 6 MV, indirect detection gave doses up to 7 % *lower* inside the field boundary and up to 13 % *higher* outside, compared to IC data. However, the direct detection profiles agreed within 1 % with IC data within the field boundary. El-Mohri *et al.* (1999) attributed this to a higher relative response of the phosphor (compared to the IC) for the low energy scatter component of the radiation field. This causes an enhanced response on centre axis compared to off-axis positions within the field, and an enhanced response outside the field. They quoted an effective atomic number (Z_{eff}) for the phosphor as approximately 60, compared with the photodiode alone (Z_{eff} = 14) giving a response with greater energy dependence for the phosphor. Differences at 15 MV between indirect detection and IC data, particularly outside field boundaries, were less pronounced, which was thought to be due to the higher energy scatter component at 15 MV. At both 6 and 15 MV, for a range of field sizes (5.0 x 5.0 cm to 20.0 x 20.0 cm), agreement between IC data and direct detection

was better than 1 % within the field boundary at up to 5.0 cm water depth. The reduced doses compared to IC data within the plain field boundary for *indirect detection* (*i.e.* copper plate/phosphor screen in place) are consistent with the dose data presented in this work with the light control screen present, which lowers the off-axis dose signal and thus increases the difference compared to IC data.

Munro *et al.* (2000a, 2000b) have identified a similar effect for a film based imaging system comprising a copper/Gd_2O_2S:Tb front screen (*i.e.* similar to camera-based or flat-panel EPIDs) and a Gd_2O_2S:Tb back screen (EC-L, Eastman Kodak Company, Rochester, NY, USA). Munro *et al.* (2000a, 2000b) developed an 'electronic cassette' comprising a 1 mm copper/220 mg cm^{-2} Gd_2O_2S:Tb screen, light pipe, photodiode and electrometer, to assess signal from the screen under different geometries. For large field sizes, moderate separations and a cassette-patient separation of 10 cm, the response of the copper/Gd_2O_2S:Tb screen was up 30 % greater than an IC, rising to as much as 70 % in extreme cases. The effect was attributed to the over-response of Gd_2O_2S:Tb to low energy photons scattered from the patient. The effect was demonstrated further in beam profile measurements using an EC-L cassette and conventional verification film (XomatV-2, Eastman Kodak Company, Rochester, NY, USA) in water equivalent phantom material for a 40.0 x 40.0 cm field size. The copper/Gd_2O_2S:Tb screen (EC-L cassette) showed over-response within the central region resulting in reduced relative doses measured off-axis, which is consistent with the data presented in this work with the light control screen present compared to IC data. Munro *et al.* (2000a, 2000b) suggested that a possible solution to reduce the scatter signal would be to use a large air gap, or place a high-Z attenuator up-stream of the image receptor. They showed that on introducing a 1.5 mm tungsten plate (Z=74) the response of the electronic cassette with field size was similar to the IC.

Dose profile data demonstrating a consistent effect on measured off-axis ratios for high-Z materials was also observed by Zhu and Yeo (1999) in a comparison of film and IC data. Film was used in solid water cassettes and in two commercial high atomic number screen cassettes: 1 mm Cu (Z=29) front/0.4 mm polyester back, and 0.25 mm Pb (Z=82) front and back. For a 20.0 x 20.0 cm field, off-axis doses for the high-Z cassettes were up to 5 % less than those measured by the chamber, suggesting that the film response was up to 5 % higher on central axis. Although differences attributable to the high-Z cassette were less marked for smaller field sizes, the solid water cassette consistently showed best agreement with the IC (maximum deviation 1–2 %). Zhu and Yeo (1999) also attributed the effect to the high-Z cassettes causing a relatively higher on-axis response of the film to low energy scattered photons.

It is interesting to note that the effect of high-Z detector materials on measured dose profiles have *not* been explicitly considered by the Rotterdam group in dosimetry studies with the camera-based SRI-100 EPID (*e.g.* Heijmen *et al.* 1995, Pasma *et al.* 1999b). The group used an IC to measure doses, and compared these to doses derived from the EPID. The IC was placed at a fixed depth in a polystyrene mini-phantom, which was 5.0 cm thick and 7.0 x 7.0 cm in cross-section. The depth of the chamber within this phantom was carefully chosen to minimise variations in the ratio of the EPID signal to the IC signal on central axis for various thicknesses of phantoms and exit-surface detector separations. Such geometry changes alter the relative amount of primary and scattered radiation reaching the detector (*e.g.* Yeboah and Pistorius 2000). The effect was therefore being minimised through the choice of chamber depth within the mini-phantom. For example, at 25 MV (d_{max} 3.0 cm) using 2.65 mm steel build-up on the EPID (water equivalent depth 21 mm) a chamber depth of 2.5 cm was used (Pasma *et al.* 1998). At 10 MV a chamber depth of 2.0 cm was used for the same EPID

build-up (Pasma *et al.* 1999b), which was described as the 'effective measurement depth' of the EPID. Clearly the optimal build-up depth for the IC is not simply matched to the metal plate thickness on the EPID. Pasma (Private Communication, 2000) gave the d_{max} value of the 10 MV beam as 2.0 cm water, and acknowledged that the cause of the different optimal chamber build-up depths was not well understood, but that depths are close to the maximum dose for each energy studied. However, despite this simplification, the method reported by the Rotterdam group for dose measurement with their EPID gave excellent agreement with IC data: agreement to within 1 % (1 SD) for open and wedge fields, and 2 % for DMLC have been reported (Pasma *et al.* 1998, 1999b).

In the case of the static wedge field, the dose measurements derived from the EPID presented here suggest dose gradients less than that suggested by the IC data. It is believed that energy dependence of the copper plate/phosphor screen detector may also be contributing to this. This is supported by a relative dose profile measured at d_{max} for a 60° wedge (15.0 x 15.0 cm) by El-Mohri *et al.* (1999) using the *direct detection* configuration of their flat-panel EPID (*i.e.* omitting the copper/phosphor screen), which showed good agreement with IC data. The spectral differences between the high dose and low dose regions of a wedge field are demonstrated by the spectra in Figure 7-23 obtained for a Varian 6 MV accelerator for a 20.0 x 20.0 cm 45° wedge field. Photon spectra are shown on central axis, at - 7.5 cm off-axis (corresponding to the 'thin' end of the wedge) and + 7.5 cm off-axis (corresponding to the 'thick' end of the wedge). As the thickness of the wedge attenuator increases (*i.e.* moving from – 7.5 cm to + 7.5 cm off-axis), the mean photon energy shifts to higher energies due to increased attenuation of low energy photons.

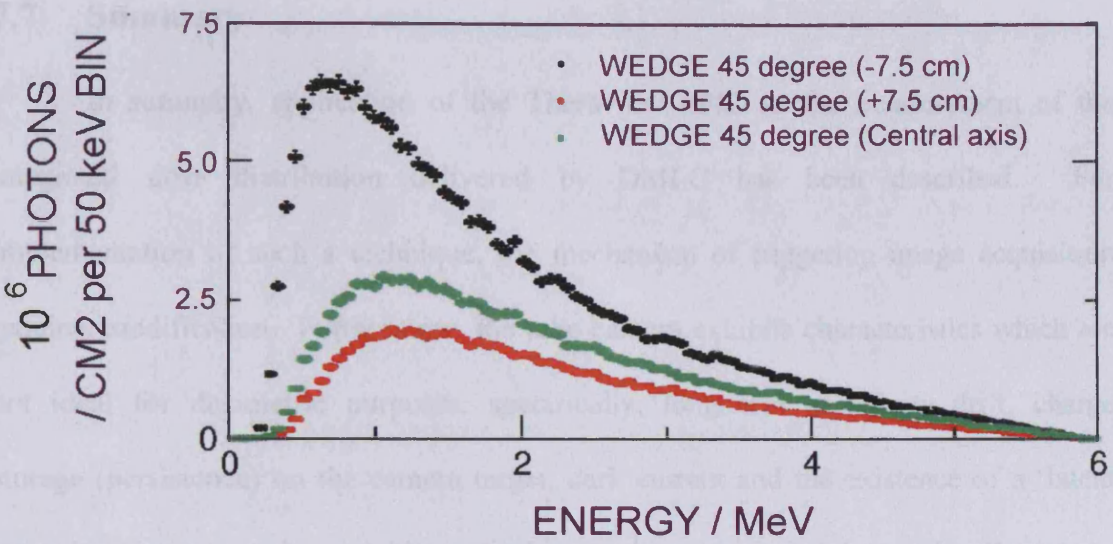

Figure 7-23: Photon spectra for a 6 MV 45° wedge field. Spectra are shown for a 20.0 x 20.0 cm field on central axis and ± 7.5 cm off-axis. Data obtained from Monte Carlo techniques for a Varian 6 MV accelerator (courtesy of Emiliano & Lewis, Velindre Hospital, Cardiff, UK).

In the EPID data presented here, no account has been of camera target dark currents (Chapter 5.3.6). It is not possible to measure dark current directly with the present system due to the trigger mechanism, and as such no correction could be applied. Images were acquired with integration periods in the range 0.25 s to 1.00 s. From the data presented in Chapter 5.3.6, the dark current contribution for these two extremes will vary by a factor of four. As larger integration periods were used with the louver and for the wedge, these measurements would be most affected. In the case of a wedge field, dark current contributions would reduce the dose gradient apparent on a plotting normalised dose, which may also contribute to the differences in dose gradients measured for the wedge using the EPID and IC (Figure 7-20 and 7-21).

The dynamic wedge data (Figure 7-22(a) and (b)) is complicated by the presence of dark current, optical scatter and charge storage on the camera tube, which will all affect the measured dose profile. The effect of delay in the triggering of image acquisition for the present hardware is also demonstrated (Figure 7-22(a)) for the dynamic wedge with the optical control screen present.

7.7 Summary

In summary, application of the Theraview EPID to the measurement of the integrated dose distribution delivered by DMLC has been described. For implementation of such a technique, the mechanism of triggering image acquisition requires modification. Furthermore, the tube camera exhibits characteristics which are not ideal for dosimetric purposes: specifically, long-term sensitivity drift, charge storage (persistence) on the camera target, dark current and the existence of a 'latent image'. Theraview also exhibits optical scattering, which is inherent in all camera-based EPIDs. In this present work a light control screen, which provides optical rejection at high angles of incidence, was studied as a means of reducing the effect on measured dose distributions. However, the screen only introduces small changes in the measured two-dimensional dose data compared with the magnitude of optical scatter reported for the system, and it was felt that the screen was limited in its effectiveness. Furthermore, caution must be exercised in the comparison of IC data with that derived from the EPID, which is based on a copper plate/phosphor screen detector, due to effects of energy dependence in the copper plate/phosphor screen. This leads to a higher relative response for the low energy scatter component of the radiation field, causing an enhanced response on centre axis compared to off-axis positions within the field.

Chapter 8. Conclusions and further work

8.1 Conclusions

The development of methods for dosimetric verification of IMRT produced by a linear accelerator operating in dynamic mode is central to the clinical introduction of IMRT. Such techniques are significantly more complex than static field radiotherapy and involve inverse treatment planning, modelling of doses delivered dynamically, and complex prescription files which must be handled without data corruption. Furthermore, operation of linear accelerators in dynamic mode is a significant development compared with conventional radiotherapy techniques using static fields, and often does not allow intuitive interpretation of dose delivery. In order to confirm the stages involved in preparing such a dose delivery together with accelerator operation, and to gain confidence in the new technology applied in the clinic, both verification techniques and methods for quality assurance of accelerator operation must be developed.

The work presented here is based on the prototype Elekta SL*i* DMLC research system (Elekta Oncology Systems, Crawley, UK). Within the UK, this system has recently been introduced clinically at the Christie Hospital (Manchester) and the Royal Marsden Hospital (Sutton). The manufacturers acknowledge various shortcomings of the present system, which further emphasises the need for verification and accelerator quality assurance. These include temporal lag of the DMLC system, operation of the accelerator in a non-clinical mode and lack of confirmation of MU, beam energy and gantry, collimator or table rotation between the DMLC control system and the accelerator.

Within both the radiotherapy and radiotherapy physics communities there is considerable interest in the field of IMRT and IMRT verification at present. As a

result, some of the work reported in the literature on the application of EPIDs has occurred concurrently with this study.

A central component to this study has been the development of a novel accelerator synchronised multi-channel electrometer (SME) designed for the continuous measurement of time varying dose signal, with high temporal resolution, from both ion chamber and semiconductor diode radiation detectors. The design and performance of the system, which includes an optically isolated interface to the accelerator dosimetry system, has been reviewed in Chapter 2. The SME has been exploited in various measurements in this present work, and is intended for *in vivo* and *in vitro* measurement of dose delivery during IMRT and accelerator beam-start quality assurance.

In Chapter 3 the SME was used to evaluate a novel method of collimator position verification during DMLC using a specially constructed array of strip ionisation chambers which located at the accessory tray of the accelerator and was oriented such that the strips were parallel to the direction of collimator motion. The prototype chamber, described and characterised in Chapter 3, was based on two banks of ten strip ionisation chambers in opposing banks formed from copper clad epoxy glass board of the type intended for printed circuit board production. Over a period of 130 days the chambers showed a mean sensitivity drift of +4.0 %. Fluctuations in sensitivity over a 9 % range were also evident, and were thought to be attributable to changes in chamber volume with temperature, associated with bowing of the construction and hence alteration of the effective collecting volume. The chamber was therefore not suitable for long-term measurements and all chamber signals were normalised to an open field signal. In the case of a dynamic wedge (in which an entire collimator bank moves simultaneously), signal from a central pair of strip ionisation chambers could be measured against accelerator MU using the SME. On comparison

of measured chamber signal with that calculated based on static field irradiations over the range of collimator motion, a systematic lag in the collimator position during DMLC was identified. This was estimated as 0.67 ± 0.08 s and is a function of the research-release Elekta SL*i* DMLC system. Repeated measurements of the wedge sequence showed the chamber signal as a function of accelerator MU to be extremely reproducible. Based on the deviation of chamber signal from the mean, an estimate for the reproducibility of collimator position of better than ±0.4 mm was made for this case with collimator speeds of up to 5.8 mm s^{-1}. The chamber signal for the dynamic wedge could also be modelled, based on the length of strip chamber irradiated and ignoring signal associated with scattered radiation or collimator transmission together with the effects of longitudinal variation in chamber sensitivity, off-axis dose rate variations and leaf penumbra. For the dynamic wedge a maximum deviation of 2.1 % (mean 0.6 %, SD 1.1 %) was obtained between chamber signal calculated from static field data and that modelled. Further test cases using DMLC sequences delivering sinusoidal dose modulations were performed. In the case of *both* collimator banks moving together, creating dose modulation parallel to leaf motion (which is an extension of the dynamic wedge), a maximum deviation between measured and modelled chamber signals of 7.7 % was obtained (mean 1.7 %, SD 2.6%). For leaves moving independently (the general case for DMLC) deviations amounted to 13.0 % maximum (mean 3.6%, SD 6.5 %). It was therefore concluded that the strip ionisation chamber was a useful device for performing collimator position verification in the case of dynamic wedges, based on chamber signals either calculated from static field irradiations or modelled, but was unsuitable for cases where the leaves moved independently. The performance of the strip ionisation chamber and the SME for collimator position verification in dynamic

wedge is substantially better than an implementation based on a single strip ionisation chamber reported by Kerr *et al.* (1997, 2000) on a Varian accelerator.

Chapters 4 – 7 are concerned with the application of a tube camera-based EPID Theraview™ (Cablon Medical BV, Leusden, The Netherlands) to IMRT verification. In Chapter 4 the characteristics of the phosphor (Gd_2O_2S:Tb) used in such EPIDs under therapy beam irradiation were investigated by means of direct measurement of phosphor luminescence using a photomultiplier tube (PMT). Using an oscilloscope the luminescent signal following each radiation pulse (approximately 3 μs duration) was observed to follow published data for primary luminescence (dominant exponential lifetime 558 μs). Using the SME, the luminescent signal from the phosphor was measured against the incident dose rate measured by a semiconductor diode detector at beam-start and beam termination. Measurements at beam termination following doses of up to 4.4 Gy showed no long-lived optical signal from the phosphor (afterglow) above the noise level of the system (SD 0.17 %). Measurements also confirmed that the optical signal from the phosphor was independent of accelerator PRF. Prior to this study, it was not readily apparent from the literature that the phosphor did *not* exhibit afterglow and that the optical signal was independent of accelerator PRF, despite widespread use of this phosphor both in camera-based EPIDs and more recently in flat-panel EPIDs based on amorphous silicon photodiode arrays.

Chapter 5 considered the properties of the EPID, which are relevant to its application to dosimetry. This EPID had not been studied previously, and the properties established are predominantly those of the tube camera. The dose response using the 'Single' mode of acquisition has been presented for two EPID systems. During initial work the reproducibility of the systems was 0.5 % (SD). However, the reproducibility was observed to be significantly reduced in studies 18-24 months later.

This was thought to be attributable to the mechanism by which image acquisition was triggered which would become increasingly susceptible to noise as the system sensitivity decreased with age. For two systems the decrease in sensitivity could be described well by a linear reduction of 0.04 % day^{-1} (approximately 14.5 % per annum). Within the limits of a 10.0 x 10.0 cm isocentre field the change in sensitivity was spatially uniform over a measurement interval of 68 days. This suggests that the spatial response of the system would be sufficiently stable for two-dimensional dose measurements. However, correction would be necessary for the spatial non-uniformity evident for the system, and for non-ideal optical effects within the imaging chain. It was found that for absolute dosimetry a 'warm-up period' for the camera control unit of at least 40 minutes is necessary in order for the sensitivity of the system to stabilise. Consideration must also be given to a 'dose history effect' in which subsequent images exhibit residual signal from the previous field attributable to charge storage (persistence) on the camera target. In repeat imaging following irradiation to 0.19 and 1.9 Gy the effect was observed to reduce with a half-life of approximately 40 seconds. Spatially non-uniform dark current was also identified for the camera target, which become increasingly significant on increasing the camera integration period. The EPID does not perform dark current subtraction, and in the present system the mechanism by which image acquisition is triggered does not allow dark current images to be acquired directly, thus making correction impossible. With regard to the geometric accuracy, inspection of an image formed by a regular transmission phantom showed no geometric distortion greater than ±1 mm across the field of view. On gantry rotation the system was shown to introduce movement in the image of an isocentrically located object of up to 5 mm at isocentre, which would require correction. In a recent study of the EPID, Partridge *et al.* (2000a) found similar geometric distortion and suggested that geometric

accuracy of ± 2 mm is likely on the basis of geometric distortion and the accuracy by which translations observed on gantry rotation could be corrected. This is likely to be the case for the system studied here. However, rigorous quality control of geometric calibration is needed due to long-term variation in pixel size calibration of up to 4 %, thought to be attributable to changes in the horizontal and vertical scan rates within the tube camera.

In Chapter 6 the EPID was applied to collimator position verification during DMLC. This was based on a method to record the cumulative accelerator MU value during the acquisition of portal images. The approach used an optically isolated interface to the beam blanking camera control signal as a trigger input to the SME in order to record the cumulative accelerator MU value at the beginning and at the end of each period of image formation. The approach allowed the EPID to be applied to collimator position verification in DMLC, which was demonstrated using a dynamic wedge test prescription. The customised interface had no effect on the operation of the commercial EPID and was therefore left permanently *in situ* during normal clinical use of the EPID. The current implementation has a maximum delay of 15 ms between a change in the status of the camera control signal and recording the accelerator MU that could be improved with implementation in hardware. The technique offers improved dose resolution from the approach of Partridge *et al.* (2000a), who used a dose display within the field of view of the Theraview EPID. Additionally, the technique avoids reduction of the EPID's field of view, does not require modification of the commercial system and provides accelerator $1/64^{th}$ MU values directly. The general principle of using an EPID control signal to trigger recording of accelerator MU may be applicable to other EPIDs with suitable knowledge of the accelerator dosimetry system.

In Chapter 7 the Theraview EPID was considered for measurement of the integrated dose distribution delivered by DMLC. Various characteristics of the system that complicate this application have been identified including sensitivity drift, the existence of a 'latent image' (on which all radiation images are superimposed), the mechanism of triggering image acquisition and charge storage (persistence) on the camera target. Assessment of the integrated dose distribution delivered by DMLC using this EPID requires:

- Modification of the trigger mechanism, for which a method has been proposed.
- Removal of image dark current, which could include the effect of integration period. The approach would involve two-dimensional correction since dark currents have been shown to be spatially non-uniform.
- Reduction of charge storage on camera target. This may be possible by improving the characteristics of the tube camera by optimising set-up, or by replacement with a camera based on charge coupled device (CCD) or charge injection device (CID) technology.
- Overcoming optical scattering within the imaging chain, which is inherent in all camera-based EPIDs.

In this present work a light control screen, which provides optical rejection at high angle of incidence, was studied as a method of reducing optical scattering. The effect on the dose distribution measured with the EPID was observed to be small, suggesting that the screen is of little benefit in removing the effects of optical scatter. This is the first reported data on the effect of such a screen on dose measurements with a camera-based EPID.

It was concluded that the collimator position verification during dynamic multileaf collimation could be performed using a strip ionisation chamber for the

special case of a dynamic wedge. Collimator position verification can also be achieved using the camera-based Theraview™ EPID in more general cases where leaves move independently. However, assessment of the integrated dose distribution using this EPID is complicated by the characteristics of the video system and requires modification of the EPID's trigger mechanism. Dose measurements also exhibit the effect of optical scattering, which is not significantly affected by introducing an optical rejection screen. For 20.0 x 20.0 cm fields, dose profiles EPID data agrees with ionisation chamber measurements in-air for plain fields within 6 %, and for static and dynamically produced wedged fields within 15-25 %. It was therefore concluded that whilst both approaches have limitations, they can be applied to the verification of IMRT within limits, but further work is required to develop an ideal method.

8.2 Further work

The SME has been exploited in various measurements in this present work, and it is anticipated that the device will be of value in other measurement applications in IMRT. These include *in vitro* and *in vivo* dosimetry, and accelerator quality assurance, particularly measurement of beam flatness, output and energy during beam-start. At present, because of limitations of the serial link to the PC, collected data is stored at the SME during the measurement, and saved back to the PC at the end of the exposure. Data can therefore only be analysed off-line. However, the present hardware includes provision for a parallel interface, which would allow real-time visualisation of the dose signals, and is the subject of future development. The SME may prove particularly useful for *in vivo* dosimetry during DMLC since it allows direct, continuous monitoring of dose delivery to patients when used in conjunction with semiconductor diode detectors. There is also considerable interest in gating accelerator dose delivery based

on respiration synchronisation (Ohara *et al.* 1989, Kubo *et al.* 2000), which may benefit from continuous dose monitoring.

For clinical implementation of a strip chamber for collimator position verification in the case of dynamic wedge delivery, the chamber would require both manufacture in different materials in order to improve long-term sensitivity stability, and re-design to overcome the effect of atmospheric conditions. As already discussed, the construction of accelerator monitor chambers could provide a good basis for this (Greene and Williams 1997). It may also be desirable to construct the device on an optically transparent membrane to avoid obscuring the light field when located at the radiation beam aperture during clinical use.

Cablon Medical BV (Leusden, The Netherlands), the commercial manufacturers of the Theraview™ EPID, are believed to be considering upgrade of the camera to CCD technology. This type of camera is used in the SRI-100/*i*View EPIDs and would overcome some of the inherent difficulties identified for dosimetry applications of a tube camera. The Theraview EPID is currently being considered locally for on-line collimator position verification ('leaf-tracking') by means of a separate control PC incorporating a frame grabber which, via optical isolation, controls the Theraview CCU and receives unprocessed video signal. It is proposed to capture a frame of incoming video whilst simultaneously recording cumulative accelerator MU as described for the present system. In this way it would be possible to verify collimator positions on-line *i.e. in real-time.* This could be performed by visual comparison against a template overlay (based on prescribed movement and measured accelerator MU) which is the approach implemented on-line by James *et al.* (2000) using the SRI-100 and a limited number of images. Comparison could also be made using an algorithm to identify leaf positions, which could accommodate a range of detected signals and gantry/collimator

rotations. In addition, it would be possible to predict collimator movement during the period of image formation (based on captured doses), which James *et al.* (2000) have shown to impose limitation on the use of a maximum gradient edge detection algorithm for long integration periods or fast moving leaves. It may be necessary for the system to include a method of overcoming drift in pixel size calibration, which has been observed to change by up to 4 % after 1 month and is thought to be attributable to drift in video scan rates of the tube camera. As discussed, the current implementation has a maximum delay of 15 ms between a change in the status of the camera control signal and recording the accelerator MU that could be improved with implementation in hardware. This would also allow twenty channels of dose data to be captured simultaneously by the SME with no additional latency. In the current implementation it was not possible to operate the multi-channel dose collection mode of the SME whilst simultaneously recording accelerator MU triggered by the beam blanking control signal, due to additional software delay of variable magnitude (estimated maximum 80 ms).

It may be possible to extend an EPID-based leaf tracking system to routine quality assurance and assessment of the performance of DMLC systems. Methods of quality assurance for static field therapy are well understood, but are presently under development for DMLC systems. Chui *et al.* (1996) at Memorial Sloan-Kettering Cancer Centre (MSKCC) (New York, USA) have reported a range of tests (designed for the Varian DMLC) based on the use of verification film to consider stability of leaf speed, leaf acceleration/deceleration, and positional accuracy. It may be possible to develop and implement such tests using an EPID for the delivery system described here. The MSKCC group has highlighted the importance of mechanical accuracy for dosimetry in DMLC (LoSasso *et al.* 1998, Chui and LoSasso 2000), as well as recent work by Budgell *et al.* (2000) for the Elekta DMLC system.

The method presented for assessment of the integrated dose distribution using the EPID could be extended to two-dimensional measurement by using a two-dimensional measurement of the dose rate distribution provided by the flood field. This could be achieved by scanning an ion chamber using an empty two-dimensional scanning water tank. It is intended to extend the measurements to comparison against predicted dose distributions based on modelled dose distributions at the portal imager in collaboration with MDS Nordion Therapy Systems (Uppsala, Sweden) using Helax-TMS (Dahlgren and Ahnesjö 2000). However, the energy dependence of a Cu/Gd_2O_2S:Tb screen which has been discussed in Chapter 7.6 must be investigated as part of such a dosimetry study, and the characteristics are applicable to both camera-based EPIDs and flat-panel EPIDs based on photodiode arrays operating in indirect detection mode. The measurement technique based on a photomultiplier tube developed in this present work could be applied to such measurements using a light pipe to collect optical signal from a small portion of the phosphor screen. This could be used to provide profile or two-dimensional data using a scanning system, which could be compared with modelled or measured ion chamber data in various geometries in order to characterise the Cu/Gd_2O_2S:Tb detector. The technique has the advantage of removing the optical mirror present in camera-based EPIDs and thus eliminating the effects of optical scattering. The camera is also removed from the detection system.

There is considerable interest in the future investigation of flat-panel EPIDs based on amorphous silicon photodiode arrays for dosimetry and IMRT verification. Current devices show good long-term stability (El-Mohri *et al.* 1999), frame rates of up to 4 frames s^{-1} (El-Mohri *et al.* 1999), clearly allowing devices to be considered for dynamic dose delivery, and have the inherent advantage of *not* exhibiting optical scattering (Munro and Bouius 1998) unlike camera-based EPIDs. Furthermore, flat-

panel EPIDs allow implementation of the direct detection mode (*i.e.* omission of copper plate/phosphor screen), which is believed to complicate dosimetry due to the energy dependence of these high-Z components (Chapter 7.6). El-Mohri *et al.* (1999) have also suggested that such EPIDs could also be used for dosimetry in an indirect detection mode using scintillators with water-equivalent properties.

Both the major accelerator manufacturers have released flat-panel EPIDs to test sites internationally, and the first UK system (developed by Varian Associates, Palo Alto, CA, USA in conjunction with the University of Michigan, Ann Arbor, Michigan, USA (Antonuk *et al.* 1998)) is under investigation at the Royal Marsden Hospital (Fulham Road, Chelsea). Scanditronix-Wellhöfer (Schwarzenbruck, Germany) are also developing a flat-panel detector based on a photodiode array with Gd_2O_2S:Tb screen purely for dosimetry purposes, and intended for mounting at the accelerator beam aperture (R Plompen, Scanditronix-Wellhöfer, Personal Communication, 2000) although this is a matter of some commercial sensitivity. Their prototype has been characterised (Paul *et al.* 1998) and a subsequent device, which acquired an image and accelerator MU at 80 ms intervals and allowed on-line analysis, has been claimed to show promise for both collimator position verification and the measurement of integrated dose distribution (Paul *et al.* 2000).

There are however several complications in the use of flat-panel EPIDs for dosimetry and IMRT verification which must be resolved in the future. There are concerns regarding lifetime of the system components (*i.e.* radiation hardness) (Boudry and Antonuk 1996). The devices are reported to exhibit image lag *i.e.* residual signal following read-out of the original exposure due to charge trapping (Siewerdsen & Jaffray 1999a, 1999b). Motion distortion associated with scanned read-out must also be overcome (Smitsmans *et al.* 2000). Furthermore, read-out must be synchronised

with the dose pulse train to avoid artefacts (Munro and Bouius 1998) and for IMRT applications it has been suggested (H Porter, Western General Hospital, Edinburgh, Private Communication, 2000) that there may be conflict between the dynamic control system of the Varian accelerator (which controls the dose pulse sequence) and required synchronisation of the flat-panel EPID.

The application of flat-panel EPIDs to dosimetry and IMRT verification is therefore likely to occupy substantial future research effort. The devices show promise in overcoming limitations of camera-based EPIDs, in particular optical scattering and non-ideal characteristics of the video system such as those highlighted in this present work.

Chapter 9. References

Agazaryan,N; Solberg,TD; Arellano,AR; Paul,TJ (2000): Dynamic multileaf collimation and three-dimensional verification of IMRT. Proceedings of the XIIIth International Conference on the Use of Computers in Radiotherapy, May 22-25 2000, Heidelberg, Germany, 280-282. Ed. Schlegel,W & Bortfeld,T, DKFZ, Heidelberg, Germany. Springer-Verlag, Heidelberg. ISBN 3-540-67176-5.

Althof,VGM; de Boer,JCJ; Huizenga,H; Stroom,JC; Visser,AG; Swanenburg,BN (1996): Physical characteristics of a commercial electronic portal imaging device. Med. Phys. 23(11), 1845-1855.

Antonuk,LE; El-Mohri,Y; Jee,K-W; Siewerdsen,JH; Maolinbay,M; Scarpine,VE; Sandler,H; Yorkston,J (1998): Initial performance evaluation of an indirect-detection, active matrix flat-panel imager (AMFPI) prototype for megavoltage imaging. Int. J. Radiation Oncology Biol. Phys. 42(2), 437-452.

Antonuk,LE; Boudry,J; Yorkstin,J; Wild,CF; Longo,MJ; Street,RA (1990): Radiation damage studies of amorphous-silicon photodiode sensors for applications in radiotherapy x-ray imaging. Nuclear Instruments and Methods in Physics Research A 299, 143-146.

Beavis,A; Kennerley,J; Whitton,VJ (1998): Virtual dosimetry: quality control dynamic intensity modulated radiation therapy. Proceedings of Radiology 1998-Imaging, Science and Oncology, 1-3 June 1998, 9.

Berzins,GJ; Lumpkins,AH; Smith,HL (1983): Characterization of fluorescent screen for imaging applications with MeV neutrons and photons. Opt. Eng. 22(5), 633-642.

Blasse,G; Grabmaier,BC (1994): Luminescent Materials. Springer-Verlag, Berlin.

Boag,JW (1966): Ionization chambers. In: Radiation dosimetry. 2nd ed. Vol. II. (Eds: Attix,FH; Roesch,WC; Tochilin,E) Academic Press, New York, USA.

Boon,SN; van Luijk,P; Schippers,JM (1998): Fast 2D phantom dosimetry for scanning proton beams. Med. Phys. 25(4), 464-475.

Boon,SN; van Luijk,P; Böhringer,T; Coray,A; Lomax,A; Pedroni,E; Schaffner,B; Schippers,JM (2000): Performance of a fluorescent screen and CCD camera as a two-dimensional dosimetry system for dynamic treatment techniques. Med. Phys. 27(10), 2198-2208.

Bortfeld,T; Boyer,AL; Schlegel,W; Kahler,DL; Waldron,TJ (1994): Realization and verification of three-dimensional conformal radiotherapy with modulated fields. Int. J. Radiation Oncology Biol. Phys. 30(4), 899-908.

Boudry,JM; Antonuk,LE (1996): Radiation damage of amorphous silicon, thin-film, field-effect transistors. Med. Phys. 23(5), 743-754.

Boyer,AL; Geis,P; Grant,W; Carol,M (1997): Modulated beam conformal therapy for head and neck tumours. Int. J. Radiation Oncology Biol. Phys. 39(1), 227-236.

Brahme,A (1984): Dosimetric precision requirements in radiation therapy. Acta Radiol. Oncol. 23, 379-391.

Brahme,A (1987): Design principles and clinical possibilities with a new generation of radiation therapy equipment. Acta Oncol. 26(6), 403-412.

Budgell,GJ; Sykes,JR; Wilkinson,JM (1998): Rectangular edge synchronisation for intensity modulated radiation therapy with dynamic multileaf collimation. Phys. Med. Biol. 43, 2769-2784.

Budgell,GJ; Mott,JHL; Willimas,PC; Brown,KJ (2000): Requirements for leaf position accuracy for dynamic multileaf collimation. Phys. Med. Biol. 45, 1211-1227.

Burman,C; Chui,C-S; Kutcher,G; Leibel,S; Zelefsky,M; LoSasso,T; Spirou,S; Wu,Q; Yang,J; Stein,J; Mohan,R; Fuks,Z; Ling,CC (1997): Planning, delivery, and quality assurance of intensity modulated radiotherapy using dynamic multileaf collimator: A

strategy for large-scale implementation for treatment of carcinoma of the prostate. Int. J. Radiation Oncology Biol. Phys. 39(4), 863-873.

Carol,MP (1995): Peacock™: A system for planning and rotational delivery of intensity-modulated fields. Int. J. of Imaging Sys. Tech. 6, 56-61.

Chang,J; Mageras,GS; Chui,CS; Stein,J; Wu,Q; Lutz,W (1998): Verification of intensity modulated beams using EPIDs. Proceedings of the 5th International Workshop on Electronic Portal Imaging, 29-31 October 1998, Phoenix, AZ, USA, (EPI98 Organising Committee), 97-98.

Chang,J; Mageras,GS; Chui,CS; Ling,CC; Lutz,W (2000): Relative profile and dose verification of intensity modulated radiation therapy. Int. J. Radiation Oncology Biol. Phys. 47(1), 231-240.

Chen,Y; Boyer,AL; Ma,C-M (2000): Calculation of x-ray transmission through a multi-leaf collimator. Med. Phys. 27(8), 1717-1726.

Chui,CS; Spirou,S; LoSasso,T (1996): Testing of dynamic multileaf collimation. Med. Phys. 23(5), 635-641.

Chui,C (1999): The effects of intra-fraction organ motion on the delivery of intensity modulated fields with a multileaf collimator. Med. Phys. 26(6), 1087. Proceedings of the 41st AAPM Meeting, July 25-29 1999, Nashville, TN.

Chui,C-S; LoSasso,T (2000): Quality assurance of IMRT. Proceedings of the XIIIth International Conference on the Use of Computers in Radiotherapy, May 22-25 2000, Heidelberg, Germany, 168-169. Ed. W Schlegel, T Bortfeld, DKFZ, Heidelberg, Germany. Springer-Verlag, Heidelberg. ISBN 3-540-67176-5.

Conte,L; Stucchi,P; Mordacchini,C; Bianchi,C; Monciardina,M; Novario,E; Mantovani,CR; Antognoni,P; Tordiglione,M (1997): The use of an electronic portal imaging device for exit dosimetry. Proceedings of the XIIth International Conference on

the Use of Computers in Radiotherapy, 27-30 May 1997, Salt Lake City, Utah, USA (Medical Physics Publishing, Madison, WI, USA), 279-281.

Convery,DJ; Webb,S (1998): Generation of discrete beam-intensity modulation by dynamic multileaf collimation under minimum leaf separation constraints. Phys. Med. Biol. 43, 2521-2538.

Curtin-Savard,AJ; Podgorsak,EB (1997): An electronic portal imaging device as a physics tool. Med. Dosim. 22(2), 101-105.

Curtin-Savard,AJ; Podgorsak,EB (1999): Verification of segmented beam delivery using a commercial electronic portal imaging device. Med. Phys. 26(5), 737-742.

Dahlgren,CV; Ahnesjö,A (2000): Use of a collapsed cone convolution for an initial investigation of portal dose image prediction. Proceedings of the XIIIth International Conference on the Use of Computers in Radiotherapy, May 22-25 2000, Heidelberg, Germany, 224-226. Ed. W Schlegel, T Bortfeld, DKFZ, Heidelberg, Germany. Springer-Verlag, Heidelberg. ISBN 3-540-67176-5.

Dearnaley,DP (1998): Prostate-UK. Proc. of the Meeting: Conformal Therapy: A Clinical Perspective Meeting, London, 19-20.

Dearnaley,DP; Khoo,VS; Norman,AR; Meyer,L; Nahum,A; Tait,D; Yarnold,J (1999): Comparison of radiation side-effects of conformal and conventional radiotherapy in prostate cancer: a randomised trial. Lancet 353, 267-272.

De Deene,Y; De Wagter,C; De Neve,W; Achten,E (1998a): 3D polymer gel dosimetry in conformal radiotherapy: Evaluation, artefacts and future perspectives. Abstracts of the 17th Annual ESTRO Meeting, Edinburgh UK, Rad. Onc. 48 (Suppl. 1), 195.

De Deene,Y; De Wagter,C; Van Duyse,B; Derycke,S; De Neve,W; Achten,E (1998b): Three-dimensional dosimetry using polymer gel and magnetic resonance imaging applied to the verification of conformal radiation therapy in head-and-neck cancer. Radiother. Oncol. 48, 283-291.

De Neve,W; De Wagter,C (1997): University Hospital, Ghent, implements beam intensity modulation in clinical practice. Wavelength (Elekta Oncology Systems) 1(1), 1-6.

Dirkx,MLP; Kroonwijk,M; de Boer,JCJ; Heijmen,BJM (1995): Daily dosimetric quality control of the MM50 Racetrack Microtron using an electronic portal imaging device. Radiother. Oncol. 37, 55-60.

Dirkx,MLP; Heijmen,BJM; Korevaar,GA; van Os,MJH; Stroom,JC; Koper,PCM; Levendag,PC (1997): Field margin reduction using intensity-modulated x-ray beams formed with a multileaf collimator. Int. J. Radiation Oncology Biol. Phys. 38(5), 1123-1129.

Dirkx,MLP; Heijmen,BJM; van Santvoort,JPC (1998): Leaf trajectory calculation for dynamic multileaf collimation to realize optimised fluence profiles. Phys. Med. Biol. 43, 1171-1184.

Dirkx,MLP; Heijmen,BJM (2000): Beam intensity modulation for penumbra enhancement and field length reduction in lung cancer treatments: a dosimetric study. Radiother. Oncol. 56, 181-188.

Dörner,K-J; Neumann,M (1995): Real time supervision of dynamic and intensity modulated radiation fields. Medizinische Physik 95 Rontgen Gedachtnis-Kongress, 20-23 September 1995, Wurzburg, Germany, (University of Wurzburg, Germany). Editor: J. Richter, 260-261.

Ellis,F; Hall,EJ; Oliver,R (1959): A compensator for variations in tissue thickness for high energy beams. Brit. J. Radiol. 32, 421-422.

El-Mohri,Y; Antonuk,LE; Yorkston,J; Jee,K-W; Maolinbay,M; Lam,KL; Siewerdsen,JH (1999): Relative dosimetry using active matrix flat-panel imager. Med. Phys. 26(8), 1530-1541.

Emami,B; Lyman,J; Brown,A; Coia,L; Goitein,M; Munzenrider,JE; Shank,B; Solin,LJ; Wesson,M (1991): Tolerance of normal tissue to therapeutic irradiation. Int. J. Radiation Oncology Biol. Phys. 21, 109-122.

Essers,M; Hoogervorst,BR; van Herk,M; Lanson,H; Mijnheer,BJ (1995): Dosimetric characteristics of a liquid-filled electronic portal imaging device. Int. J. Radiation Oncology Biol. Phys. 33(5), 1265-1272.

Essers,M; Mijnheer,BJ (1999): *In vivo* dosimetry during external photon beam radiotherapy. Int. J. Radiation Oncology Biol. Phys. 43(2), 245-259.

Galbraith,DM; Martell,ES; Fueurstake,B; Norrlinger,B; Schwendener,H; Rawlinson,JA (1990): A dose-per-pulse monitor for a dual-mode medical accelerator. Med. Phys. 17(3), 470-473.

Galvin,JM; Chen,X-G; Smith,RM (1993): Combining multileaf fields to modulate fluence distributions. Int. J. Radiation Oncology Biol. Phys. 27, 697-705.

Glendinning,AG; Bonnett,DE (2000a): Dosimetric properties of the Theraview™ fluoroscopic electronic portal imaging device. Brit. J. Radiol. 73, 517-530.

Glendinning,AG; Bonnett,DE (2000b): Dosimetric properties of the Theraview electronic portal imaging device. Proc. 6th International Workshop on Electronic Portal Imaging (EPI 2K), June 5-7th 2000, Brussels, Belgium, 79. Academic Hospital - Free University, Brussels, Belgium.

Glendinning,AG; Hunt,SG; Bonnett,DE (2001a): A method for controlling image acquisition in electronic portal imaging devices. Phys. Med. Biol. 46, N39-N44.

Glendinning,AG; Hunt,SG; Bonnett,DE (2001b): Measurement of the response of Gd_2O_2S:Tb phosphor to 6MV x-rays. Phys. Med. Biol. 46, 517-530.

Glendinning,AG; Hunt,SG; Bonnett,DE (2001c): Recording accelerator monitor units during electronic portal imaging: application to collimator position verification in IMRT. Phys. Med. Biol. 46, N159-N167.

Greene,D; Willimas,PC (1997): Linear accelerators for radiation therapy. 2nd ed. Institute of Physics Publishing, Bristol.

Groh,BA; Hess,BM; Spies,L; Bortfeld,T (1998): Megavoltage computed tomography with an amorphous silicon detector array. Proceedings of the 5th International Workshop on Electronic Portal Imaging, 29-31 October 1998, Phoenix, AZ, USA, (EPI98 Organising Committee), 93-94.

Guan,H; Zhu,Y (1998): Feasibility of megavoltage portal CT using an electronic portal imaging device (EPID) and a multi-level scheme algebraic reconstruction technique (MLS-ART). Phys. Med. Biol. 43, 2925-2937.

Haas,OCL (1997): Optimisation and control systems modelling in radiotherapy treatment planning. Ph.D. Dissertation, Coventry University.

Hector,CL; Webb,S; Evans,PM (2000): The dosimetric consequences of inter-fraction patient movement on conventional and intensity modulated breast radiotherapy treatments. Radiother. Oncol. 54, 57-64.

Heijmen,BJ; Pasma,KL; Kroonwijk,M; Althof,VGM; de Boer,JCJ; Visser,AG; Huizenga,H (1995): Portal dose measurement in radiotherapy using an electronic portal imaging device (EPID). Phys. Med. Biol. 40, 1943-1955.

Hilsebecher,J; Bortfeld,T; Schlegel,W (1997): Considerations about the technical properties of an electronic portal imaging device. Proceedings of the XIIth International Conference on the Use of Computers in Radiotherapy, 27-30 May 1997, Salt Lake City, Utah, USA (Medical Physics Publishing, Madison, WI, USA), 285-287.

ICRU (1976): Determination of absorbed dose in a patient irradiated by beams of X and Gamma rays in radiotherapy procedures. Report 24. International Commission on Radiological Units, Washington, DC.

IPEM (1996): Institute of Physics and Engineering in Medicine. Report 68, A guide to commissioning and quality control of treatment planning systems. 1st. ed. Ed. J Shaw. Institute of Physics and Engineering in Medicine, York. ISBN 0 904 181 839.

IPEM (1999): Institute of Physics and Engineering in Medicine. Physics aspects of quality control in radiotherapy. 1st ed. Ed. WPM Mayles, RA Lake, *et al.* Institute of Physics and Engineering in Medicine, York. ISBN 0 904 181 91X.

James,HV; Atherton,S; Budgell,GJ; Kirby,MC; Williams,PC (2000): Verification of dynamic multileaf collimation using an electronic portal imaging device. Phys. Med. Biol. 45, 495-509.

Johansson,K-A; Karlsson,R; Thilander,A (1987): A small cylindrical ionisation chamber with watertight protection. Test according to international recommendations and evaluation of the applicability of these recommendations. Report GU-RADFYS 87:13, Dept of Radiation Physics, University of Göteborg, S-413 45, Göteborg, Sweden. October 1987.

Jordan,TJ; Williams,PC (1994): The design and performance characteristics of a multileaf collimator. Phys. Med. Biol. 39, 231-251.

Källman,P; Lind,B; Eklöf,A; Brahme,A (1988): Shaping of arbitrary dose distributions by dynamic multileaf collimation. Phys. Med. Biol. 33(11), 1291-1300.

Kerr,AT; Amm,D; Rutkevich,T (1997): A strip ion chamber for on-line monitoring of dynamic wedge treatments. Med. Phys. 24(7), 1200. Abstract 43rd Annual Meeting of the Canadian Organisation of Medical Physicists.

Kerr,A; Rutkevich,T; Amm,D (2000): A strip ion chamber for on-line monitoring of dynamic wedge treatments. Med. Phys. Submitted September 1999.

Kestin,LL; Sharpe,MB; Frazier,RC; Vicini,FA; Yan,D; Matter,RC; Martinez,AA; Wong,JW (2000): Intensity modulation to improve dose uniformity with tangential breast radiotherapy: initial clinical experience. Int. J. Radiation Oncology Biol. Phys. 48(5), 1559-1568.

Kijewski,PK; Chin,LM; Bjärngard,BE (1978): Wedge shaped dose distributions by computer-controlled collimator motion. Med. Phys. 5:, 426-9.

Kippenes,H; Gavin,PR; Rogers,D; Phillips,MH (1998): *In vivo* measurements of intensity modulated beam dosimetry. Proceedings of the Elekta Oncology Systems First Users Conference (Palm Springs, California, USA), 110-115.

Kirby,MC; Williams,PC (1993): Measurement possibilities using an electronic portal imaging device. Radiother. Oncol. 29, 237-243.

Kirby,MC (1995): A multipurpose phantom for use with electronic portal imaging devices. Phys. Med. Biol. 40, 323-334.

Kirby,MC; Williams,PC (1995): The use of an electronic portal imaging device for exit dosimetry and quality control measurements. Int. J. Radiation Oncology Biol. Phys. 31(3), 593-603.

Kirby,MC (1996): The consequences of fixed-pattern noise and image movement on electronic portal images. Phys. Med. Biol. 41, 2345-2356.

Kubo,HD; Len,PM; Minohara,S; Mostafavi,H (2000): Breathing-synchronised radiotherapy program at the University of California Davis Cancer Center. Med. Phys. 27(2), 346-353.

Leibel,SA; Ling,CC; Kutcher,GJ; Mohan,R; Cordon-Cordo,C; Fuks,Z (1991): The biological basis for conformal three-dimensional radiation therapy. Int. J. Radiation Oncology Biol. Phys. 21, 805-811.

Leong,J (1986): Use of digital fluoroscopy as an on-line verification device in radiation therapy. Phys. Med. Biol. 31, 985-992.

Ling,CC; Burman,C; Chui,CS; Kutcher,GJ; Leibel,SA; LoSasso,T; Mohan,R; Bortfeld,T; Reinstein,L; Spirou,S; Wang,XH; Wu,Q; Zelefsky,M; Fuks,Z (1996): Conformal radiation treatment of prostate cancer using inversely-planned intensity-modulated photon beams produced with dynamic multileaf collimation. Int. J. Radiation Oncology Biol. Phys. 35(4), 721-730.

Löf,J; Lind,BK; Brahme,A (1998): An adaptive control algorithm for optimization of intensity modulated radiotherapy considering uncertainties in beam profiles, patient set-up and internal organ motion. Phys. Med. Biol. 43, 1605-1628.

Lomax,A (1999): Intensity modulated methods for proton radiotherapy. Phys. Med. Biol. 44, 185-205.

LoSasso,T; Chui,C-S; Linc,CC (1998): Physical and dosimetric aspects of a multileaf collimation system used in the dynamic mode for implementing intensity modulated radiotherapy. Med. Phys. 25(10), 1919-1927.

Low,DA; Gerber,RL; Mutic,S; Purdy,JA (1998a): Phantoms for IMRT dose distribution measurement and treatment verification. Int. J. Radiation Oncology Biol. Phys. 40(5), 1231-1235.

Low,DA; Mutic,S; Dempsey,JF; Gerber,RL; Bosch,WR; Perez,CA; Purdy,JA (1998b): Quantitative dosimetric verification of an IMRT planning and delivery system. Radiother. Oncol. 49, 305-316.

Luchka,K; Chen,D; Shalev,S; Gluhchev,G; Rajapakshe,R (1996): Assessing radiation and light field congruence with a video based electronic portal imaging system. Med. Phys. 23(7), 1245-1252.

Luchka,K; Rajapakshe,R; Shalev,S (1997): Characterization and correction of geometric distortions in clinical radiotherapy images. Proceedings of the XIIth International

Conference on the Use of Computers in Radiotherapy, 27-30 May 1997, Salt Lake City, Utah, USA (Medical Physics Publishing, Madison, WI, USA), 293-294.

Ma,L; Geis,PB; Boyer,AL (1997): Quality assurance for dynamic multileaf collimator modulated fields using a fast beam imaging system. Med. Phys. 24(8), 1213-1220.

Ma,L; Boyer,AL; Xing,L; Ma,C-M (1998): An optimized leaf-setting algorithm for beam intensity modulation using dynamic multileaf collimators. Phys. Med. Biol. 43, 1629-1643.

Mackie,TR; Holmes,T; Swerdloff,S; Reckwerdt,P; Deasy,JO; Yang,J; Paliwal,B; Kinsella,T (1993): Tomotherapy: A new concept for the delivery of dynamic conformal radiotherapy. Med. Phys. 20(6), 1709-1719.

Mainprize,JG; Yaffe,MJ (1998): The effect of phosphor persistence on image quality in digital x-ray scanning systems. Med. Phys. 25(12), 2440-2454.

Maryanski,MJ; Schulz,RJ; Ibbott,GS; Gatenby,JC; Xie,J; Horton,D; Gore,JC (1994): Magnetic resonance imaging of radiation dose distributions using a polymer-gel dosimeter. Phys. Med. Biol. 39, 1437-1455.

Mattsson,LO; Johansson,K-A; Svensson,H (1981): Calibration and use of plane-parallel ionization chambers for the determination of absorbed dose in electron beams. Acta Radiol. Oncol. 20 Fasc. 6, 385-399.

Meertens,H; van Herk,M; Weeda,J (1985): A liquid ionisation detector for digital radiography of therapeutic megavoltage photon beams. Phys. Med. Biol. 30(4), 313-321.

Meyer,J; Glendinning,AG; Mills,JA; Bonnett,DE; Haas,OCL; Burnham,KJ (2000): Limitation of intensity modulation for radiotherapy of the prostate. Brit. J. Radiol. Suppl. 73, 1655. Proceedings of Radiology 2000 - Imaging, Oncology and Science, 22-24 May 2000, Birmingham, UK.

Midgley,S; Millar,RM; Dudson,J (1998): A feasibility study for megavoltage cone beam CT using a commercial EPID. Phys. Med. Biol. 43, 155-169.

Mijnheer,BJ; Battermann,JJ; Wambersie,A (1987): What degree of accuracy is required and can be achieved in photon and neutron therapy? Radiother. Oncol. 8, 237-252.

Milliken,BD; Turian,JV; Hamilton,RJ; Rubin,SJ; Kuchnir,FT; Yu,CX; Wong,JW (1998): Verification of the omni wedge technique. Med. Phys. 25(8), 1419-1423.

Mohan,R; Wang,X; Jackson,A; Bortfeld,T; Boyer,AL; Kutcher,GJ; Leibel,SA; Fuks,Z; Ling,CC (1994): The potential limitations of the inverse radiotherapy technique. Radiother. Oncol. 32, 232-248.

Mosleh-Shirazi,MA; Evans,PM; Swindell,W; Webb,S; Partridge,M (1998a): A cone-beam megavoltage CT scanner for treatment verification in conformal radiotherapy. Radiother. Oncol. 48, 319-328.

Mosleh-Shirazi,MA; Evans,PM; Swindell,W; Symonds-Tayler,JRN; Webb,S (1998b): Rapid portal imaging with a high-efficiency, large field-of-view detector. Med. Phys. 25(12), 2333-2346.

Mott,JHL; Hounsell,AR; Budgell,GJ; Wilkinson,JM; Williams,PC (1999): Customised compensation using intensity modulated beams delivered by dynamic multileaf collimation. Radiother. Oncol. 53, 59-65.

Moy,JP; Koch,A; Nielsen,MB (1993): Conversion efficiency and time response of phosphors for fast X-ray imaging with synchrotron radiation. Nuclear Instruments and Methods in Physics Research A 326, 581-586.

Munro,P; Rawlinson,JA; Fenster,A (1990): A digital fluoroscopic imaging device for radiotherapy localization. Int. J. Radiation Oncology Biol. Phys. 18(3), 641-649.

Munro,P (1995): Portal Imaging Technology: Past, Present, and Future. Semin. Radiat. Oncol. 5(2), 115-133.

Munro,P; Bouius,DC (1998): X-ray quantum limited portal imaging using amorphous silicon flat-panel arrays. Med. Phys. 25(5), 689-702.

Munro,P; Bouius,DC; Moseley,J; Martin,L; Zhang,Y; Jaffray,DA (1998): Glaring errors in transit dosimetry. Proceedings of the 5th International Workshop on Electronic Portal Imaging, 29-31 October 1998, Phoenix, AZ, USA (EPI98 Organising Committee), 128-129.

Munro,P; Mulligan,M; Heerema,T (2000a): EC-L film, EPIDs and scattered x-ray photons. Proceedings of the 6th International Workshop on Electronic Portal Imaging (EPI 2K), June 5-7th 2000, Brussels, Belgium, 52. Academic Hospital - Free University, Brussels, Belgium.

Munro,P; Mulligan,M; Heerema,T (2000b): Effects of x-ray scatter on the response of EC-L film and EPIDs. Digest of Papers of the 2000 World Congress on Medical Physics and Biomedical Engineering and Proceedings of the 22nd Annual International Conference on the IEE Engineering in Medicine and Biology Society, July 23-28 2000, Chicago's Navy pier, Chicago, USA.

Murmann,A; Lassen,S; Nyström,H (1999): Verification of intensity modulated radiation therapy with electronic portal imaging. Abstracts of the 5th Biennial ESTRO Meeting on Physics for Clinical Radiotherapy, Gottingen, Germany, 6-11 April 1999. Rad. Oncol. 51, Suppl. 1, A165.

Nakagawa,K; Aoki,Y; Akanuma,A; Onogi,Y; Terahar,A; Sakata,K; Muta,N; Sasaki,Y; Kawakami,H; Hanakawa,K (1994): Real-time monitoring in dynamic conformation therapy. Int. J. of Imaging Sys. Tech. 30(5), 1233-1238.

NE Technology Ltd. (1990): Instruction Manual for a 0.6 cc robust ionisation chamber Type 2581. NE Technologies Ltd., Reading, UK.

Nisbet,A; Thwaites,DI (1998): Polarity and ion recombination correction factors for ionization chambers employed in electron beam dosimetry. Phys. Med. Biol. 43, 435-443.

Nutting,C; Dearnaley,DP; Webb,S (2000): Intensity modulated radiation therapy: a clinical review. Brit. J. Radiol. 73, 459-469.

Ohara,K; Okumura,T; Akisada,M; Inada,T; Mori,T; Yokota,H; Calguas,MJB (1989): Irradiation synchronized with respiration gate. Int. J. Radiation Oncology Biol. Phys. 17, 853-857.

Oldham,M; Webb,S (1997): Intensity-modulated radiotherapy by means of static tomotherapy: A planning and verification study. Med. Phys. 24(6), 827-836.

Oldham,M; Baustert,I; Lord,C; Smith,TAD; McJury,M; Warrington,AP; Leach,MO; Webb,S (1998): An investigation into the dosimetry of nine-field tomotherapy irradiation using BANG-gel dosimetry. Phys. Med. Biol. 43, 1113-1132.

Paliwal,BR; Zaini,M; McNutt,T; Fairbanks,EJ; Kitchen,R (1996): A consistency monitor for radiation therapy. Med. Phys. 23(10), 1805-1807.

Parsaei,H; El-Khatib,E; Rajapakshe,R (1998): The use of an electronic portal imaging system to measure portal dose and portal dose profiles. Med. Phys. 25(10), 1903-1909.

Partridge,M; Evans,PM; Msoleh-Shirazi,A; Convery,D (1998): Independent verification using portal imaging of intensity-modulated beam delivery by the dynamic MLC technique. Med. Phys. 25(10), 1872-1879.

Partridge,M; Symonds-Tayler,JRN; Evans,PM (1999a): A large-area ionisation chamber for portal image calibration. Phys. Med. Biol. 44, 271-279.

Partridge,M; Evans,PM; Symonds-Tayler,JRN (1999b): Optical scattering in camera-based electronic portal imaging. Phys. Med. Biol. 44, 2381-2396.

Partridge,M; Symonds-Tayler,JRN; Evans,PM (2000a): IMRT verification with a camera-based electronic portal imaging device. Phys. Med. Biol. 45, N183-N196 .

Partridge,M; Evans,PM; van Herk,M; Ploeger,LS; Budgell,GJ; James,HV (2000b): Leaf position verification during dynamic beam delivery: A comparison of three applications using electronic portal imaging. Med. Phys. 27(7), 1601-1609.

Pasma,KL; Kroonwijk,M; Visser,AG; Heijmen,BJM (1997): Portal dose measurements with a video-based electronic portal imaging device using a deconvolution algorithm. Proceedings of the XIIth International Conference on the Use of Computers in Radiotherapy, 27-30 May 1997, Salt Lake City, Utah, USA, 282-284. Medical Physics Publishing, Madison WI, USA.

Pasma,KL; Kroonwijk,M; de Boer,JCJ; Visser,AG; Heijmen,BJM (1998): Accurate portal dose measurement with a fluoroscopic electronic portal imaging device (EPID) for open and wedged beams and dynamic multileaf collimation. Phys. Med. Biol. 43, 2047-2060.

Pasma,KL; Kroonwijk,M; van Dieren,EB; Visser,AG; Mijnheer,BJM (1999a): Verification of compensator thickness using a fluoroscopic electronic portal imaging device. Med. Phys. 26(8), 1524-1529.

Pasma,KL; Dirkx,MLP; Kroonwijk,M; Visser,AG; Heijmen,BJM (1999b): Dosimetric verification of intensity modulated beams produced by dynamic multileaf collimation using an electronic portal imaging device. Med. Phys. 26(11), 2373-2378.

Pasma,KL; Kroonwijk,M; Quint,S; Visser,A; Heijmen,BJM (1999c): Transit dosimetry with an electronic portal imaging device (EPID) for 115 prostate cancer patients. Int. J. Radiation Oncology Biol. Phys. 45(5), 1297-1303.

Paul,T; Leu,M; Rosemark,P; Solberg,T; Smathers,J (1998): Characterization of an a-Si:H (Amorphous Silicon) array detector for real-time dosimetric verification in dynamically shaped radiotherapy. Med. Phys. 25(7) Part 1, A151.

Paul,T; Solberg,T; Leu,M; Rosemark,P; Mollenhauer,U; Agazarian,N; Smathers,J (2000): Real-time verification and feedback for clinically deliverable IMRT plans. Proceedings of

the 1st International Workshop on IMRT in Clinical Practice (IMRT 2K), June 8-9th, Brussels, Belgium, 43. Academic Hospital, Free University, Brussels.

Purdy,JA (1996): Intensity modulated radiation therapy. Int. J. Radiation Oncology Biol. Phys. 35(4), 845-846.

Rajapakshe,R; Radcliffe,TJ; Shalev,S (1993): Temporal and spatial statistics of image noise in real-time video imaging: a study of on-line portal imaging. Proceedings of the International Society for Optical Engineering, Physics of Medical Imaging, Newport Beach, CA, USA (Society of Photo-Optical Instrumentation Engineers, Bellingham, Washington, USA) 1896, 62-72.

Rajapakshe,R; Shalev,S (1996): Output stability of a linear accelerator during the first three seconds. Med. Phys. 23(4), 517-519.

Rajapakshe,R; Parsaei,H; Wolters,J; El-Khatib,E; Luchka,KB; Shalev,S (1996): Exit Dosimetry with electronic portal imaging devices. Proceedings of the 4th International Workshop on Electronic Portal Imaging, 10-12 June 1996, Amsterdam, The Netherlands (Medical Faculty, Free University, Amsterdam, The Netherlands), 49.

Rajapakshe,R (1998): Calibration of an electronic portal imaging device for exit dosimetry. Proceedings of the 5th International Workshop on Electronic Portal Imaging, 29-31 October 1998, Phoenix, AZ, USA (EPI98 Organising Committee), 140-141.

Roback,DM; Gerbi,BJ (1995): Evaluation of electronic portal imaging device for missing tissue compensator design and verification. Med. Phys. 22(12), 2029-2034.

Royal College of Radiologists (1996): Guidelines for the management of the unscheduled interruption or prolongation of a radical course of radiotherapy. Board of the Faculty of Clinical Oncologists, Royal College of Radiologists, London, UK. RCR Ref. No. BFCO(96)4. ISBN 1 872599 26 5.

Rudin,S; Patel,JJ; Bednarek,DR (1998): Decay time measurements of imaging phosphor materials. Med. Phys. 25(7) Part 1, A214.

Sandel,BR; Collins,DF; Broadfoot,AL (1986): Effect of phosphor persistence on photometry with image intensifiers and integrating readout devices. Applied Optics 25(20), 3697-3704.

Shalev,S; Lee,T; Leszczynski,K; Cosby,S; Chu,T (1989): Video techniques for on-line portal imaging. Comp. Med. Imag. Graphics 13(3), 217-226.

Shepherd,JA; Gruner,SM; Tate,MW; Tecotzky,M (1995): A study of persistence in gadolinium oxysulphide x-ray phosphors. Proceedings of the International Society for Optical Engineering, 13 July 1995, San Diego, CA, USA (Society of Photo-Optical Instrumentation Engineering, Washington,USA) 2519, 24-30.

Siewerdsen,JH; Jaffray,DA (1999a): A ghost story: spatio-temporal response characteristics of an indirect-detection flat-panel imager. Med. Phys. 26(8), 1624-1641.

Siewerdsen,JH; Jaffray,DA (1999b): Cone-beam computed tomography with a flat-panel imager : Effects of image lag. Med. Phys. 26(12), 2635-2647.

Smitsmans,MHP; Ploeger,LS; Gilhuijs,KGA; van Herk,M (2000): A system for field shape verification during dynamic IMRT. Proceedings of the 6th International Workshop on Electronic Portal Imaging (EPI 2K), June 5-7th 2000, Brussels, Belgium, 60. Academic Hospital - Free University, Brussels, Belgium.

Steel,GG (Ed.) (1997): Basic Clinical Radiobiology. 2nd ed. Arnold, London.

Svenson,R; Källman,P; Brahme,A (1994): An analytical solution for the dynamic control of multileaf collimators. Phys. Med. Biol. 39, 37-61.

Swank,RK (1974): Measurement of absorption and noise in an x-ray image intensifier. J. Appl. Phys. 45(8), 3673-3678.

Swindell,W (1991): The lens coupling efficiency in megavoltage imaging. Med. Phys. 18(6), 1152-1153.

Symonds-Tayler,JRN; Partridge,M; Evans,PM (1997): An electronic portal imaging device for transit dosimetry. Phys. Med. Biol. 42, 2273-2283.

Tait,D (1990): Conformal therapy. Br. J. Cancer 62, 702-704.

Thwaites,DI; Burns,DT; Klevenhagen,SC; Nahum,AE; Pitchford,WG (1996): The IPEMB code of practice for electron dosimetry for radiotherapy beams of initial energy from 2 to 50 MeV based on air kerma calibration. Phys. Med. Biol. 41, 2257-2603.

Tsai,J-S; Wazer,DE; Ling,MN; Wu,JK; Fagundes,M; DiPetrillo,T; Kramer,B; Koistinen,M; Engler,MJ (1998): Dosimetric verification of the dynamic intensity modulated radiation therapy of 92 patients. Int. J. Radiation Oncology Biol. Phys. 40(5), 1213-1230.

van Herk,M; Boellaard,R; Brugmans,M; van Dalen,A (1996): Feasibility of the PortalVision system for verification of dynamic therapy. Proceedings of the 4th International Workshop on Electronic Portal Imaging, 10-12 June 1996, Amsterdam, The Netherlands (Medical Faculty, Free University, Amsterdam, The Netherlands), 53.

van Herk,M; Meertens,H (1988): A matrix ionisation chamber imaging device for on-line patient set-up verification during radiotherapy. Radiother. Oncol. 11, 369-378.

van Santvoort,JPC; Heijmen,BJM (1996): Dynamic multileaf collimation without 'tongue-and-groove' underdosage. Phys. Med. Biol. 41, 2091-2105.

Verellen,D; Linthout,N; van den Berge,D; Bel,A; Storme,G (1997): Initial experience with intensity-modulated conformal radiation therapy for treatment of the head and neck region. Int. J. Radiation Oncology Biol. Phys. 39(1), 99-114.

Visser,AG; Huizenga,H; Althof,VGM; Swanenburg,BN (1990): Performance of a prototype fluoroscopic radiotherapy imaging system. Int. J. Radiation Oncology Biol. Phys. 18, 43-50.

Vos,PH; Vossepoel,AM (1994): Verification using digital portal imaging: implementation and clinical use. Proceedings of the XIth International Conference on the Use of Computers in Radiotherapy, 20-24 March 1995, Manchester, UK (Medical Physics Publishing, Madison,WI, USA), 114-115.

Wang,X; Spirou,S; LoSasso,T; Stein,J; Chui,C-S; Mohan,R (1996): Dosimetric verification of intensity-modulated fields. Med. Phys. 23(3), 317-327.

Webb,S (1997): The Physics of Conformal Radiotherapy: Advances in Technology. 1st ed. Institute of Physics Publishing, Bristol.

Webb,S (1998): Advances in treatment with intensity-modulated conformal radiotherapy. Tumori 84, 112-126.

Wilkinson,J; Williams,P; Hounsell,A; Budgell,G; Mott,J (1998): Customised compensation and class solutions. Proceedings of the Elekta Oncology Systems First Users Conference (Palm Springs, California, USA), 66-74.

Wittkämper,FW; Burgmans,MJP; Lebesque,JV; van der Horst,A; Mijnheer (1998): Clinical implementation of IMRT in the Netherlands Cancer Institute. Proceedings of the Elekta Oncology Systems First Users Conference (Palm Springs, California, USA), 76-83.

Yeboah,C; Pistorius,S (2000): Monte Carlo studies of the exit photon spectra and dose to a metal/phosphor portal imaging system. Med. Phys. 27(2), 330-339.

Yin,F-F; Schell,MC; Rubin,P (1994): A technique of automating compensator design for lung inhomogeneity correction using an electronic portal imaging device. Med. Phys. 21(11), 1729-1732.

Yu,CX; Jaffray,DA; Wong,JW (1998): The effects of intra-fraction organ motion on the delivery of dynamic intensity modulation. Phys. Med. Biol. 43, 91-104.

Zeman,HD; Samant,SS; Lovhoiden,G; Weinberg,B; Sawant,A (1998): Portal imaging with a CsI(Tl) transparent scintillator x-ray detector. Proceedings of the International Society for Optical Engineering, Physics of Medical Imaging, Newport Beach, CA, USA, 3336, 175-186. Society of Photo-Optical Instrumentation Engineers, Bellingham, Washington, USA.

Zhu,Y; Jiang,X-Q; van Dyk,J (1995): Portal dosimetry using a liquid ion chamber matrix: Dose response studies. Med. Phys. 22(7), 1101-1106.

Zhu,Y; Yeo,JI (1999): Portal dosimetry using x-ray film: An experimental and computational study. Med. Phys. 26(11), 2403-2409.